The impact of microorganisms on the surface of pyrite: Implications for bioflotation

by

Sian La Vars, B. Tech (Forensic and Analytical Chemistry) (Hons)

Thesis
Submitted to Flinders University
for the degree of

Doctor of Philosophy

College of Science and Engineering

14th November 2018

Abstract

Sulfide minerals are of significance in the mineral processing industry as major sources of base metals; however, their similar physicochemical properties make them challenging to separate. Bioflotation is the process by which microorganisms modify the mineral hydrophobicity, enabling selective separation of sulfide minerals. This has several advantages over traditional froth flotation, with the microorganisms being environmentally friendly and non-pathogenic.

To determine if it is the extracellular polymeric substances (EPS), or the combination of EPS and microorganisms that alter the hydrophobicity of the gangue mineral pyrite, the microbial strains *Acidithiobacillus ferrooxidans*, *Leptospirillum ferrooxidans*, and *Acidianus brierleyi* were investigated. Cell growth and solution conditions were examined, and propagation of cells on the surface of pyrite was investigated. The physical and chemical properties of the mineral surface was studied using scanning electron microscopy (SEM), energy dispersive X-ray spectroscopy (EDX), atomic force microscopy (AFM), contact angle, photoemission electron microscopy (PEEM), scanning transmission X-ray microscopy (STXM), near edge adsorption fine structure (NEXAFS) and time of flight – secondary ion mass spectroscopy (ToF-SIMS).

This study found both *A. ferrooxidans* and *L. ferrooxidans* displayed attachment at very early stages of exposure, with no obvious preference for surface defects. The most significant difference in hydrophobicity between pyrite exposed to bacteria and the control occurs at the earliest exposure. *L. ferrooxidans* and *A. ferrooxidans* showed decreases in contact angle of 36° and 25°, respectively.

The decrease in hydrophobicity observed in pyrite exposed to mesophiles coincides with the presence of polysaccharide and fatty acid-type structures. It is proposed that these compounds assist with initial cell adhesion to pyrite, before cells produce hydrophobic proteins as colonies begin to spread on the surface. This study suggests that the nature of bacterial excretions changes over the course of exposure, with significant difference in EPS production between strains, which suggests the point of cell harvest and EPS extraction may impact mineral separation efficiency.

It was found that the presence of yeast extract in the growth medium of *A. brierleyi* made it impossible to determine with accuracy the action of EPS on the surface, and potentially impeded reactions on the surface. Investigation of the impact of *A. brierleyi* on pyrite in the absence of yeast extract found a decrease in contact angle of 24° compared to the control at 2 h.

It was found that *A. brierleyi* produced significantly less EPS than the other strains investigated, and that this strain is unlikely to alter the surface through direct attack, with little to no cell attachment observed on the pyrite surface.

These studies have shown that EPS production by cells at early stages of attachment creates significant improvement in the wettability of pyrite, without the need for extensive biofilm formation. This has important implications for the depression of pyrite for bioflotation, which would benefit from short periods of exposure and low cell density requirements. The analytical techniques listed previously were successfully applied to the investigation of physical properties and chemical species on the pyrite surface, and enabled to identification of polysaccharide and lipid-type compounds as being responsible for the decreased hydrophobicity of the mineral.

Declaration

I certify that this thesis does not incorporate without acknowledgment any material previously submitted for a degree or diploma in any university; and that to the best of my knowledge and belief it does not contain any material previously published or written by another person except where due reference is made in the text

Sian La Vars, B. Tech (Forensic and Analytical Chemistry) (Hons)

..... Date: 12 / 04 / 2018

(Signature)

Table of Contents

Table of Figures

Glossary

AFM	Atomic Force Microscopy
BSA	Bovine Serum Albumin
BSE	Backscattered Electrons
CAH	Contact Angle Hysteresis
CCD	Charge Coupled Device
DNA	Deoxyribonucleic Acid
DSM 150	Thermophile medium solution
DSMZ	Deutsche Sammlung von Mikroorganism und Zellkulturen
EDTA	Ethylenediaminetetra acetic acid
EDX	Energy Dispersive X-ray Spectroscopy
Eh	Solution potential
EPUS	Elliptically Polarized Undulator
FESEM	Field Emission Scanning Electron Microscope
HH	Mesophile medium solution
HMDS	Hexamethyl-disilazane
ICPOES	Induction Coupled Plasma Optical Emission Spectroscopy
LMIG	Liquid Metal Ion Gun
NEXAFS	Near Edge X-ray Adsorption Fine Structure
NSRRC	National Synchrotron Radiation Research Centre, Taiwan
OD	Optical Density
OSA	Optical Selection Aperture/ Order Sorting Aperture
PEEM	Photoemission Electron Microscopy
PSI	Paul Scherrer Insitut
RF	Radio Frequency
ROI	Regions of Interest
SE	Secondary Electrons
SEM	Scanning Electron Microscopy
SLS	Swiss Light Source
STXM	Scanning Transmission Electron Microscopy
TEY	Total Electron Yield
ToF-SIMS	Time of Flight – Secondary Ion Mass Spectrometry
UV	Ultraviolet light
UV-Vis	Ultraviolet – Visible Spectrophotometry

Acknowledgements

First and foremost, I wish to thank my principle supervisor Associate Professor Sarah Harmer for her unwavering support and guidance, and for providing me with the opportunity to work in such an exciting and diverse field. Without her continuing advice and knowledge, this body of work would not have been possible. I also wish to thank my co-supervisor, Professor Jamie Quinton, for his counsel, advice and perspective. May the force be with you.

For Dr Chris Gibson, Dr Ashley Slattery and Dr John Denman, I could not have done this without your training, your time, your humour, your patience and your instruments (AFM, SEM, ToF-SIMS). Thank you all. My gratitude is also extended to Dr Jason Young and Dr Daniel Jardine at Flinders Analytical for their assistance and advice on solution analysis, and to the wonderful staff at Adelaide Microscopy for their assistance in sample preparation.

David Vincent and Dr Sean Graney, you were there for any and every little emergency in our new lab, thank you for not getting sick of the sight of me!

For the members of the Harmer research group – especially Belinda and Zoe – thank you for the caffeine, the sympathy, the practical solutions, the support, and most importantly, your friendship. This would have been a whole lot harder without you.

I am extremely grateful for the staff at the BL05B2 beamline at the NSRRC for their invaluable assistance. Patrick, you keep us fuelled for those long nights at the synchrotron; thank you. I also wish to thank Dr Benjamin Watts at the PolLux beamline at the SLS for his training on the STXM.

My eternal gratitude goes to my wonderful family. Mum and Dad, I would not have been able to do this if not for you. Words are not enough. Thanks Gran, Pa and Nan, for all your love, forever. Thanks Jarryd, and my amazing Uncles Ross, Nev, Bob, and Brian, and Aunts Andrea and Robin, for your support and for giving me places to live while I made this journey. Thanks to all my friends who came along for the ride; there are too many of you to mention and not enough space in the world. And for Oskar, for being there every step of the way, for being there every day, even while working on his own thesis. This thesis is all of yours as much as it is mine.

This work has been supported by the Australian Research Council under FT110100099. The authors acknowledge the facilities, and the scientific and technical assistance, of the Australian Microscopy & Microanalysis Research Facility at the South Australian Regional Facility (SARF) SA Nodes, Flinders University and Adelaide University.

Publication List

Journal Articles

S. M. La Vars, K. Newton, J. S. Quinton, P.-Y. Cheng, D.-H. Wei, Y.-L. Chan, S. L. Harmer, *Surface chemical characterisation of pyrite exposed to Acidithiobacillus ferrooxidans and associated extracellular polymeric substances*, Minerals, 2018. 8(**3**): 132

M. H. Wahid, E. Eroglu, **S. M. LaVars**, K. Newton, C. T. Gibson, U. H. Stroeher, X. Chen, R. A. Boulos, C. L. Raston, S. L. Harmer, *Microencapsulation of bacterial strains in graphene oxide nano-sheets using vortex fluidics*, RSC Adv., 2015. 47(**5**): p 37424-37430

Oral Presentations

Sian La Vars, Jamie S. Quinton, Sarah L. Harmer, Flinders Centre for NanoScale Science and Technology 4th Annual Conference, Adelaide, Australia, July of 2014, "Photoelectron Emission Microscopy (PEEM) strengths, weaknesses and applications for material surface studies"

Sian La Vars, 3 Minute Thesis, Flinders University, competition finalist, 2013, "The Bioflotation of Minerals"

Poster Presentations

S.M. La Vars, J. S. Quinton, S.L. Harmer, ANZSMS conference, 2017, "Surface chemical changes induced by mesophiles on pyrite"

S.M. La Vars, J. S. Quinton, S.L. Harmer, CNST conference, 2016, "Interactions of *A. brierleyi* with Pyrite, and the Importance of Yeast Extract"

S.M. La Vars, J. S. Quinton, S.L. Harmer, CNST conference 2015, "ToF-SIMS and Captive Bubble Analysis of Pyrite Exposed to *Acidithiobacillus ferrooxidans*"

S.M. La Vars, K. Newton, J. S. Quinton, S.L. Harmer, ICONN 2014, "Propagation of Acidithiobacillus ferrooxidans (A.f) on pyrite surfaces investigated by Scanning Electron Microscopy (SEM) and sessile drop contact angle"

S.M. La Vars, J. S. Quinton, S.L. Harmer, CNST conference, 2012, "The role of EPS extracted from bacteria in the bioflotation of pyrite and chalcopyrite"

1 Introduction

1.1 Project Context

Bioflotation is the application of microorganisms and/or their excretions to the separation of minerals by the selective alteration of their surface properties [1-5]. Ore containing valuable or precious metals is made to repel water and float while the unwanted ore, commonly known as gangue, is made to attract water to remain in the waste materials known as tailings [2, 6, 7]. Traditional froth flotation uses chemical reagents to selectively alter a minerals propensity for repelling or attracting water, however there are major health and environmental issues surrounding many of these reagents [6-8]. The use of microorganisms to replace these chemical reagents has several significant advantages, however the fundamental understanding of microbial interactions with mineral surfaces is still open to debate [4, 9-11].

Chalcopyrite ($CuFeS_2$), a sulfide mineral, is the world's primary source of copper [8, 12]. Copper is used in plumbing, electronic products, car components and building construction, which makes chalcopyrite a desirable commercial mineral [1, 8, 12]. Pyrite (FeS_2) is also a sulfide mineral, and although it can be used as a source of sulfur, it is generally considered an undesirable gangue mineral that is often found in ores along with the copper-containing chalcopyrite [6, 8]. To extract the copper from chalcopyrite, these two minerals must be first separated from each other.

In industry, froth-flotation is a common process for separating the desirable sulfide minerals from the gangue sulfide minerals [6, 7]. To achieve this, various chemicals are required to selectively alter the mineral surface chemistry so that the required minerals float and the gangue sinks, or vice versa [2, 6]. Unfortunately, the chemicals used to bring about these changes in mineral hydrophobicity – propensity for repelling water – are often harsh and environmentally hazardous [8]. For example, sodium ethyl xanthate, a commonly used collector in the separation of sulfide minerals, has caused the residents near a mine in Stawell to complain of "foul odour, headache, dizziness and nausea", and has also caused the evacuation of 100 people from a railway and the hospitalization of 6 people in Alice Springs [13]. Another commonly used compound in the separation of sulfides – sodium cyanide – has caused several human fatalities through mine tailings contaminating water sources [14], as well as a significant amount of wildlife fatalities, with 800 birds dying in just one accidental release in the Northern Territory in 2002 [15].

It has been proposed that microorganisms might be superior over environmentally hazardous and corrosive chemicals – which are costly to store and difficult to handle – for modifying mineral

hydrophobicity, as they are environmentally friendly and non-pathogenic [1-5]. There have been several major obstacles identified by studies that must be overcome for bioflotation to be applied at an industrial scale; uncertainty about quantity of microorganisms or their products required for flotation, unfamiliarity with applying microorganisms to an industrial scale operation, and the costs associated with processes required to operate with microorganisms as flotation agents [16-18].

To date, the mechanism of cell interaction with minerals has not been fully elucidated, and no specific biomolecules have been identified as potential products that may enhance mineral recovery or depression in bioflotation [17]. Many microorganisms are natural producers of extracellular polymeric substances (EPS), which enable them to adhere to surfaces they contact and form a biofilm. Currently, it is not known whether it is EPS or the combination of EPS and microbial cells that affects hydrophobicity, and although several mechanisms have been suggested, opinion is divided as to whether EPS mediates the process between cell and mineral, or whether it is EPS that alters the mineral directly. Current thinking is also divided as to whether contact between either EPS or cells and mineral is a prerequisite for any alteration in hydrophobicity [4, 9-11].

1.2 Project Aims

This project aims to identify the mechanism through which several different acidophilic microorganisms alter the surface properties of the gangue sulfide mineral pyrite, with specific attention to the role played by extracellular polymeric substances (EPS).

The aims of this thesis are:

1) To elucidate the mechanism(s) through which three different microorganisms interact with the sulfide mineral pyrite, a ubiquitous gangue mineral. As each microorganism utilises different nutrient sources – ferrous iron, elemental sulfur, or a combination of both – it is possible that each will respond uniquely to the pyrite mineral.

2) To identify components in the excretions of the microorganisms and their relation to the mineral surface properties and solution chemistry, and compare excretions across strains. If cells require attachment to the mineral surface, their excretions are likely to exhibit different characteristics to planktonic cells that do not attach to the mineral.

3) To correlate the microbial metabolic products, inorganic surface species, and surface morphology produced during the interaction of microorganisms with pyrite with changes in the surface hydrophobicity of the mineral surface. This has potentially important implications for the field of bioflotation, which would ideally require low cost, high

efficiency alternatives to current chemical flotation reagents. This will be dependent on time, temperature, pH, cell concentration and growth rate, and is likely to vary across each strain. The formation of biofilm across the mineral surface is expected.

1.3 Structure of Thesis

This thesis will continue in Chapter 2 with a literature review on the principles behind froth flotation and bioflotation, and the current knowledge and use of the microorganisms applied to these systems.

Chapter 3 describes the principles behind the analytical techniques used in this project, along with the experimental methods used to grow the microorganisms and the preparation of samples.

Chapters 4 through 6 show the experimental results and interpretation of each of the microorganisms examined over the course of this project, with the intent of determining the effect of cells and their excretions on the hydrophobicity of the mineral pyrite, and determining the mechanism through which the cells interact with the mineral.

In Chapter 4, pyrite was exposed to the bacterium *Acidithiobacillus ferrooxidans*, finding extracellular polymeric substances mediates attachment of cells to the surface, but that cells are not required to colonise the surface for EPS to decrease the hydrophobicity of pyrite in short periods of time. Polysaccharide-type compounds were identified as key components responsible for the decrease in hydrophobicity.

The bacterium *Leptospirillum ferrooxidans* was exposed to pyrite in Chapter 5, with similar results observed as the previous chapter. The proportion of EPS on the surface of pyrite exposed to *L. ferrooxidans* was found to be greater, suggesting this strain would be ideal for EPS extraction experiments, and that fewer cells are required for better separation.

Chapter 6 shows the investigation of *Acidianus brierleyi* and its interaction with pyrite, finding cells do not appear to attach to the pyrite surface and do not produce EPS in large enough quantities to attach. The lack of attachment may be due to preferential consumption of yeast extract rather than the mineral.

In Chapter 7, a comparison is made to *Acidianus brierleyi* and its interaction with pyrite without the presences of the growth enhancement of yeast extract that is typically included in the growth medium. It was found that the removal of yeast extract did not alter cell attachment, however there

were significant chemical changes on the surface suggesting some cell products are present on the surface over periods when hydrophobicity is decreased.

Chapter 8 will present a summary of the work and the major conclusions drawn from this project, as well as suggestions for potential pathways for future investigations of this system.

1.4 References

1. Chen, M.-L., Zhang, L., Gu, G.-H., Hu, Y.-H., Su, L.-J., *Effects of microorganisms on surface properties of chalcopyrite and bioleaching.* Transactions of Nonferrous Metals Society of China, 2008. **18**(6): p. 1421-1426.
2. Govender, Y., Gericke, M,, *Extracellular polymeric substances (EPS) from bioleaching systems and its application in bioflotation.* Minerals Engineering, 2011. **24**(11): p. 1122-1127.
3. Rao, H.K., Vilinska, A., Chernyshova, I. V., *Minerals bioprocessing: R & D needs in mineral biobeneficiation.* Hydrometallurgy, 2010. **104**(3–4): p. 465-470.
4. Farahat, M., Hirajima, T., Sasaki, K., Aiba, Y., Doi, K., *Adsorption of SIP E. coli onto quartz and its applications in froth flotation.* Minerals Engineering, 2008. **21**(5): p. 389-395.
5. Mehrabani, J.V., Mousavi, S. M., Noaparast, M., *Evaluation of the replacement of NaCN with Acidithiobacillus ferrooxidans in the flotation of high-pyrite, low-grade lead–zinc ore.* Separation and Purification Technology, 2011. **80**(2): p. 202-208.
6. Nagaraj, D.R., *Minerals Recovery and Processing*, in *Kirk-Othmer Encyclopedia of Chemical Technology*. 2000, John Wiley & Sons, Inc. p. 595-679.
7. Kawatra, S.K. *Flotation Fundamentals*. Mining Engineering Handbook, 2009. 30.
8. Wills, B.A., *Wills' Mineral Processing Technology*. 7th ed, ed. T.J. Napier-Munn. 2006, Oxford: Elsevier. 444.
9. Brandl, H., *Microbial Leaching of Metals*, in *Biotechnology Set*. 2008, Wiley-VCH Verlag GmbH. p. 191-224.
10. Crundwell, F.K., *How do bacteria interact with minerals?* Hydrometallurgy, 2003. **71**(1–2): p. 75-81.
11. Rohwerder, T., Sand, W., *Mechanisms and biochemical fundamentals of bacterial metal sulfide oxidation*, in *Microbial Processing of Metal Sulfides*, E.R.D.a.W. Sand, Editor. 2007 Springer. p. 35-58.
12. Buckley, A.N., Woods, R., *An X-ray photoelectron spectroscopic study of the oxidation of chalcopyrite.* Australian Journal of Chemistry, 1984. **37**(12): p. 2403-2413.
13. *Sodium Ethyl Xanthate*, in *Priority Existing Chemical*. 1995, Worksafe Australia: Sydney. p. 1-66.
14. Eisler, R., Wiemeyer, S. N., *Cyanide hazards to Plants and Animals from Gold Mining and Related Water Issues.* Rev Environ Contam Toxicol, 2004. **183**: p. 21-54.
15. *Sodium Cyanide*, in *Priotrity Existing Chemical Assessment Report No. 31*. 2010, Department of Health and Ageing NICNAS. p. 1-333.
16. Smith, R.W., Miettinen, M., *Microorganisms in flotation and flocculation: Future technology or laboratory curiosity?* Minerals Engineering, 2006. **19**(6–8): p. 548-553.
17. Behera, S.K., Mulaba-Bafubiandi, A. F., *Microbes Assisted Mineral Flotation a Future Prospective for Mineral Processing Industries: A Review.* Mineral Processing and Extractive Metallurgy Review, 2017. **38**(2): p. 96-105.
18. Otsuki, A., Ohshima, H., *Use of Microorganisms for Complex Ore Beneficiation: Bioflotation as an Example*, in *Encyclopedia of Biocolloid and Biointerface Science 2V Set*. 2016, John Wiley & Sons, Inc. p. 108-117.

2 Literature Review

This review will encompass current industrial practices around the flotation of sulfide ores, the physical and structural properties of the minerals of interest, and current studies into the use of microorganisms for selective mineral surface modification. The advantages and limitations of bioflotation will be explored, as will the mechanisms of microbial-mineral interactions that drive mineral surface modification, over which current literature is divided.

The microorganisms of interest to this study are described, and their previous applications in the field of both bioleaching and bioflotation will be reviewed, as will current understanding of microbial products and their extraction for mineral modification. The analytical techniques applied to the aqueous media solutions and mineral surfaces in previous studies will be explored to demonstrate their suitability and limitations to this investigation.

2.1 Froth Flotation

Froth flotation is a method of separating valuable minerals from unwanted minerals, referred to as gangue. This technique is applied to ores containing coal, precious metals and both sulfidic and non-sulfidic ores, and has allowed the mining of low-grade ores to become economically viable [1, 2]. The process of froth flotation is used to treat complex sulfide mineral ores containing the base metals copper, lead, zinc and nickel, as well as valuable metals such as gold and platinum [2].

Froth flotation first requires the ore to be reduced to fine particulates, typically 38-75 µm in size, to maximise the efficiency with which the particles interact with the air bubbles [3]. It is then placed in a vat of water to be constantly agitated whilst air is pumped through via a rotating shaft. In this system, hydrophilic particles sink to be washed away, whereas hydrophobic particles attach to the air bubbles and float to the surface, where they are either scooped off, or collected through an over-flow system (see Figure 2.1) [1, 2, 4, 5].

Figure has been removed due to copyright restrictions

Figure 2.1: Schematic of a froth flotation cell adapted from [6].

The hydrophobicity of the minerals is determined by the surface chemistry and morphology of the particles involved, and is strongly influenced by pH, oxidation-reduction potential (Eh),

temperature, surface heterogeneity and oxidation [1, 2, 5, 7]. Where flotation is not naturally occurring, or when the minerals in the ore have similar hydrophobicity, chemical regulators called flotation reagents are used to alter the surface chemistry of minerals and aid separation in the froth-flotation system [1, 5]. These flotation reagents shall be discussed in more detail in section 2.1.2.

Changes in the surface chemistry of the minerals can occur naturally prior to flotation upon exposure to air, water and pre-processing solutions in a process called leaching; a series of chemical reactions by which valuable metals can be extracted from a mineral by converting the metal to a water-soluble form. It is often used both pre- and post-flotation to economically draw greater amounts of desired metals such as copper and gold from gangue ore [2, 8]. Tailings – the waste slurry from the flotation process – is often pumped into "heaps", where the natural oxidation of sulfide minerals in the presence of water produces sulfuric acid, and oxidants in the form of reduced metal ions leached from the mineral that return to react again [9-11]. These reactions are of importance for sulfide mineral processing, and are dependent on the individual mineral, as will be discussed in the following sections.

2.1.1 Sulfide Minerals

2.1.1.1 Pyrite

Pyrite (FeS_2) is the most commonly occurring sulfide mineral in the Earth's crust, and is often associated with high-value metals such as gold, and economically useful copper sulfide ores [12, 13]. Pyrite is naturally hydrophobic, especially at low pH, due to sulfur-rich species on the mineral surface, and as such floats readily in aqueous solutions under a wide range of conditions [14, 15]. The efficient separation of pyrite, an undesirable gangue mineral, from valuable metal ore is of high industrial importance.

The pyrite unit cell, shown in Figure 2.2, has a cubic, face-centred crystallographic arrangement. The Fe ions occupy the face centre and corner positions on the unit cell at the centre of a distorted octahedral arrangement, while the edges and centre of the cube are occupied by S anion pairs [16]. This results in the six-fold coordination of Fe ions, with each S coordinated to one S and six Fe in a distorted tetrahedral arrangement, with the layers alternating in orientation [16, 17]. The interatomic distance between the sulfur-sulfur bonds is 2.14 Å, while the iron-sulfur bonds are 2.27 Å in length [18]. The unit cell contains four FeS_2 formula units. This arrangement has a density of approximately 5.02 $g.cm^{-3}$. Pyrite is naturally found with a cubic {100} [17] morphology, but can also occur in {210} and {111} morphologies that form pyritohedral and octahedral structures, respectively [12, 19].

Figure has been removed due to copyright restrictions

Figure 2.2: Pyrite unit cell diagram [20].

The oxidation states of pyrite are considered to be $Fe^{2+}(S_2)^{2-}$, with the electronic structure consisting of covalently bonded overlap of the Fe 3*d* and S 3*p* valence electrons [12, 19, 21]. The valence band consists primarily of non-bonding Fe 3*d* t_{2g} states, below which a bonding S 3*p* – Fe 3*d* e_g occurs, with the conduction band consisting of mixed Fe 3*d* e*g and S 3*p* states [12]. Pyrite is a semiconductor, and is diamagnetic with no magnetic moment at room temperature due to its low-spin configuration, with a band gap of 0.95 eV. It can vary between p- and n-type depending on the Fe: S ratio and amount of trace elements present in the lattice [12, 16, 19, 21, 22].

Oxidation can occur on exposure of pyrite to oxygen and water in atmosphere, and the surface species that occur when pyrite is oxidised include jarosites, iron oxides, hydroxides and sulfates [4, 12, 22]. The oxidation reactions postulated by previous leaching studies that produce acid, ferric iron and sulfate species are shown in Equations 2.1-2.3 [2, 10-12, 19, 23].

$$4FeS_2 + 14O_2 + 4H_2O \rightarrow 4Fe^{2+} + 8SO_4^{2-} + 8H^+ \quad (2.1)$$

$$Fe^{2+} + ¼O_2 + H^+ \rightarrow Fe^{3+} + ½H_2O \quad (2.2)$$

$$FeS_2 + 14Fe^{3+} + 8H_2O \rightarrow 15Fe^{2+} + 2SO_4^{2-} + 16H^+ \quad (2.3)$$

Various sulfoxy intermediates and Fe(III)-oxyhydroxides are also produced during this oxidation process, although their formation is affected by temperature and pH [10, 23-25]. These reactions, shown in Equations 2.4 and 2.5, occur at the surface of the mineral, altering the surface chemistry continuously. The pH must remain low to prevent the formation of unwanted jarosites, which forms at 30°C in the pH range of 2.0-2.6, and may form at lower pH when solution has a high redox potential [25-27].

Iron hydroxide formation:

$$Fe^{3+} + 3H_2O \rightarrow Fe(OH)_3 + 3H^+ \quad (2.4)$$

Jarosite formation:

$$3Fe^{3+} + 2SO_4^{2-} + K^+ + 6H_2O \rightarrow KFe_3(SO_4)_2(OH)_6 + 6H^+ \quad (2.5)$$

Because of the ubiquitous nature of pyrite, it is often found as a major part of complex sulfidic ores that include copper sulfides such as chalcopyrite, which will be described in the following section [12-14, 28, 29].

2.1.1.2 Chalcopyrite

Chalcopyrite ($CuFeS_2$) is an important copper-bearing sulfide ore that is abundantly available in the Earth's surface, and is a primary source of copper [8, 30, 31]. It is commonly found in complex sulfidic ores, making froth flotation essential for the separation of chalcopyrite from the gangue sulfides for the recovery of copper from concentrate [8]. Like pyrite, chalcopyrite is naturally floatable over a range of conditions; however, as chalcopyrite provides copper ions to solution, undesirable activation of gangue minerals can occur, causing them to be collected and lowering the quality of the concentrate [14, 15, 28]. Activation will be briefly discussed in section 2.1.2.3. Due to the commercial value of copper, the need for sustainable, low cost, and high efficiency processing of chalcopyrite is of great industrial importance as high-grade ore becomes less readily available [8, 32].

This mineral has the crystallographic structure of a face centred tetragonal lattice, where copper and iron alternate positions on the corners of the cell, the structure shown in Figure 2.3. Each sulfur atom is coordinated to two of both copper and iron atoms, each iron and copper atom is coordinated to four S [8, 19]. The interatomic distance between the copper-sulfur bonds is 2.30 Å, while the iron-sulfur bonds are 2.26 Å in length, and the copper-iron, copper-copper and iron-iron bonds are all 3.71 Å [18].

Figure has been removed due to copyright restrictions

Figure 2.3: Chalcopyrite unit cell diagram adapted from [19].

The oxidation states of chalcopyrite are considered to be $Cu^{1+}Fe^{3+}(S_2)^{2-}$, with the electronic structure consisting of Fe 3*d* – S 3*p* antibonding orbitals at the lowest empty orbitals, with the highest empty orbitals consisting of Cu 3*d* – S 3*p* orbitals [18, 19, 33, 34]. Fe 3*d* orbitals are observed over a wide energy range mixed into bonding orbitals [18, 34]. Chalcopyrite is a semiconductor, is antiferromagnetic at room temperature, and is predominantly n-type although there are some naturally occurring p-type chalcopyrite structures, with a band gap of between 0.33-0.6 V [19, 35].

Oxidation of chalcopyrite forms a passivation layer consisting of elemental sulfur, polysulfides and iron sulfate precipitates, and it is these sulfur-rich species that provide chalcopyrite with its natural hydrophobicity [4, 31, 36]. The proposed reactions by which chalcopyrite oxidises and passivates, and the oxidation products and ionic species that form are shown in Equations 2.6-2.10 [2, 8, 32, 37].

$$2CuFeS_2 + 8.5O_2 + 6H_2O + CO_2 \rightarrow 2Fe(OH)_3 + 2CuSO_4 + 2H_2SO_4 + H_2CO_3 \quad (2.6)$$

$$CuFeS_2 + 3H_2O \rightarrow Fe(OH)_3 + CuS + S^0 + 3H^+ + 3e^- \quad (2.7)$$

$$CuFeS_2 + 4H^+ + O_2 \rightarrow Cu^{2+} + Fe^{2+} + 2S^0 + 2H_2O \quad (2.8)$$

$$2CuFeS_2 + 8.5O_2 + 2H_2O \rightarrow 2CuSO_4 + Fe_2O_3 + 2H_2SO_4 \quad (2.9)$$

$$2CuFeS_2 + 8.5O_2 + 2H_2SO_4 \rightarrow 2CuSO_4 + Fe_2O_3 + 4S^0 + 2H_2O \quad (2.10)$$

The iron ions released as the surface oxidises also promote surface leaching, shown in Equations 2.11 and 2.12 [8, 32].

$$Fe^{2+} + ¼O_2 + H^+ \rightarrow Fe^{3+} + ½H_2O \quad (2.11)$$

$$CuFeS_2 + 4Fe^{3+} \rightarrow Cu^{2+} + 5Fe^{2+} + 2S^0 \quad (2.12)$$

Under reducing conditions, elemental sulfur can also form on the surface of chalcopyrite, promoting the flotation of chalcopyrite via the proposed reactions shown in Equations 2.13-2.15 [32]. This process creates hydrogen sulfide gas, which is poisonous, corrosive and flammable.

$$CuFeS_2 + Fe^{2+} + Cu^{2+} + 2H^+ \rightarrow Cu_2S + 2Fe^{3+} + H_2S \quad (2.13)$$

$$Cu_2S + 4Fe^{3+} \rightarrow 2Cu^{2+} + 4Fe^{2+} + S^0 \quad (2.14)$$

$$H_2S + 2Fe^{3+} \rightarrow Fe^{2+} + 3H^+ + S^0 \quad (2.15)$$

Oxidation processes are thought to be catalysed by the presence of microorganisms in leaching, and it is these microorganisms that are now being applied to other areas of mineral processing where the surface chemistry of the minerals is of paramount importance, including flotation [10, 12, 38-40]. The application of microorganisms to flotation will be discussed in section 2.2.

2.1.2 Flotation Reagents

Current industrial practices use chemical methods, known in general as flotation regulators, to alter the surfaces of chalcopyrite and pyrite to maximise efficiency and recovery using froth flotation.

Flotation regulators are classified by function, with each type of regulator performing a specific task in the froth-flotation system; collectors aid flotation, depressants hinder flotation, activators promote collectors on the mineral surface, and frothers stabilise the air bubbles for more effective recovery. The most commonly used regulators for sulfide mineral froth flotation are described below.

2.1.2.1 Collectors

Xanthates, thionocarbamates and dithiophosphates are commonly used collectors for sulfide minerals, the molecules of which adsorb onto the surface of the desired minerals and make them hydrophobic, facilitating the attachment of particles to the air bubbles, allowing them to float [2, 41]. In the case of sulfide minerals, the collectors attach through chemisorption and surface chemical interactions with the molecules or ions of the collector [42]. The structures of these collectors are shown in Figure 2.4.

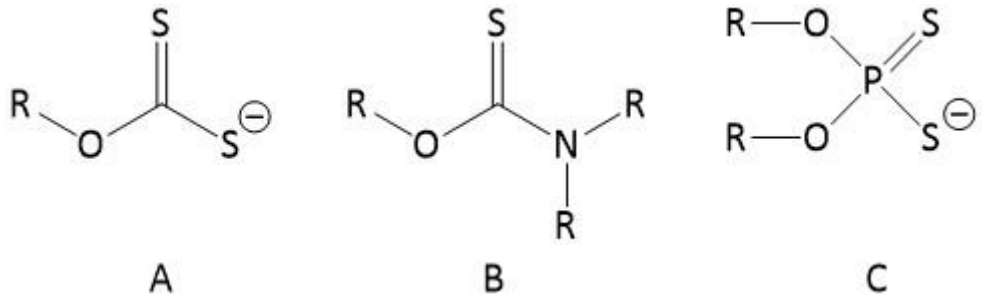

Figure 2.4: Chemical structures of xanthate collector (A); thionocarbamate collector (B); and dithiophosphate collector (C).

Adsorption reactions between the mineral and collector molecule occur when the ionic polar head group of the collector chemisorbs onto ionic surface sites through covalent or coordinate bonds. An example of such reactions are the copper xanthate complexes formed during the flotation of chalcopyrite through the redox reaction of the xanthate on the mineral surface, which is shown in Equation 2.16, where M represents the metal of the sulfide [2, 4, 41, 43].

$$2MS + 4ROCS^{2-}\ (\text{xanthate}) + 3H_2O \rightarrow 2M(ROCS_2)_2 + S_2O_3^{2-} + 6H^+ + 8e^- \qquad (2.16)$$

Only a monolayer of the collector on the surface is required to facilitate the irreversible attachment of the mineral to the air bubbles, as higher concentrations can reduce selectivity of the collector, or form multilayers of collector, reducing the water-repelling effect [2]. When the hydrophobic carbon chain of the collector attaches to an air bubble, the chemisorbed chalcopyrite rises to the surface of the flotation cell with the air bubble [2, 4, 5, 41, 42].

The collectors commonly used for sulfide flotation are variously unstable, toxic, corrosive and/or flammable substances, each of which is especially harmful to waterways and aquatic organisms [2, 44, 45]. The oxidation reactions that cause xanthate to bond with the minerals produces acid (see Equation 16), and this can also negatively impact the environment [2].

2.1.2.2 Depressants

Inorganic depressants form complexes with metal ions on the mineral surface, blocking collector binding sites. They also dissolve some metals into solution, which bind with the collectors to form soluble complexes. Both actions prevent the collectors from adsorbing onto the mineral surface, which either causes the minerals to become hydrophilic or preserves their hydrophilicity, preventing them from rising to the surface with the collectors [2, 5]. The inorganic compound sodium cyanide is the most widely used depressant for pyrite, and although low molecular weight polymers such as starch, tannin, dextrin and quebracho have been used with some success in other systems, they have not yet been effectively applied to pyrite and chalcopyrite [2, 41].

Sodium cyanide is selective for pyrite over chalcopyrite, with the reaction forming ferric ferrocyanide, shown in Equations 2.17 and 2.18 [2, 4, 5, 41, 46-48].

$$NaCN + H_2O \leftrightarrow HCN + NaOH \quad (2.17)$$

$$7Fe^{2+} + 18HCN \rightarrow Fe_4[Fe(CN)_6]_3 + 18H^+ + 4e^- \quad (2.18)$$

Cyanide is an extremely toxic substance that starves the body of oxygen by binding to iron-carrying enzymes; it is expensive to use and hazardous to the environment, making it a highly undesirable chemical to use in industry [2, 46-49].

2.1.2.3 Activators

Soluble salts can be used to aid the attachment of a collector to some mineral surfaces where such an interaction might not normally occur, facilitating flotation [41]. Activators such as copper sulfate ionise in solution, with those ions forming insoluble metal sulfides on the mineral surface [2, 5]. This prevents collectors from binding to soluble ions, and instead promotes collector adsorption to the mineral, which facilitates flotation [2, 5]. While salts such as copper sulfate are commonly used to activate sulfide minerals such as sphalerite (ZnS) and pyrite, they are not often used for chalcopyrite, as it already contains copper [2, 4, 5, 50].

Although not as hazardous as xanthates or cyanide, activators can still cause environmental issues if they are released into any waterways. Copper sulfate, as an example, is toxic for marine environments with the concentration limit applied to protect aquatic organisms as low as 0.004

mg/L, and may persist in the environment upon accidental release [51, 52]. Copper sulfate can also negatively impact human health from relatively minor skin irritation, to being fatal upon ingestion of as little a teaspoon-full of the solid, with chronic exposure resulting in damage to the human reproductive system and to the liver [52].

2.1.2.4 Frothers

These chemicals are used to stabilise the froth that is formed by the air bubbles by adsorbing onto the air-water interface and reducing the surface tension [2]. In early froth flotation systems, pine oil and cresol were used as frothers, but currently compounds such as methyl isobutyl carbinol (MIBC) and polyglycols are commonly used frothers, as are aliphatic alcohols with a chain length of between 5-8 carbon atoms [4, 5, 41, 42, 50]. The compounds used as frothers are generally flammable materials, and can be considered dangerous for that reason [53].

Although effective, all flotation regulators currently used in the flotation of sulfide minerals possess undesirable qualities. Each compound has the potential to negatively impact both the environment and handlers, as well as increase storage, usage and disposal costs.

2.1.3 Effects of Eh and pH

In leachate and in flotation cells, the solution potential and pH are modified to alter recovery of sulfide minerals and base metals, as these conditions impact bubble-particle interactions, the mineral surface charge, and how collectors and depressants adsorb on the mineral surface [54]. Oxidation-reduction (redox) potential, referred to as Eh, is related to the chemical oxidation, reduction and adsorption reactions that take place at the interface between the mineral and solution [54, 55]. The Eh is a measure of the transfer of electrons between chemical species, and is dictated by the Nernst equation for each individual redox reaction and the pH of the solution [19, 55].

$$\mathrm{Eh} = \frac{\Delta G^{\circ}}{nF} + \frac{RT}{nF}\log_{10}\mathrm{Q} - \frac{RTh}{nF}\mathrm{pH} \qquad (2.19)$$

Where ΔG° is the Gibb's free energy of the reaction, R is the gas constant, F is the Faraday constant, Q is the reaction quotient, *n* is the number of electrons and *h* is the number of protons. The Eh and pH of a solution at any given temperature and pressure will indicate what redox species are present in the leachate [19, 55]. The measurement of Eh is made with the assumption that all the species involved in redox reactions in the system are at equilibrium, and it is impossible to know which species make individual contributions to the Eh of the solution without making assumptions as to which species are present [55]. However, the Eh can provide information on the oxidative or reductive environment in the system; a higher Eh value indicates more oxidative conditions, while

lower Eh values indicate a more reductive environment [54-56]. A specific example of this would be higher Eh promoting the formation of ferric iron species, while a lower Eh promotes the formation of ferrous iron species, both solid precipitates and ionic species [55].

Previous studies have identified the manual modification of Eh by the addition of oxidative/reductive agents as an important factor in the collectorless flotation of sulfide minerals [54, 56]. In the bioleaching of pyrite and chalcopyrite, high solution potentials were found relate to greater leaching of iron from the ore and the promotion of jarosite ($KFe_3(SO_4)_2(OH)_6$) [25, 57]. Ionic strength has also been identified as a determining factor in cell adhesion, as altering the ionic strength of the solution by the addition of electrolytes changes the electrostatic interactions between the cells and the minerals [58]. The Eh is an important indicator of solution conditions, and can be a powerful tool in understanding the species present during mineral bioleaching.

Several studies have investigated the effect of pH in the recovery of sulfide minerals, observing elemental sulfur is less stable at neutral to basic pH, the region in which many flotation studies are performed [56, 59] The flotation of sphalerite from pyrite by a variety of collectors was most effective at neutral to alkaline pH values as it assists the formation of copper-collector complexes [59]. The initial pH of solution has been found to impact the bioleaching rate of pyrite, suggesting that at low pH the Fe^{3+} ion concentration is greater and promotes mineral oxidation, and prevents jarosite formation [25]. Significant decreases in mineral leachate pH has been related to the growth cycle of cells, with greater populations promoting the oxidation of iron in solution, with low pH also associated with greater adhesion forces between sulfide minerals and cells [60, 61]. Several studies have identified the formation of jarosites and other iron oxides such as ferrihydrite and goethite as surface products at pH values over 2 [25, 56, 57].

Monitoring both the Eh and the pH of solution is necessary to understand the chemical reactions taking place both on the mineral surface and in solution, and the method used to record these values will be discussed in Chapter 3, section 3.4.2. These conditions are also important for the microorganisms that occur naturally around sulfide mineral deposits and in leaching heaps, and as such are factors that must be considered when applying microorganisms to flotation. The application of microorganisms to froth flotation systems will be discussed in the following section.

2.2 Bioflotation

In bioflotation, microorganisms and their extracellular polymeric substances (EPS) are used instead of chemicals to improve the separation of minerals by acting as flotation reagents to alter the surface charge, hydrophobicity and surface chemistry of the minerals [62-65]. Microorganisms can

selectively interact with the gangue and the desired minerals, and can also be used in conjunction with chemical flotation reagents [46, 50]. Common in bioflotation investigations include pre-concentrating the microorganisms or the addition of synthetic flotation reagents to cultures, which has been shown to negatively impact cell activity [48, 49, 66, 67].

Much research has been done on the flotation of sulfide ores, with emphasis on the removal of pyrite and the replacement of chemical reagents with microorganisms [40]. To select appropriate microorganisms for bioflotation applications, it is first necessary to understand their structures, classifications and requisite nutrient sources and growth conditions. A general overview of microorganisms is provided in the following section, followed by details of the individual strains used for this study and their previous applications to bioflotation.

2.2.1 Microorganisms

Microorganisms are classified by the nature of their molecular and cellular characteristics, such as the structure of their cell wall, their nutrient sources and their use of atmospheric oxygen [68]. Gram positive cells have multiple layers of peptidoglycan that retain crystal violet dye when stained, while gram negative cell have a phospholipid and lipopolysaccharide outer membrane with an internal peptidoglycan layer that does not retain crystal violet dye when stained [68]. Both bacteria and archaea are prokaryotic cells, meaning they have no membrane-bound nucleus, with archaea being distinguishable from bacteria by the fact their cell walls contain no peptidoglycan or muramic acid [68-70].

The life cycle of bacteria and archaea grown in batch cultures such as the ones used for these experiments have four phases; Lag phase, exponential phase, stationary phase and decline phase. The lag phase occurs immediately after inoculation, where the initial cell population is stable. This is followed by the exponential phase, where the cells divide at a constant rate and the cell population increases. When the exponential growth slows due to exhaustion of nutrients, and the cell population stabilizes again, it is said to have reached the stationary phase, and it is from this phase that inocula are taken to start the next batch culture. The Decline/Death phase follows the stationary phase, and occurs when the number of viable cells starts to decrease [71-73]. Microbial growth curves are generated by plotting the number of cells per mL over time, encompassing the different phases of growth, as shown in Figure 2.5 [71, 72].

Figure has been removed due to copyright restrictions

Figure 2.5: Typical bacterial growth curve adapted from [71]

Microorganisms can be further classified by how they obtain their energy. Autotrophic cells make their own nutrients from inorganic compounds, heterotrophic bacteria utilize organic compounds as food sources [68]. Chemoautotrophs get their energy from the redox reactions of chemicals, obtaining the necessary carbon from the atmosphere, and mixotrophs can use a combination of energy sources [68]. Microorganisms that require oxygen to grow are called obligate aerobes, those that cannot use oxygen are called obligate anaerobes, and cells that can use oxygen when it is present but can survive without it are called facultative anaerobes [68]. Due to the challenges that surround maintaining anaerobic conditions, all the microorganisms used in this study were grown under aerobic conditions.

Microorganisms may be further described by their ideal growth conditions, including temperature and pH required for optimal growth. Mesophilic cells grow best at temperatures between 15°C and 45°C, while thermophilic cells prefer to grow at elevated temperatures in the range of 40°C to 85°C, and their growth will slow or even stop completely at lower temperatures [39]. Acidophilic microorganisms are of interest for mineral processing applications, as they grow best under acidic pH conditions. Extreme acidophiles prefer to grow at pH<3, while moderate acidophiles grow best at pH 3-6 [31, 74].

Bacteria that have been most commonly and effectively used for bioflotation of sulfide minerals are *Acidithiobacillus ferrooxidans*, *Leptospirillum ferrooxidans* and *Acidithiobacillus thiooxidans*; they can be used in combination or separately in various applications toward sulfide mineral separation. These bacteria have been shown to affect the surface chemistry of sulfide minerals and as such are excellent reagents for the alteration of the flotation properties of the minerals due to their ability to adhere to and/or oxidise mineral surfaces [40, 64]. The mechanism through which this occurs is currently unknown, although there are several proposed mechanisms that will be discussed in section 2.3. The following sections describe the acidophiles used in this study and how they have been previously applied to bioflotation.

2.2.2 *Acidithiobacillus ferrooxidans*

A. ferrooxidans has been explored for its uses in bioleaching, and has also previously been used in the bioflotation of sulfide minerals in several studies [46, 48, 49, 66]. It has been used as a depressant for pyrite from lead-zinc ore, as it oxidises iron ions and elemental sulfur, decreasing the hydrophobicity of the mineral surface while a chemical collector was used to float the desired minerals. It was found that the bacteria were equal to the sodium cyanide depressant in its efficiency, and even increased the grade of the recovered zinc, however, this paper does not investigate the any changes in surface of the minerals due to the bacteria [49]. Another study by the same author found *A. ferrooxidans* confirmed those findings, and models were fitted to the trends observed to enable the prediction of the bacterial responses, although this paper does not address the nature of the bacterial action on the minerals that causes the separation [46]. This bacterium has also successfully decreased the hydrophobicity of pyrite to selectively separate it from both chalcopyrite and arsenopyrite in the presence of collector [48]. *A. ferrooxidans* has also been used to depress pyrite, due to it binding well to iron-bearing minerals, and was used with the aim of depressing pyrite more effectively than chemical depressants [66]. It was found that this bacterium selectively depressed 77-95% of pyrite, while allowing the recovery of 72-100% of the other sulfide minerals, including chalcocite, molybdenite, millerite and galena [66].

This bacterium is Gram negative, and is able to oxidise ferrous iron to ferric iron and elemental sulfur to sulfate to obtain energy [75, 76]. This bacterium is rod-shaped, grows between 1-3 µm long, and its surface charge can vary depending on the substrate on which it is grown, due to the different proteins the bacteria produce to metabolize different nutrient sources [23, 49]. *A. ferrooxidans* has been extensively applied in sulfide bioleaching due to its high tolerance for metal ions, with some studies suggesting preference for iron over sulfur as a nutrient source [75, 77-82].

Several studies have investigated surface chemicals and properties of *A. ferrooxidans* cells in response to different leaching conditions, reporting proteins, exopolymers that vary from strain to strain, as well as gene expression [23, 83-86]. Studies that have investigated the EPS of *A. ferrooxidans* have observed sulfur globules, noting that EPS is essential for adhesion of this bacteria to sulfide minerals, and that stripping cells inhibited cell interaction with minerals [61, 76, 84, 87-90]. Several of these studies have suggested that the attachment to sulfide minerals is site-specific, with cells preferring surface defects [84, 85].

Studies that have investigated *A. ferrooxidans* as a suitable microorganism for bioflotation found the initial hydrophobicity of the mineral is an important factor in attachment of *A. ferrooxidans* to various mineral surfaces [85, 89, 91]. Although previous studies have demonstrated its suitability

for bioflotation application, the mechanism through which this bacterium alters the mineral surface, and the nature of the cellular products involved is still a matter of divided opinion [40, 46, 48, 49, 64].

2.2.3 *Leptospirillum ferrooxidans*

Few studies have applied *L. ferrooxidans* to the bioflotation of sulfide minerals, and those that have report conflicting results. Pecina *et al* floated sulfide minerals with *L. ferrooxidans* and synthetic collector, finding that recovery of chalcopyrite was improved and pyrrhotite was weakly depressed, positing that this was related to the readiness of the mineral to be oxidised and produce elemental sulfur on the surface, improving the hydrophobicity [92]. A similar study by Vilinska *et al* contradicts these results, finding that *L. ferrooxidans* depresses chalcopyrite due to its greater affinity for the chalcopyrite surface [93]. They attributed this affinity to greater number of surface defects (scratches, voids, etc.), which are suggested to have more readily available nutrients due accelerated dissolution of the mineral surface occurring at these sites [93-95].

L. ferrooxidans, though able to oxidise iron, has not been as extensively investigated as *A. ferrooxidans* in terms of bioflotation, but is commonly investigated in terms of bioleaching and often combined with other strains [25, 96, 97]. *Leptospirillum ferrooxidans* is a Gram-negative bacterium that was first reported by Markosyan in 1972 [98]. This bacterium are curved rods between 1-3.3 µm in length, get their nutrients solely from the oxidation of ferrous iron and grow ideally in aerobic, mesophilic and acidic conditions [98].

Leptospirillum ferrooxidans has previously been applied to bioleaching studies and has the advantage of being able to withstand slightly higher temperatures than *A. ferrooxidans*, although still within the mesophilic temperature range of 20-40°C [97, 99]. This strain is comparable in growth activity compared to *A. ferrooxidans* within the mesophilic temperature range, however Sand *et al* has determined that its iron-oxidising activity is not as strong when grown on soluble iron(II) [96]. Harneit *et al* has demonstrated that *L. ferrooxidans* has an affiliation for pyrite, however they noted that there were differences in cell behaviour between strains and that there were complications in analysing EPS components due to hydrolysis [84].

2.2.4 *Acidianus brierleyi*

The archaeon *A. brierleyi* are 1-1.5 µm round, instead of rod-shaped, Gram negative, and able to oxidise both iron(II) and sulfur, which indicates the potential to be selective in binding to sulfide minerals [100, 101]. This microorganism is less tolerant of high concentrations of iron as *A. ferrooxidans*, however has a higher tolerance of copper of up to 10 $g.L^{-1}$ [102, 103]. An important

factor to note is that *A. brierleyi* can also make use of organic carbon, which has been noted to enhance its growth, and has been used by most of the studies mentioned here [101, 102, 104-115]. Segerer *et al* suggest that the cells are both autotrophic and mixotrophic and might be able to grow on yeast extract without the presence of elemental sulfur under aerobic conditions [100]. This information is crucial to not only understanding the interactions between *A. brierleyi* and the mineral surface, but also has implications for this strains applicability to bioflotation if the question of yeast-extract involvement is not explored.

A. brierleyi has been used successfully in bioleaching systems where higher temperatures are desired, with several studies concluding that this archaeon accelerates copper and iron sulfide leaching, although there is no consensus on the mechanism [105, 106, 108-115]. Although leaching was effective, little information on the chemistry of the mineral surfaces was given, leaving a gap in the knowledge with respect to how *A. brierleyi* interacts with sulfide minerals [106, 109]. Studies have proposed *A. brierleyi* possesses a higher tolerance to salinity and lower pH, of which mesophilic bacteria as less tolerant [78, 116]. These bioleaching studies show that *A. brierleyi* can alter the surfaces of mineral sulfides, strongly suggesting that this archaeon may be successfully applied to a bioflotation system, however there is some disagreement in the literature as to the likely surface species. Larsson et al has used *A. brierleyi* to oxidise the surface of pyrite, potentially increasing hydrophilic species on the surface [110], while Jordan *et al* claims that *A. brierleyi* leaches both copper and iron(II), producing elemental sulfur which would increase mineral hydrophobicity [117]. The lack of studies applying this microorganism to bioflotation reveal a need for further investigation in this area.

The use of these microorganisms in the field of bioflotation provides potential solutions to a variety of problems currently faced by the tradition flotation methods described in section 2.1, however bioflotation also has several important limitations. These advantages and disadvantages will be discussed in the following sections.

2.2.5 Advantages of Bioflotation

Microorganisms are non-toxic, environmentally friendly alternatives to chemical collectors and depressants that are just as effective as flotation reagents [47, 48, 63, 64, 118]. Microorganisms are economically viable and biodegradable, and biosurfactants have a higher surface activity [47, 48, 53, 118]. They are also more tolerant to changes in their surrounding conditions such as pH, salinity and temperature, as well as providing a higher selectivity for the desired metals [119].

The iron-oxidizing bacterium *Acidithiobacillus ferrooxidans* (formerly known as *Thiobacillus ferrooxidans*) has been shown to selectively adsorb onto minerals that contain ferrous iron in a previous study, in which the bacterium where exposed to pyrite and chalcopyrite, which contain ferrous iron, and quartz and galena (PbS), which do not. Ferrous and ferric ions were also added to the bacteria whilst being exposed to the minerals to assess what effect iron in solution on the adsorption to the mineral surfaces [120]. It was found that *A. ferrooxidans* selectively adhered to the minerals that contained ferrous iron, and that if ferrous iron was in the solution, it hindered the bacteria from adsorbing onto the minerals [120]. As several bacterial strains are known iron-oxidizers, it is predicted that they too will be selective towards minerals that contain ferrous iron.

2.2.6 Disadvantages of Bioflotation

One potential issue with industrial scale bioflotation is the number of cells required (10-100 times more) to effect separation in comparison to chemical reagents [121]. This is because the microorganisms can be slow growing, and more time is required for them to reproduce to get a high enough cell concentration. Other issues include the uncertainty of the industrial applications with respect to the culturing conditions and the handling of microorganisms, and the costs surrounding materials and operation of bioflotation facilities [64, 121, 122].

Bioflotation has been explored in many previous studies using a variety of minerals and microorganisms, under a multitude of growth and reaction conditions, which often makes it difficult to compare the results of one experiment with another. Even the media used to grow the microorganisms may vary from group to group, the recipes and concentrations of the nutrients not being standardised. This variety makes direct comparison of results difficult, but it also shows that bioflotation is an area of expanding interest and the importance of fully elucidating how it works is becoming ever more important.

Although a wide variety of research has been conducted in the field of bioflotation, gaps in the current knowledge with respect to the precise nature of the interactions between microorganisms and minerals, including the chemistry of how the surfaces of sulfide minerals are altered by the bacteria and their EPS. Many papers in this field are driven by the separation efficiency obtainable using bacteria, rather than understanding the nature of bacterial-mineral interactions and the chemistry of the species involved, which will be explored further in the following section.

2.3 Microbial-Mineral Interactions

The mechanism through which microorganisms interact with minerals in a bioflotation system is an area of continuing investigation, and is still a source of uncertainty. There are several competing schools of thought when it comes to precisely how microorganisms cause minerals to behave as they do in these systems. There are ostensibly three possibilities when it comes to microbial-mineral interactions in both bioleaching and bioflotation systems, and each proposed mechanism has its followers and critics. Figure 2.6 shows an illustration of each mechanism; the direct contact mechanism (a), the indirect mechanism (b), and the indirect contact mechanism (c).

Figure has been removed due to copyright restrictions

Figure 2.6: The three proposed mechanisms for bacterial-mineral interactions; (a) direct contact mechanism, (b) indirect mechanism, (c) indirect contact mechanism, adapted from [123].

These three mechanisms have also been suggested to work in conjunction with each other, and although several studies propose one may dominate over the others, one of the challenges is isolating the effect of microorganisms from inorganic redox leaching reactions [10, 31, 81, 109, 118, 124-128]. Each of the mechanisms and the studies that support them are described in the following sections, typically in terms of leaching, however several studies relate these mechanisms to the impact of cells on mineral floatability.

2.3.1 Direct Contact Mechanism

The direct mechanism, illustrated in Figure 2.6(a) implies that the microbial cells must be touching and attached to the mineral surface to affect any physical changes [110]. In the case of bioleaching, the cells must have direct physical contact with the mineral to oxidise pyrite and/or chalcopyrite, creating the reactions shown in Equations 2.20 and 2.21, respectively [105, 109, 110, 126, 128]:

$$4FeS_2 + 15O^{2+} + 2H_2O \rightarrow \text{bacteria} \rightarrow 4Fe^{3+} + 4H^{+} + 8SO_4^{2-} \quad (2.20)$$

$$4CuFeS_2 + 17O_2 + 2H_2SO_4 \rightarrow 4CuSO_4 + 2Fe_2(SO_4)_3 + 2H_2O \quad (2.21)$$

The microorganisms attach to the mineral surface and the adsorbed cells proceed to attack the mineral enzymatically via stoichiometric oxidation to either oxidise or cause dissolution [31, 39, 105, 109]. This proposed mechanism implies the oxidant must be of biological origins and not ferric ions or oxygen [31, 123].

The key part of this mechanism is the adhesion of cells to the mineral, and what follows the attachment process are further reactions, including oxidation reactions, between the products of microbial metabolic processes and the mineral surface [93]. For adhesion of microbial cells to the mineral surface to occur in the first place, conditions such as surface charge, hydrophobicity and ionic strength must be conducive, as does nutrient availability, although once adhesion has occurred, it tends to be very strong, especially to sulfide minerals [47, 48, 129].

Previous studies have attempted to provide evidence for the direct attachment mechanism through a variety of methods. Devasia *et al* determined *A. ferrooxidans* cultures grown on ferrous iron were not as efficiently leached as sulfur grown culture, indicating the direct mechanism dominates leaching, as greater iron concentration does not impact dissolution [130]. This is supported by other studies that have found iron concentration alone is not an indication of mineral dissolution, but that cell attachment is necessary as the dissolution by cells is an enzymatically driven process [105, 108]. Larsson *et al* physically separated cells from pyrite by a membrane, suggesting removing cells will impact leaching if the direct mechanism dominant, observing higher pyrite oxidation rates and increased cell growth when cells were in contact with the mineral [110].

For the purposes of bioflotation, the directly attached cells can make the mineral surface more hydrophobic or more hydrophilic [47, 48]. Studies have suggested that the direct action of the cells is the most efficient means of iron oxidation, producing oxygenated products which can promote hydrophilicity, or that cells themselves are hydrophilic [26, 131]. There is also the suggestion that cells adsorbed onto pyrite eliminate sulfur species from the surface, removing hydrophobic species and promoting depression [49]. This apparently contradictory evidence is part of the reason there is still debate as to whether the direct mechanism or the indirect mechanism is responsible for surface changes in the minerals.

2.3.2 Indirect Mechanism

The indirect mechanism, illustrated in Figure 2.6(b) is the most widely accepted for describing a leaching system, but could arguably be said to occur in a flotation system as well. In this mechanism neither microorganism nor EPS come into direct contact with the mineral surface to alter its chemistry or cause any reactions. Instead, the cells in solution act as a catalyst for the oxidation of ferrous to ferric ions, and it is the latter that oxidise the sulfides, with the production of ferric ions by microorganisms shown in Equation 2.22, and the oxidation of pyrite and chalcopyrite by ferric ions shown in Equations 2.23 and 2.24, respectively [31, 39, 105, 109, 123, 126, 128]. The ferric ions are constantly being regenerated by the microorganisms, and no direct action on the sulfide surface is required [110].

$$2Fe^{2+} + ½O_2 + 2H^+ \rightarrow \text{microorganisms} \rightarrow 2Fe^{3+} + H_2O \quad (2.22)$$

$$FeS_2 + 8H_2O + 14Fe^{3+} \rightarrow 15Fe^{2+} + 2SO_4^{2-} + 16H^+ \quad (2.23)$$

$$CuFeS_2 + 2Fe_2(SO_4)_3 \rightarrow CuSO_4 + 5FeSO_4 + 2S^0 \quad (2.24)$$

As was mentioned previously, oxidation products on the surface alter the mineral behaviour in both bioleaching and flotation systems, however opinion is still divided on whether cell attachment plays a role [37, 132, 133]. Crundwell *et al* suggest that cell attachment may accelerate mineral dissolution, but maintain that the indirect mechanism is the driver of mineral leaching [123]. Another study suggested that cells that oxidise ferrous iron remain in solution, meaning the dissolution of chalcopyrite is driven by the indirect mechanism as few cells attach to the surface [89]. The indirect mechanism has been posited as the preferred mechanism for thermophiles like *A. brierleyi*, with little attachment claiming to have been observed, or proposed as being necessary for leaching to occur [104, 117, 134].

Few papers have examined the indirect mechanism in respect to mineral bioflotation, with most studies working towards metal recovery by mineral bioleaching. Yang *et al* suggest that the ferric iron and protons produced by microorganisms act on sulfide mineral surfaces, promoting iron and copper dissolution and making the surface sulfur-rich, and therefore hydrophobic [24]. This contradicts the findings of proponents of the direct mechanism, which is why both these mechanisms are still accepted explanations for surface alterations.

2.3.3 Indirect Contact Mechanism

Figure 2.6(c) illustrates the indirect contact mechanism, which is another possibility in a flotation system that is not as well investigated as the other mechanisms. For this mechanism to work, the layer of EPS that surrounds cells adheres to the mineral surface and forms a biofilm, in which ferrous ions are oxidized to ferric ions which then bioleach the mineral. The microbial cells do not directly take part [31, 123]. If the indirect contact mechanism is correct, then the presence of EPS alone should be sufficient to cause mineral dissolution or change is hydrophobicity [135].

The reactions in the indirect contact mechanism occur in EPS chains that act to form a complex with ferric ions, which then increase the activity of oxidative attack on the sulfide by concentrating the ferric ions [31, 135]. The production of EPS is affected by the nature of the mineral surface, by the attachment process itself, and by the growth medium and substratum; for example, sulfur-grown cells produce EPS, but do not attach so well to pyrite and pyrite-grown cells [135].

Several studies have suggested that EPS around cells provide a reaction space for the oxidation of ferrous iron to ferric iron, however opinion is divided on whether cells must be in contact with the mineral surface. Kinzler *et al* suggest the EPS matrix allows the iron to interact with the mineral through electrostatic forces, while Harneit *et al* propose it is the ferric iron complexed in EPS that allows the cells to attach to the minerals [84, 136]. This contradicts the findings of Gehrke *et al* that suggest that the oxidation of iron that happens in EPS around the cells without need for attachment, and as such, the catalytic effect of ferric ions produced by cells is sufficient evidence for the indirect mechanism [137]. Mikkelsen *et al* report that cells must maintain ferric iron concentration for pyrite dissolution, whether or not they contact the mineral [138].

There is currently no consensus in the literature as to which mechanism is correct, or whether multiple mechanistic processes cause the behaviour of the minerals in solution to change. This overview of our current understanding of microbial-mineral interactions is general, and may not necessarily apply to every strain and every mineral. Separating out the action of cellular products from cells requires understanding of the composition of extracellular substances and their extraction. The following section details current knowledge and practices around the extraction and application of microbial products to bioflotation.

2.4 Extracellular Polymeric Substances

Extracellular polymeric substances (EPS) are excreted by microorganisms as part of the cycle of adhesion and biofilm development on a wide range of surfaces, ranging from medical implants to minerals [137, 139]. The extraction and analysis of EPS has been previously investigated in studies on a variety of applications including bioleaching [84, 90, 125, 135-137, 140-142], bioflotation [53, 63, 118, 119, 143-145], biomineralization [146, 147], biofilms [139, 148-151], and cell adhesion [87, 89, 152, 153]. Generally, the composition of EPS has been found to consist of varying amounts of carbohydrates, proteins, fatty acids, phosphorous, nucleic acids, uronic acids and humic acids [136, 154, 155].

Work has also gone into determining whether extractions of microorganisms can function as flotation reagents. Several studies have reported both improved flotation and depression of a variety of sulfide minerals using extracted EPS. It has been reported that EPS enhances the flotation of chalcopyrite [63], while another study found rhamnolipids improved iron mineral flotation, but had a negative impact on copper and molybdenum recovery [53]. Several studies have demonstrated that different growth conditions of microorganism cultures, including but not limited to iron source, pH, and added metal ion concentrations impact EPS production by cells, and thus altered the

extracted EPS behaviour upon exposure to minerals. One study reported that EPS composition depends on nutrient source, altering polysaccharides and protein production, reducing and promoting hydrophobicity, respectively [145]. Another study observed adsorption of EPS onto the different minerals was altered by pH, with EPS increased the dissolution of the minerals at low pH, and consumed metal ions over a pH range of 3-7 [156]. Previous studies have suggested that EPS loosely bound to cells is different in composition to EPS tightly bound to the cells [157, 158]. Due to different growth conditions and extraction methods, results are difficult to compare across studies.

Bioleaching is another area where EPS research has implications for mineral dissolution and heavy metal adsorption. Several studies have reported that the composition of EPS impacts the number of binding sites for metal ions, and the ability of EPS to adsorb soluble metal ions, and that this can be altered by metal ion concentration, nutrient sources and pH [84, 90, 137, 140, 142, 159-162]. Comte *et al* found decreasing the pH significantly lowered the number of binding sites in EPS, concluding metal affinity was potentially dependant on the nature of EPS components, the metal, or a combination of both [159]. A study by Anand *et al*, however, found the ability of EPS to capture ions was improved by having cells, rather than as an extracted product [118]. Several studies have identified phosphorous and Fe(III) granules in the EPS matrix, and suggest phosphorous binds to the iron to reduce intracellular concentrations of iron ions and promote iron oxidation [141, 152, 153].

Previous studies have performed a variety of EPS extractions, some isolating one kind of compound or comparing total extraction yield, with comparisons of both chemical and physical techniques to explore efficacy, and in some cases to investigate whether the techniques are causing chemical or intracellular contamination [82, 163-167]. The bodies of work that compared extraction techniques report non-uniform qualitative results, with differing yields of organic carbon, protein and carbohydrate [155, 166, 168, 169]. These various results indicate that extraction methods change the structural conformation of EPS and cause chemical contamination or reactions [155, 157, 158, 166-169]. Previous attempts made in the literature to monitor intracellular contamination of EPS have found that exact measurement is not possible due to the nature of EPS including the compounds that typically indicate lysis [170, 171]. Complex media are also likely to interfere with quantification and qualification of results [157]. The processes of EPS extraction and analysis have implications for the resulting data and usage of any extracted products, and although these products have been explored through the comparison of extraction techniques, there are no standard methods applied to EPS extraction and analysis, and results reported often do not agree [89, 150, 171].

The importance of EPS to the mechanisms through which microorganisms interact with their environment and impact their adhesion and surface effects in relation to substrates is still contentious, and EPS analysis and applications will have a significant impact in the field of minerals processing [125, 135]. In summary, the aspects of EPS analysis that are important for bioflotation:

- Detection of DNA is not necessarily an indicator of intracellular contamination [170, 171].
- EPS extraction methods alter the structure of components being extracted, especially by chemical methods, distorting results and making comparison challenging [89, 155, 163, 166, 172].
- Targeting specific types of component do not fully measure all aspects of EPS [169].
- The nutrient sources used to grow microorganisms can have a significant impact of the quantification and qualification of any EPS extracted or analysed *in situ* [82, 84, 137, 157].
- *In situ* analysis of EPS in whole biofilm is complex, but may produce a more reliable indication of the chemical components involved in biofilm [166, 172].

The following section details the work of previous studies that have applied a variety of analytical techniques to biomaterial and mineral systems, demonstrating how they may be used to explore mineral surfaces, microorganisms and their excretions.

2.5 Key Surface Analytical Techniques Applied for Mineral-Bacterial Interface Studies

The analytical techniques in this section have previously been applied to systems comparable to those investigated in this work. Those studies are outlined in the following sections to demonstrate the suitability of these analytical instruments for application to this investigation, and to highlight important findings that impact the methods and analysis performed in this body of work. The theory behind each method mentioned here, and the sample preparation techniques employed, are explained in Chapter 3.

2.5.1 Scanning Electron Microscopy and Energy Dispersive X-ray Spectroscopy

Scanning electron microscopy (SEM) and energy dispersive X-ray spectroscopy (EDX), the theory of which is detailed in Chapter 3, section 3.9, have previously been applied to obtain images of the mineral surfaces under investigation. Several studies have effectively applied SEM to the visualisation of pyrite and other sulfide minerals, using it to identify secondary mineral precipitates, observe the texture and homogeneity of mixed mineral systems and to observe the degradation of

the mineral surface [25, 26, 75, 80, 138, 173-176]. Images of various microorganisms have also been presented in the literature, with the intention of proving cell attachment to surfaces or investigating cell morphology [39, 47, 61, 89, 177]. Many of these studies used EDX to provide the elemental composition of the minerals and to identify organic matter on the surface of samples [39, 174, 178].

Often, the SEM images presented in the literature are obtained from mineral samples in bioleaching studies without preservation of the cells on the surface, as such no bacteria are visible due to cell lysis [25, 26, 105, 176, 179-181]. This may also cause abiotic samples to contain greater proportions of oxidation products due to the air-drying process [25, 26, 180, 181]. Previous studies have different sample preparation methods, making direct comparison between studies challenging, and very few present abiotic control samples that enable effective comparison of chemical leaching and bioleaching [47, 60, 62, 74, 75, 80, 85, 113, 138, 140]. Some investigations provide no direct quantification of the cells attached to the surface, or quantify the size of mineral precipitates and/or etch pits observed on the minerals [75, 140, 182].

SEM is an effective means of presenting high-resolution images of minerals and cells, and although attachment has been demonstrated by some microorganisms in previous studies [39, 47, 61, 89, 177], the question remains as to how attachment of cells may be related to the flotation or depression of pyrite. To relate cell attachment to the bioflotation of pyrite, SEM and EDX are essential tools for identifying the cell population on the pyrite as it develops over time and distinguishing cells from mineral precipitates by the elemental composition.

2.5.2 Atomic Force Microscopy

Atomic force microscopy (AFM) is a technique that has been used to characterise a wide variety of organic and inorganic surfaces, including mapping the morphology of polymer films exposed to proteins [183-185], as a method of inferring the wettability of heterogeneous surfaces in conjunction with other surface techniques [186], as a means of investigating cells on a surface [84, 125, 129, 135, 136, 187-191], and adhesion forces involved in cell attachment to surfaces [61, 89, 192]. The theory behind AFM and how the technique measures surface morphology and topography is discussed in detail in Chapter 3, section 3.10.

Very few studies have used AFM to measure mineral roughness in relation to exposure to sulfur and/or iron oxidising microorganisms. Lara *et al* used roughness values to define insoluble sulfur species on the surface, suggesting that bacteria made pre-treated pyrite smoother by consuming elemental sulfur species which made the abiotic surfaces rougher in comparison [190]. AFM has

been applied to cells dried and in liquid on a variety of surfaces in previous studies, usually with the aim of measuring cell morphology or distribution across a surface [84, 125, 129, 135, 136, 187-191]. AFM has also been used to measure the forces involved in cell adhesion with previous work suggesting the process is governed mostly by hydrophobic interactions, with electrostatic interactions having smaller effect [61, 89, 192]. Cell distribution across a surface has also been previously investigated using AFM, typically in conjunction with epifluorescence microscopy [84, 188-191].

Studies that have used AFM to image cell morphology in liquid AFM mode have noted that cell adhesion to the cantilever in this mode of operation can severely reduce image quality, although cells do lose height when dehydrated [129, 187, 188]. Chau *et al* observed that roughness of a surface impacts the hydrophobicity, and the topography influences how a solution will interact, observing that the rougher the surface, the more hydrophobic in nature it may be expected to be [193]. Roughness can also impact contact angle hysteresis, causing the difference in advancing and receding contact angles to increase and become difficult to replicate, and as such must be considered when measuring the contact angle of mineral surfaces [194]. A rougher surface may also impact microorganism attachment behaviour, with several studies observing cell preference for surface defects rather than smoother regions of a surface [84, 85]. This behaviour may also impact biofilm formation.

Changes in roughness on the surface can also enable the quantification of leaching occurring on the mineral surface. AFM is an important tool not just as a visualisation technique, but as a method of quantifying the roughness of the mineral exposed to microorganisms under leaching and flotation conditions [190, 193, 195]. This will enable the separation of physical properties from the chemical properties of the minerals exposed to microorganisms.

2.5.3 Contact Angle Measurements

Contact angle measurements are used to quantify how well a surface attracts or repels a solvent, with the quality of water repulsion known as wettability. The theory behind contact angle measurements collected by the sessile drop and captive bubble methods are detailed in Chapter 3, sections 3.15 and 3.16, respectively. Contact angle measurements have been applied to a variety of surfaces as a method of measuring the physical property of wettability, and there is a variety of techniques that have been applied to relate the physical and chemical properties of the surface to contact angle [193, 196, 197].

The basis for separation by traditional froth flotation and bioflotation is the hydrophobicity of different mineral surfaces, and therefore the accurate measurement of hydrophobicity is of high importance [5, 193]. Methods for measuring surface hydrophobicity have been developed for use on contact lenses, reverse osmosis membranes, and polymer surfaces [196, 198-201]. Several studies have performed contact angle measurements on mineral and/or cell surfaces to relate chemical species on the surface; explain the propensity of cells to adhere to mineral surfaces; or measure the impact of cells on mineral hydrophobicity. Studies that have analysed the contact angle of cells use one of two methods to measure cell hydrophobicity; performing sessile drop measurements on air-dried cell lawn after culture filtration [58, 61, 89, 117, 120, 202, 203], and by mixing an aliquot containing a known number of cells with an organic solvent and measuring the optical density of the aqueous phase using UV-visible spectrophotometry to determine phase preference, and hence hydrophobicity [62, 117, 120, 130, 158]. Sharma *et al* suggested that the growth conditions of the cells have a strong impact on cell surface properties such as hydrophobicity, an idea also suggested by Vilinska *et al* [58, 203]. Studies that report the impact of microorganisms on contact angle often provide variable results for the same strain of microorganism, depending on the mineral substrate. Chen *et al* observed that chalcopyrite became increasingly hydrophobic upon exposure to *A. ferrooxidans*, suggesting this may be caused by formation of elemental sulfur on the surface through direct attack [124]. In contrast, Liu *et al* observed that pyrite became increasingly hydrophilic due to *A. ferrooxidans* by adhering to the surface [26].

Chau *et al* studied the effects of roughness, particle size and the kinetics and thermodynamics (see Section 3.15) of contact angle measurements and the implications for flotation practices, and suggest not enough study is being done to relate surface characteristics to contact angle in a reliable way [193]. Many studies have related the flotation recovery of mineral particles, rather than solid surfaces, with contact angle. The relation of contact angle to recovery in froth flotation is heavily dependent on particle size, with a minimum contact angle required for a given particle size, with larger particles (≥37 μm) floating more readily than fine (≤37 μm) particles [204, 205]. This is due to small particles having lower collisions with bubbles in the flotation cell, and being unable to displace the water layer to come into three-phase contact with the bubbles [205]. As such, minerals ground to smaller particle sizes will tend to be less hydrophobic, and altering contact angle as well as bubble size can improve recovery [206]. A study by Chipfunhu *et al* investigated the flotation of single size fraction of quartz particles with hydrophobicity controlled by selective methylation, the results of which agree with previous studies that conclude a minimum critical contact angle exists for any given particle size [205]. This study also suggests that, for a mineral of given particle size, a

difference in contact angle of just 3° can alter mineral recovery by up to 18%, demonstrating even small changes in mineral hydrophobicity can alter flotation recovery significantly [205].

Many previous investigations on the effects of bacterial exposure to sulfide minerals do not report contact angles on pure mineral, but instead report flotation recovery [50, 53, 62, 64, 66, 93], with many using collector to aid separation rather than microorganisms or their excretions alone [46-49, 63, 92, 156, 202, 207, 208]. There is a lack of uniformity in approach to contact angle measurement of minerals for bioflotation purposes, with many papers not displaying the error associated with their data, or reporting changes to the contact angle of the mineral surface after exposure to cells [58, 89, 120, 130]. The measurement of mineral wettability has many challenges, including the small sample area, the variation in roughness of the surface, the concentration of flotation reagents as well as the exposure time to those reagents [5, 193].

Contact angle measurements on solid mineral surfaces will enable the direct comparison between the distribution of cells on the surface, surface roughness and the chemical species on the surface with mineral wettability. This will enable the identification of microorganisms and their excretions that have the potential to act as efficient reagents for bioflotation.

2.5.4 Near Edge X-ray Adsorption Fine Structure

Near edge X-ray fine structure (NEXAFS), also known as X-ray absorption near edge structure (XANES), occurs over the photon energies close to the absorption edge of an atom, and depends on the electronic structure and chemical environment of the atom, which dictate the final valence state of photoexcited core electrons [209-211]. The details behind the NEXAFS technique are discussed in Chapter 3, section 3.11.

Previous studies have applied NEXAFS to a wide range of materials, providing surface chemistry and electronic structure information on carbon [212] and titania [213] nanotubes, graphite [212, 214, 215], and polymers [216]. NEXAFS has been used to investigate a range of minerals, for the purposes of elucidating oxidation states, identifying mineral phases in heterogeneous ores, and to explore the effects of a range of reaction conditions on mineral surfaces [24, 33, 217-223]. Other studies have used NEXAFS to identify formal valence states of chemical structures [33, 220-222]. Colliex *et al* and Wu *et al* related well-characterised structures to the signals observed in the NEXAFS spectra, and linked spectral features to atomic arrangement and electronic structure [221, 222]. However, Goh *et al* suggest that no method of NEXAFS collection was able to reliably indicate formal oxidation state [220].

NEXAFS has also been used to study various kinds of biomineralization [146, 147, 178, 224] and organic matter in soil [225, 226], and has been used extensively to collected information on a wide variety of soft matter and biomaterials, as the chemical bonds and molecular orbitals of hydrocarbons can allow a fingerprint analysis of their associated spectra [209]. Several studies have used NEXAFS to investigate protein adsorption onto polymer substrates [148, 183-185, 227-232]. Studies have utilised low molecular weight elements NEXAFS such as N, C, O and Ca K-edge to map proteins and extracellular polymers on a variety of substrates [150, 160, 165, 233-239].

Several difficulties surround the use and interpretation of NEXAFS spectra, including the occurrence of radiation damage [216], and the non-uniform calibration of the absorption edge throughout the literature [240]. Plekan *et al* also found NEXAFS alone is insufficient to tell the difference between where a protein is chemisorbed or physisorbed onto pyrite surfaces [234].

NEXAFS spectra are obtained by spectromicroscopic techniques such as photoelectron emission microscopy, and microspectroscopic techniques such as scanning transmission electron microscopy, which will be discussed in the following sections. As this technique can provide chemical bonding information, it can provide atom-specific information about the electronic and chemical structure of microbial products and the mineral surface, as features of the spectra are related to oxidation state, chemical bonds or molecular orbitals [209-211]. This will enable the identification of oxidation products, and major EPS components that contribute to the hydrophobicity of the mineral surface, and contribute to the elucidation of the mechanism through which microorganisms interact with the mineral.

2.5.5 Photoemission Electron Microscopy

Photoemission electron microscopy (PEEM) is a synchrotron-based spectromicroscopic technique that has previously been applied to a range of soft-matter and thin films where surface sensitivity and spatial elemental mapping is desirable for analysis [241]. The PEEM station collects secondary electrons emitted from the sample upon photon irradiation, and uses an all-electrostatic column to magnify the field of view defined by the objective lens [242]. The theory and operation of PEEM, and its advantages compared to other X-ray analysis techniques, will be discussed in Chapter 3, section 3.12.

Previous studies have used PEEM to analyse mineral surfaces under different oxidation conditions. Acres *et al* used PEEM for the analysis of freshly polished and oxidised pentlandite, pyrrhotite and chalcopyrite, and were able to map mineral domains, from which NEXAFS spectra were extracted to identify oxidation products and intergrown mineral [217]. Smith *et al* explored the difficulties of

mineral analysis overcome by micro-area-selectable analysis using PEEM, including improved spatial clarity and comparable spectral quality to other X-ray absorption techniques [223]. Applications of PEEM to mineral systems have so far been limited, however the technique has been extensively applied to a variety of biomaterials and soft matter, with protein absorption and polymer films being of great interest to a variety of medical applications [148, 185, 227, 231].

There are several limitations that must be considered when using PEEM. Importantly, samples must have smooth to be suitable for PEEM, as field emissions occur from high-points or edges and must be removed by polishing samples flat [217, 223]. Mineral surfaces can also have charging issues that can prevent the collection of quality images, leading to some samples requiring conductive coatings [223]. A further limitation to the technique is the difficulty associated with quantifying signal intensities, meaning it is not possible to determine the concentration of species on the sample surface [231].

These studies demonstrate PEEM as being highly valuable for studying the effect of microorganisms on mineral surfaces, with its advantages of surface-sensitivity, high spatial resolution and ability to obtain elemental and chemical state images to powerfully complement spectra obtained with NEXAFS [227, 229, 241-243]. This will enable the identification of microbial and EPS components on the surface of minerals that may be suitable for bioflotation.

2.5.6 Scanning Transmission X-ray Microscopy

Scanning Transmission X-ray Microscopy (STXM) is a microspectroscopic technique that has previously been applied to a range of soft materials and biomaterials that would not retain their chemical and/or physical characteristics under more typical synchrotron analysis techniques, enabling chemical and elemental mapping of biological samples [148, 244]. The theory and benefits of STXM will be discussed in detail in Chapter 3, section 3.13. Many studies have used STXM to characterise polymer systems and protein adsorption to polymer phases, with STXM allowing the analysis of hydrated samples, which is not possible with ultrahigh vacuum surface analysis methods, and eliminating the need for fluorescent probes [148, 150, 185, 228, 230, 231, 244, 245].

Mitsunobu *et al* presented carbon and iron STXM images of pyrite exposed to *A. ferrooxidans*, successfully identifying proteins and polysaccharides as present in the cells and at the cell/pyrite interface [140]. Very few studies have been applied to sulfide minerals for surface modification by microorganisms, however similar systems have been reported in the literature, often in combination with NEXAFS spectra. Several studies on biomineralization have utilised STXM [131, 146, 160, 224, 237, 246], while biofilms and their components have been studied extensively by STXM in

previous investigations [148, 150, 151, 165, 178, 232, 233, 238, 247, 248]. Previous work has mapped biofilm components, including protein, lipids and polysaccharides, as well as the distribution of metals such as iron and nickel in the biofilm matrix [148, 150, 165, 232, 233, 247]. Stewart-Ornstein *et al* and Boese *et al* investigated proteins and peptides in isolation as compounds that contribute to a variety of biological environments [238, 248].

As a relatively new analysis technique, there are several limitations to the use of STXM for the visualisation of biofilm components. These include a dependence on the quality of reference spectra, the high statistical quality of images required for analysis, and the possibility of absorption saturation on thick samples (≥200 nm for dry samples) [150]. The overlapping of spectral features is also a possibility when attempting to map biofilm components, and the silicon nitride window required for STXM samples adds an optical element to the laser light path, limiting the working distance of the lenses in the instrument [150].

The STXM technique is a valuable tool for exploring micro and nanoscale regions of minerals exposed to cells, providing the advantage of a smaller radiation dose and the ability to analyse wet cells that may be used to provide insight into the mechanisms of bacterial-mineral interactions. The ability to map EPS components and their distribution around mineral particles can be used to assess the suitability of microorganisms and their excretions for application in bioflotation.

2.5.7 Time of Flight – Secondary Ion Mass Spectroscopy

Time of Flight – Secondary Ion Mass Spectroscopy (ToF-SIMS) is a surface sensitive technique that can provide qualitative and semi-quantitative information on the chemistry of the outer-most atomic layers of a sample, making it ideal for application to mineral processing where the outermost layer dictates floatability. The theory behind ToF-SIMS is discussed in detail in Chapter 3, section 3.14.

Several studies have applied ToF-SIMS to the study of flotation of sulfide minerals, relating measured surface fragments and elements to the hydrophobicity, variously reporting that the secondary ions Mg^+, Al^+, Si^+, K^+, Ca^+, Fe^+, Cu^+, $FeOH^+$, O^-, S^-, $OC_2H_5^-$, SO_3^-, SO_4^-, S_2^-, and S_3^- could be used to classify minerals and predict floatability [208, 217, 219, 249-251]. Studies by Brito e Abreu *et al* found that they could predict the contact angle of untreated chalcopyrite based on the secondary ions detected on the surface, even though the areas of analysis are very different between these techniques [208, 249]. ToF-SIMS has also been applied extensively to the analysis of carbonaceous material ranging from polymers to complex tissue samples [252-254]. This technique offers a method of relating chemical composition of biomaterials and cell surfaces and components

to wettability, reporting oxygenated hydrocarbons produced less hydrophobic surfaces, while proteins provide more hydrophobic character [255-257]. These studies not only suggest that ToF-SIMS is a valuable technique for the analysis of the outermost layers of a surface that determine hydrophobicity, but that it can also be used to fingerprint mixtures of large, complex biomolecules [166, 253, 258, 259].

The ToF-SIMS analysis of biological samples has several limitations that must be considered when performing surface analysis. The intensity of a fragment depends on the surrounding environment, known as matrix effects, make the intensity of a fragment unable to be directly related to concentration on the surface [252]. Poly dimethyl siloxane (PDMS) contamination has been described by Brouwer *et al* as a serious contamination issue that reduces signal strength from biological samples [166]. Breitenstein *et al* acknowledge that structure of cellular material may be preserved by fixative, but that chemical alterations are taking place, indicating that sample preparation is crucial to the accurate reporting of cellular material [172]. To date, many studies focus on specific chemical structures and method development for biological studies, rather than examining the whole EPS matrix, as the analysis of complex biological samples is convoluted and requires multivariate statistical analysis to elucidate patterns in fragmentation and identification of common structures [172, 187, 259-263].

The use of ToF-SIMS to identify fragments related to the hydrophobicity of sulfide minerals, and to fingerprint large biomolecules, make it an ideal technique to relate the surface chemistry of minerals and microorganisms to bioflotation. This technique will enable the comparison of EPS profiles of different microorganisms, the identification of EPS components, and the changes in the surface chemistry of the mineral over the course of exposure. Combined with the microscopic techniques discussed earlier, ToF-SIMS can provide comprehensive surface analysis to assess the suitability of microorganisms and their EPS as flotation reagents for sulfide minerals.

2.6 Summary of Literature Review

The scope of the literature review presented here has covered the major aspects of sulfide mineral bioflotation. This included an overview of the froth flotation process, the solution and surface chemistry involved, the minerals of significance and their physical and chemical properties. Several microorganisms of interest to this investigation have been described with their previous applications in the field of mineral processing, and current investigations of EPS extraction and analysis have been reviewed. The three previously proposed mechanisms – direct contact, indirect contact, and indirect – through which cells interact with mineral surfaces have been explored. The current debate

as to which mechanism most accurately describes the interaction, with emphasis on the necessity of attachment and the role of EPS, has been highlighted.

This literature review has highlighted the need for multiple analytical techniques in a fundamental study on microbial action on sulfide minerals to elucidate the role of attachment and EPS in surface modification. It has been demonstrated that cell attachment and excretions and their impact on the surface of pyrite requires in-depth chemical and physical analysis to assess the suitability of microorganisms as bioflotation reagents. A multifaceted approach to the analysis of the mineral surface and solution conditions is required to elucidate the physical and chemical changes that are likely to be beneficial for the bioflotation process.

2.7 References

1. Nagaraj, D.R., *Minerals Recovery and Processing*, in *Kirk-Othmer Encyclopedia of Chemical Technology*. 2000, John Wiley & Sons, Inc. p. 595-679.
2. Wills, B.A., *Wills' Mineral Processing Technology*. 7th ed, ed. T.J. Napier-Munn. 2006, Oxford: Elsevier. 444.
3. Jameson, G.J., Nguyen, A.V., Ata, S., *The Flotation of Fine and Coarse Particles*, in *Froth Flotation: A Century of Innovation*, G.J. Maurice C. Fuerstenau, Roe-Hoan Yoon, Editor. 2007, Society for Mining, Metallurgy, and Exploration: Littleton, Colarado. p. 339-372.
4. Fuerstenau, M.C., Chander, S., Woods, R., *Sulphide Mineral Flotation*, in *Froth Flotation: A Century of Innovation*, M.C. Fuerstenau, Jameson, G., Yoon, R.-H., Editor. 2007, Society for Mining, Metallurgy, and Exploration: Littleton, Colarado. p. 425-464.
5. Kawatra, S.K. *Flotation Fundamentals*. Mining Engineering Handbook, 2009. 30.
6. Yudiarto, A., *Extraction Process For Pb and Zn from Galena (PbS) and Sphalerite (ZnS) Ores*, in *Extractive Metallurgy*. 2008: Jakarta.
7. Ralston, J., Fornasiero, D., Grano, S., *Pulp and Solution Chemistry*, in *Froth Flotation: A Century of Innovation*, M.C. Fuerstenau, Jameson, G., Yoon, R.-H., Editor. 2007, Society for Mining, Metallurgy, and Exploration: Littleton, Colerado. p. 227-258.
8. Wang, S., *Copper leaching from chalcopyrite concentrates.* JOM Journal of the Minerals, Metals and Materials Society, 2005. **57**(7): p. 48-51.
9. Hayes, S.M., Root, R. A., Perdrial, N., Maier, R. M., Chorover, J., *Surficial weathering of iron sulfide mine tailings under semi-arid climate.* Geochimica et Cosmochimica Acta, 2014. **141**: p. 240-257.
10. Brandl, H., *Microbial Leaching of Metals*, in *Biotechnology Set*. 2008, Wiley-VCH Verlag GmbH. p. 191-224.
11. Petersen, J., Dixon, D. G., *Thermophilic heap leaching of a chalcopyrite concentrate.* Minerals Engineering, 2002. **15**(11): p. 777-785.
12. Murphy, R., Strongin, D. R., *Surface reactivity of pyrite and related sulfides.* Surface Science Reports, 2009. **64**(1): p. 1-45.
13. Doyle, C.S., Kendelewicz, T., Bostick, B. C., Brown, G. E., *Soft X-ray spectroscopic studies of the reaction of fractured pyrite surfaces with Cr(VI)-containing aqueous solutions.* Geochimica et Cosmochimica Acta, 2004. **68**(21): p. 4287-4299.
14. Mitchell, T.K., Nguyen, A. V., Evans, G. M., *Heterocoagulation of chalcopyrite and pyrite minerals in flotation separation.* Advances in Colloid and Interface Science, 2005. **114-115**(Supplement C): p. 227-237.

15. Fuerstenau, M.C., Sabacky, B. J., *On the natural floatability of sulfides.* International Journal of Mineral Processing, 1981. **8**(1): p. 79-84.
16. von Oertzen, G.U., Jones, R. T., Gerson, A. R., *Electronic and optical properties of Fe, Zn and Pb sulfides.* Physics and Chemistry of Minerals, 2005. **32**(4): p. 255-268.
17. Ndlovu, S., Monhemius, A. J., *The influence of crystal orientation on the bacterial dissolution of pyrite.* Hydrometallurgy, 2005. **78**(3): p. 187-197.
18. Edelbro, R., Sandström, Å. Paul, J., *Full potential calculations on the electron bandstructures of Sphalerite, Pyrite and Chalcopyrite.* Applied Surface Science, 2003. **206**(1): p. 300-313.
19. Vaughan, D.J., Craig, J.R., *Mineral Chemistry of Metal Sulfides*. 1978: Cambridge University Press.
20. *Ferrous iron compound: structure of pyrite*. Sulphides 2010 [cited 2017; Available from: https://www.britannica.com/science/mineral-chemical-compound/Sulfides.
21. Womes, M., Karnatak, R. C., Esteva, J. M., Lefebvre, I., Allan, G., Olivier-Fourcades, J., Jumas, J. C., *Electronic structures of FeS and FeS2: X-ray absorption spectroscopy and band structure calculations.* Journal of Physics and Chemistry of Solids, 1997. **58**(2): p. 345-352.
22. Rimstidt, J.D., Vaughan, D. J., *Pyrite oxidation: a state-of-the-art assessment of the reaction mechanism.* Geochimica et Cosmochimica Acta, 2003. **67**(5): p. 873-880.
23. Sharma, P.K., Das, A., Hanumantha Rao, K., Forssberg, K. S. E., *Surface characterization of Acidithiobacillus ferrooxidans cells grown under different conditions.* Hydrometallurgy, 2003. **71**(1–2): p. 285-292.
24. Yang, Y., Harmer, S., Chen, M., *Synchrotron X-ray photoelectron spectroscopic study of the chalcopyrite leached by moderate thermophiles and mesophiles.* Minerals Engineering, 2014. **69**: p. 185-195.
25. Zhang, Y.-S., Qin, W.-Q., Wang, J., Zhen, S.-J., Yang, C.-R., Zhang, J.-W., Nai, S.-S., Qiu, G.-Z., *Bioleaching of chalcopyrite by pure and mixed culture.* Transactions of Nonferrous Metals Society of China, 2008. **18**(6): p. 1491-1496.
26. Liu, H., Gu, G., Xu, Y., *Surface properties of pyrite in the course of bioleaching by pure culture of Acidithiobacillus ferrooxidans and a mixed culture of Acidithiobacillus ferrooxidans and Acidithiobacillus thiooxidans.* Hydrometallurgy, 2011. **108**(1–2): p. 143-148.
27. Xia, J.-L., Yang, Y., He, H., Zhao, X.-J., Liang, C.-L., Zheng, L., Ma, C.-Y., Zhao, Y.-D., Nie, Z.-Y., Qiu, G.-Z., *Surface analysis of sulfur speciation on pyrite bioleached by extreme thermophile Acidianus manzaensis using Raman and XANES spectroscopy.* Hydrometallurgy, 2010. **100**(3–4): p. 129-135.
28. He, S., Fornasiero, D., Skinner, W., *Correlation between copper-activated pyrite flotation and surface species: Effect of pulp oxidation potential.* Minerals Engineering, 2005. **18**(12): p. 1208-1213.
29. Nesbitt, H.W., Muir, I. J., *X-ray photoelectron spectroscopic study of a pristine pyrite surface reacted with water vapour and air.* Geochimica et Cosmochimica Acta, 1994. **58**(21): p. 4667-4679.
30. Pradhan, N., Nathsarma, K. C., Srinivasa Rao, K., Sukla, L. B., Mishra, B. K., *Heap bioleaching of chalcopyrite: A review.* Minerals Engineering, 2008. **21**(5): p. 355-365.
31. Watling, H.R., *The bioleaching of sulphide minerals with emphasis on copper sulphides — A review.* Hydrometallurgy, 2006. **84**(1–2): p. 81-108.
32. Tao, H., Dongwei, L., *Presentation on mechanisms and applications of chalcopyrite and pyrite bioleaching in biohydrometallurgy – a presentation.* Biotechnology Reports, 2014. **4**(Supplement C): p. 107-119.
33. Mikhlin, Y., Tomashevich, Y., Tauson, V., Vyalikh, D., Molodtsov, S., Szargan, R., *A comparative X-ray absorption near-edge structure study of bornite, Cu5FeS4, and*

chalcopyrite, CuFeS2. Journal of Electron Spectroscopy and Related Phenomena, 2005. **142**(1): p. 83-88.
34. Tossell, J.A., Urch, D. S., Vaughan, D. J., Wiech, G. , *The electronic structure of CuFeS2, chalcopyrite, from x-ray emission and x-ray photoelectron spectroscopy and Xα calculations.* The Journal of Chemical Physics, 1982. **77**(1): p. 77-82.
35. Pridmore, D.F., Shuey R.T. , *The electrical resistivity of galena, pyrite, and chalcopyrite.* American Mineralogist, 1976. **61**(3-4): p. 248-259.
36. Hackl, R.P., Dreisinger, D. B., Peters, E., King, J. A., *Passivation of chalcopyrite during oxidative leaching in sulfate media.* Hydrometallurgy, 1995. **39**(1–3): p. 25-48.
37. Buckley, A.N., Woods, R., *An X-ray photoelectron spectroscopic study of the oxidation of chalcopyrite.* Australian Journal of Chemistry, 1984. **37**(12): p. 2403-2413.
38. Liang, H.C., Thomson, B. M., *Minerals and Mine Drainage.* Water Environment Research, 2009. **81**(10): p. 1615-1663.
39. Clark, M.E., Batty, J. D., van Buuren, C. B., Dew, D. W., Eamon, M. A., *Biotechnology in minerals processing: Technological breakthroughs creating value.* Hydrometallurgy, 2006. **83**(1–4): p. 3-9.
40. Rao, H.K., Vilinska, A., Chernyshova, I. V., *Minerals bioprocessing: R & D needs in mineral biobeneficiation.* Hydrometallurgy, 2010. **104**(3–4): p. 465-470.
41. Nagaraj, D.R., Ravishankar, S.A., *Flotation Reagents - A Critical Overview from an Industry Perspective*, in *Froth Flotation: A Century of Innovation*, G.J. Maurice C. Fuerstenau, Roe-Hoan Yoon, Editor. 2007, Societyof Mining, Metallurgy and Exploration: Littleton, Colarado. p. 375-424.
42. Chander, S., Nagaraj, D. R., *Flotation: Flotation Reagents*, in *Encyclopedia of Separation Science*, D.W. Editor-in-Chief: Ian, Editor. 2007, Academic Press: Oxford. p. 1-14.
43. Leppinen, J.O., *FTIR and flotation investigation of the adsorption of ethyl xanthate on activated and non-activated sulfide minerals.* International Journal of Mineral Processing, 1990. **30**(3–4): p. 245-263.
44. *PubChem Compound Database; CID=9274*. 2005 Dec 9 2017]; Available from: https://pubchem.ncbi.nlm.nih.gov/compound/9274
45. *Dithiophosphates with thionocarbamates*. [cited 2017 9 Dec 2017]; Available from: http://www.danafloat.com/uk/mineral_collectors/262T.
46. Mehrabani, J.V., Mousavi, S. M., Noaparast, M., *Evaluation of the replacement of NaCN with Acidithiobacillus ferrooxidans in the flotation of high-pyrite, low-grade lead–zinc ore.* Separation and Purification Technology, 2011. **80**(2): p. 202-208.
47. Chandraprabha, M.N., Natarajan, K. A., *Surface chemical and flotation behaviour of chalcopyrite and pyrite in the presence of Acidithiobacillus thiooxidans.* Hydrometallurgy, 2006. **83**(1–4): p. 146-152.
48. Chandraprabha, M.N., Natarajan, K. A., Somasundaran, P., *Selective separation of pyrite from chalcopyrite and arsenopyrite by biomodulation using Acidithiobacillus ferrooxidans.* International Journal of Mineral Processing, 2005. **75**(1–2): p. 113-122.
49. Mehrabani, J.V., Noaparast, M., Mousavi, S. M., Dehghan, R., Rasooli, E., Hajizadeh, H., *Depression of pyrite in the flotation of high pyrite low-grade lead–zinc ore using Acidithiobacillus ferrooxidans.* Minerals Engineering, 2010. **23**(1): p. 10-16.
50. Langwaldt, J., Kalapudas, R., *Bio-benefication of multimetal black shale ore by flotation.* Pyhsicochemical Problems of Mineral Processing, 2007. **41**: p. 291-299.
51. Gunther, F.A., Gunther, J.D., *Residue Reviews: Residues of Pesticides and Other Contaminants in the Total Environment*. 2013: Springer New York.
52. Pohanish, R.P., *C*, in *Sittig's Handbook of Toxic and Hazardous Chemicals and Carcinogens (Sixth Edition)*, R.P. Pohanish, Editor. 2012, William Andrew Publishing: Oxford. p. 498-846.
53. Khoshdast, H., Sam, A., Manafi, Z., *The use of rhamnolipid biosurfactants as a frothing agent and a sample copper ore response.* Minerals Engineering, 2012. **26**(0): p. 41-49.

54. Ralston, J., *Eh and its consequences in sulphide mineral flotation.* Minerals Engineering, 1991. **4**(7): p. 859-878.
55. Garrels, R.M., Christ, C.L., *Solutions, Minerals, and Equilibria*. 1990: Jones and Bartlett.
56. Hayes, R.A., Ralston, J., *The collectorless flotation and separation of sulphide minerals by Eh control.* International Journal of Mineral Processing, 1988. **23**(1): p. 55-84.
57. Yang, H.-Y., Liu, W., Chen, G.-B., Liu, Y.-Y., Tong, L.-L., Jin, Z.-N., Liu, Z.-L., *Function of microorganism and reaction pathway for carrollite dissolution during bioleaching.* Transactions of Nonferrous Metals Society of China, 2015. **25**(8): p. 2718-2754.
58. Vilinska, A., Hanumantha Rao, K., *Surface Thermodynamics and Extended DLVO Theory of Acidithiobacillus ferrooxidans Cells Adhesion on Pyrite and Chalcopyrite*. Vol. 2. 2009.
59. Shen, W.Z., Fornasiero, D., Ralston, J., *Effect of collectors, conditioning pH and gases in the separation of sphalerite from pyrite.* Minerals Engineering, 1998. **11**(2): p. 145-158.
60. Yu, J.-Y., McGenity, T. J., Coleman, M. L., *Solution chemistry during the lag phase and exponential phase of pyrite oxidation by Thiobacillus ferrooxidans.* Chemical Geology, 2001. **175**(3): p. 307-317.
61. Diao, M., Nguyen, T. A. H., Taran, E., Mahler, S., Nguyen, A. V., *Differences in adhesion of A. thiooxidans and A. ferrooxidans on chalcopyrite as revealed by atomic force microscopy with bacterial probes.* Minerals Engineering, 2014. **61**(0): p. 9-15.
62. Farahat, M., Hirajima, T., Sasaki, K., Aiba, Y., Doi, K., *Adsorption of SIP E. coli onto quartz and its applications in froth flotation.* Minerals Engineering, 2008. **21**(5): p. 389-395.
63. Govender, Y., Gericke, M,, *Extracellular polymeric substances (EPS) from bioleaching systems and its application in bioflotation.* Minerals Engineering, 2011. **24**(11): p. 1122-1127.
64. Smith, R.W., Miettinen, M., *Microorganisms in flotation and flocculation: Future technology or laboratory curiosity?* Minerals Engineering, 2006. **19**(6–8): p. 548-553.
65. Natarajan, K.A., Das, A., *Surface chemical studies on 'Acidithiobacillus' group of bacteria with reference to mineral flocculation.* International Journal of Mineral Processing, 2003. **72**(1–4): p. 189-198.
66. Nagaoka, T., Ohmura, N., Saiki, H., *A novel mineral processing by flotation using Thiobacillus ferrooxidans*, in *Process Metallurgy*, R. Amils and A. Ballester, Editors. 1999, Elsevier. p. 335-342.
67. Jafari, M., Shafaei, S., Abdollahi, H., Gharabaghi, M., Chehreh Chelgani, S., *A Comparative Study on the Effect of Flotation Reagents on Growth and Iron Oxidation Activities of Leptospirillum ferrooxidans and Acidithiobacillus ferrooxidans.* Minerals, 2017. **7**(1): p. 2.
68. Betsy, T., Keogh, J., *Microbiology Demystified*. 2005: McGraw-Hill Education.
69. Rodgers, K., Kadner, R. J. *Bacteria*. Encyclopædia Britannica 2017 [cited 2017; Available from: https://www.britannica.com/science/bacteria.
70. Niederberger, T. *Archaea*. Encyclopædia Britannica 2015 [cited 2017; Available from: https://www.britannica.com/science/archaea.
71. Todar, K., *Todar's Online Textbook of Bacteriology*. 2006: University of Wisconsin-Madison Department of Bacteriology.
72. Ullmann, A., *Selected Papers in Molecular Biology by Jacques Monod*. 2012: Elsevier Science.
73. Zwietering, M.H., Jongenburger, I., Rombouts, F. M., van 't Riet, K., *Modeling of the bacterial growth curve.* Appl Environ Microbiol, 1990. **56**(6): p. 1875-81.
74. Watling, H.R., Perrot, F. A., Shiers, D. W., *Comparison of selected characteristics of Sulfobacillus species and review of their occurrence in acidic and bioleaching environments.* Hydrometallurgy, 2008. **93**(1–2): p. 57-65.
75. Pacholewska, M., *Microbial leaching of blende flotation concentrate using Acidithiobacillus ferrooxidans and Acidithiobacillus thiooxidans.* Physicochemical Problems of Mineral Processing, 2003. **37**: p. 57-68.

76. Beard, S., Paradela, A., Albar, J. P., Jerez, C. A., *Growth of Acidithiobacillus Ferrooxidans ATCC 23270 in Thiosulfate Under Oxygen-Limiting Conditions Generates Extracellular Sulfur Globules by Means of a Secreted Tetrathionate Hydrolase.* Front Microbiol, 2011. **2**(79).
77. Brunner, B., Yu, J.-Y., Mielke, R. E., MacAskill, J. A., Madzunkov, S., McGenity, T. J., Coleman, M., *Different isotope and chemical patterns of pyrite oxidation related to lag and exponential growth phases of Acidithiobacillus ferrooxidans reveal a microbial growth strategy.* Earth and Planetary Science Letters, 2008. **270**(1–2): p. 63-72.
78. Deveci, H., Akcil, A., Alp, I., *Bioleaching of complex zinc sulphides using mesophilic and thermophilic bacteria: comparative importance of pH and iron.* Hydrometallurgy, 2004. **73**(3–4): p. 293-303.
79. Dong, Y., Lin, H., Xu, X., Zhou, S., *Bioleaching of different copper sulfides by Acidithiobacillus ferrooxidans and its adsorption on minerals.* Hydrometallurgy, 2013. **140**(0): p. 42-47.
80. He, H., Xia, J.-L., Hong, F.-F., Tao, X.-X., Leng, Y.-W., Zhao, Y.-F., *Analysis of sulfur speciation on chalcopyrite surface bioleached with Acidithiobacillus ferrooxidans.* Minerals Engineering, 2012. **27–28**(0): p. 60-64.
81. Hocheng, H., Chang, J. H., Hsu, H. S., Han, H. J., Chang, Y. L., Jadhav, U. U., *Metal removal by Acidithiobacillus ferrooxidans through cells and extra-cellular culture supernatant in biomachining.* CIRP Journal of Manufacturing Science and Technology, 2012. **5**(2): p. 137-141.
82. Mykytczuk, N.C.S., Trevors, J. T., Ferroni, G. D., Leduc, L. G., *Cytoplasmic membrane response to copper and nickel in Acidithiobacillus ferrooxidans.* Microbiological Research, 2011. **166**(3): p. 186-206.
83. Felício, A.P., de Oliveira, E., Odena, M. A., Garcia Jr, O., Bertolini, M. C., Ferraz, L. F. C., Ottoboni, L. M. M., Novo, M. T. M., *Differential proteomic analysis of Acidithiobacillus ferrooxidans cells maintained in contact with bornite or chalcopyrite: Proteins involved with the early bacterial response.* Process Biochemistry, 2011. **46**(3): p. 770-776.
84. Harneit, K., Göksel, A., Kock, D., Klock, J. H., Gehrke, T., Sand, W., *Adhesion to metal sulfide surfaces by cells of Acidithiobacillus ferrooxidans, Acidithiobacillus thiooxidans and Leptospirillum ferrooxidans.* Hydrometallurgy, 2006. **83**(1–4): p. 245-254.
85. Tan, S.N., Chen, M., *Early stage adsorption behaviour of Acidithiobacillus ferrooxidans on minerals I: An experimental approach.* Hydrometallurgy, 2012. **119–120**(0): p. 87-94.
86. Zhu, J., Jiao, W., Li, Q., Liu, X., Qin, W., Qiu, G., Hu, Y., Chai, L., *Investigation of energy gene expressions and community structures of free and attached acidophilic bacteria in chalcopyrite bioleaching.* Journal of Industrial Microbiology & Biotechnology, 2012. **39**(12): p. 1833-1840.
87. Chandraprabha, M.N., Natarajan, K. A., *Role of outer membrane exopolymers of Acidithiobacillus ferrooxidans in adsorption of cells onto pyrite and chalcopyrite.* International Journal of Mineral Processing, 2013. **123**(0): p. 152-157.
88. Yu, R.-L., Ou, Y., Tan, J.-X., Wu, F.-D., Sun, J., Miao, L., Zhong, D.-L., *Effect of EPS on adhesion of Acidithiobacillus ferrooxidans on chalcopyrite and pyrite mineral surfaces.* Transactions of Nonferrous Metals Society of China, 2011. **21**(2): p. 407-412.
89. Zhu, J., Li, Q., Jiao, W., Jiang, H., Sand, W., Xia, J., Liu, X., Qin, W., Qiu, G., Hu, Y., Chai, L., *Adhesion forces between cells of Acidithiobacillus ferrooxidans, Acidithiobacillus thiooxidans or Leptospirillum ferrooxidans and chalcopyrite.* Colloids and Surfaces B: Biointerfaces, 2012. **94**: p. 95-100.
90. Yu, R.-L., Liu, J., Chen, A., Zhong, D.-L., Li, Q., Qin, W.-Q., Qiu, G.-Z., Gu, G.-H., *Interaction mechanism of Cu2+, Fe3+ ions and extracellular polymeric substances during bioleaching chalcopyrite by Acidithiobacillus ferrooxidans ATCC2370.* Transactions of Nonferrous Metals Society of China, 2013. **23**(1): p. 231-236.

91. Wang, Z.-H., Xie, X.-H., Liu, J.-S., *Experimental measurements of short-term adsorption of Acidithiobacillus ferrooxidans onto chalcopyrite.* Transactions of Nonferrous Metals Society of China, 2012. **22**(2): p. 442-446.
92. Pecina, E.T., Rodríguez, M., Castillo, P., Díaz, V., Orrantia, E., *Effect of Leptospirillum ferrooxidans on the flotation kinetics of sulphide ores.* Minerals Engineering, 2009. **22**(5): p. 462-468.
93. Vilinska, A., Hanumantha Rao, K., *Leptospirillum ferrooxidans-sulfide mineral interactions with reference to bioflotation and bioflocculation.* Transactions of Nonferrous Metals Society of China, 2008. **18**(6): p. 1403-1409.
94. Vera, M., Schippers, A., Sand, W., *Progress in bioleaching: fundamentals and mechanisms of bacterial metal sulfide oxidation—part A.* Applied Microbiology and Biotechnology, 2013. **97**(17): p. 7529-7541.
95. Andrews, G.F., *The selective adsorption of Thiobacilli to dislocation sites on pyrite surfaces.* Biotechnology and Bioengineering, 1988. **31**(4): p. 378-381.
96. Sand, W., Rohde, K., Sobotke, B., Zenneck, C., *Evaluation of Leptospirillum ferrooxidans for Leaching*. Vol. 58. 1992. 85-92.
97. Ban, J.-R., Gu, G.-H., Hu, K.-T., *Bioleaching and electrochemical property of marmatite by Leptospirillum ferrooxidans.* Transactions of Nonferrous Metals Society of China, 2013. **23**(2): p. 494-500.
98. Hippe, H., *Leptospirillum gen. nov. (ex Markosyan 1972), nom. rev., including Leptospirillum ferrooxidans sp. nov. (ex Markosyan 1972), nom. rev. and Leptospirillum thermoferrooxidans sp. nov. (Golovacheva et al. 1992).* International Journal of Systematic and Evolutionary Microbiology, 2000. **50**(2): p. 501-503.
99. Schippers, A., *Microorganisms involved in bioleaching and nucleic acid-based molecular methods for their identification and quantification*, in *Microbial Processing of Metal Sulfides*, E.R.D.a.W. Sand, Editor. 2007, Springer: Dordrecht, Netherlands. p. 3-33.
100. Segerer, A., Neuner, A., Kristjansson, J. K., Stetter, K. O., *Acidianus infernus gen. nov., sp. nov., and Acidianus brierleyi comb. nov.: Facultatively Aerobic, Extremely Acidophilic Thermophilic Sulfur-Metabolizing Archaebacteria.* International Journal of Systematic Bacteriology, 1986. **36**(4): p. 559-564.
101. Shiers, D.W., Ralph, D. E., Watling, H. R., *A comparative study of substrate utilisation by Sulfobacillus species in mixed ferrous ion and tetrathionate growth medium.* Hydrometallurgy, 2010. **104**(3–4): p. 363-369.
102. Nemati, M., Harrison, S. T. L., *A comparative study on thermophilic and mesophilic biooxidation of ferrous iron.* Minerals Engineering, 2000. **13**(1): p. 19-24.
103. Norris, P.R., Clark, D. A., Owen, J. P., Waterhouse, S., *Characteristics of Sulfobacillus acidophilus sp. nov. and other moderately thermophilic mineral-sulphide-oxidizing bacteria.* Microbiology, 1996. **142**(4): p. 775-783.
104. Bharadwaj, A., Ting, Y.-P., *Bioleaching of spent hydrotreating catalyst by acidophilic thermophile Acidianus brierleyi: Leaching mechanism and effect of decoking.* Bioresource Technology, 2013. **130**(0): p. 673-680.
105. Konishi, Y., Asai, S., Tokushige, M., Suzuki, T., *Kinetics of the bioleaching of chalcopyrite concentrate by acidophilic thermophile acidianus brierleyi.* Biotechnol Prog, 1999. **15**(4): p. 681-8.
106. Konishi, Y., Kogasaki, K., Asai, S., *Bioleaching of pyrite by Acidianus brierleyi in a continuous-flow stirred-tank reactor.* Chemical Engineering Science, 1997. **52**(24): p. 4525-4532.
107. Konishi, Y., Matsui, M., Fujiwara, H., Nomura, T., Nakahara, K., *Zinc Leaching from Fly Ash in Municipal Waste Incineration by Thermophilic Archaean Acidianus brierleyi Growing on Elemental Sulfur.* Separation Science and Technology, 2003. **38**(16): p. 4117-4130.

108. Konishi, Y., Nishimura, H., Asai, S., *Bioleaching of sphalerite by the acidophilic thermophile Acidianus brierleyi.* Hydrometallurgy, 1998. **47**(2–3): p. 339-352.
109. Konishi, Y., Tokushige, M., Asai, S., Suzuki, T., *Copper recovery from chalcopyrite concentrate by acidophilic thermophile Acidianus brierleyi in batch and continuous-flow stirred tank reactors.* Hydrometallurgy, 2001. **59**(2–3): p. 271-282.
110. Larsson, L., Olsson, G., Hoist, O., Karlsson, H. T., *Oxidation of pyrite by Acidianus brierleyi: Importance of close contact between the pyrite and the microorganisms.* Biotechnology Letters, 1993. **15**(1): p. 99-104.
111. Meng, C., Shi, X., Lin, H. , Chen, J., Guo, Y., *UV induced mutations in Acidianus brierleyi growing in a continuous stirred tank reactor generated a strain with improved bioleaching capabilities.* Enzyme and Microbial Technology, 2007. **40**(5): p. 1136-1140.
112. Sasaki, K., Takatsugi, K., Hirajima, T., *Effects of initial Fe2+ concentration and pulp density on the bioleaching of Cu from enargite by Acidianus brierleyi.* Hydrometallurgy, 2011. **109**(1–2): p. 153-160.
113. Takatsugi, K., Sasaki, K., Hirajima, T., *Mechanism of the enhancement of bioleaching of copper from enargite by thermophilic iron-oxidizing archaea with the concomitant precipitation of arsenic.* Hydrometallurgy, 2011. **109**(1–2): p. 90-96.
114. Zhu, W., Xia, J.-L., Peng, A.-A., Nie, Z.-Y., Qiu, G,-Z., *Characterization of apparent sulfur oxidation activity of thermophilic archaea in bioleaching of chalcopyrite.* Transactions of Nonferrous Metals Society of China, 2013. **23**(8): p. 2383-2388.
115. Zhu, W., Xia, J.-L., Yang, Y., Nie, Z.-Y., Zheng, L., Ma, C.-Y., Zhang, R.-Y., Peng, A.-A., Tang, L., Qiu, G.-Z., *Sulfur oxidation activities of pure and mixed thermophiles and sulfur speciation in bioleaching of chalcopyrite.* Bioresource Technology, 2011. **102**(4): p. 3877-3882.
116. Deveci, H., Jordan, M. A., Powell, N., Alp, I., *Effect of salinity and acidity on bioleaching activity of mesophilic and extremely thermophilic bacteria.* Transactions of Nonferrous Metals Society of China, 2008. **18**(3): p. 714-721.
117. Jordan, M.A., Barr, D. W., Phillips, C. V., *Iron and sulphur speciation and cell surface hydrophobicity during bacterial oxidation of a complex copper concentrate.* Minerals Engineering, 1993. **6**(8–10): p. 1001-1011.
118. Anand, P., Modak, J. M., Natarajan, K. A., *Biobeneficiation of bauxite using Bacillus polymyxa: calcium and iron removal.* International Journal of Mineral Processing, 1996. **48**(1–2): p. 51-60.
119. Menezes, C.T., Barros, E. C., Rufino, R. D., Luna, J. M., Sarubbo, L. A., *Replacing Synthetic with Microbial Surfactants as Collectors in the Treatment of Aqueous Effluent Produced by Acid Mine Drainage, Using the Dissolved Air Flotation Technique.* Appl Biochem Biotechnol, 2010. **163**: p. 540-546.
120. Ohmura, N., Kitamura, K., Saiki, H., *Selective Adhesion of Thiobacillus ferrooxidans to Pyrite.* Applied and Environmental Microbiology, 1993. **59**(12): p. 4044-4050.
121. Otsuki, A., Ohshima, H., *Use of Microorganisms for Complex Ore Beneficiation: Bioflotation as an Example*, in *Encyclopedia of Biocolloid and Biointerface Science 2V Set*. 2016, John Wiley & Sons, Inc. p. 108-117.
122. Behera, S.K., Mulaba-Bafubiandi, A. F., *Microbes Assisted Mineral Flotation a Future Prospective for Mineral Processing Industries: A Review.* Mineral Processing and Extractive Metallurgy Review, 2017. **38**(2): p. 96-105.
123. Crundwell, F.K., *How do bacteria interact with minerals?* Hydrometallurgy, 2003. **71**(1–2): p. 75-81.
124. Chen, M.-L., Zhang, L., Gu, G.-H., Hu, Y.-H., Su, L.-J., *Effects of microorganisms on surface properties of chalcopyrite and bioleaching.* Transactions of Nonferrous Metals Society of China, 2008. **18**(6): p. 1421-1426.
125. Sand, W., Gehrke, T., Jozsa, P.-G., Schippers, A., *(Bio)chemistry of bacterial leaching—direct vs. indirect bioleaching.* Hydrometallurgy, 2001. **59**(2): p. 159-175.

126. Rodríguez, Y., Ballester, A., Blázquez, M. L., González, F., Muñoz, J. A., *New information on the pyrite bioleaching mechanism at low and high temperature.* Hydrometallurgy, 2003. **71**(1–2): p. 37-46.
127. Acharya, C., Sukla, L. B., Misra, V. N., *Biodepyritisation of coal.* Journal of Chemical Technology & Biotechnology, 2004. **79**(1): p. 1-12.
128. Rodríguez, Y., Ballester, A., Blázquez, M. L., González, F., Muñoz, J. A., *New information on the chalcopyrite bioleaching mechanism at low and high temperature.* Hydrometallurgy, 2003. **71**(1–2): p. 47-56.
129. Grantham, M.C., Dove, P. M., *Investigation of bacterial-mineral interactions using Fluid Tapping Mode™ Atomic Force Microscopy.* Geochimica et Cosmochimica Acta, 1996. **60**(13): p. 2473-2480.
130. Devasia, P., Natarajan, K. A., *Adhesion of Acidithiobacillus ferrooxidans to mineral surfaces.* International Journal of Mineral Processing, 2010. **94**(3–4): p. 135-139.
131. Coker, V.S., Byrne, J. M., Telling, N. D., Van Der Laan, G., Lloyd, J. R., Hitchcock, A. P., Wang, J., Pattrick, R. A. D., *Characterisation of the dissimilatory reduction of Fe(III)-oxyhydroxide at the microbe – mineral interface: the application of STXM–XMCD.* Geobiology, 2012. **10**(4): p. 347-354.
132. Buckley, A.N., Woods, R., *The surface oxidation of pyrite.* Applied Surface Science, 1987. **27**(4): p. 437-452.
133. Woodcock, J.T., Sparrow, G. J., Bruckard, W. J., Johnson, N. W., Dunne, R., *Plant Practice: Sulphide Minerals and Precious Metals*, in *Froth Flotation: A Century of Innovation*, M.C. Fuerstenau, Jameson, G., Yoon, R.-H., Editor. 2007, Society for Mining, Metallurgy, and Exploration: Littleton, Colarado. p. 781-794.
134. Jordan, M.A., McGinness, S., Phillips, C. V., *Acidophilic bacteria—their potential mining and environmental applications.* Minerals Engineering, 1996. **9**(2): p. 169-181.
135. Rohwerder, T., Sand, W., *Mechanisms and biochemical fundamentals of bacterial metal sulfide oxidation*, in *Microbial Processing of Metal Sulfides*, E.R.D.a.W. Sand, Editor. 2007 Springer. p. 35-58.
136. Kinzler, K., Gehrke, T., Telegdi, J., Sand, W., *Bioleaching—a result of interfacial processes caused by extracellular polymeric substances (EPS).* Hydrometallurgy, 2003. **71**(1–2): p. 83-88.
137. Gehrke, T., Telegdi, J., Thierry, D., Sand, W., *Importance of Extracellular Polymeric Substances from Thiobacillus ferrooxidans for Bioleaching.* Appl Environ Microbiol, 1998. **64**(7): p. 2743-7.
138. Mikkelsen, D., Kappler, U., Webb, R. I., Rasch, R., McEwan, A. G., Sly, L. I., *Visualisation of pyrite leaching by selected thermophilic archaea: Nature of microorganism–ore interactions during bioleaching.* Hydrometallurgy, 2007. **88**(1–4): p. 143-153.
139. Pflumm, M., *Caught on film.* Nat Med, 2011. **17**(6): p. 650-653.
140. Mitsunobu, S., Zhu, M., Takeichi, Y., Ohigashi, T., Suga, H., Jinno, M., Makita, H., Sakata, M., Ono, K., Mase, K., Takahashi, Y., *Direct Detection of Fe(II) in Extracellular Polymeric Substances (EPS) at the Mineral-Microbe Interface in Bacterial Pyrite Leaching*. Vol. 31. 2016.
141. Usher, K.M., Shaw, J. A., Kaksonen, A. H., Saunders, M., *Elemental analysis of extracellular polymeric substances and granules in chalcopyrite bioleaching microbes.* Hydrometallurgy, 2010. **104**(3–4): p. 376-381.
142. Zeng, W., Qiu, G., Zhou, H., Liu, X., Chen, M., Chao, W., Zhang, C., Peng, J., *Characterization of extracellular polymeric substances extracted during the bioleaching of chalcopyrite concentrate.* Hydrometallurgy, 2010. **100**(3–4): p. 177-180.
143. Badireddy, A.R., Chellam, S., Gassman, P. L., Engelhard, M. H., Lea, A. S., Rosso, K. M., *Role of extracellular polymeric substances in bioflocculation of activated sludge microorganisms under glucose-controlled conditions.* Water Research, 2010. **44**(15): p. 4505-4516.

144. Faust, L., Temmink, H., Zwijnenburg, A., Kemperman, A. J. B., Rijnaarts, H. H. M., *High loaded MBRs for organic matter recovery from sewage: Effect of solids retention time on bioflocculation and on the role of extracellular polymers.* Water Research, 2014. **56**(0): p. 258-266.
145. Poorni, S., Natarajan, K. A., *Flocculation behaviour of hematite–kaolinite suspensions in presence of extracellular bacterial proteins and polysaccharides.* Colloids and Surfaces B: Biointerfaces, 2014. **114**(0): p. 186-192.
146. Chan, C.S., Fakra, S. C., Edwards, D. C., Emerson, D., Banfield, J. F., *Iron oxyhydroxide mineralization on microbial extracellular polysaccharides.* Geochimica et Cosmochimica Acta, 2009. **73**(13): p. 3807-3818.
147. Miot, J., Benzerara, K., Morin, G., Kappler, A., Bernard, S., Obst, M., Férard, C., Skouri-Panet, F., Guigner, J.-M., Posth, N., Galvez, M., Brown Jr, G. E., Guyot, F., *Iron biomineralization by anaerobic neutrophilic iron-oxidizing bacteria.* Geochimica et Cosmochimica Acta, 2009. **73**(3): p. 696-711.
148. Hitchcock, A.P., Morin, C., Zhang, X., Araki, T., Dynes, J. J., Stöver, H., Brash, J., Lawrence, J. R., Leppard, G. G., *Soft X-ray spectromicroscopy of biological and synthetic polymer systems.* Journal of Electron Spectroscopy and Related Phenomena, 2005. **144–147**(0): p. 259-269.
149. Ivleva, N., Wagner, M. , Horn, H., Niessner, R., Haisch, C., *Towards a nondestructive chemical characterization of biofilm matrix by Raman microscopy.* Analytical and Bioanalytical Chemistry, 2009. **393**(1): p. 197-206.
150. Lawrence, J.R., Swerhone, G. D. W., Leppard, G. G., Araki, T., Zhang, X., West, M. M., Hitchcock, A. P., *Scanning Transmission X-Ray, Laser Scanning, and Transmission Electron Microscopy Mapping of the Exopolymeric Matrix of Microbial Biofilms.* Applied and Environmental Microbiology, 2003. **69**(9): p. 5543-5554.
151. Neu, T.R., Manz, B., Volke, F., Dynes, J. J., Hitchcock, A. P., Lawrence, J. R., *Advanced imaging techniques for assessment of structure, composition and function in biofilm systems.* FEMS Microbiol Ecol, 2010. **72**(1): p. 1-21.
152. Parikh, S.J., Chorover, J., *ATR-FTIR Spectroscopy Reveals Bond Formation During Bacterial Adhesion to Iron Oxide.* Langmuir, 2006. **22**(20): p. 8492-8500.
153. Parikh, S.J., Mukome, F. N. D., Zhang, X,, *ATR–FTIR spectroscopic evidence for biomolecular phosphorus and carboxyl groups facilitating bacterial adhesion to iron oxides.* Colloids and Surfaces B: Biointerfaces, 2014. **119**: p. 38-46.
154. Li, Q., Wang, Q., Zhu, J., Zhou, S., Gan, M., Jiang, H., Sand, W., *Effect of Extracellular Polymeric Substances on Surface Properties and Attachment Behavior of Acidithiobacillus ferrooxidans.* Minerals, 2016. **6**(4): p. 100.
155. Comte, S., Guibaud, G., Baudu, M., *Relations between extraction protocols for activated sludge extracellular polymeric substances (EPS) and EPS complexation properties: Part I. Comparison of the efficiency of eight EPS extraction methods.* Enzyme and Microbial Technology, 2006. **38**(1–2): p. 237-245.
156. Santhiya, D., Subramanian, S., Natarajan, K. A., *Surface Chemical Studies on Sphalerite and Galena Using Extracellular Polysaccharides Isolated from Bacillus polymyxa.* Journal of Colloid and Interface Science, 2002. **256**(2): p. 237-248.
157. Xu, C., Santschi, P. H., Schwehr, K. A., Hung, C.-C., *Optimized isolation procedure for obtaining strongly actinide binding exopolymeric substances (EPS) from two bacteria (Sagittula stellata and Pseudomonas fluorescens Biovar II).* Bioresource technology, 2009. **100**(23): p. 6010-6021.
158. Basuvaraj, M., Fein, J., Liss, S. N., *Protein and polysaccharide content of tightly and loosely bound extracellular polymeric substances and the development of a granular activated sludge floc.* Water Research, 2015. **82**: p. 104-117.

159. Comte, S., Guibaud, G., Baudu, M., *Biosorption properties of extracellular polymeric substances (EPS) towards Cd, Cu and Pb for different pH values.* Journal of Hazardous Materials, 2008. **151**(1): p. 185-193.
160. Obst, M., Dynes, J. J., Lawrence, J. R., Swerhone, G. D. W., Benzerara, K., Karunakaran, C., Kaznatcheev, K., Tyliszczak, T., Hitchcock, A. P., *Precipitation of amorphous CaCO3 (aragonite-like) by cyanobacteria: A STXM study of the influence of EPS on the nucleation process.* Geochimica et Cosmochimica Acta, 2009. **73**(14): p. 4180-4198.
161. Guibaud, G., Tixier, N., Bouju, A., Baudu, M., *Relation between extracellular polymers' composition and its ability to complex Cd, Cu and Pb.* Chemosphere, 2003. **52**(10): p. 1701-1710.
162. Tourney, J., Ngwenya, B. T., *The role of bacterial extracellular polymeric substances in geomicrobiology.* Chemical Geology, 2014. **386**(0): p. 115-132.
163. Guo, X., Liu, J., Xiao, B., *Evaluation of the damage of cell wall and cell membrane for various extracellular polymeric substance extractions of activated sludge.* Journal of Biotechnology, 2014. **188**: p. 130-135.
164. Azeredo, J., Oliveira, R., *A new method for precipitating bacterial exopolysaccharides.* Biotechnology Techniques, 1996. **10**(5): p. 341-344.
165. Dynes, J.J., Lawrence, J. R., Korber, D. R., Swerhone, G. D., Leppard, G. G., Hitchcock, A. P., *Morphological and biochemical changes in Pseudomonas fluorescens biofilms induced by sub-inhibitory exposure to antimicrobial agents.* Can J Microbiol, 2009. **55**(2): p. 163-78.
166. de Brouwer, J.F.C., Cooksey, K. E., Wigglesworth-Cooksey, B., Staal, M. J., Stal, L. J., Avci, R., *Time of Flight-Secondary Ion Mass Spectrometry on isolated extracellular fractions and intact biofilms of three species of benthic diatoms.* Journal of Microbiological Methods, 2006. **65**(3): p. 562-572.
167. Redmile-Gordon, M.A., Brookes, P. C., Evershed, R. P., Goulding, K. W. T., Hirsch, P. R., *Measuring the soil-microbial interface: Extraction of extracellular polymeric substances (EPS) from soil biofilms.* Soil Biology and Biochemistry, 2014. **72**(0): p. 163-171.
168. Alasonati, E., Slaveykova, V. I., *Effects of extraction methods on the composition and molar mass distributions of exopolymeric substances of the bacterium Sinorhizobium meliloti.* Bioresource Technology, 2012. **114**: p. 603-609.
169. Liu, H., Fang, H. H. P., *Extraction of extracellular polymeric substances (EPS) of sludges.* Journal of Biotechnology, 2002. **95**(3): p. 249-256.
170. Frølund, B., Palmgren, R., Keiding, K., Nielsen, P. H., *Extraction of extracellular polymers from activated sludge using a cation exchange resin.* Water Research, 1996. **30**(8): p. 1749-1758.
171. Pellicer-Nàcher, C., Domingo-Félez, C., Mutlu, A. G., Smets, B. F., *Critical assessment of extracellular polymeric substances extraction methods from mixed culture biomass.* Water Research, 2013. **47**(15): p. 5564-5574.
172. Breitenstein, D., Rommel, C. E., Stolwijk, J., Wegener, J., Hagenhoff, B., *The chemical composition of animal cells reconstructed from 2D and 3D ToF-SIMS analysis.* Applied Surface Science, 2008. **255**(4): p. 1249-1256.
173. Smart, R.S.C., *Surface layers in base metal sulphide flotation.* Minerals Engineering, 1991. **4**(7–11): p. 891-909.
174. Knipe, S.W., Mycroft, J. R., Pratt, A. R., Nesbitt, H. W., Bancroff, G. M., *X-ray photoelectron spectroscopic study of water adsorption on iron sulphide minerals.* Geochimica et Cosmochimica Acta, 1995. **59**(6): p. 1079-1090.
175. Zhang, L.-M., Peng, J.-H., Wei, M.-M., Ding, J.-N., Zhou, H.-B., *Bioleaching of chalcopyrite with Acidianus manzaensis YN25 under contact and non-contact conditions.* Transactions of Nonferrous Metals Society of China, 2010. **20**(10): p. 1981-1986.
176. Sasaki, K., Nakamuta, Y., Hirajima, T., Tuovinen, O. H., *Raman characterization of secondary minerals formed during chalcopyrite leaching with Acidithiobacillus ferrooxidans.* Hydrometallurgy, 2009. **95**(1–2): p. 153-158.

177. Wang, H., Ding, S., Wang, G., Xu, X., Zhou, G., *In situ characterization and analysis of Salmonella biofilm formation under meat processing environments using a combined microscopic and spectroscopic approach.* International Journal of Food Microbiology, 2013. **167**(3): p. 293-302.
178. Maclean, L.C.W., Tyliszczak, T., Gilbert, P. U. P. A., Zhou, D., Pray, T. J., Onstott, T. C., Southam, G., *A high-resolution chemical and structural study of framboidal pyrite formed within a low-temperature bacterial biofilm.* Geobiology, 2008. **6**(5): p. 471-480.
179. Nazari, B., Jorjani, E., Hani, H., Manafi, Z., Riahi, A., *Formation of jarosite and its effect on important ions for Acidithiobacillus ferrooxidans bacteria.* Transactions of Nonferrous Metals Society of China, 2014. **24**(4): p. 1152-1160.
180. Stott, M.B., Watling, H. R., Franzmann, P. D., Sutton, D., *The role of iron-hydroxy precipitates in the passivation of chalcopyrite during bioleaching.* Minerals Engineering, 2000. **13**(10–11): p. 1117-1127.
181. Gleisner, M., Herbert, R. B., Frogner Kockum, P. C., *Pyrite oxidation by Acidithiobacillus ferrooxidans at various concentrations of dissolved oxygen.* Chemical Geology, 2006. **225**(1): p. 16-29.
182. He, H., Xia, J.-L., Yang, Y., Jiang, H., Xiao, C.-Q., Zheng, L., Ma, C.-Y., Zhao, Y.-D., Qiu, G.-Z., *Sulfur speciation on the surface of chalcopyrite leached by Acidianus manzaensis.* Hydrometallurgy, 2009. **99**(1): p. 45-50.
183. Leung, B.O., Hitchcock, A. P., Brash, J. L., Scholl, A., Doran, A., *An X-ray Spectromicroscopy Study of Protein Adsorption to Polystyrene−Poly(ethylene oxide) Blends.* Langmuir, 2010. **26**(18): p. 14759-14765.
184. Leung, B.O., Hitchcock, A. P., Cornelius, R. M., Brash, J. L., Scholl, A., Doran, A., *Using X-PEEM to study biomaterials: Protein and peptide adsorption to a polystyrene–poly(methyl methacrylate)-b-polyacrylic acid blend.* Journal of Electron Spectroscopy and Related Phenomena, 2012. **185**(10): p. 406-416.
185. Hitchcock, A.P., Leung, B. O., Brash, J. L., Scholl, A., Doran, A., *Soft X-ray Spectromicroscopy of Protein Interactions with Phase-Segregated Polymer Surfaces*, in *Proteins at Interfaces III State of the Art*. 2012, American Chemical Society. p. 731-760.
186. Priest, C., Stevens, N., Sedev, R., Skinner, W. M., Ralston, J., *Inferring wettability of heterogeneous surfaces by ToF-SIMS.* Journal of Colloid and Interface Science, 2008. **320**(2): p. 563-568.
187. Dague, E., Delcorte, A., Latgé, J.-P., Dufrêne, Y. F., *Combined Use of Atomic Force Microscopy, X-ray Photoelectron Spectroscopy, and Secondary Ion Mass Spectrometry for Cell Surface Analysis.* Langmuir, 2008. **24**(7): p. 2955-2959.
188. Mangold, S., Laxander, M., Harneit, K., Rohwerder, T. , Claus, G., Sand, W., *Visualization of Acidithiobacillus ferrooxidans biofilms on pyrite by atomic force and epifluorescence microscopy under various experimental conditions.* Hydrometallurgy, 2008. **94**(1–4): p. 127-132.
189. Florian, B., Noël, N., Thyssen, C., Felschau, I., Sand, W., *Some quantitative data on bacterial attachment to pyrite.* Minerals Engineering, 2011. **24**(11): p. 1132-1138.
190. Lara, R.H., Valdez-Pérez, D., Rodríguez, A. G., Navarro-Contreras, H. R., Cruz, R., García-Meza, J. V., *Interfacial insights of pyrite colonized by Acidithiobacillus thiooxidans cells under acidic conditions.* Hydrometallurgy, 2010. **103**(1–4): p. 35-44.
191. Florian, B., Noël, N., Sand, W., *Visualization of initial attachment of bioleaching bacteria using combined atomic force and epifluorescence microscopy.* Minerals Engineering, 2010. **23**(6): p. 532-535.
192. Lower, S.K., Tadanier, C. J., Hochella, M. F., *Measuring interfacial and adhesion forces between bacteria and mineral surfaces with biological force microscopy.* Geochimica et Cosmochimica Acta, 2000. **64**(18): p. 3133-3139.

193. Chau, T.T., Bruckard, W. J., Koh, P. T. L., Nguyen, A. V., *A review of factors that affect contact angle and implications for flotation practice.* Advances in Colloid and Interface Science, 2009. **150**(2): p. 106-115.
194. Li, D., Neumann, A. W., *Surface heterogeneity and contact angle hysteresis.* Colloid and Polymer Science, 1992. **270**(5): p. 498-504.
195. Vilalta-Clemente, A., Gloystein, K., *Principles of Atomic Force Microscopy.* Physics of Advanced Materials Winter School, 2008: p. 14-18.
196. Campbell, D., Carnell, S. M., Eden, R. J., *Applicability of contact angle techniques used in the analysis of contact lenses, part 1: comparative methodologies.* Eye Contact Lens, 2013. **39**(3): p. 254-62.
197. Marmur, A., *Contact-angle hysteresis on heterogeneous smooth surfaces: theoretical comparison of the captive bubble and drop methods.* Colloids and Surfaces A: Physicochemical and Engineering Aspects, 1998. **136**(1): p. 209-215.
198. Baek, Y., Kang, J., Theato, P., Yoon, J., *Measuring hydrophilicity of RO membranes by contact angles via sessile drop and captive bubble method: A comparative study.* Desalination, 2012. **303**: p. 23-28.
199. Eral, H.B., 't Mannetje, D. J. C. M., Oh, J. M., *Contact angle hysteresis: a review of fundamentals and applications.* Colloid and Polymer Science, 2013. **291**(2): p. 247-260.
200. Njobuenwu, D.O., Oboho E. O., Gumus, R. H., *Determination of Contact Angle from Contact Area of Liquid Droplet Spreading on Solid Substrate.* Leonardo Electronic Journal of Practices and Technologies, 2007.
201. Read, M.L., Morgan, P. B., Kelly, J. M., Maldonado-Codina, C., *Dynamic Contact Angle Analysis of Silicone Hydrogel Contact Lenses.* Journal of Biomaterials Applications, 2010. **26**(1): p. 85-99.
202. Farahat, M., Hirajima, T., Sasaki, K., *Adhesion of Ferroplasma acidiphilum onto pyrite calculated from the extended DLVO theory using the van Oss–Good–Chaudhury approach.* Journal of Colloid and Interface Science, 2010. **349**(2): p. 594-601.
203. Sharma, P.K., Hanumantha Rao, K., Forssberg, K. S. E., Natarajan, K. A., *Surface chemical characterisation of Paenibacillus polymyxa before and after adaptation to sulfide minerals.* International Journal of Mineral Processing, 2001. **62**(1–4): p. 3-25.
204. Crawford, R.R., J., *The influence of particle size and contact angle in mineral flotation.* International Journal of Mineral Processing, 1988. **23**(1): p. 1-24.
205. Chipfunhu, D., Zanin, M., Grano, S., *Flotation behaviour of fine particles with respect to contact angle.* Chemical Engineering Research and Design, 2012. **90**(1): p. 26-32.
206. Ralston, J., Fornasiero, D., Grano, S., Duan, J., Akroyd, T., *Reducing uncertainty in mineral flotation—flotation rate constant prediction for particles in an operating plant ore.* International Journal of Mineral Processing, 2007. **84**(1): p. 89-98.
207. Somasundaran, P., Ren, Y., Rao, M. Y., *Applications of biological processes in mineral processing.* Colloids and Surfaces A: Physicochemical and Engineering Aspects, 1998. **133**(1): p. 13-23.
208. Brito e Abreu, S., Skinner, W., *Predicting the surface chemistry contribution to the flotation recovery of chalcopyrite by ToF-SIMS.* Minerals Engineering, 2011. **24**(2): p. 160-168.
209. Feng, J., Scholl, A., *Photoemission Electron Microscopy (PEEM)*, in *Science of Microscopy*, P. Hawkes and J.H. Spence, Editors. 2007, Springer New York. p. 657-695.
210. Stohr, J., *NEXAFS Spectroscopy*. Springer Series in Surface Sciences. Vol. 25. 1992, Heidelberg: Springer-Verlag Berlin 404.
211. Schöll, A., Zou, Y., Schmidt, Th., Fink, R., Umbach, E., *Energy calibration and intensity normalization in high-resolution NEXAFS spectroscopy.* Journal of Electron Spectroscopy and Related Phenomena, 2003. **129**(1): p. 1-8.
212. Hemraj-Benny, T., Banerjee, S., Sambasivan, S., Balasubramanian, M., Fischer, D. A., Eres, G., Puretzky, A. A., Geohegan, D. B., Lowndes, D. H., Han, W., Misewich, J. A., Wong, S.

S., *Near-Edge X-ray Absorption Fine Structure Spectroscopy as a Tool for Investigating Nanomaterials.* Small, 2006. **2**(1): p. 26-35.
213. Rosenberg, R.A., Love, P. J., Rehn, V., *Polarization-dependent C(K) near-edge x-ray-absorption fine structure of graphite.* Physical Review B, 1986. **33**(6): p. 4034-4037.
214. Milev, A.S., Tran, N. H., Kannangara, G. S. K., Wilson, M. A., *Unoccupied electronic structure of ball-milled graphite.* Physical Chemistry Chemical Physics, 2010. **12**(25): p. 6685-6691.
215. Richter, C., Jaye, C., Panaitescu, E., Fischer, D. A., Lewis, L. H., Willey, R. J., Menon, L., *Effect of potassium adsorption on the photochemical properties of titania nanotube arrays.* Journal of Materials Chemistry, 2009. **19**(19): p. 2963-2967.
216. Rightor, E.G., Hitchcock, A. P., Ade, H., Leapman, R. D., Urquhart, S. G., Smith, A. P., Mitchell, G., Fischer, D., Shin, H. J., Warwick, T., *Spectromicroscopy of Poly(ethylene terephthalate): Comparison of Spectra and Radiation Damage Rates in X-ray Absorption and Electron Energy Loss.* The Journal of Physical Chemistry B, 1997. **101**(11): p. 1950-1960.
217. Acres, R.G., Harmer, S.L., Beattie, D.A., *Synchrotron PEEM and ToF-SIMS study of oxidized heterogenous pentlandite, pyrrhotite and chalcopyrite.* Journal of Synchrotron Radiation, 2010. **17**: p. 606-615.
218. Buckley, A.N., Goh, S.W., Fan, L.-J., *Ex Situ Surface Chemical Characterization in Minerals Processing Research: The Effect of Hydrophilic Organic Solvents on Sulfide Mineral Surfaces.* ECS - The Electrochemical Society, 2010. **28**(6): p. 69-80.
219. Kalegowda, Y., Chan, Y.-L., Wei, D.-H., Harmer, S. L., *X-PEEM, XPS and ToF-SIMS characterisation of xanthate induced chalcopyrite flotation: Effect of pulp potential.* Surface Science, 2015. **635**: p. 70-77.
220. Goh, S.W., Buckley, A. N., Lamb, R. N., Rosenberg, R. A., Moran, D., *The oxidation states of copper and iron in mineral sulfides, and the oxides formed on initial exposure of chalcopyrite and bornite to air.* Geochimica et Cosmochimica Acta, 2006. **70**(9): p. 2210-2228.
221. Colliex, C., Manoubi, T., Ortiz, C., *Electron-energy-loss-spectroscopy near-edge fine structures in the iron-oxygen system.* Physical Review B, 1991. **44**(20): p. 11402-11411.
222. Wu, Z.Y., Gota, S., Jollet, F., Pollak, M., Gautier-Soyer, M., Natoli, C. R., *Characterization of iron oxides by x-ray absorption at the oxygen K edgeusing a full multiple-scattering approach.* Physical Review B, 1997. **55**(4): p. 2570-2577.
223. Smith, A.D., Cressey, G., Schofield, P. F., Cressey, B. A., *Development of X-ray photoemission electron microscopy (X-PEEM) at the SRS.* J Synchrotron Radiat, 1998. **5**(Pt 3): p. 1108-10.
224. Hunter, R.C., Hitchcock, A. P., Dynes, J. J., Obst, M., Beveridge, T. J., *Mapping the Speciation of Iron in Pseudomonas aeruginosa Biofilms Using Scanning Transmission X-ray Microscopy.* Environmental Science & Technology, 2008. **42**(23): p. 8766-8772.
225. Solomon, D., Lehmann, J., Harden, J., Wang, J., Kinyangi, J., Heymann, K., Karunakaran, C., Lu, Y., Wirick, S., Jacobsen, C., *Micro- and nano-environments of carbon sequestration: Multi-element STXM–NEXAFS spectromicroscopy assessment of microbial carbon and mineral associations.* Chemical Geology, 2012. **329**(0): p. 53-73.
226. Wan, J., Tyliszczak, T., Tokunaga, T. K., *Organic carbon distribution, speciation, and elemental correlations within soil microaggregates: Applications of STXM and NEXAFS spectroscopy.* Geochimica et Cosmochimica Acta, 2007. **71**(22): p. 5439-5449.
227. Morin, C., Hitchcock, A. P., Cornelius, R. M., Brash, J. L., Urquhart, S. G., Scholl, A., Doran, A., *Selective adsorption of protein on polymer surfaces studied by soft X-ray photoemission electron microscopy.* Journal of Electron Spectroscopy and Related Phenomena, 2004. **137–140**(0): p. 785-794.

228. Koprinarov, I.N., Hitchcock, A. P., McCrory, C. T., Childs, R. F., *Quantitative Mapping of Structured Polymeric Systems Using Singular Value Decomposition Analysis of Soft X-ray Images.* The Journal of Physical Chemistry B, 2002. **106**(21): p. 5358-5364.
229. Ade, H., Hitchcock, A. P., *NEXAFS microscopy and resonant scattering: Composition and orientation probed in real and reciprocal space.* Polymer, 2008. **49**(3): p. 643-675.
230. Urquhart, S.G., Hitchcock, A. P., Smith, A. P., Ade, H. W., Lidy, W., Rightor, E. G., Mitchell, G. E., *NEXAFS spectromicroscopy of polymers: overview and quantitative analysis of polyurethane polymers.* Journal of Electron Spectroscopy and Related Phenomena, 1999. **100**(1–3): p. 119-135.
231. Hitchcock, A.P., *Soft X-ray spectromicroscopy of polymers and biopolymer interfaces.* Journal of Synchrotron Radiation, 2001. **8**(2): p. 66-71.
232. Hitchcock, A.P., Dynes, J. J., Lawrence, J. R., Obst, M., Swerhone, G. D., Korber, D. R., Leppard, G. G., *Soft X-ray spectromicroscopy of nickel sorption in a natural river biofilm.* Geobiology, 2009. **7**(4): p. 432-53.
233. Lawrence, J.R., Leppard, G. G., Hitchcock, A. P., Neu, T. R., *Mapping Biopolymer Distributions In Microbial Communities*, in *Flocculation in Natural and Engineered Environmental Systems*. 2004, CRC Press. p. 121-142.
234. Plekan, O., Feyer, V., Šutara, F., Skála, T., Švec, M., Cháb, V., Matolín, V., Prince, K. C., *The adsorption of adenine on mineral surfaces: Iron pyrite and silicon dioxide.* Surface Science, 2007. **601**(9): p. 1973-1980.
235. Hardie, A.G., Dynes, J. J., Kozak, L. M., Huang, P. M., *The role of glucose in abiotic humification pathways as catalyzed by birnessite.* Journal of Molecular Catalysis A: Chemical, 2009. **308**(1–2): p. 114-126.
236. Singh, B., Fang, Y., Cowie, B. C. C., Thomsen, L., *NEXAFS and XPS characterisation of carbon functional groups of fresh and aged biochars.* Organic Geochemistry, 2014. **77**(0): p. 1-10.
237. Kalirai, S.S., Lam, K. P., Bazylinski, D. A., Lins, U., Hitchcock, A. P., *Examining the chemistry and magnetism of magnetotactic bacterium Candidatus Magnetovibrio blakemorei strain MV-1 using scanning transmission X-ray microscopy.* Chemical Geology, 2012. **300–301**(0): p. 14-23.
238. Stewart-Ornstein, J., Hitchcock, A. P., Hernandez Cruz, D., Henklein, P., Overhage, J., Hilpert, K., Hale, J. D., Hancock, R. E., *Using intrinsic X-ray absorption spectral differences to identify and map peptides and proteins.* J Phys Chem B, 2007. **111**(26): p. 7691-9.
239. Zubavichus, Y., Fuchs, O., Weinhardt, L., Heske, C., Umbach, E., Denlinger, J. D., Grunze, M., *Soft X-Ray-Induced Decomposition of Amino Acids: An XPS, Mass Spectrometry, and NEXAFS Study.* Radiation Research, 2004. **161**(3): p. 346-358.
240. Johnson, B., Klaer, J., Merdes, S., Gorgoi, M., Höpfner, B., Vollmer, A., Lauermann, I., *Limitations of Near Edge X-ray Absorption Fine Structure as a tool for observing conduction bands in chalcopyrite solar cell heterojunctions.* Journal of Electron Spectroscopy and Related Phenomena, 2013. **190**: p. 42-46.
241. Swiech, W., Fecher, G. H., Ziethen, Ch., Schmidt, O., Schönhense, G., Grzelakowski, K., M. Schneider, C., Frömter, R., Oepen, H. P., Kirschner, J., *Recent progress in photoemission microscopy with emphasis on chemical and magnetic sensitivity.* Journal of Electron Spectroscopy and Related Phenomena, 1997. **84**(1): p. 171-188.
242. Wei, D.H., Chan, Y.-L., Hsu, Y.-J., *Exploring the magnetic and organic microstructures with photoemission electron microscope.* Journal of Electron Spectroscopy and Related Phenomena, 2012. **185**(10): p. 429-435.
243. Scholl, A., *Applications of photoemission electron microscopy (PEEM) in magnetism research.* Current Opinion in Solid State and Materials Science, 2003. **7**(1): p. 59-66.
244. Leung, B.O., Brash, J. L., Hitchcock, A. P., *Characterization of Biomaterials by Soft X-Ray Spectromicroscopy.* Materials, 2010. **3**(7): p. 3911-3938.

245. Hitchcock, A.P., Morin, C., Heng, Y. M., Cornelius, R. M., Brash, J. L., *Towards practical soft X-ray spectromicroscopy of biomaterials.* Journal of Biomaterials Science, Polymer Edition, 2002. **13**(8): p. 919-937.
246. Dynes, J.J., Tyliszczak, T., Araki, T., Lawrence, J. R., Swerhone, G. D. W., Leppard, G. G., Hitchcock, A. P., *Speciation and Quantitative Mapping of Metal Species in Microbial Biofilms Using Scanning Transmission X-ray Microscopy.* Environmental Science & Technology, 2006. **40**(5): p. 1556-1565.
247. Hitchcock, A.P., Dynes, J. J., Johansson, G., Wang, J., Botton, G., *Comparison of NEXAFS microscopy and TEM-EELS for studies of soft matter.* Micron, 2008. **39**(3): p. 311-319.
248. Boese, J., Osanna, A., Jacobsen, C., Kirz, J., *Carbon edge XANES spectroscopy of amino acids and peptides.* Journal of Electron Spectroscopy and Related Phenomena, 1997. **85**(1–2): p. 9-15.
249. Brito e Abreu, S., Brien, C., Skinner, W., *ToF-SIMS as a New Method to Determine the Contact Angle of Mineral Surfaces.* Langmuir, 2010. **26**(11): p. 8122-8130.
250. Kalegowda, Y., Harmer, S. L., *Chemometric and Multivariate Statistical Analysis of Time-of-Flight Secondary Ion Mass Spectrometry Spectra from Complex Cu–Fe Sulfides.* Analytical Chemistry, 2012. **84**(6): p. 2754-2760.
251. Khmeleva, T.N., Georgiev, T. V., Jasieniak, M., Skinner, W. M., Beattie, D. A., *XPS and ToF-SIMS study of a chalcopyrite–pyrite–sphalerite mixture treated with xanthate and sodium bisulphite.* Surface and Interface Analysis, 2005. **37**(8): p. 699-709.
252. Belu, A.M., Graham, D. J., Castner, D. G., *Time-of-flight secondary ion mass spectrometry: techniques and applications for the characterization of biomaterial surfaces.* Biomaterials, 2003. **24**(21): p. 3635-3653.
253. Belu, A.M., Davies, M. C., Newton, J. M., Patel, N., *TOF-SIMS Characterization and Imaging of Controlled-Release Drug Delivery Systems.* Analytical Chemistry, 2000. **72**(22): p. 5625-5638.
254. Cizaire, L., Martin, J. M., Le Mogne, Th., Gresser, E., *Chemical analysis of overbased calcium sulfonate detergents by coupling XPS, ToF-SIMS, XANES, and EFTEM.* Colloids and Surfaces A: Physicochemical and Engineering Aspects, 2004. **238**(1): p. 151-158.
255. Urquhart, A.J., Taylor, M., Anderson, D. G., Langer, R., Davies, M. C., Alexander, M. R., *TOF-SIMS Analysis of a 576 Micropatterned Copolymer Array To Reveal Surface Moieties That Control Wettability.* Analytical Chemistry, 2008. **80**(1): p. 135-142.
256. Pradier, C.M., Rubio, C., Poleunis, C., Bertrand, P., Marcus, P., Compère, C., *Surface Characterization of Three Marine Bacterial Strains by Fourier Transform IR, X-ray Photoelectron Spectroscopy, and Time-of-Flight Secondary-Ion Mass Spectrometry, Correlation with Adhesion on Stainless Steel Surfaces.* The Journal of Physical Chemistry B, 2005. **109**(19): p. 9540-9549.
257. Tervahattu, H., Juhanoja, J., Kupiainen, K., *Identification of an organic coating on marine aerosol particles by TOF-SIMS.* Journal of Geophysical Research: Atmospheres, 2002. **107**(D16): p. ACH 18-1-ACH 18-7.
258. Briggs, D., Vickerman, J. C., *ToF-SIMS : surface analysis by mass spectrometry*. 2001, Chichester : IM ; Manchester: SurfaceSpectra
259. Berman, E.S.F., Kulp, K. S., Knize, M. G., Wu, L., Nelson, E. J., Nelson, D. O., Wu, K. J., *Distinguishing Monosaccharide Stereo- and Structural Isomers with TOF-SIMS and Multivariate Statistical Analysis.* Analytical Chemistry, 2006. **78**(18): p. 6497-6503.
260. Berman, E.S.F., Wu, L., Fortson, S. L., Kulp, K. S., Nelson, D. O., Wu, K. J., *Chemometric and statistical analyses of ToF-SIMS spectra of increasingly complex biological samples.* Surface and Interface Analysis, 2009. **41**(2): p. 97-104.
261. Sjövall, P., Johansson, B., Lausmaa, J., *Localization of lipids in freeze-dried mouse brain sections by imaging TOF-SIMS.* Applied Surface Science, 2006. **252**(19): p. 6966-6974.

262. Vaidyanathan, S., Fletcher, J. S., Lockyer, N. P., Vickerman, J. C., *TOF-SIMS investigation of Streptomyces coelicolor, a mycelial bacterium.* Applied Surface Science, 2008. **255**(4): p. 922-925.
263. Tian, X., Reichenbach, S.E., Tao, Q., Henderson, A. *Classification and Cluster Analysis of Complex Time-of-Flight Secondary Ion Mass Spectrometry for Biological Samples*. in *2009 International Conference on Bioinformatics, Computational Biology, Genomics and Chemoinformatics*. 2009. Orlando, Florida, USA.: International Society for Research in Science and Technology.

3 Materials, Methods and Techniques

To investigate the interaction of the microorganisms with mineral surfaces, a variety of analytical techniques were employed. This chapter details the methods of bacterial culture growth and monitoring, the solution reduction potential (Eh) and pH, and, with attention given to sample preparation, surface analysis techniques employed and the data analyses performed on the results collected from each technique.

3.1 Materials

Table 3.1 shows the compounds used over the duration of this project, the chemical formulas, the commercial source and the purity of each chemical involved.

Table 3.1: Chemical compounds used for this study.

Chemical	Formula	Supplier and Purity
1,10-phenanthroline (Ferroin)	$C_{12}H_8N_2$	Scharlau, 0.025 M
Ammonium sulfate	$(NH_4)_2SO_4$	Chem-Supply, AR
Bovine serum albumin (BSA)	-	Sigma Aldritch, LR
Calcium chloride dihydrate	$CaCl_2.2H_2O$	Merck, AR
Calcium nitrate tetrahydrate	$Ca(NO_3)_2.4H_2O$	Chem-Supply, AR
Cerium sulfate	$Ce(SO_4)_2$	Fluka, 0.05 M
Deoxyribonucleic acid (DNA) from salmon testes	-	Sigma Aldritch
D-glucose anhydrous	$C_6H_{12}O_6$	Chem-Supply, AR
D-glucuronic acid	$C_6H_{10}O_7$	Sigma Aldritch, LR
Ethanol	C_2H_5OH	Chem-Supply, AR VMR, AR
Ethylenediaminetetra acetic acid (EDTA)	$C_{10}H_{162}N_2O_8$	Chem-Supply, AR
Ferrous sulfate heptahydrate	$FeSO_4.7H_2O$	Chem-Supply, LR
Glutaraldehyde 25%	$CH_2(CH_2CHO)_2$	ProSciTech, 25%, EM
Glycerol	$C_3H_8O_3$	Merck, AR
Hexamethyl-disilazane (HMDS)	$[(CH_3)_3Si]_2NH$	ProSciTech, 100%
Humic acid	-	Sigma Aldritch, Tech
Magnesium chloride hexahydrate	$MgCl_2.6H_2O$	Merck, AR
Magnesium sulfate heptahydrate	$MgSO_4.7H_2O$	Chem-Supply, AR

Osmium Tetroxide	OsO_4	ProSciTech, 2%
Phosphate Buffered Saline (PBS)	-	ProSciTech
Potassium dihydrogen orthophosphate	KH_2PO_4	Merck, AR
Potassium phosphate dibasic	K_2HPO_4	Chem-Supply, AR
Potassium chloride	KCl	Chem-Supply, AR
Sodium Alginate	$[C_6H_8O_6]_n$	Chem-Supply, LR
Sodium chloride	NaCl	Chem-Supply, AR
Sodium hydroxide	NaOH	Chem-Supply, AR
Sulfur flowers	S	Scharlau, extra pure
Sulfuric acid	H_2SO_4	Optigen Scientific, LR
Yeast extract	-	Chem-Supply, Microbiology grade

All water used in this study was purified by a Millipore Milli-Q Advantage A10 water purification system, with a typical resistivity of 18.2 MΩ/cm at 25°C.

Yeast extract is the water-soluble extract of autolysed *S. cerevislae* yeast, and contains a range of peptides, amino acids, nucleobases, trace elements and B complex vitamins. The vitamin contents of the yeast extract are shown in Table 3.2, as provided by Scharlau Microbiology (non-exhaustive).

Table 3.2: Vitamin content of yeast extract, as provided by Scharlau Microbiology

Chemical Name	Vitamin Descriptor	Concentration (ppm)
Thiamine	B1	85
Riboflavin	B2	105
Pantothenic acid	B5	300
Pyridoxine	B6	65
Biotin	B8	7
Folic acid	B9	40
Cyanocobalamin	B12	10 mcg/kg
Niacin	B3 (PP Factor)	800

Yeast extract also contains varying amounts of amino acids, with the percentage of free amino acids shown in Figure 3.7, as provided by the manufacturer.

Figure has been removed due to copyright restrictions

Figure 3.7: Yeast extract amino acid content ((Free/Total) x100), provided by Scharlau Microbiology.

3.2 Minerals

The two major sources of cubic pyrite used to produce tiles for expose to bacterial cultures were obtained from Navajun, La Rioja, Spain and sourced from Peru, respectively. These pyrite cubes (A: $Fe_{1.00}S_{1.88}$, B: $Fe_{1.00}S_{2.13}$) were found to be high purity by microprobe, with the trace components listed in Table 3.3.

Table 3.3: Microprobe results of cubic pyrite from Spain (A), and from Peru (B).

Cubic Pyrite A		Cubic Pyrite B	
Element	*Atomic %*	*Element*	*Atomic %*
S	65.15	S	67.94
Fe	34.73	Fe	31.88
Ni	0.035	Ni	0.07
As	0.023	Co	0.08
Zn, Co, Cd, Se, Mn, Ag, In, Cu	< 0.012	Pb, Cd, Se, Cu, Mn, Ag, Zn, Sb, Cr	<0.01

X-ray diffraction (XRD) was performed and showed cubic pyrite A to be majority pyrite with little trace mineral, and cubic pyrite B to be majority pyrite with calcite, muscovite and kaolinite inclusions. These inclusions were visibly different to the pyrite and were avoided during surface analysis. The preparation of the cubic pyrite for exposure experiments is described in section 3.4.

Bulk pyrite for culture feedstock was sourced from Peru through GEOdiscoveries. The pyrite was ground using a rubber lined Galigher mill in deionized water, with steel rods as the grinding media, and wet-sieved to a size fraction of +38, -75 µm particle size, d_{80} = 50 µm, by Amdel Mineral Laboratories. This ground pyrite was also found to be high purity using microprobe, with the trace components listed in Table 3.4.

Table 3.4: Elemental analysis of ground pyrite by microprobe, presented as atomic percent (%).

Ground Pyrite	
Element	*Atomic %*
S	68.216
Fe	31.514
Cu	0.147
Co	0.036
Zn	0.055
Se, Cd, Ag, Mn, Ni, Cr, Sb, Pb, As	< 0.01

The use of ground mineral as nutrient source for bacterial and archaeon cultures is described in the following section.

3.3 Microorganism Cultures

Two strains of mesophiles and one strain of extreme thermophile were used in this study. The growth conditions are outlined below, with more details on the individual strain morphologies, cell growth cycles and descriptions of cell classifications can be found in Chapter 2, section 2.2.1.

3.3.1 Mesophiles

The mesophilic bacterial strains *Acidithiobacillus ferrooxidans* (DSM 14887) and *Leptospirillum ferrooxidans* (DSM 2705) were purchased as live cultures from DSMZ (Leibniz-Institut DSMZ-Deutsche Sammlung von Mikroorganism und Zellkulturen). The *A. ferrooxidans* and *L. ferrooxidans* were grown on the recommended HH medium, DSMZ Medium 882. The medium consists of two solutions, made separately and combined after autoclaving. Solution A consists of 0.132 g $(NH_4)_2SO_4$, 0.053 g $MgCl_2.6H_2O$, 0.027 g KH_2PO_4, $CaCl_2.2H_2O$ in 950 mL Milli-Q (18.2 MΩ/cm at 25°C) water adjusted to pH 1.8 with H_2SO_4. Solution B consists of 20 g $FeSO_4.7H_2O$ in 50 mL 0.25N H_2SO_4. Cultures were grown autoclave-sterilized conical flasks in an orbital mixer shaken at 155 rpm and 30°C. These cultures were continuously subcultured once they had reached the stationary phase into fresh HH medium at 5% inoculum (150 mL total volume) as stock culture.

Once the growth on HH medium with ferrous sulfate as the soluble Fe^{2+} source was determined to be well established by both cell counting and iron consumption, cultures were adjusted to use pyrite as their iron source. Cultures were determined established after several growth cycles occur over the same time frame under the same conditions. Ground pyrite of the size fraction +35 µm < -75 µm

was UV sterilised and added to the amount of 20 g per flask with each inoculation (10% inoculum in 300 mL total volume). Solution B was omitted from the medium preparation and the other recommended ingredients were prepared in 1L of Milli-Q (18.2 MΩ/cm at 25°C) water adjusted to pH 1.8 with H_2SO_4 to maintain identical component concentrations. This medium will be referred to as HH medium unless otherwise specified. The mineral-based stock cultures were grown in autoclave-sterilized conical flasks in an orbital mixer shaken at 155 rpm and 30°C. These cultures were continuously subcultured once they had reached the stationary phase into fresh HH medium with new mineral at 10% inoculum.

3.3.2 Thermophile

The thermophilic archaeon *Acidianus brierleyi* (DSM 1651) was purchased as a live culture from DSMZ (Leibniz-Institut DSMZ-Deutsche Sammlung von Mikroorganism und Zellkulturen) and grown in the recommended medium, DSM 150 medium. This medium consists of 3.00 g $(NH_4)_2SO_4$, 0.38 g K_2HPO_4, 0.50 g $MgSO_4.7H_2O$, 0.10 g KCl, 0.14 g $Ca(NO_3)_2$ and 0.2 g yeast extract in 1L Milli-Q (18.2 MΩ/cm at 25°C) water adjusted to pH 1.5-2.5. Sulfur flowers were sterilised by a combination of steaming for 3 h in a water bath on 3 successive days and UV light, with 10 g added to the culture per litre of medium made. The cultures grown on sulfur were recultured every 3 weeks at 10% inoculum (300 mL total volume) in autoclave-sterilized conical flasks in an orbital mixer shaken at 155 rpm and 60°C. The *A. brierleyi* took much longer to adapt to growth on pyrite, as elemental sulfur was required for effective cell growth, and as such was recultured every 3 months. Like the other strains, the *A. brierleyi* was subcultured for experiments at the stationary phase.

3.4 Sample Preparation

3.4.1 Cutting and Polishing

The cube of pyrite, approximately 4 cm^3, was cut into pieces of approximately 1-2 mm thickness and 5 mm^2 in area using a slow diamond saw. The pyrite tiles were sanded to produce two flat faces as parallel as possible of a thickness between 2-4 mm using 180 grit Trojan wet/dry silicon carbide sandpaper and ultrapure Milli-Q water as lubricant. Each piece was engraved on the back face with a diamond tip engraving tool to mark the opposite from the working face.

Each piece had the working face sanded using 400 grit Trojan wet/dry silicon carbide sandpaper and ultrapure Milli-Q water as lubricant. The pieces were polished by working in a tight 2-4 cm figure-eight pattern that reduces any scratches left by the sanding process. The sanding process is

then repeated using 800 grit and 1200 grit Trojan wet/dry silicon carbide sandpaper, respectively, rinsing with water between each grade sandpaper.

The final stage of polishing is completed by placing a small amount of 1 µm Struers diamond paste onto a Buehler TriDent polishing pad. The working face is then pressed over the diamond paste and worked in a tight 1.5-3 cm figure-eight pattern. The piece is then moved to a clean section of the polishing pad and worked in the same figure-eight pattern to remove excess diamond paste and washed in ultrapure water, wiping dry with Kimtech particle-free cellulose wipes.

To minimise oxidation of samples, the final wet/dry sandpaper polish and diamond paste polish was conducted immediately prior to sonication. Tiles were placed in Milli-Q water to be cleaned of residue using a Soniclean benchtop sonicator. Tiles were sonicated working face up for 4 minutes at 43-45 kHz and power level of 70W to remove any diamond paste residue. The process was then repeated working face down. Samples were then blotted dry using Kimtech particle-free cellulose wipes and transferred to a clean watch glass, where they were placed working face down in the laminar flow hood and sterilised for 15 minutes under UV light. The samples were then turned working face up and sterilised under UV light for another 15 minutes.

3.4.2 Attachment Experiments

Immediately after the polishing, cleaning and sterilization processes described in the previous section were completed, the polished pyrite pieces were placed working face up into a conical flask using long, sterile forceps. The tiles were then covered carefully with the appropriate amount of the required medium to prevent samples turning working face down during experiments. To monitor the Eh and pH of the media over the course of exposure experiments, aliquots were taken using sterile 5 mL pipette and filtered through 0.22 µm syringe filter to remove cells and particles. Measurements were performed in triplicate using an Orion Star A211 Benchtop pH Meter (Thermo Scientific) and an Ag/AgCl reference electrode stored in 3M KCl.

The sample flasks were inoculated from pyrite-adjusted culture (10% inoculum) into Solution A of HH medium with no additional iron source in the case of *A. ferrooxidans* and *L. ferrooxidans*, or DSM 150 medium, either with or without yeast, in the case of *A. brierleyi*. Samples were removed by long, sterile forceps in the laminar flow hood at 2, 6, 12, 24, 72 and 168 h. If the samples were not for immediate analysis and storage was required, samples were snap-frozen in a small volume of fresh sterile media in v-bottomed tubes using liquid nitrogen and stored long term in a -80 °C freezer.

3.5 Ultra Violet-Visible Spectrophotometry

Ultra Violet-Visible (UV-Vis) Spectrophotometry is a commonly used technique to monitor cell growth by measuring the absorbance of culture in the 500-600 nm region of the light spectrum, which can be directly related to cell population. As the population of cells in the culture increase, so does the absorbance of culture solution.

UV-Vis Spectrophotometry measures light absorption by solutions at a specific wavelength (λ) in the Ultra Violet and visible region of the electromagnetic spectrum. This absorbance (A) is governed by the Bouguer-Lambert-Beer law (shortened to Beer's Law), shown in Equation 3.25.

$$\log_{10}\left(\frac{I_0}{I}\right)_\lambda = A_\lambda = \varepsilon_\lambda c l \qquad (3.25)$$

Where the absorbance is determined by the logarithm of intensity of light of a specific wavelength entering the sample (I_0), and the intensity of the light emerging from the sample (I). Absorbance can be determined from the Beer's Law equation where ε is the molar absorption coefficient or molar absorptivity ($Lmol^{-1}cm^{-1}$), c is the concentration of the substance being measured ($molL^{-1}$), and *l* is the pathlength of the sample (cm). The molar absorptivity is dependent on the substance being measured and the wavelength λ (nm) while the pathlength of the sample is determined by the width of the cuvette, which in this case is 1 cm.

To account for light being reflected by the cuvette, a reference measurement must be made with a control solution, such as water. In microbiology, optical density (OD) is often used when monitoring the growth of cultures, making use of the fact that as the number of cells in a culture increases, the greater the amount of light they will scatter or absorb in the spectrophotometer. The OD is dependent on the thickness of the sample, and applies Beer's law in Equation 3.26, when the path length is 1 cm

$$OD_\lambda = \frac{A_\lambda}{l} \qquad (3.26)$$

OD was not accurate for cultures containing mineral particles or sulfur flower, as the particulates distort the absorbance values measured by giving artificially higher absorbance values.

3.5.1 Sample Preparation

Minimal sample preparation is required for OD measurements using UV-Vis Spectroscopy. 2.5 mL of culture was pipetted directly into a 1 cm plastic cuvette at desired time intervals and taken immediately to the instrument for measurement. Samples were agitated by shaking immediately

before measuring to ensure homogeneity of solution. Controls were performed with ferrous sulfate solution to determine the optimal wavelength for monitoring cell growth and eliminate any absorption by the medium itself, and it was ascertained that blank measurements could be taken using media solution.

3.5.2 Data Collection and Analysis

Spectra were obtained in triplicate using a Varian Cary 50 UV-Vis Spectrophotometer in dual beam mode with baseline correction over a wavelength range of 200-800 nm with a scan rate of 24000.00 nm/min with 5.00 nm data interval and collection time of 0.0125 seconds, software version 4.10 (464).

The wavelengths used to track bacterial growth were 500, 600 and 660 nm. This is the common spectral region, as it is the scattering of light rather than absorbance being measured and at these wavelengths there is little interference from the media and a reduction in the risk of UV cell mutation [1-6].

3.6 Cerium(IV) Sulfate Titration

Both mesophilic strains of bacteria oxidise Fe^{2+} to Fe^{3+}, and this consumption can be measured using colorimetric redox titration of the filtered culture against cerium(IV) sulfate with 1,10-phenanthroline, also known as Ferroin, as an indicator. The balanced chemical equation is shown in Equation 3.27, and the half-cell equations for this titration are shown in Equations 3.28 and 3.29 [7, 8]:

$$2Ce(SO_4)_2 + 2\ FeSO_4 \rightarrow Ce_2(SO_4)_3 + Fe_2(SO_4)_3 \qquad (3.27)$$

$$Fe^{2+}_{(aq)} \rightarrow Fe^{3+}_{(aq)} + e^- \qquad (3.28)$$

$$Ce^{4+}_{(aq)} + e^- \rightarrow Ce^{3+}_{(aq)} \qquad (3.29)$$

The Ferroin forms a complex with the Fe(II) ions, with three Ferroin molecules for every iron(II) ion, making a red coloured solution. This becomes pale blue in colour when the indicator complexes with Fe(III) instead.

3.6.1 Sample Preparation

An aliquot of 5 mL was taken from each culture and was filtered into a conical flask (100 mL) through a 0.22 µm syringe filter to remove the bacterial cells and mineral particles. 1-3 drops of Ferroin was added to the flask. Titrations of the filtered culture against the 0.05 $molL^{-1}$ cerium(IV)

sulfate solution were performed in triplicate on samples taken at regular intervals to plot the growth cycle of the cells.

3.6.2 Data Collection and Analysis

The concentration of iron(II) sulfate in the solution was calculated using the molar solution equation once the average titre volume of cerium sulfate was known. The calculated iron concentration at the desired time intervals over the growth cycle of the bacteria gave an indication of the rate at which the iron sulfate was consumed. The formula required for the concentration calculation is shown in Equation 3.30, where n is the number of moles, C is the concentration of the solution ($molL^{-1}$), and V is the volume of the solution (L).

$$n = CV \tag{3.30}$$

3.7 Inductively Coupled Plasma Optical Emission Spectroscopy

Inductively coupled plasma optical emission spectroscopy (ICP-OES) is an analytical technique used for the detection of trace elements in solution, and can be used to obtain iron and soluble sulfur concentrations in culture solutions. It utilizes argon gas, which travels through a quartz torch, at the end of which is are induction coils of a radio frequency generator (RF) that create an electromagnetic field. The electromagnetic field ionises the argon gas, causing the argon atom to lose electrons, which are caught and accelerated by the magnetic field. These electrons collide with more argon atoms, creating a chain reaction that turns the gas into a plasma consisting of atoms, electrons and ions. This argon plasma is sustained by the RF providing energy through the coil; this process is the inductive coupling process [9]. A schematic of the ICP torch is shown in Figure 3.8.

Figure has been removed due to copyright restrictions

Figure 3.8: Cross section of an ICP torch and load coil adapted from [9].

The sample solution is nebulised into aerosol, where it is carried along by the argon gas to the centre of the plasma, which desolvates, vaporises and atomises the aerosol. The atoms then go through the excitation and ionization process, where a core electron in the ground state is excited to a higher state, relaxing to release a photon of specific energy, the emission wavelength being specific to the atom. The intensity of the emission at these specific wavelengths is measured to determine the concentration of the desired element [9].

3.7.1 Sample Preparation

A minimum of 5 mL of mineral culture solution is syringe filtered through a 0.2 µm microfilter into a sterile centrifuge tube. Each sample was diluted to a 1 in 10 final volume and acidified to 2% with nitric acid prior to analysis.

3.7.2 Data Collection and Analysis

Detection limits vary from element to element; 10 mg/L for iron, 100 mg/L for sulfur, 0.3 mg/L for copper, 8 mg/L for potassium. The instrument error of 10% must be considered for final detected concentrations of elements. It is also important to note that in this case ICP-OES is unable to distinguish between valency or chemical state. For example, the sulfur concentration as determined by ICP-OES describes all soluble sulfur species, including sulfates, sulfites and sulfides.

3.8 Cell Counting

Growth of all cultures was monitored solely by counting the cells in 2.5×10^{-7} mL using a haemocytometer with a grid area of 0.0025 mm. Equation 3.31 is used to determine the number of cells in the culture, where n is the average number of cells and V is the volume of the chamber.

$$\text{Cell Conc. (cells. mL)} = \left(\frac{\text{n}}{\text{V(mL)}}\right) \tag{3.31}$$

3.8.1 Sample Preparation

The haemocytometer was prepared by placing the glass cover slip firmly over the grids. A 10 µL sample of culture was pipetted directly on the slide at the edge of the coverslip, allowing capillary action to draw the solution over the haemocytometer grid.

3.8.2 Data Collection and Analysis

The cells in the haemocytometer were counted using an Olympus BH-2 optical microscope, with the number of cells in five randomly selected 2.5 um^2 squares counted. The number of cells per mL was calculated from the average cell count value of 5 grid squares that were 2.5×10^{-7} mL in volume, as per Equation 31. Each 5-square count was performed in triplicate per sample with a total of 15 squares counted.

3.9 Scanning Electron Microscopy and Energy Dispersive X-ray Analysis

Scanning electron microscopy is a technique that uses electrons to generate an image of a sample. When a beam of high energy electrons is scanned over a solid sample, the interactions of the electrons with the sample produces secondary electrons (SE), backscattered electrons (BSE) and characteristic X-rays [10, 11]. The amount of SE, BSE and X-rays produced by the electron beam depends on the energy of the incident beam and the density of the sample, as shown in Figure 3.9. In SEM it is the secondary electrons that are detected to produce the image, with the brightness in the image being proportional to the amount of electrons produced from the sample [11]. Secondary electrons are produced when the incident electrons displace electrons from the atoms in the sample, and these electrons escape the surface from a depth of up to 10-15 nm of an energy range between 2-50 eV, and are detected [11]. The images collected by the detection of secondary electrons supply information such as morphology and topography of the sample [10].

Figure has been removed due to copyright restrictions

Figure 3.9: Interaction volumes of secondary electrons, backscattered electrons and X-rays, adapted from [11]

An Energy Dispersive X-ray (EDX) Analyser is often used in conjunction with SEM to perform elemental characterisation of the sample. Characteristic X-rays are caused by incoming electrons "knocking out" an electron from the inner orbital shell of an atom, causing a hole in the orbital which an electron of higher energy from an outer shell fills, as is shown in Figure 3.10. When the atom relaxes and an electron from the outer shell fills the hole in the inner shell, the excess energy is manifested in the form of an X-ray with an energy that is characteristic of the parent element and the specific electron shells involved.

Figure has been removed due to copyright restrictions

Figure 3.10: Schematic of secondary electron and X-ray generation, adapted from [12]

The information provided by the EDX, however, can come from a depth of up to 2 µm, and therefore much of the signal will come from the bulk of the sample, rather than the outermost

surface. Although the EDX can be used for elemental identification, it is not as surface-sensitive or chemically specific as some other techniques that will be discussed later in this chapter.

3.9.1 Sample Preparation

Pyrite samples were removed from the cultures and placed in 3% glutaraldehyde in phosphate buffered saline solution, pH = 7.4, and kept in the fridge at 4 °C for a minimum of 12 h, before dehydration and sputter coating.

Samples were rinsed by immersion in phosphate buffered saline solution for 10 min and post-fixed by immersion in 1% osmium tetroxide for 30 min. The samples were then dehydrated by immersion in increasingly concentrated ethanol solutions for 10 minutes per rinse starting at 1 × 70% v/v, and followed by 1 × 90% v/v, 1 × 95% v/v and 2 × 100% v/v, with a final rinse in hexamethyl-disilazane (HMDS) for 30 min [13, 14]. Samples were then air dried and mounted to SEM stubs using carbon tape, and sputter coated with 3 nm of platinum using a Cressington 208 High Resolution Sputter Coater.

3.9.2 Data Collection and Analysis

Samples were analysed on either a Philips XL30 Field Emission Scanning Electron Microscope (FESEM) or an Inspect FEI F50 Scanning Electron Microscope with a field emission electron emitter and EDX, backscatter, and secondary electron (SE) detectors. The primary electron beam accelerating voltage of 10 kV was used with spot size 3 when in Secondary Electron (SE) mode and spot size 6 when in EDX mode. Spot size refers collectively to the diameter of the probe, probe current and probe convergence in arbitrary units, with smaller numbers providing improved spatial resolution but less electrons generated, and vice versa [15]. A smaller spot size provides a spot diameter approaching 10 nm, while larger spot sizes provides a probe diameter approaching 100 nm [16]. Elemental quantification data obtained using EDX was processed using TEAM EDX software version 4.1 to apply an eZAF matrix calculation to quantify elements detected [17]. The eZAF applies matrix corrections to the measurements based on mean atomic number, absorption of X-rays and secondary X-rays or X-ray fluorescence to calculate the elemental composition of the sample [11].

The software ImageJ was used to count the number of cells on the surface of the mineral, with an average of 6 images covering an area of $4.8 \times 10^{-3} \pm 3.9 \times 10^{-5}$ mm^2. The percentage coverage of cells on the surface was calculated by measuring the average cell size, and multiplying by the number of cells per unit area. Pits and scratches on the surface were also measured using ImageJ.

3.10 Atomic Force Microscopy

Atomic Force Microscopy (AFM), which is type of scanning probe microscopy, has three different modes of operation; contact mode; non-contact mode; and tapping mode. Regardless of the mode, the AFM operates by measuring the forces between the tip of the cantilever (shown in Figure 3.11) and the surface of the sample. The presence of either attractive or repulsive forces will result in a flexing of the cantilever, and the deflection is detected by a laser. The laser is reflected from the back of the cantilever and detected by a position-sensitive detector, thus giving topographical information about the sample surface. The peizocrystal scanner moves in the x and y direction as required when voltage or pressure is applied, and the detector supplies information in the z direction. This results in topographical information about the sample surface down to the molecular level [18].

Figure has been removed due to copyright restrictions

Figure 3.11: Schematic of tip-sample interactions for an Atomic Force Microscope [18].

Data was collected in Tapping Mode to reduce both damage to the sample and the likelihood of tip contamination. In this mode, the cantilever oscillates at a constant amplitude. When forces between the tip and sample cause this amplitude to change, the scanner changes height to compensate, and this change in the z direction is measured and recorded as an image. This mode also gives information about surface adhesion and other mechanical properties by mapping the phase of the cantilever oscillation. The tip and the surface are constantly interacting in this mode.

3.10.1 Sample Preparation

Samples intended for AFM were removed from culture at selected time periods and snap frozen in fresh medium appropriate to the strain and were stored at -80°C to preserve the sample until ready for analysis. Samples to be analysed were removed from the freezer and defrosted to ambient conditions immediately before being mounted on the sample holders with carbon tape.

3.10.2 Data Collection and Analysis

AFM measurements were carried out using a Multimode Nanoscope V in tapping mode over a 10 µm spot size with a minimum of 5 spots per sample. The collected images were analysed for surface roughness using the NanoScope Analysis software, version 1.40. Images were flattened in

the software, and only the most necessary image processing to remove scan lines was done to maintain the integrity of the data. Surface roughness can be calculated in two different ways: R_a and R_q. R_a is the mean surface roughness, which is the mean value of the surface relative to the centre plane for which the dimensions above and below are equal. R_a is calculated by Equation 3.32, where N is the number of data points for the given area and Z_j is the surface relative to the centre plane [19].

$$R_a = \frac{1}{N}\sum_{j=1}^{N}|Z_j| \tag{3.32}$$

R_q is the root mean square of the height (Z) data, and represents the standard deviation of the Z values within a given area. R_q is calculated by Equation 3.33, where Z_i is the current value and N is the number of data points all for the given area [19].

$$R_q = \sqrt{\frac{\sum(Z_i)^2}{N}} \tag{3.33}$$

Roughness values are dependent on not only sample preparation but also on the dimensions of the tip being used to scan the surface, so while they can be compared for similar samples, the calculated roughness values are not absolute.

3.11 Near Edge X-ray Absorption Fine Structure

Near Edge X-ray Absorption Fine Structure (NEXAFS) occurs at photon energies close to the element-specific X-ray absorption edge, an example of which can be found in Figure 3.12. NEXAFS is used to probe element-specific intra-molecular bonding and molecular orbitals involved in bonding, as well as providing information on electronic configuration and chemicals states [20, 21]. Spectra can be obtained by different detection methods. For PEEM, the total electron yield (TEY) is used, which will be discussed in section 3.12. For STXM, the transmission method is used, and will be discussed in section 3.13.

Figure has been removed due to copyright restrictions

Figure 3.12: Schematic of an X-ray absorption spectra [22].

NEXAFS spectra are produced by the interaction of a tuneable photon energy source that has been monochromatised with electrons in the atoms of the sample, a schematic of which is shown in

Figure 3.13. Atoms of the target element absorb incident X-rays and a core electron is ejected to unoccupied states or a partially filled orbital (e_P), creating a core hole [20, 21, 23]. This core hole then decays as a higher energy electron fills the hole, releasing energy either by the emission of Auger electrons (e_A), or by the production of photons. NEXAFS spectra collected by the measurement of total electron yield are more surface sensitive (top 10 nm of the surface or better), as fluorescent X-rays escape from deeper in the bulk sample (up to 200 nm) [20, 21, 23]. The energy absorption of each transition depends on the chemical and electronic properties of the atom.

Figure has been removed due to copyright restrictions

Figure 3.13: Schematic of the incident photon exciting a core level electron to produce either a fluorescent photon or an Auger electron [24].

Table 3.5 shows the transitions observed in Fe L-edge NEXAFS spectra from previous studies of similar samples for the evaluation and identification of Fe L-edge NEXAFS spectra collected during this study.

Table 3.5: Energies and assignments of spectral features of Fe *L*-edge NEXAFS spectra of pyrite and related oxidation products

Absorption Energy (eV)	Assignment	References
707-707.6	Transitions to the Fe 3*d* (eg)	[25-28]
707.8-710.5	Fe 2*p* to Fe 3*d* states hybridized with O 2*p* states of iron oxidation products hematite, magnetite, goethite and wüstite	[27, 29, 30]
707.9-708.8	Fe 3*d* states hybridized with S 3*p* states	[25-28]
712-715	S 3*p* states hybridized with Fe 4*s* and 4*p* states	[25, 26]
719.7-721.1	Fe L_2	[25, 26]

The Fe L_3 peak of pyrite appears as two overlapping peaks with a difference in energy equal to or just over 1 eV, that does not appear to be necessarily indicative of Fe(II) and Fe(III) respectively, but rather is intrinsic to pyrite, with multiple transitions of Fe 3*d* electrons overlapping in the same region, including those of potential oxidation products [25, 27, 28].

Table 3.6, shown, was constructed for the evaluation and identification of carbon K-edge NEXAFS spectra by compiling previously identified features of similar samples and carbon compounds. Any of these peaks can be expected in microbial samples, with differences observed in peak intensity and energy depending on the composition of the EPS matrix.

Table 3.6: Summary of C K-edge NEXAFS signal energies and their associated transitions as found in literature.

Absorption Energy (eV)	Assignment	References
283.7-284.3	C 1s (C=O) → $\pi^*_{C=O}$ (Quinonic)	[31, 32]
284.9-285.7	C 1s (C=C) → $\pi^*_{C=C}$ (Aromatic)	[32-38]
285-285.3	C 1s (C-H) → π^*_{C-H}	[31]
286.3-286.8	C 1s (C-R) → π^*_{C-R} (Aromatic)	[31]
286.7	C 1s (C=O) → $\pi^*_{C=O}$ (Ketone)	[32, 39]
286-287	C 1s (C=C) → $\pi^*_{C=C}$	[37, 38]
287-287.5	C 1s (C=N) → $\pi^*_{C=N}$ (Amide)	[32, 35, 37]
287.1-287.9	C 1s (C-H) → σ^*_{C-H} (Aliphatic)	[32, 37, 40]
288.2-288.4	C 1s (C=O) → $\pi^*_{C=O}$ (Protein)	[32, 33, 37-39, 41-45]
288.4-288.8	C 1s (C=O) → $\pi^*_{C=O}$ (Carboxyl)	[31, 33, 35-37, 39, 40]
288.8-289.2	C 1s (C-H) → σ^*_{C-H}	[44]
289.3-289.8	C 1s (C=N) → $\pi^*_{C=N}$ (Amide)	[37, 38]
289.6-289.8	C 1s (C-O) → σ^*_{C-O}	[37]
289-290	C 1s (C=O) → $\pi^*_{C=O}$ (Carbonyl)	[34, 35]
290.2-290.5	C 1s (C=O) → $\pi^*_{C=O}$ (Carbonate)	[32, 39, 43]
291-294.4	C 1s (C-C) → π^*_{C-C}, σ^*_{C-C}	[38, 40]
297	K L_3	[32, 42]
298-300	C 1s (C=C) → $\pi^*_{C=C}$	[38]
300	K L_2	[32, 42]
302-305	C 1s (C=C) → $\pi^*_{C=C}$ C 1s (C=O) → $\sigma^*_{C=O}$	[38, 40]

The techniques mentioned previously in this section that are used to produce NEXAFS spectra will be discussed in the following sections.

3.12 Photoelectron Emission Microscopy

Photoelectron Emission Microscopy (PEEM) is a spectromicroscopy technique which combines high lateral resolution parallel imaging with Near Edge X-ray Absorption Fine Structure (NEXAFS) spectroscopy for the chemical composition of surfaces. PEEM utilises synchrotron light sources, with tuneable soft X-rays used to map specific chemical and elemental species on a surface. Images can be collected at discrete energies for a selected element, and processed to remove topography by background subtraction of an image collected at an energy prior to the absorption edge of interest. Bright regions on the image are areas rich in that element or chemical environment. The excitation energy can also be varied across a range to encompass an absorption edge, generating a "3D" image where each pixel in the image represents a full NEXAFS spectrum over the selected energy range. This allows the production of spectra from regions of interest (ROIs) on the surface of the sample for selected elements.

In PEEM, monochromatized X-rays are directed at the sample surface, where they are absorbed by causing an electron in the inner orbital to be ejected, creating a core hole [46]. The Auger and inelastically scattered electrons emitted by this excitation and relaxation process cause a cascade of secondary electrons, and those electrons with energy greater than the workfunction of the surface escape into the vacuum [46]. These electrons are accelerated by a strong electric field and magnified by the series of lenses shown in Figure 3.14, before being detected using a CCD (Charged Coupled Device) detector coupled with a phosphor screen.

Figure has been removed due to copyright restrictions

Figure 3.14: PEEM optics of beamline BL05B2, NSRRC, Taiwan [47].

Photoelectron Emission Microscopy (PEEM) offers several advantages over other surface analysis techniques in the information it supplies. Soft X-rays not penetrate as deeply into the sample, as electrons that are not close to the surface are more likely to be unable to overcome the work function of the sample and be reabsorbed rather than escape the surface [48]. For metals and semi-conductors such as pyrite, this depth is approximately within 5 nm of the surface, although it is dependent on the sample matrix and the energy of the element of interest [48]. This makes PEEM much more surface-sensitive, and has ability to map where chemical environments for specific elements appear and what they are associated with [20, 46]. Combining the images collected using

PEEM with NEXAFS provides chemical bonding information and element oxidation state information of the elements on the surface. By taking images of the same area at different energies at different edges, information about phases, oxidation and chemical associations can be deduced [20].

3.12.1 Sample Preparation

Samples intended for PEEM analysis were snap frozen in fresh HH medium and stored in a freezer at -80°C. Samples were transported frozen on dry ice, and kept frozen until ready for analysis.

3.12.2 Data Collection and Analysis

X-PEEM measurements were carried out on beamline BL05B2 at the National Synchrotron Radiation Research Centre (NSRRC) in Hsinchu, Taiwan [49]. The beamline uses an elliptically polarized undulator (EPU5) and a spherical-grating monochromator, yielding very high photon flux of between 10^{11} and 10^{13} photons s^{1} 200mÅ^{-1} over 60-1400 eV. The real-time, sample surface images were acquired by a CCD detector behind a phosphor screen in 54 total electron yield (TEY) mode. The analysis chamber vacuum was held at ultrahigh vacuum ($1x10^{-9}$ Torr). Movie stacks of images were acquired while scanning the desired photon energy ranges across the C *K*-edge (280-300 eV) and Fe *L*-edge (699-730 eV), so that each pixel in the stacked image contained a complete NEXAFS spectrum.

All images were background-corrected using "XSM reader" software provided by the NSRRC PEEM [50]. The images ranged between 37 to 450 µm in size, with $8.1x10^{5}$ pixels per image. For the 450 µm images each pixel is 0.45 µm, while for the 37 µm images, each pixel is 0.04 µm. Topographical effects were removed from the images by dividing by an image collected from background region prior to the edge to remove background energy signals.

The Fe L-edge NEXAFS spectra were calibrated using standards of iron at 706.8 eV [27]. The C K-edge NEXAFS spectra were calibrated to the π* C=C eV peak of graphite at 285.4 eV [51] and to the π* C=O peak of bovine serum albumin (BSA) at 288.2 eV [52, 53], respectively. All spectra were pre-edge and post-edge corrected by linear pre- and post-edge fit using Athena software [54]. All spectra were normalised to the corrected pre- and post-edge regions to arbitrary intensities of 0 and 1, respectively.

3.13 Scanning Transmission X-ray Microscopy

A sample is analysed in STXM by having monochromatic X-rays (generated by a synchrotron X-ray source) focussed on the sample by a Fresnel zone plate, with the transmitted X-rays detected as the sample is scanned at the focal point of the X-rays. STXM can be combined with NEXAFS as a spectrum of the sample can be produced by scanning across the desired range of photon energy when focussed on a spot on the sample [55]. A simplified schematic of the STXM is shown in Figure 3.15.

Figure has been removed due to copyright restrictions

Figure 3.15: Schematic of the STXM technique (a) and Photograph of the major components of the PolLux STXM (b), provided by the Paul Scherrer Institut [56].

STXM has three major advantages over electron microscopy: A comparatively smaller radiation dose, making them ideal for radiation sensitive samples; no need for ultrahigh vacuum, meaning a reduced loss of volatile species which is especially important when analysing organic compounds; and the ability to analyse in liquid [57]. The major disadvantage of STXM is the limitation of sample preparation. Samples thicker than 1-2 µm may not allow the X-rays to transmit, preventing the collection of any spectra from those regions [55, 57].

3.13.1 Sample Preparation

Sterile tubes containing live 2-week-old cultures of *L. ferrooxidans* grown on both pyrite and chalcopyrite were transported to the Swiss Light Source (SLS) by courier. 5 mL aliquots of culture were inoculated at 10% inoculum in fresh medium with -38 µm size fraction pyrite on site at the Swiss Light Source (SLS), with samples taken at 2 and 24 h. The cultures as transported at 2 weeks old were also sampled for analysis. See section 3.3 of this chapter for more general information on bacterial growth, and Chapter 5, section 5.3.1 for further detail on the growth of *L. ferrooxidans* on pyrite and chalcopyrite.

Culture samples were agitated and larger particles allowed to settle slightly so that the finer particles (< 5 µm) remained in the supernatant. A syringe was used to withdraw 1 mL of culture, and 1 drop was applied to a 0.5 or 1 mm silicon nitride window. Drops were reapplied as the previous drop dried until to build a sparse layer of mineral particles over the surface.

Standard solutions of bovine serum albumin (BSA), deoxyribonucleic acid (DNA), sodium alginate and glucuronic acid were made by weighing out 0.05 g of each and adding to a volumetric flask (5 mL) and making up to the line for 1% w/v solutions. A drop of solution was applied using a syringe to a 0.5 or 1 mm silicon nitride window and allowed to dry. The windows were checked to make sure the samples were not too thick, to be sure the window remained unbroken under an optical microscope.

3.13.2 Data Collection and Analysis

STXM analysis was performed at the PolLux beamline at the Paul Scherrer Institut (PSI) Swiss Light Source (SLS). Images were collected over an area of 20 µm under Helium atmosphere with a dwell time of 5-40 µs and a focal length of 1057-4148 µm depending on the element being investigated. Image stacks were collected by scanning energy the range of 280-320 eV for the C *K*-edge, so that each pixel of the image contained a complete Near-edge X-ray Absorption Fine Structure (NEXAFS) spectrum taken at 0.1 eV increments. Images stacks were converted from transmission to optical density (OD) and aligned using the aXis2000 software (version 11 May 2016) [58]. The alignment process ensures the x, y limits are the same for each image in the stack using a polynomial 2-d transformation to align successive images to 4 fiducial points on the first image. After alignment is performed, the spectra of regions of interest (ROIs) were exported. Conversion to OD was performed by dividing the image or spectrum by a spectrum collected on a blank window. NEXAFS spectra around the Cu and Fe *L*-edge within the energy ranges of 928-955 eV and 700-732 eV, respectively, were collected by line scan, and images were collected at specific energies within these ranges. Line scans are performed by scanning the sample along a single line drawn along the sample in an area of interest over the energy range of interest. Images were converted to OD and background corrected using the aXis2000 software (version 11 May 2016) [58]. All NEXAFS spectra collected were pre- and post- edge corrected and normalised using the Athena software [54] after energy calibration to the DNA carbon standard at 285.1 eV [37, 38], the Fe(II) L_3 peak of pyrite 708.3 eV [25, 27], and the Cu(I) L_3 peak of chalcopyrite at 932.6 eV [27, 59].

3.14 Time of Flight – Secondary Ion Mass Spectrometry

Time of Flight Secondary Ion Mass Spectrometry (ToF-SIMS), is a highly sensitive technique for surface analysis, which enables the investigation of the composition of the outermost atomic layers of a surface [59-62]. Ions from a primary ion source bombard the surface and collide with the atoms of the sample, which in turn can collide with each other, causing a cascade of atoms in motion.

Typically, the primary ion source is an inert gas such as helium or argon, or a liquid metal source such as gallium or gold. Only atoms and molecular fragments in the first 1-3 monolayers leave the surface; the process is illustrated in Figure 3.16 [59-62].

Figure has been removed due to copyright restrictions

Figure 3.16: An illustration of the SIMS process, adapted from [62]

The fragments that leave the surface and enter the flight tube, where a fixed potential accelerates them based on their charge (either positive or negative). The fragments are separated by the amount of time it takes them to travel to the detector. As the kinetic energy of an object is directly proportional to its mass and the square of its velocity, separation of fragments occurs by the equation shown in Equation 3.34 [62].

$$t = L\left(\frac{m}{2zV}\right)^{1/2} \tag{3.34}$$

Where the time of flight (t) is dictated by the length of the flight path (L), the mass (m) and the charge (z) of the fragment and the fixed potential (V) that accelerates the fragment along the flight path. This fragment separation generates a spectrum based on the mass-to-charge ratio m/z as the time of flight for each particle is detected and related to mass. By this equation, a fragment of greater mass will travel more slowly along the flight path [61, 62].

As the intensity of peaks in ToF-SIMS vary depending on the matrix of the surface, this technique cannot be considered quantitative, and the relative intensities of the peaks must be used for qualitative analysis [62].

3.14.1 Sample Preparation

Samples intended for ToF-SIMS analysis were placed in V-bottomed tubes containing fresh medium and snap frozen in liquid nitrogen. The tubes were then stored in a freezer at -80°C until analysis. All samples were transported on ice and kept frozen until placed directly onto the sample stage while still cold.

3.14.2 Data Collection and Analysis

ToF-SIMS experiments were performed using a Physical Electronics Inc. PHI TRIFT V nanoTOF instrument equipped with a pulsed liquid metal $^{79+}$Au primary ion gun (LMIG), operating at 30 kV

energy. “Unbunched” beam settings were used to optimise spatial resolution. A cold stage was employed to prevent the loss of volatile species to the vacuum. A minimum temperature of -70 °C was reached and maintained for the duration of analysis. This step was added after comparison to samples analysed at room temperature, which displayed less fragmentation and less higher molecular weight fragments than the sample collected at the sub-zero temperatures. The mass spectra and images obtained by ToF-SIMS was analysed using WinCadenceN software version 1.8.1.3.

The mass spectra were calibrated to the CH_3^+, $C_2H_5^+$ and $C_3H_7^+$ peaks for positive ion mass spectra, and CH^-, C_2H^- and Cl^- peaks in the negative ion mass spectra. Both positive and negative spectra were collected over an area of 100 μm^2, with a minimum of 5 areas collected per sample [63, 64]. The intensities of the secondary ions in each spectrum were normalised to the total ion yield, with a statistical analysis of the mean carried out using a Student t-distribution with 95% probability, with results plotted using 95% confidence intervals [59, 63, 64].

To remove topography, called a topographical strip, from the fragment images, the collected images were loaded and the appropriate functions were performed in the WinCadenceN software per Equation 3.35, where I_f is the fragment image and I_T is the total ion image. Scalars are applied to account for the large number of counts in the total ion image compared to the fragment image.

$$Topographical\ Strip = \frac{(I_f - 1)\left(\frac{I_T}{I_f}\right)100}{(I_T - I_f)+1} \tag{3.35}$$

To represent the hydrocarbons, carbohydrates and proteins present on the surface, positive fragments with little ambiguity as to their identity were selected to provide total proportion on the surface. For hydrocarbons, the fragments CH_3^+, $C_2H_3^+$, $C_2H_5^+$, $C_3H_3^+$, $C_3H_5^+$, $C_3H_7^+$, $C_4H_5^+$, $C_4H_7^+$, $C_4H_9^+$, $C_5H_3^+$, $C_5H_5^+$, C_5H7^+, $C_6H_7^+$, and $C_6H_9^+$ are presented. For polysaccharides, the fragments CH_3O^+, $C_2H_5O^+$, $C_3H_7O^+$, $C_2H_5O_2^+$, $C_4H_5O^+$, $C_4H_7O^+$, $C_4H_9O^+$, and $C_3H_5O_3^+$ are presented. For proteins, the fragments CHN^+, CH_4N^+, $C_3H_6N^+$, $C_3H_5N_2^+$, $C_4H_8N^+$, $C_5H_{10}N^+$, and $C_5H_{12}N^+$ are presented.

As the S_2^- and SO_2^- fragments mass-to-charge ratios are so close (*m/z* 63.941 and 63.962, respectively), the mass resolution is insufficient to separate them. This is also true for the SO_4^- and HPO_4^- fragments (*m/z* 95.956 and 95.961, respectively). As such, the S_2^- and SO_2^- fragments and the SO_4^- and HPO_4^- fragments are presented as combined species. It should be noted that although other phosphorous fragments have been detected, they occur with low frequency, and as such it is reasonable to assume that most of the SO_4^-/HPO_4^- signal is due to the sulfate fragment.

3.15 Sessile Drop Contact Angle

Sessile drop is a technique that is used to determine the contact angle using drop shape analysis. This can thereby determine the wettability of a surface, and in this case, whether a surface could be hydrophobic or hydrophilic. The Young equation, shown in Equation 3.36, is one of the possible equation used to describe this system. It takes into consideration the surface tension between the three phases (solid, liquid and gas) involved when the droplet is at thermodynamic equilibrium [65].

$$\gamma LV\cos\theta = \gamma SV - \gamma SL \quad (3.36)$$

The equation relates to the interfacial tensions between the solid and the liquid (γSL), the solid and the vapour (γSV), the liquid and the vapour (γLV), and the angle created by these three phases is the contact angle (θ), as shown in Figure 3.17 [65].

Figure has been removed due to copyright restrictions

Figure 3.17: Cross section of interfacial tensions and contact angle of a drop on a solid substrate adapted from [65]

To measure the contact angle, a 1 μL drop of liquid is placed on the sample surface. The angle between the substrate and the edge of the drop is then measured, with an angle above 90° indicating an increasingly hydrophobic surface, and an angle below 90° indicating an increasingly hydrophilic surface, as is illustrated in Figure 3.18 [65].

Figure has been removed due to copyright restrictions

Figure 3.18: Diagram of increasing surface hydrophobicity, as measured by contact angle, adapted from [65].

Contact angle hysteresis (CAH) in an effect that must be considered when measuring surface wettability to obtain the most accurate representation of the hydrophobicity of the sample. CAH is defined as the difference between the advancing and receding contact angle. The advancing contact angle occurs as a water droplet is first placed on the surface and the volume is increased to the largest measured angle. The receding contact angle occurs when the droplet is reduced in volume on the surface to the smallest measured angle. The contact hysteresis can provide more information

about the sample surface, including factors such as surface homogeneity caused by both chemical and physical properties, and roughness [66].

3.15.1 Sample Preparation

Pyrite samples intended for sessile drop contact angle studies were prepared by the method described in Section 3.4 of this chapter and into newly inoculated cultures. Samples were removed from culture flasks and allowed to air dry for up to 10 minutes before being analysed. Samples were placed on the stage and a straight needle used to pump a single droplet onto the surface and adjust the volume accordingly.

3.15.2 Data Analysis

Sessile drop contact angle experiments were performed using the Sinterface Profile Analysis Tensiometer PAT1 Version 8, with the angle cosθ determined using the Sinterface software. Both the left and right side of the bubbles were used, and the experiment was conducted in triplicate.

3.16 Captive Bubble Contact Angle

An example of a captive bubble contact angle analysis cell is shown in Figure 3.19. Briefly, a "J" needle is used to apply a bubble of air directly to the mineral surface. Receding and advancing contact angle measurements are collected by increasing and decreasing the volume of the bubble respectively, while minimising the distortion of the bubble by the needle.

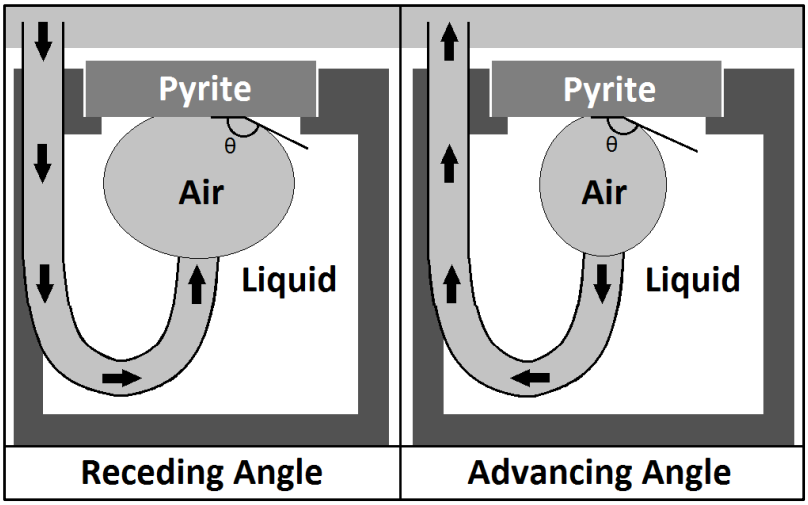

Figure 3.19: An illustration of the captive bubble method for advancing and receding angle measurement (not to scale).

The captive bubble contact angle technique applies the same principles as sessile drop, and is a measurement of the surface tension between the solid, liquid and gas phases, as is shown in Figure

3.20 [67, 68]. In the case of captive bubble contact angle, when θ is less than 90°, the surface is hydrophobic, and when θ is greater than 90°, the surface is hydrophilic [67].

Figure has been removed due to copyright restrictions

Figure 3.20: Captive bubble contact angle cross section adapted from [67]

As is the case in the sessile drop contact angle technique, CAH must be considered by measuring both advancing and receding contact angles. The advancing angle is measured as the volume of the bubble is decreased and the receding angle is measured as the volume of the bubble is increased. These recorded angles are not taken by a single static measurement, but an average of five angles taken as the volume of the bubble is decreased and increased, respectively [66, 67, 69, 70]. Figure 3.21 shows the expanding and contracting bubble as receding and advancing contact angles are measured.

Figure has been removed due to copyright restrictions

Figure 3.21: Schematic of captive bubble pumping onto a surface for receding contact angle (top), and being withdrawn from the surface for advancing contact angle (bottom), adapted from [70].

Captive bubble contact angle has several advantages over sessile drop contact angle for the purposes of these studies. Firstly, the samples are not dehydrated to take measurements as they can be kept in solution and transferred to the analysis cell without drying [67, 68]. This means that reactions such as oxidation of the sulfide mineral surface with the air that would occur as the samples are dehydrated are prevented, providing a more accurate in situ measurement of sample wettability [67]. Secondly, keeping the samples wet prevent any cells adhered to the surface from lysing as the sample is dried; this creates a more accurate *in situ* measurement of the effects of cell adhesion and whole biofilm on the mineral surfaces, rather than just adsorbed EPS and lysed cells [67, 71]. Finally, on hydrophilic surfaces, such as those that may be expected on oxidised or EPS-covered mineral surfaces, a drop of liquid on a dry surface has an angle approaching 0°, making the contact angle difficult to measure accurately. The captive bubble angle on such a hydrophilic surface approaches 180°, making the angles much easier to measure accurately [66]. Several studies

compare of methods of contact angle measurements, finding less oscillation in highest contact angle values obtained for a surface for captive bubble than sessile drop [66, 67, 72].

3.16.1 Sample Preparation

Samples were removed from experimental culture flasks and placed in the sterile medium appropriate to the strain in use, to prevent drying before being loaded directly into the quartz cell for analysis. The apparatus consists of a 50 mm^3 quartz cell containing the desired solution and sample holder.

The volume of the bubble was increased over a period of approximately 60 s, with an image of the bubble captured after every volume increase to capture the receding angles. The process was repeated withdrawing volume from the bubble to capture the advancing phase. Based on the captive bubble methods found in previous studies [67, 70], the last 5 images taken before the bubble was removed from the surface were used for the advancing angle, and the central 5 images from the receding phase were used for the receding angle. This is to ensure that the layer of liquid at the interface when the bubble is first placed on the surface has drained, ensuring the measurement is of the bubble/surface, and to allow the bubble to reach equilibrium at each volume [71]. Both the left and right side of the bubbles were used, and the experiment was conducted in triplicate, with a total of 30 measurements used to calculate average advancing and receding angles.

3.16.2 Data Analysis

Captive bubble experiments were performed using the Sinterface Profile Analysis Tensiometer PAT1 Version 8, and the contact angles from the images captured by the Sinterface PAT1 CCD camera were analysed using ImageJ imaging analysis software [73].

3.17 References

1. Burnett, P.-G.G., Heinrich, H., Peak, D., Bremer, P. J., McQuillan, A. J., Daughney, C. J., *The effect of pH and ionic strength on proton adsorption by the thermophilic bacterium Anoxybacillus flavithermus.* Geochimica et Cosmochimica Acta, 2006. **70**(8): p. 1914-1927.
2. Burnett, P.-G.G., Daughney, C. J., Peak, D., *Cd adsorption onto Anoxybacillus flavithermus: Surface complexation modeling and spectroscopic investigations.* Geochimica et Cosmochimica Acta, 2006. **70**(21): p. 5253-5269.
3. Burnett, P.-G.G., Handley, K., Peak, D., Daughney, C. J., *Divalent metal adsorption by the thermophile Anoxybacillus flavithermus in single and multi-metal systems.* Chemical Geology, 2007. **244**(3–4): p. 493-506.
4. Baumler, D.J., Jeong, K.-C., Fox, B. G., Banfield, J. F., Kaspar, C. W., *Sulfate requirement for heterotrophic growth of "Ferroplasma acidarmanus" strain fer1.* Research in Microbiology, 2005. **156**(4): p. 492-498.

5. Grzeszik, C., Lubbers, M., Reh, M., Schlegel, H.G., *Genes encoding the NAD-reducing hydrogenase of Rhodococcus opacus MR11*. Microbiology, 1997. **143**: p. 1271-1286.
6. Hocheng, H., Chang, J. H., Hsu, H. S., Han, H. J., Chang, Y. L., Jadhav, U. U., *Metal removal by Acidithiobacillus ferrooxidans through cells and extra-cellular culture supernatant in biomachining.* CIRP Journal of Manufacturing Science and Technology, 2012. **5**(2): p. 137-141.
7. Jordan, M.A., Barr, D. W., Phillips, C. V., *Iron and sulphur speciation and cell surface hydrophobicity during bacterial oxidation of a complex copper concentrate.* Minerals Engineering, 1993. **6**(8–10): p. 1001-1011.
8. Duarte, J.C., Estrada, P. C., Pereira, P. C., Beaumont, H. P., *Thermophilic vs. mesophilic bioleaching process performance.* FEMS Microbiology Reviews, 1993. **11**(1–3): p. 97-102.
9. Boss, C.B., Fredeen, K. J., *Concepts, Instrumentation, and Techniques in Inductively Coupled Plasma Optical Emission Spectrometry*. 1997: Perkin-Elmer.
10. Swapp, S. *Geochemical Instrument Analysis: Scanning Electron Microscopy*. [Website] 2012 7/7/2012 [cited 2012 19/7/2012]; Available from: http://serc.carleton.edu/research_education/geochemsheets/techniques/SEM.html.
11. *MyScope: training for advanced research*. 2014 April 15, 2014 [cited 2017 21/08]; Available from: ww.ammrf.org.au/myscope.
12. Henry, D. *Generation of Characteristic x-Rays*. [Website] 2012 [cited 2012 19/7/2012]; Available from: http://serc.carleton.edu/research_education/geochemsheets/xrays.html.
13. Franzblau, R.E., Daughney, C. J., Swedlund, P. J., Weisener, C. G., Moreau, M., Johannessen, B., Harmer, S. L., *Cu(II) removal by Anoxybacillus flavithermus–iron oxide composites during the addition of Fe(II)aq.* Geochimica et Cosmochimica Acta, 2016. **172**: p. 139-158.
14. Bui, L.M.G., Turnidge, J. D., Kidd, S. P., *The induction of Staphylococcus aureus biofilm formation or Small Colony Variants is a strain-specific response to host-generated chemical stresses.* Microbes and Infection, 2015. **17**(1): p. 77-82.
15. Microanalysis, C.F.f.A.M.a. *Introduction to Energy Dispersive X-ray Spectrometry (EDS)*. 2015 [cited 2017; Available from: http://cfamm.ucr.edu/manuals.html.
16. Hafner, B., *Scanning electron microscopy primer*. Characterization Facility, University of Minnesota-Twin Cities, 2007: p. 1-29.
17. Horny, P., Lifshin, E., Campbell, H., Gauvin, R., *Development of a New Quantitative X-Ray Microanalysis Method for Electron Microscopy.* . Microscopy and Microanalysis, 2010. **16**(6): p. 821-830.
18. Frangis, N. *Principles of Atomic Force Microscopy (AFM)*. Physics of Advanced Materials Winter School, 2008. 1-10.
19. *Nanoscope Software 6.13 User Guide*. 2004: Veeco Instruments Inc. 218.
20. Stohr, J., *NEXAFS Spectroscopy*. Springer Series in Surface Sciences. Vol. 25. 1992, Heidelberg: Springer-Verlag Berlin 404.
21. Ade, H., Hitchcock, A. P., *NEXAFS microscopy and resonant scattering: Composition and orientation probed in real and reciprocal space.* Polymer, 2008. **49**(3): p. 643-675.
22. Besley, N.A., Asmuruf, F. A., *Time-dependent density functional theory calculations of the spectroscopy of core electrons.* Physical Chemistry Chemical Physics, 2010. **12**(38): p. 12024-12039.
23. Hemraj-Benny, T., Banerjee, S., Sambasivan, S., Balasubramanian, M., Fischer, D. A., Eres, G., Puretzky, A. A., Geohegan, D. B., Lowndes, D. H., Han, W., Misewich, J. A., Wong, S. S., *Near-Edge X-ray Absorption Fine Structure Spectroscopy as a Tool for Investigating Nanomaterials.* Small, 2006. **2**(1): p. 26-35.
24. Watts, B., Thomsen, L., Dastoor, P. C., *Methods in carbon K-edge NEXAFS: Experiment and analysis.* Journal of Electron Spectroscopy and Related Phenomena, 2006. **151**(2): p. 105-120.

25. Womes, M., Karnatak, R. C., Esteva, J. M., Lefebvre, I., Allan, G., Olivier-Fourcades, J., Jumas, J. C., *Electronic structures of FeS and FeS2: X-ray absorption spectroscopy and band structure calculations.* Journal of Physics and Chemistry of Solids, 1997. **58**(2): p. 345-352.
26. Fleet, M.E., *XANES Spectroscopy of sulphur in Earth Materials*. Vol. 43. 2005. 1811-1838.
27. Goh, S.W., Buckley, A. N., Lamb, R. N., Rosenberg, R. A., Moran, D., *The oxidation states of copper and iron in mineral sulfides, and the oxides formed on initial exposure of chalcopyrite and bornite to air.* Geochimica et Cosmochimica Acta, 2006. **70**(9): p. 2210-2228.
28. Doyle, C.S., Kendelewicz, T., Bostick, B. C., Brown, G. E., *Soft X-ray spectroscopic studies of the reaction of fractured pyrite surfaces with Cr(VI)-containing aqueous solutions.* Geochimica et Cosmochimica Acta, 2004. **68**(21): p. 4287-4299.
29. van Aken, P.A., Lauterbach, S., *Strong magnetic linear dichroism in Fe L23 and O K electron energy-loss near-edge spectra of antiferromagnetic hematite α-Fe2O3.* Physics and Chemistry of Minerals, 2003. **30**(8): p. 469-477.
30. van Aken, P.A., Liebscher, B., *Quantification of ferrous/ferric ratios in minerals: new evaluation schemes of Fe L 23 electron energy-loss near-edge spectra.* Physics and Chemistry of Minerals, 2002. **29**(3): p. 188-200.
31. Hardie, A.G., Dynes, J. J., Kozak, L. M., Huang, P. M., *The role of glucose in abiotic humification pathways as catalyzed by birnessite.* Journal of Molecular Catalysis A: Chemical, 2009. **308**(1–2): p. 114-126.
32. Wan, J., Tyliszczak, T., Tokunaga, T. K., *Organic carbon distribution, speciation, and elemental correlations within soil microaggregates: Applications of STXM and NEXAFS spectroscopy.* Geochimica et Cosmochimica Acta, 2007. **71**(22): p. 5439-5449.
33. Coker, V.S., Byrne, J. M., Telling, N. D., Van Der Laan, G., Lloyd, J. R., Hitchcock, A. P., Wang, J., Pattrick, R. A. D., *Characterisation of the dissimilatory reduction of Fe(III)-oxyhydroxide at the microbe – mineral interface: the application of STXM–XMCD.* Geobiology, 2012. **10**(4): p. 347-354.
34. Croll, L.M., Britten, J. F., Morin, C., Hitchcock, A. P., Stover, H. D., *Integrating near-edge X-ray absorption fine structure (NEXAFS) microscopy and crystallography: the effects of molecular order.* J Synchrotron Radiat, 2003. **10**(Pt 3): p. 265-8.
35. Boese, J., Osanna, A., Jacobsen, C., Kirz, J., *Carbon edge XANES spectroscopy of amino acids and peptides.* Journal of Electron Spectroscopy and Related Phenomena, 1997. **85**(1–2): p. 9-15.
36. Morin, C., Hitchcock, A. P., Cornelius, R. M., Brash, J. L., Urquhart, S. G., Scholl, A., Doran, A., *Selective adsorption of protein on polymer surfaces studied by soft X-ray photoemission electron microscopy.* Journal of Electron Spectroscopy and Related Phenomena, 2004. **137–140**(0): p. 785-794.
37. Solomon, D., Lehmann, J., Harden, J., Wang, J., Kinyangi, J., Heymann, K., Karunakaran, C., Lu, Y., Wirick, S., Jacobsen, C., *Micro- and nano-environments of carbon sequestration: Multi-element STXM–NEXAFS spectromicroscopy assessment of microbial carbon and mineral associations.* Chemical Geology, 2012. **329**(0): p. 53-73.
38. Stewart-Ornstein, J., Hitchcock, A. P., Hernandez Cruz, D., Henklein, P., Overhage, J., Hilpert, K., Hale, J. D., Hancock, R. E., *Using intrinsic X-ray absorption spectral differences to identify and map peptides and proteins.* J Phys Chem B, 2007. **111**(26): p. 7691-9.
39. Chan, C.S., Fakra, S. C., Edwards, D. C., Emerson, D., Banfield, J. F., *Iron oxyhydroxide mineralization on microbial extracellular polysaccharides.* Geochimica et Cosmochimica Acta, 2009. **73**(13): p. 3807-3818.
40. Koprinarov, I.N., Hitchcock, A. P., McCrory, C. T., Childs, R. F., *Quantitative Mapping of Structured Polymeric Systems Using Singular Value Decomposition Analysis of Soft X-ray Images.* The Journal of Physical Chemistry B, 2002. **106**(21): p. 5358-5364.

41. Dynes, J.J., Lawrence, J. R., Korber, D. R., Swerhone, G. D., Leppard, G. G., Hitchcock, A. P., *Morphological and biochemical changes in Pseudomonas fluorescens biofilms induced by sub-inhibitory exposure to antimicrobial agents.* Can J Microbiol, 2009. **55**(2): p. 163-78.
42. Kalirai, S.S., Lam, K. P., Bazylinski, D. A., Lins, U., Hitchcock, A. P., *Examining the chemistry and magnetism of magnetotactic bacterium Candidatus Magnetovibrio blakemorei strain MV-1 using scanning transmission X-ray microscopy.* Chemical Geology, 2012. **300–301**(0): p. 14-23.
43. Lawrence, J.R., Swerhone, G. D. W., Leppard, G. G., Araki, T., Zhang, X., West, M. M., Hitchcock, A. P., *Scanning Transmission X-Ray, Laser Scanning, and Transmission Electron Microscopy Mapping of the Exopolymeric Matrix of Microbial Biofilms.* Applied and Environmental Microbiology, 2003. **69**(9): p. 5543-5554.
44. Miot, J., Benzerara, K., Morin, G., Kappler, A., Bernard, S., Obst, M., Férard, C., Skouri-Panet, F., Guigner, J.-M., Posth, N., Galvez, M., Brown Jr, G. E., Guyot, F., *Iron biomineralization by anaerobic neutrophilic iron-oxidizing bacteria.* Geochimica et Cosmochimica Acta, 2009. **73**(3): p. 696-711.
45. Obst, M., Dynes, J. J., Lawrence, J. R., Swerhone, G. D. W., Benzerara, K., Karunakaran, C., Kaznatcheev, K., Tyliszczak, T., Hitchcock, A. P., *Precipitation of amorphous CaCO3 (aragonite-like) by cyanobacteria: A STXM study of the influence of EPS on the nucleation process.* Geochimica et Cosmochimica Acta, 2009. **73**(14): p. 4180-4198.
46. Scholl, A., *Applications of photoemission electron microscopy (PEEM) in magnetism research.* Current Opinion in Solid State and Materials Science, 2003. **7**(1): p. 59-66.
47. *BL05B2 Photoemission Electron Microscopy*. 2012; Available from: http://efd.nsrrc.org.tw.
48. Hahner, G., *Near edge X-ray absorption fine structure spectroscopy as a tool to probe electronic and structural properties of thin organic films and liquids.* Chemical Society Reviews, 2006. **35**(12): p. 1244-1255.
49. Wei, D.H., Chan, Y.-L., Hsu, Y.-J., *Exploring the magnetic and organic microstructures with photoemission electron microscope.* Journal of Electron Spectroscopy and Related Phenomena, 2012. **185**(10): p. 429-435.
50. Yin, G.-C., Wei, D.-H., Hsu, Y.-J., Tsang, K. L. *The Image Acquisition and Analysis Program For PEEM Station*. in *AIP Conference Proceedings* 2004. San Fransisco, California, USA.
51. Brandes, J.A., Cody, G. D., Rumble, D., Haberstroh, P., Wirick, S., Gelinas, Y., *Carbon K-edge XANES spectromicroscopy of natural graphite.* Carbon, 2008. **46**(11): p. 1424-1434.
52. Hitchcock, A.P., Morin, C., Heng, Y. M., Cornelius, R. M., Brash, J. L., *Towards practical soft X-ray spectromicroscopy of biomaterials.* Journal of Biomaterials Science, Polymer Edition, 2002. **13**(8): p. 919-937.
53. Hitchcock, A.P., Morin, C., Zhang, X., Araki, T., Dynes, J. J., Stöver, H., Brash, J., Lawrence, J. R., Leppard, G. G., *Soft X-ray spectromicroscopy of biological and synthetic polymer systems.* Journal of Electron Spectroscopy and Related Phenomena, 2005. **144–147**(0): p. 259-269.
54. Ravel, B., Newville, M., *ATHENA, ARTEMIS, HEPHAESTUS: data analysis for X-ray absorption spectroscopy using IFEFFIT.* Journal of Synchrotron Radiation, 2005. **12**(4): p. 537-541.
55. Koprinarov, I. and A.P. Hitchcock, *X-ray Spectromicroscopy of Polymers: An introduction for the non-specialist*. 2000.
56. *PolLux Endstation*. [cited 2017; Available from: https://www.psi.ch/sls/pollux/endstation.
57. de Smit, E., Swart, I., Creemer, J. F., Hoveling, G. H., Gilles, M. K., Tyliszczak, T., Kooyman, P. J., Zandbergen, H. W., Morin, C., Weckhuysen, B. M., de Groot, F. M. F., *Nanoscale chemical imaging of a working catalyst by scanning transmission X-ray microscopy.* Nature, 2008. **456**(7219): p. 222-225.
58. Hitchcock, A.P. *aXis 2000 - Analysis of X-ray Images and Spectra*. 2017 25/07/2017 [cited 2017; Available from: http://unicorn.mcmaster.ca/axis/aXis2000-windows-pre-IDL8.3.html.

59. Acres, R.G., Harmer, S.L., Beattie, D.A., *Synchrotron PEEM and ToF-SIMS study of oxidized heterogenous pentlandite, pyrrhotite and chalcopyrite.* Journal of Synchrotron Radiation, 2010. **17**: p. 606-615.
60. Acres, R.G., Harmer, S. L., Beattie, D. A., *Synchrotron XPS, NEXAFS, and ToF-SIMS studies of solution exposed chalcopyrite and heterogeneous chalcopyrite with pyrite.* Minerals Engineering, 2010. **23**(11–13): p. 928-936.
61. Belu, A.M., Graham, D. J., Castner, D. G., *Time-of-flight secondary ion mass spectrometry: techniques and applications for the characterization of biomaterial surfaces.* Biomaterials, 2003. **24**(21): p. 3635-3653.
62. Briggs, D., Vickerman, J. C., *ToF-SIMS : surface analysis by mass spectrometry*. 2001, Chichester : IM ; Manchester: SurfaceSpectra
63. Smart, R.S.C., Jasieniak, M., Prince, K. E., Skinner, W. M., *SIMS studies of oxidation mechanisms and polysulfide formation in reacted sulfide surfaces.* Minerals Engineering, 2000. **13**(8): p. 857-870.
64. Piantadosi, C., Smart, R. St. C., *Statistical comparison of hydrophobic and hydrophilic species on galena and pyrite particles in flotation concentrates and tails from TOF-SIMS evidence.* International Journal of Mineral Processing, 2002. **64**(1): p. 43-54.
65. Njobuenwu, D.O., Oboho E. O., Gumus, R. H., *Determination of Contact Angle from Contact Area of Liquid Droplet Spreading on Solid Substrate.* Leonardo Electronic Journal of Practices and Technologies, 2007.
66. Eral, H.B., 't Mannetje, D. J. C. M., Oh, J. M., *Contact angle hysteresis: a review of fundamentals and applications.* Colloid and Polymer Science, 2013. **291**(2): p. 247-260.
67. Campbell, D., Carnell, S. M., Eden, R. J., *Applicability of contact angle techniques used in the analysis of contact lenses, part 1: comparative methodologies.* Eye Contact Lens, 2013. **39**(3): p. 254-62.
68. Baek, Y., Kang, J., Theato, P., Yoon, J., *Measuring hydrophilicity of RO membranes by contact angles via sessile drop and captive bubble method: A comparative study.* Desalination, 2012. **303**: p. 23-28.
69. Drelich, J., Miller, J. D., Good, R. J., *The Effect of Drop (Bubble) Size on Advancing and Receding Contact Angles for Heterogeneous and Rough Solid Surfaces as Observed with Sessile-Drop and Captive-Bubble Techniques.* Journal of Colloid and Interface Science, 1996. **179**(1): p. 37-50.
70. Read, M.L., Morgan, P. B., Kelly, J. M., Maldonado-Codina, C., *Dynamic Contact Angle Analysis of Silicone Hydrogel Contact Lenses.* Journal of Biomaterials Applications, 2010. **26**(1): p. 85-99.
71. Loeb, G.I., *The Properties of Nonbiological Surfaces and Their Characterization*, in *Bacterial Adhesion: Mechanisms and Physiological Significance*, D.C. Savage, Fletcher, M., Editor. 1985, Plenum Press: New York. p. 111-127.
72. Marmur, A., *Contact-angle hysteresis on heterogeneous smooth surfaces: theoretical comparison of the captive bubble and drop methods.* Colloids and Surfaces A: Physicochemical and Engineering Aspects, 1998. **136**(1): p. 209-215.
73. Beaussart, A., Mierczynska-Vasilev, A. M., Harmer, S. L., Beattie, D. A., *The role of mineral surface chemistry in modified dextrin adsorption.* Journal of Colloid and Interface Science, 2011. **357**(2): p. 510-520.

4 Characterisation of *Acidithiobacillus ferrooxidans* and Pyrite: Growth Behaviour and Mineral Surface Properties.

4.1 Introduction

The bacterial strain *A. ferrooxidans* has been applied to both leaching and flotation in numerous studies due to its ability to oxidise both iron and sulfur, which were detailed in Chapter 2, section 2.2.2 [1-7]. Many flotation studies using *A. ferrooxidans* focus on mineral recovery, and as such there is a need for greater characterisation to be performed on the mineral surface and the cell attachment behaviour to fully understand how mineral recovery is improved by this bacterium [1-3, 6].

Previous investigations have successfully applied *A. ferrooxidans* as a depressant for pyrite from more commercially desirable sulfide minerals, attributing this action to cell attachment to the surface [1-3]. Other studies have demonstrated the ability of *A. ferrooxidans* to act as a collector, promoting the flotation of sphalerite [8]. Such studies have suggested the ability of microorganisms to act as depressants is due to the presence of hydrophilic polysaccharides [9-11], while the collector-like ability is caused by higher concentrations of hydrophobic proteins [12] in the extracellular polymeric substances (EPS) produced by the cells. The concentration and time at which the polysaccharides and proteins are produced during biofilm formation is not well known and may impact the use of *A. ferrooxidans* for bioflotation.

Many previous studies on the application of *A. ferrooxidans* to both bioflotation and bioleaching involve processing of the cells, including washing and artificially concentrating the cells by centrifugation before exposing the cells to the mineral [1, 13-19], which may be altering natural cell behaviour and changing the nature of their excretions, in turn altering how the cells respond to the mineral surface. Many studies show adsorption of the cells on the surfaces being studied rather than direct monitoring of cell populations in solution [3, 6, 8, 13, 20-29]. This makes determining the true mechanism through which cells interact with the surface of pyrite – direct contact, indirect contact or indirect – challenging, as the experimental conditions may artificially alter the bacterial excretions [30, 31].

As the hydrophobicity of a mineral surface is dependent on the surface roughness and chemical heterogeneity of the first few atomic layers [32-34], the EPS components on the surface of pyrite must be assessed by surface sensitive techniques. The inorganic mineral oxidation products and organic species produced by *A. ferrooxidans* in contact with the pyrite surface over time must be

identified. This will enable the correlation with the physical properties of the mineral, most importantly the hydrophobicity, with the microbial products produced by *A. ferrooxidans* over the course of initial exposure through to biofilm development.

4.2 Experimental

4.2.1 Mineral Preparation

The bulk pyrite for culture growth is described in in Chapter 3, section 3.2, Table 3.4. The cubic pyrite used for this investigation and the preparation of mineral tile samples are described in Chapter 3, sections 3.2 and 3.4, respectively.

Tiles were either snap frozen in HH medium for AFM, PEEM and ToF-SIMS analysis or stored in fixative for dehydration and sputtering coating for SEM by methods described in Chapter 3, section 3.9.

4.2.2 Cell Growth and Monitoring

Cultures of *A. ferrooxidans* (DSM 14887) were received live from the DSMZ (Deutsche Sammlung von Mikroorganismen und Zellkulturen) and inoculated into HH medium and continuously subcultured as described in Chapter 3, section 3.3.1. Cultures were monitored by cerium(IV) sulfate titration and direct counting, as described in Chapter 3, sections 3.6 and 3.8, respectively.

4.2.3 Surface Characterisation

Surface analysis of pyrite control and those exposed to *A. ferrooxidans* were performed using Scanning Electron Microscope (SEM), Energy Dispersive X-ray spectroscopy (EDX), Atomic Force Microscopy (AFM), sessile drop and captive bubble contact angle, Photoemission Electron Microscopy (PEEM) and Near-edge X-ray Absorption Fine Structure (NEXAFS), and Time of Flight – Secondary Ion Mass Spectroscopy (ToF-SIMS). Details for these techniques can be found in Chapter 3, sections 3.9, 3.10, 3.11, 3.12, 3.14, 3.15, and 3.16.

4.3 Results and Discussion

4.3.1 Growth of *Acidithiobacillus ferrooxidans* on Pyrite

4.3.1.1 Cell Growth

The live culture of *A. ferrooxidans* was first cultured on HH medium containing ferrous sulfate, with growth of this culture monitored by titrating against cerium(IV) sulfate to determine the

concentration of Fe(II), from which the bacteria obtain their energy as it oxidises to Fe(III) [8, 35]. Different inoculum volumes were trialled to determine growth rate after the initial inoculation of received culture into fresh medium. A control solution of HH medium containing ferrous sulfate was also monitored over time under the same temperature and mixing conditions to ascertain if any abiotic oxidation occurred. Figure 4.22 shows the concentration curves of the different inoculum volumes and HH medium control grown with ferrous sulfate.

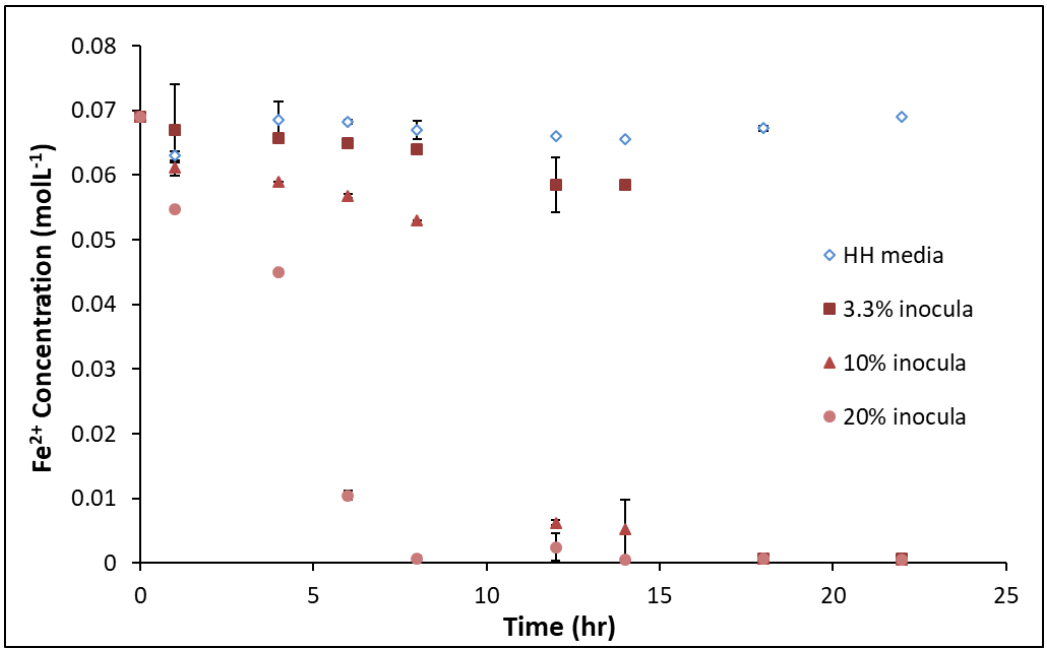

Figure 4.22: Ferrous iron titration curves of *A. ferrooxidans* in HH medium containing ferrous sulfate at 3.3%, 10% and 20% inoculum and HH medium with ferrous sulfate control solution

A 5% inoculum volume was selected for base culture of *A. ferrooxidans* grown on ferrous iron, and it was from such a base culture that cultures to be adapted to mineral were subcultured. The HH medium control containing ferrous sulfate showed no indication of abiotic iron oxidation over the course of the growth cycle. *A. ferrooxidans* was adapted to grow on pyrite by subculturing from cultures grown on soluble ferrous sulfate into HH medium with 20 g of UV sterilised pyrite replacing the ferrous sulfate, as described in Chapter 3, section 3.3.1. Cultures were inoculated at 10% with *A. ferrooxidans*. Growth curves were determined by counting, and a typical growth curve is shown in Figure 4.23.

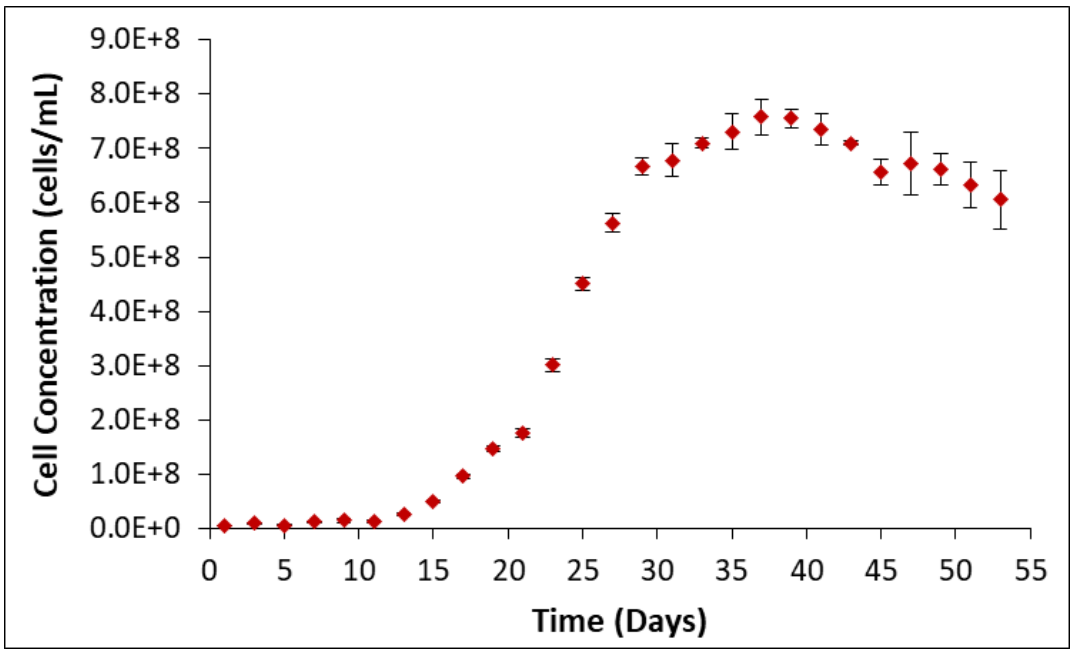

Figure 4.23: Typical growth curve of *A. ferrooxidans* on pyrite (+38, -75 um) at 10% inoculum.

The variability observed in bacterial culture development using different sources of ferrous iron illustrates perfectly how variable the bacterial growth rate can be; When grown on a solution that contains soluble ferrous sulfate, *A. ferrooxidans* typically reach the exponential phase between 20-40 hours, completing a growth cycle in approximately 96 hours (Figure 4.22). *A. ferrooxidans* grown on pyrite typically reaches the exponential phase between 20-30 days, completing a growth cycle in approximately 7 weeks (Figure 4.23). Final cell concentrations of *A. ferrooxidans* on pyrite were found to be over $7.5x10^8$ cells/mL.

The results presented here agree with the final cell concentrations previously described growth of *A. ferrooxidans* on both ferrous sulfate and pyrite. Previous studies of *A. ferrooxidans* on a variety of substrates ranges between 10^7 and 10^9 cells/mL, with stationary phase reached typically between 4-16 days on mineral or ore sources and 10-40 hours on a variety of media solutions [1-3, 14, 15, 18, 19, 28, 35-42]. Inoculum volumes, growth rate and adaptability to various minerals can vary greatly over time as the bacteria settle into a regular growth cycle, and individual lab strains might behave differently, making direct comparison challenging.

4.3.1.2 Eh and pH Monitoring

The changes in Eh and pH of the system is of crucial importance to the inorganic chemical species reacting on the pyrite surface, as well as for the maintenance of the culture. Different Eh values promote the flotation or depression of minerals, as Eh relates not only to the concentration of ions in solution, but to the surface species forming on the mineral surface [43]. Higher Eh indicates more oxidizing conditions, which promotes the formation of hydrophilic oxidation products on the

surface [43, 44]. The pH relates to Eh, as lower pH solutions are more reductive, with some collectors being ineffective at lower pH [43-45]. The Eh and pH curves of the HH medium and *A. ferrooxidans* pyrite leachate is shown in Figure 4.24. The Eh values of *A. ferrooxidans* exposed to pyrite are reported relative to an Ag/AgCl electrode at 1 atm, with an average temperature of 21.4 ± 1.3 °C, while the average temperature of the pyrite exposed to HH medium was 24.0 ± 0.7 °C.

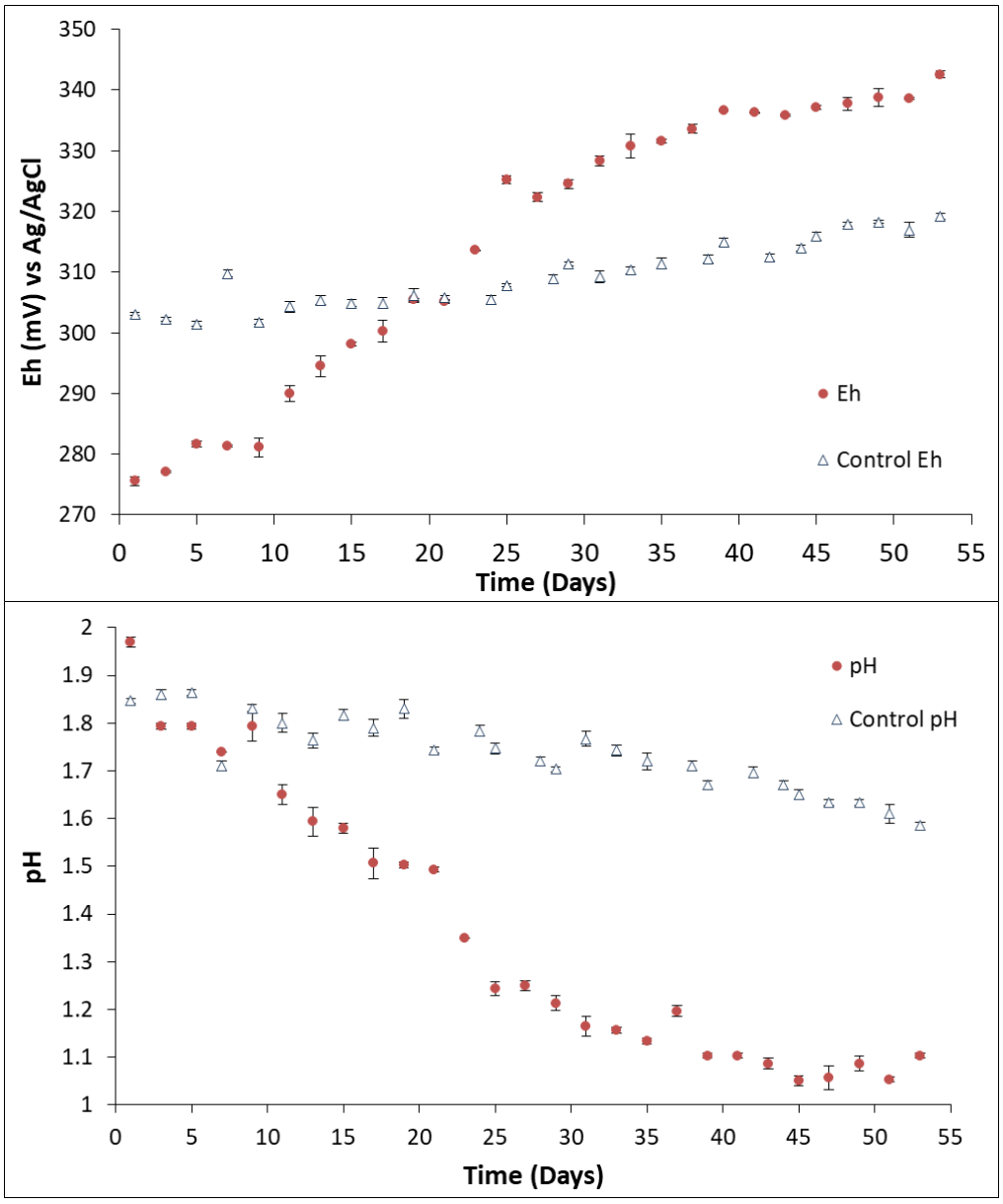

Figure 4.24: Typical Eh (top) and pH (bottom) curves of *A. ferrooxidans* on pyrite (+38, -75 um) at 10% inoculum (●), and HH medium (Δ).

The pH of the *A. ferrooxidans* culture grown on pyrite starts at just under 2, dropping to just above pH 1 by day 45, where sits between 1 and 1.1 for the remainder of the exposure, while the Eh steadily increases from just over 275 mV to just over 340mV. The pH of the HH medium control solution starts at just over 1.8, falling to just below 1.6 over 53 days, while the Eh starts at just over 300 mV, rising to just under 320 mV.

Previous studies have measured the Eh and pH of leachate of pyrite using *A. ferrooxidans*, a summary of which can be found in Table 4.7. All potentials reported here have been converted to Ag/AgCl reference electrode values where possible.

Table 4.7: Previous Eh and pH studies of *A. ferrooxidans* bioleaching pyrite.

Duration (days)	Eh $_{init.}$ (mV)	Eh $_{fin.}$ (mV)	pH $_{init.}$	pH $_{fin.}$	Reference
18	200	500	2	1.8	[37]
29	380	610	1.8	0.9	[15]
29[a]	380	380	1.8	1.6	[15]
24	-	-	2.05	1.8	[40]
24[a]	-	-	2.05	1.92	[40]
35	400	700	-	-	[46]
10[b]	380	570	1.7	1.75	[2]
20[a]	270	420	1.5	1.65	[38]

[a] Abiotic control, [b] No reference electrode information supplied

Several of the studies listed in this table performed no control experiments for comparison of their bioleaching results [2, 37, 46] while Yu *et al* performed control experiments at a fraction number of time points of their bioleaching experiments [40]. The lack of rigorous control experiments being presented in previous studies makes comparison between different experiments difficult. The studies on pyrite leaching by Liu *et al* [15] agrees most strongly with the pH data recorded in this study, while the results of Sharma *et al* [37] agree most strongly with the Eh results recorded here. The studies on pyrite leaching by *A. ferrooxidans* observed a decrease in pH between 2 and 0.9, and an increase in Eh between 200 mV and 700 mV which agrees with the range of values observed over the leaching of pyrite in this study. The lower initial Eh observed in the biotic solution compared to the abiotic control solution was also observed in a study by Xia *et al*, who found that the Eh of a culture of *A. manzaensis* was lower than the Eh of the abiotic control at identical initial iron concentration and pH [38].

The surface and solution reactions that previous studies have been proposed to occur in the leaching of pyrite produce ions in solution as per Equations 4.37-4.43, and a variety of oxidation products such as jarosite per Equation 4.44 (Where $M^+ = K^+$, Na^+ or H_3O^+) [37, 47-55]. These reactions also contribute to the pH of solution as leaching of the mineral produces H^+ in solution, as per Equations

4.37 and 4.38, and to the Eh of the mineral by increasing the concentration of a variety of ions in solution with differing oxidative ability [37, 47-55].

$$FeS_2 + 14Fe^{3+} + 8H_2O \rightarrow 15Fe^{2+} + 2SO_4^{2-} + 16H^+ \quad (4.37)$$

$$2FeS_2 + 7O_2 + 2H_2O \rightarrow 2FeSO_4 + 2H_2SO_4 \quad (4.38)$$

$$4FeS_2 + 3O_2 + 6H_2SO_4 \rightarrow 2Fe_2(SO_4)_3 + 8S^0 + 6H_2O \quad (4.39)$$

$$4Fe^{2+} + O_2 + 4H^+ \rightarrow 4Fe^{3+} + 2H_2O \quad (4.40)$$

$$Fe^{3+} + 3H_2O \rightarrow Fe(OH)_3 + 3H^+ \quad (4.41)$$

$$FeS_2 + 2Fe^{3+} \rightarrow 3Fe^{2+} + 2S^0 \quad (4.42)$$

$$2S^0 + 3O_2 + 2H_2O \rightarrow 4H^+ + 2SO_4^{2-} \quad (4.43)$$

$$3Fe^{3+} + 2SO_4^{2-} + M^+ + 6H_2O \rightarrow MFe_3(SO_4)_2(OH)_6 + 6H^+ \quad (4.44)$$

The results here show the pH decreases as the pyrite oxidises and produces H^+, per Equations 4.37, 4.38, 4.41 and 4.43. The pH values measured over the course of these experiments suggests that the consumption of sulfuric acid is outweighed by production, with the pH never greater than the initial value measured for the medium solution. This promotes the formation of iron hydroxides on the mineral surface (Equation 4.41), and soluble sulfates in solution (Equations 4.37, 4.38, 4.43), increasing in concentration over time. Lower pH is also less conducive to the formation of jarosite, as per Equation 4.44 [56]. These reactions are also dependent on solution temperature and Eh.

The Eh values increase over time, suggesting oxidative conditions are occurring, promoting the formation of hydrophilic iron (hydr)oxides and oxygenated sulfur species on the surface, and the oxidation of ferrous iron to ferric iron in solution. The difference between the Eh values of the culture and the abiotic control is most pronounced at early exposure stages, suggesting that the presence of cells accelerates the oxidation of the pyrite surface. These results would suggest higher concentrations of ferric iron and soluble sulfur species may be expected in the solution where *A. ferrooxidans* is in contact with pyrite. A more detailed investigation of the ions contributing to the increase in Eh is possible using titration and Inductively Coupled Plasma Optical Emission Spectroscopy (ICPOES).

4.3.1.3 Inductively Coupled Plasma Optical Emission Spectroscopy, Cerium(IV) Sulfate Titration

Total iron was measured in solution by ICPOES, and ferrous iron concentration was determined by colorimetric titration against cerium(IV) sulfate, with ferric iron calculated by subtracting ferrous iron concentration from the total iron concentration. The sulfur concentration represented here describes all soluble sulfur species, and is unable to differentiate types of sulfur, i.e. sulfates, sulfites, etc. The ferrous iron, ferric iron and soluble sulfur concentrations of the leachate of pyrite exposed to HH medium and *A. ferrooxidans* culture are shown in Figure 4.25.

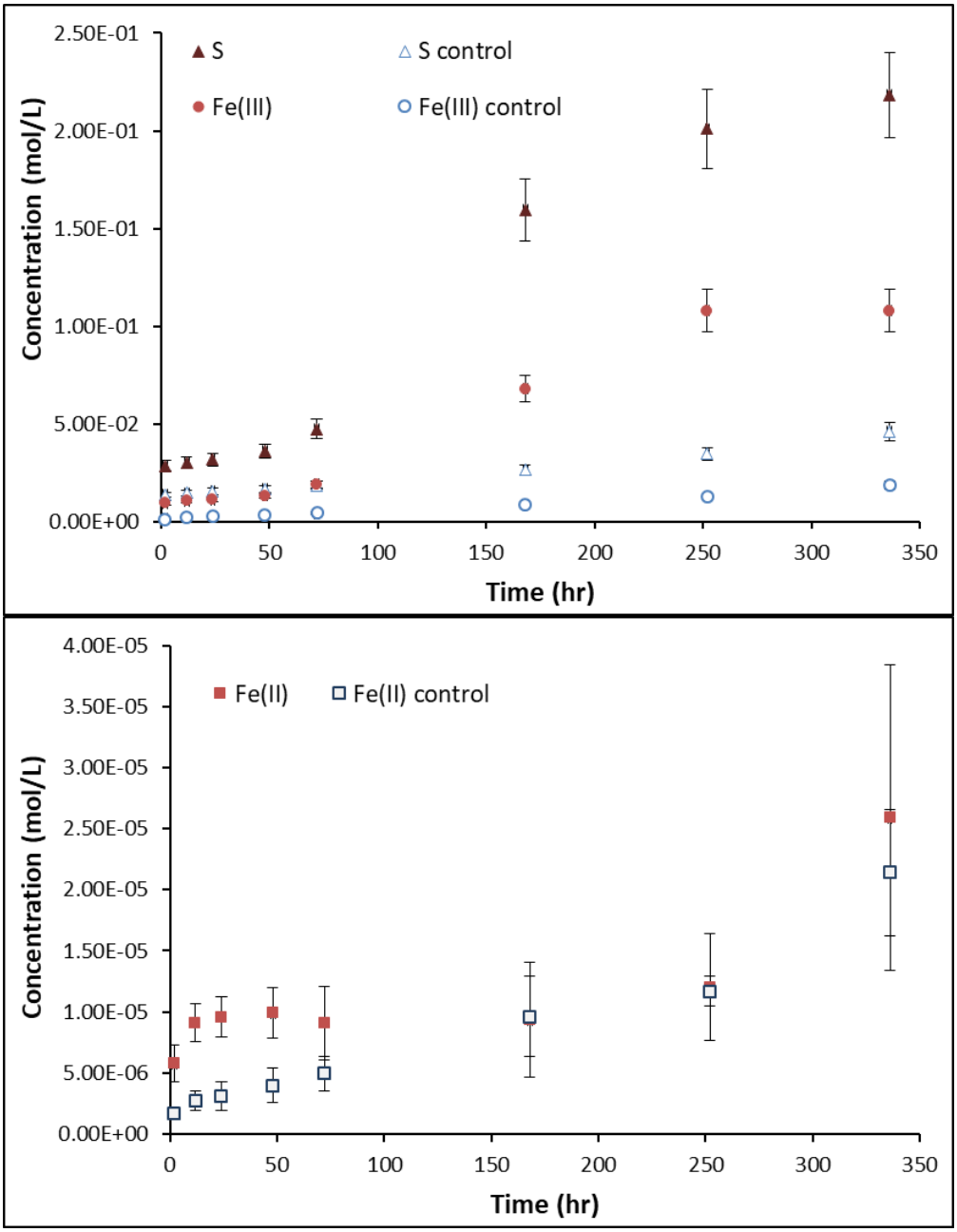

Figure 4.25: Typical concentration curves of ferric iron (top) of *A. ferrooxidans* on pyrite (●), and HH medium (○). and solubilised sulfur (top) in *A. ferrooxidans* on pyrite (▲), and HH medium (Δ). Typical concentration curves of ferrous iron (bottom) of *A. ferrooxidans* on pyrite (■), and HH medium (□),

The concentration in solution of Fe^{3+} of pyrite exposed to *A. ferrooxidans* remains around $1.0x10^{-2}$ mol/L for the first 48 h, then increases to 0.1 mol/L by 250 h, and remains unchanged by 336 h. The concentration of Fe^{2+} increases initially over the first 12 h from $5.784x10^{-6}$ mol/L to remain consistently around $9.4x10^{-6}$ mol/L for 168 h, then increases to a final concentration of $2.6x10^{-5}$ mol/L at 336 h. The concentration of dissolved sulfur in solution follows a similar trend to that of Fe^{3+}, remaining around $3.17x10^{-2}$ mol/L for the first 48 h, then increasing to a final concentration of 0.22 mol/L. Unlike the Fe^{3+} curve, which plateaus after 250 h, the dissolved sulfur concentration continues to increase.

The initial Fe^{3+} concentration in the HH medium leachate was found to be $1.3x10^{-3}$ mol/L, increasing in an almost linear fashion to a final concentration of $1.9x10^{-2}$ mol/L. The concentration of Fe^{2+} likewise increases in an almost linear fashion from an initial concentration of $1.74x10^{-6}$ mol/L to a final concentration of $2.14x10^{-5}$ mol/L after 336 h. The concentration of dissolved sulfur in the HH medium also follows a near linear increase from an initial concentration of $1.38x10^{-2}$ mol/L to a final concentration of $4.59x10^{-2}$ mol/L after 336 h.

The ferric iron concentrations in pyrite leaching by *A. ferrooxidans* previously reported range between 0 mol/L and 0.13 mol/L, with the concentrations reported in this study falling within that range and agreeing most strongly with the pyrite leaching study by Liu *et al* [15]. The concentration of ferrous iron reported in this study also agree with previous studies, with the final ferrous iron concentrations reported ranging between 0 mol/L and 0.69 mol/L [15, 40]. The total sulfur concentration reported in this study is lower than the concentrations observed in previous studies, with concentrations ranging between 0.46 and 12.7 mol/L, but is greater than the sulfate concentrations previously reported by Brunner *et al* of $2.2x10^{-2}$ mol/L [40, 57].

The trends identified in previous studies of iron concentration in leachate of pyrite under abiotic conditions also agree with the results presented here, with both Fe^{2+} and Fe^{3+} increasing in concentration, but not to the same extent as the samples containing *A. ferrooxidans* [15, 37, 40]. Studies by Gleisner *et al* and Yu *et al* found that the total sulfur in solution increased over the course of leaching of pyrite by *A. ferrooxidans*, as was also observed in this study, as did the total sulfur in the abiotic controls presented to a lesser extent [40, 57].

Brunner *et al* proposed that *A. ferrooxidans* oxidises sulfur initially, then changes preferred energy source to ferrous iron at the exponential phase, which frees up ferric iron ions that promote faster leaching [14], which explains why here the sulfur and Fe^{3+} concentration in solution does not increase initially, while Fe^{2+} does, before dipping again as the cells start to use it as a food source. This suggests that not only is the concentration of all ions greater in *A. ferrooxidans* culture

solutions, but that all species are leaching from pyrite into solution at a greater rate in the culture compared to the HH medium control. This agrees with the Eh results, which increases as the concentration of both ferric iron and oxidised sulfur species increase in the culture solution. The concentration of these irons, as predicted, show more significant increases in the presence of *A. ferrooxidans* compared to the abiotic HH medium solution.

Although the exponential phase of *A. ferrooxidans* does not begin until day 20 of exposure to pyrite, the leaching of iron and sulfur-species from the mineral appears immediate, accompanied by a decrease in pH and an increase in Eh as sulfuric acid is produced and ferrous iron is oxidised to ferric iron and the leaching of the mineral is perpetuated. To relate the solution ion content, Eh and pH to the mechanism of *A. ferrooxidans* interaction with the surface of pyrite, and to identify secondary mineral formation and leaching progression, it is necessary to investigate the surface using imaging techniques.

4.3.2 Scanning Electron Microscopy and Energy Dispersive X-ray Spectroscopy

Scanning Electron Microscopy (SEM) coupled with Energy Dispersive X-ray Spectroscopy (EDX) was employed to look at the distribution of cells on the pyrite surface, to observe the morphology of the pyrite surface, and to measure the elemental composition of the mineral and debris on the surface. A comparison was made between the abiotic control pyrite surface, which was expected to leach due to the acidic medium, and the pyrite exposed to *A. ferrooxidans*. The number of cells attached to the surface, the regions of the surface they are attaching to as well as the physical properties of the surface such as the pitting were investigated. The surface properties will affect the hydrophobicity of the surface, impacting how the mineral might respond in a flotation system.

SEM images of polished pyrite, shown below in Figure 4.26, show the pyrite surface prior to exposure to the abiotic medium and to live culture shows a relatively smooth and clean surface with some naturally occurring voids and pits. Some scratches from the grinding and polishing process remain visible on the surface, and silicate inclusions are visible on the surface at low magnification.

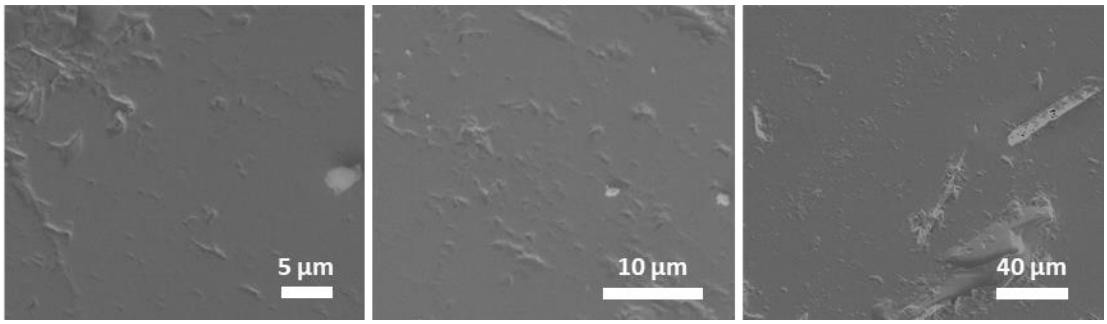

Figure 4.26: Typical SEM images of bare polished pyrite

These images agree with those obtained of clean, untreated pyrite surfaces observed in previous studies [15, 38], and serve as an initial point of comparison for both biotic and abiotic exposure experiments. Typical SEM images obtained for pyrite upon exposure to HH medium control in comparison to pyrite exposed to *A. ferrooxidans* are shown in Figure 4.27.

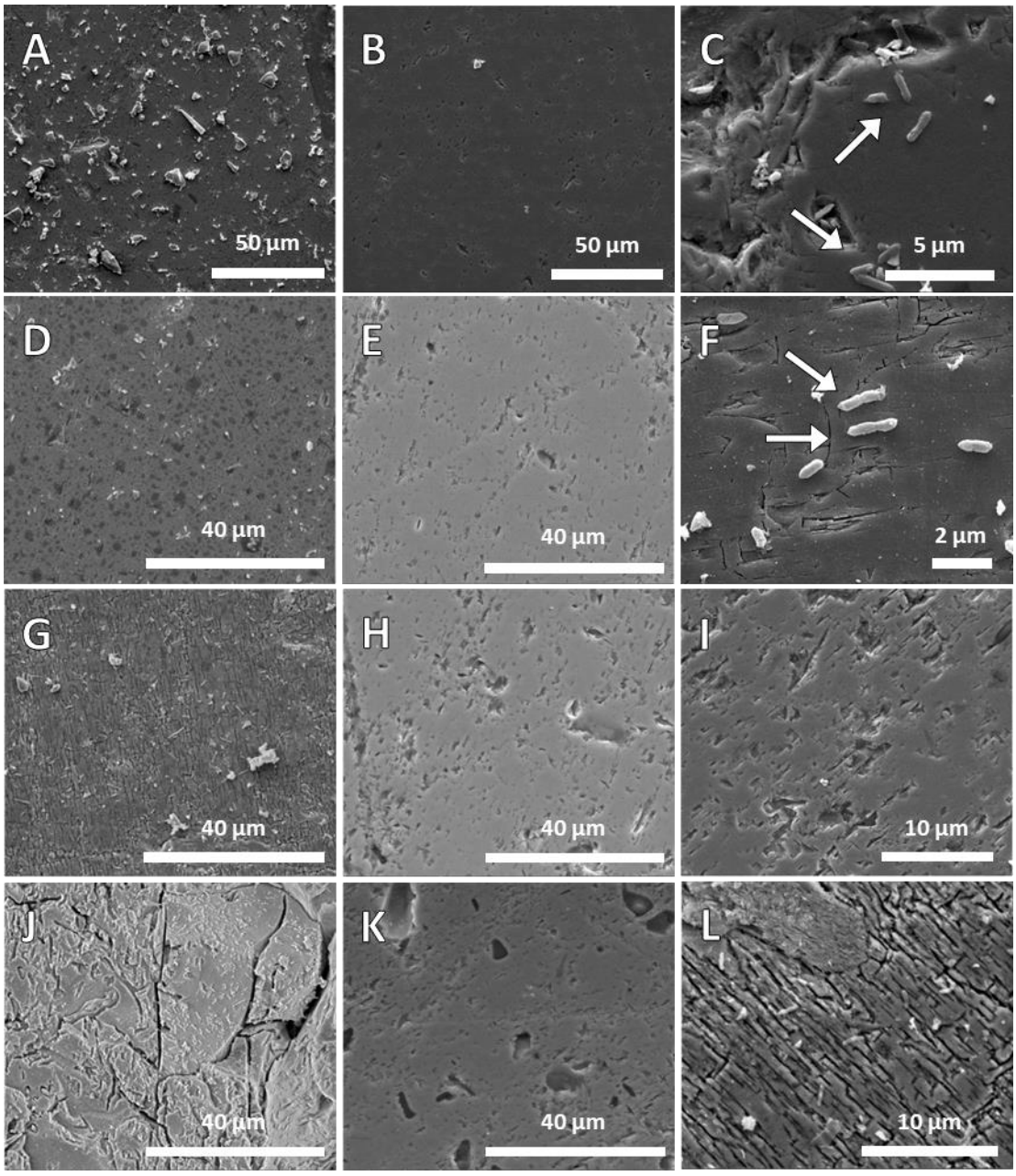

Figure 4.27: Pyrite tiles exposed to *A. ferrooxidans* for 2 h (A), 24 h (D), 72 h (G) and 168 h (J), pyrite tiles exposed to HH medium for 2 h (B), 24 h (E), 72 h (H) and 168 h (K), close-up of *A. ferrooxidans* cells, indicated by arrows (C), in the process of cell division (F), etch pits (I) leaching rivers (L).

After 2 h of exposure to *A. ferrooxidans*, mineral debris was observed on the surface of the pyrite, the pitting character seems very similar between sample exposed to culture and the medium control sample and the bare polished pyrite shown in Figure 4.26. Cells can already be seen on the surface, and at this stage there seems to be no preference for site defects, as cells were found on smooth

areas of the surface (see Figure 4.27(C)). If each cell is an average of 0.56 μm^2 in area, cell coverage at this stage of exposure has been calculated at approximately 0.35 ± 0.08 %. This level of coverage of *A. ferrooxidans* cells agrees with that on chalcopyrite after 1 h as observed by Tan *et al* of less than 1 % [29]. There was some pitting, typically regularly orientated and 0.8-1.8 μm in length and 0.2-0.8 μm wide, shown in Figure 4.27(I), with some scratches remaining on the surface from the polishing process that appear to be a nexus for the etch pits. After 24 h of exposure to *A. ferrooxidans*, we can now see cells reproducing by cell division on the surface, and cells present on the surface in greater numbers, as is shown in Figure 4.27(D). There was still a large amount of loose debris on the surface. Cell coverage at this stage of exposure has been was found to have increased to 0.68 ± 0.25 %, almost double that found at 2 h. The same size range pitting observed at 2 h exposure and scratches are observed at this period of exposure. After 72 h of exposure, cells appear to be more concentrated surface defects and voids, as well as on the edges of the sample where bacterial colonies are starting to grow. Cells appear more concentrated around surface defects such as cracks, shelves and voids, however they are not restricted to these areas. This is likely due to the sheltering they experience in these voids, coupled with the lack of motility, meaning the cells are unable to move themselves in the culture solution and relying on the mixing of the culture flasks to bring the cells in contact with the surface. The pyrite surface is showing rivers of cracks and appear deeper than the finer cracks observed at 24 h, typical rivers are shown in Figure 4.27(L). These surface artefacts have been observed in a previous study by Karavaiko *et al*, who determined that they are not caused by direct bacterial action, but rather abiotic leaching along crystal boundaries [58]. Etch pits of the same dimensions as earlier exposures are still visible on the surface. Cells cover the surface with an even distribution, with coverage of 1.40 ± 0.23%. The extent of cell coverage on the surface at this stage has almost doubled from that observed at 24 h, which is an accelerated growth compared to that seen of cells in solution, indicating a potential preference of cells to propagate on the mineral surface compared to solution, which may rely on the leaching of solution for enough nutrients to start the exponential phase observed through the solution counts presented in the previous section. After 168 h of exposure to *A. ferrooxidans*, very advanced pitting can be observed on the surface with more advanced dissolution observed compared to 72 h of exposure. This agrees with the study by Liu *et al*, which also identified that the pitting occurred much more so than the control sample [15]. Cells can be observed in greater numbers on the surface, with bacterial colonies forming not just in surface defects but on more exposed regions of the mineral as well, shown in Figure 4.27(J). Although densely populated cell colonies are now observed, they are not distributed evenly across the surface. Regions of high cell population were found to have a surface coverage of 4.58 ± 1.86 %. Cells are observed in the process of cell division, indicating that the cells are reproducing on the surface after irreversibly

attaching rather than having been caught by the motion of mixing, shown in Figure 4.27(F). These results suggest cell coverage increases over the course of exposure, with *A. ferrooxidans* showing no obvious preference for surface defects at early stages of attachment, and longer periods of exposure (168 h) are required for the formation of biofilm to occur.

The pyrite exposed to HH medium for 2 h is similar in appearance to the pyrite exposed to culture for this period, and indistinguishable from the images taken of the bare polished pyrite shown in Figure 4.26. The surface shows some pitting, typically regularly orientated and 0.8-1.8 μm in length and 0.2-0.8 μm wide, with some scratches remaining on the surface from the polishing process that appear to be a nexus for the etch pits. After 24 h of there is less debris on the surface compared to pyrite exposed to culture, and the surface does not appear to be as pitted. After 72 h of exposure, the surface shows etch pits that appear of the same dimensions of those observed over earlier periods of exposure. After 168 h of exposure, the dissolution is more advanced compared to 72 h of exposure. These results suggest that the presence of *A. ferrooxidans* accelerates the leaching of the surface, which correlates with the increase in ferric iron and soluble sulfur in solution and the increasing Eh/ decreasing pH observed in the previous section.

Previous studies who investigated pyrite leaching by *A. ferrooxidans* observed a variety of mineral morphologies. Several studies observed etch pits similar in appearance to those described in Figure 1, with Gleisner *et al* quantifying the pits dimensions and finding them to be 0.2-0.3 μm wide, which agrees with the etch pit dimensions found here [15, 40, 57]. These etch pits were attributed to ferric iron leaching of the surface along crystal faces, rather than direct leaching by *A. ferrooxidans* cells, and the lack of cells around etch pits on pyrite and the presence of etch pits on the control pyrite surface agrees with those observations [15, 40]. Abiotic leaching is contradicted by Mitsunobu *et al*, who observe pits that are similar in size to cells, and conclude they are caused by cells, which is refuted by the results presented in this work [59]. Xia *et al* observed a smooth mineral surface on pyrite after 20 days of chemical leaching at pH 1.5, as did Mitsunobu *et al* over 28 days at pH 3, both of which agrees with the comparatively smooth control surfaces observed in this study [38, 59].

Very few papers performed control abiotic leaching for comparison to bioleaching for the purposes of SEM. Xia *et al* observed a smooth mineral surface on pyrite after 20 days of chemical leaching compared to leaching with *A. ferrooxidans* at pH 1.5, as did Mitsunobu *et al* over 28 days at pH 3, both of which agrees with the comparatively smooth control surfaces observed in this study [38, 59]. The lack of control images collected in biotic leaching studies, combined with the lack of

consistency in sample preparation and pH of leaching solutions, makes comparing results challenging, and isolating bacterial action from chemical leaching more difficult.

Several studies air-dry their samples, which makes observation of cells on the surface impossible [15, 38, 57]. Poor sample preparation may have led to misinterpretation of data, such as suggesting cells are not attaching to the surface, when samples have not been appropriately prepared and cells are destroyed or removed by the vacuum [38, 59]. Many of these studies investigate leaching, and as such are also observing much longer periods (16-70 days) of exposure than is suitable for flotation studies [15, 38, 40, 57, 59]. This makes this study important for providing information on shorted periods of exposure of minerals to microorganisms.

EDX analysis was performed on the surface and on the artefacts observed on the surface to enable identification of the elements present and their atomic ratios, which can be used to indicate potential mineral oxidation products. The EDX analysis of the pyrite surface exposed to *A. ferrooxidans* are shown in Figure 4.28 as average atomic percentage. The elements Mg, Al and Na were detected at levels below 2%.

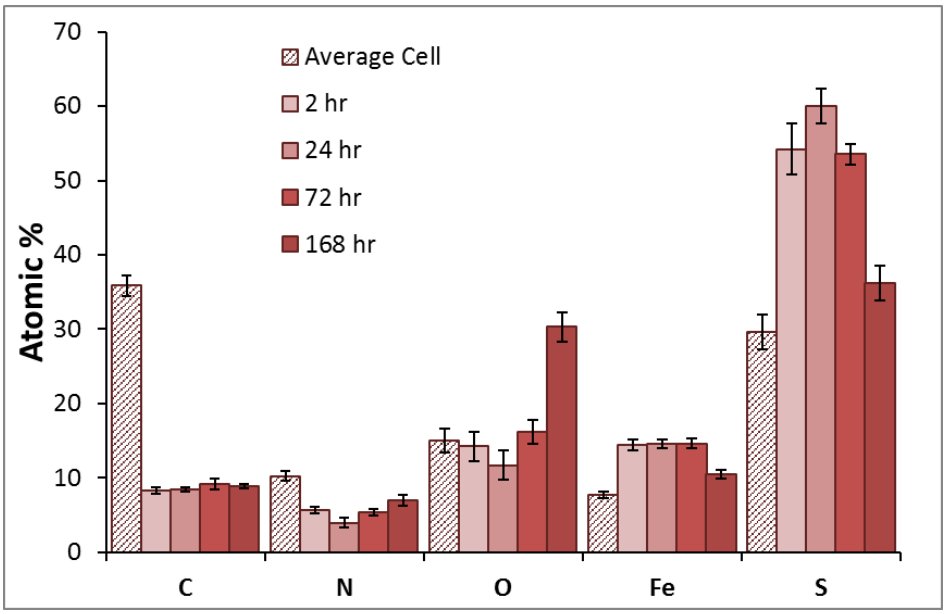

Figure 4.28: Average atomic percentage of pyrite exposed to *A. ferrooxidans* for 2, 24, 72 and 168 h, and the average atomic percentage of individual *A. ferrooxidans* cells (striped), as determined by EDX

The individual cells of *A. ferrooxidans* present a significant carbon signal when compared with the mineral measured, however cells are typically not thick enough to block all signal from the bulk mineral beneath, which is why the pyrite signals of Fe and S are still observed. The EDX atomic percentages of the pyrite surface exposed to *A. ferrooxidans* are relatively stable and within standard deviation for the first 72 h of exposure. This could be due in part to the fact that EDX penetrates the surface up to 5 μm, and presents significant bulk pyrite signal [60]. After 168 h, a

significant increase in oxygen and decrease in sulfur is observed, while the remaining atomic percentages are relatively stable. This increased oxygen percentage after 168 h suggests that oxidation products are a greater presence on the surface. A similar method was used by Watling *et al* to confirm *S. acidophilus* cells on pyrite and chalcopyrite surfaces by their large carbon contribution [61].

The atomic percentages of pyrite exposed to HH medium control do not show the same extent of oxidation, with atomic percentages across every time of exposure within standard deviation. In contrast to the samples exposed to *A. ferrooxidans*, there was no detected nitrogen signal, with a detection limit of 0.1% [60], and the atomic percentage of both carbon and oxygen detected was lower. Silicate crystal inclusions were highly visible in the control pyrite samples, and these regions were avoided. The EDX analysis of the pyrite surface exposed to HH medium are shown in Figure 4.29 as average atomic percentage. The elements Al and Si were detected at levels below 2.5%.

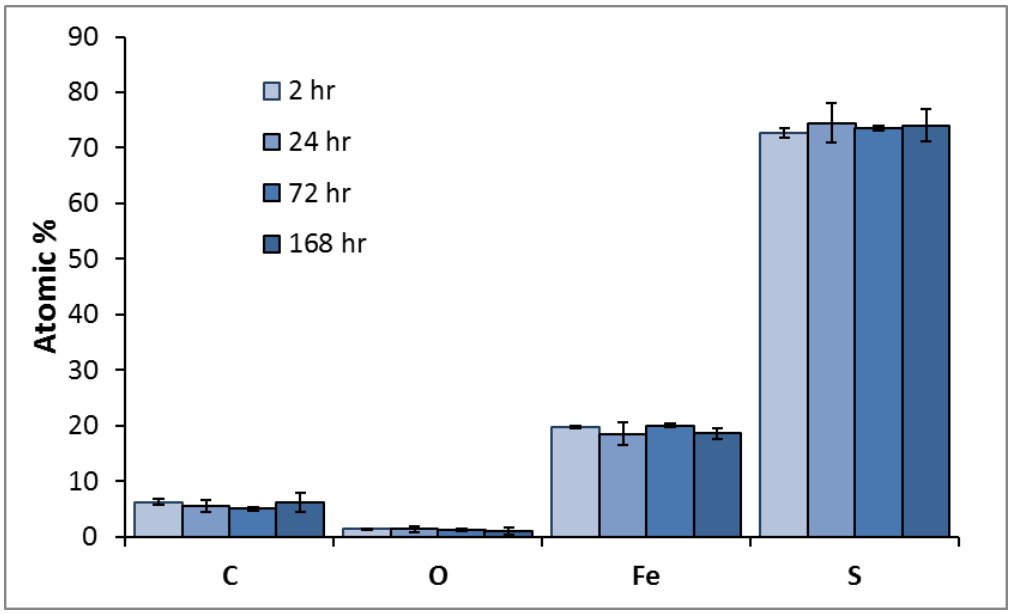

Figure 4.29: Average atomic percentage of pyrite exposed to HH medium for 2, 24, 72 and 168 h, as determined by EDX

The atomic percentage results for the pyrite exposed to the HH medium control agree with the findings of Mikkelsen *et al*, who did not find any evidence of leaching residues such as jarosites and iron oxy-hydroxides using EDX on their pyrite control samples until after 35 days of exposure [52]. Several previous studies have reported iron and sulfur atomic ratios of between 1:1.12 and 1:2 for pyrite leached by *A. ferrooxidans*, suggesting an iron rich surface, and attributed it to sulfur dissolving as sulfate, agreeing with their SEM analysis of a surface covered in iron precipitates such as jarosite [56, 57]. However, these studies have either air dried their samples, or not disclosed their sample preparation, which would potentially artificially introduce more iron oxides to the surface.

They have also not provided control experiments [56, 57]. This suggests the control surface is sulfur-rich, which agrees with the ICPOES results that show greater concentration of iron leaching into solution than sulfur.

As the sampling depth of EDX is up to 5 µm, other experiments will be needed to investigate the outermost atomic layers with minimal bulk pyrite contribution, and to relate physical properties to chemical species on the surface [60, 62, 63].

4.3.3 Atomic Force Microscopy

Atomic force microscopy (AFM) allows for a direct measurement of the changes in roughness of the surface that was observed using SEM. Roughness of a surface strongly impacts the hydrophobicity of a surface, and the topography influences how a solution will interact with the surface. Measuring the roughness using AFM allows comparison to be made between the physical characteristics of the mineral surface, the chemical changes measured by the qualitative analytical techniques described previously and the hydrophobicity of the sample as measured by contact angle [64]. Typical AFM images obtained for pyrite after different periods of exposure to *A. ferrooxidans* are shown in Figure 4.30.

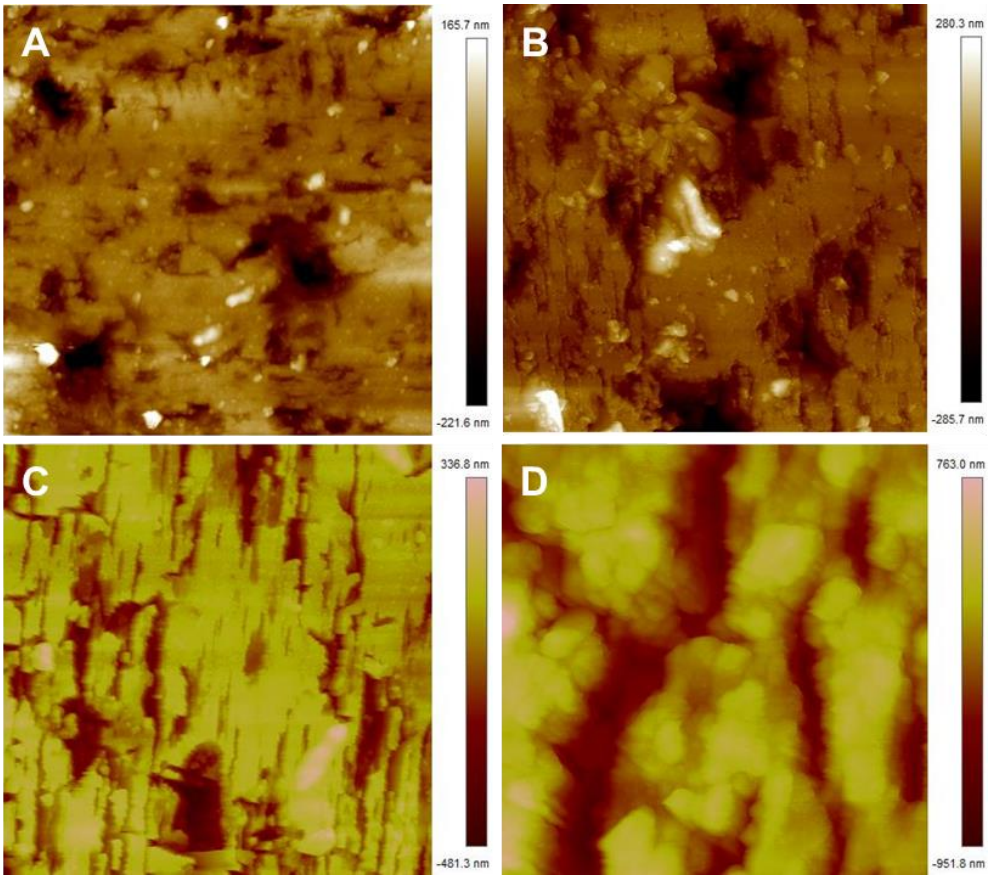

Figure 4.30: 10 x 10 µm AFM height images of pyrite exposed to *A. ferrooxidans* for 2 h (A); 24 h (B); 72 h (C); 168 h (D).

At least four images like those shown in Figure 4.30 were obtained per sample, always over an area of 10 µm, to calculate the average roughness of the sample. Minimal image processing was performed on the raw data to ensure the roughness values calculated by the NanoScope software were as close as possible to the images measured. Two different methods, Ra and Rq, were used to calculate the average roughness of the pyrite surface was described in Chapter 3, section 3.10.2, and both are displayed in Figure 4.31 with the error bars representing the 95% confidence interval.

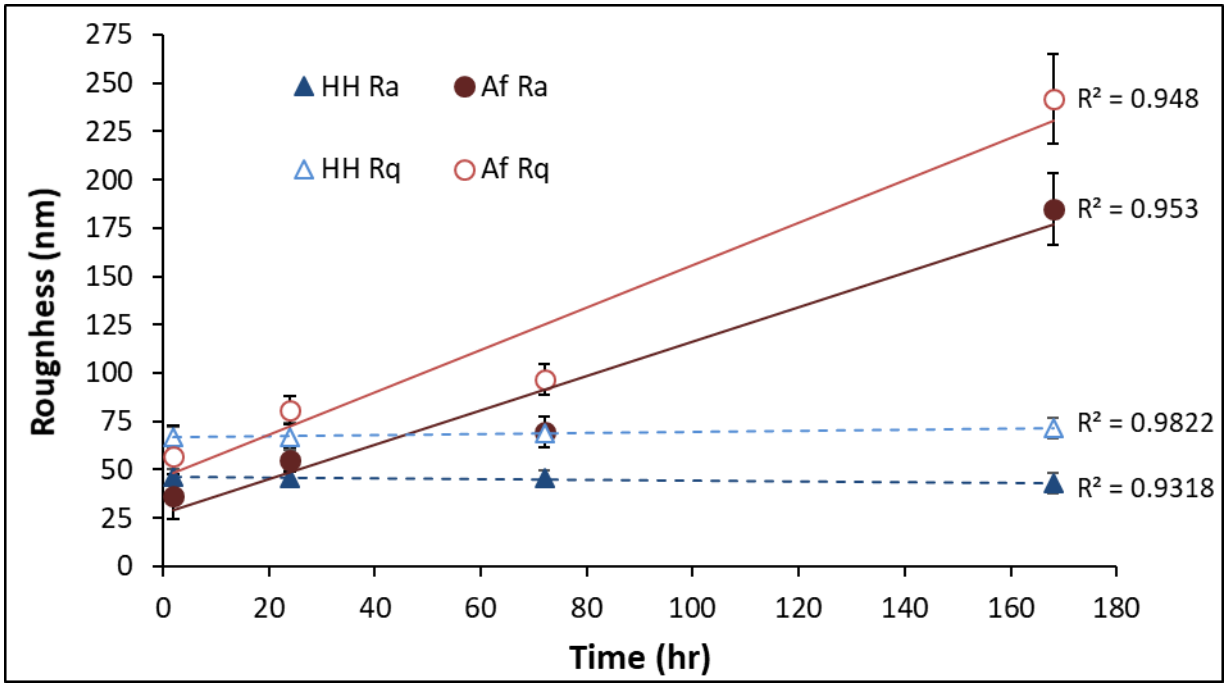

Figure 4.31: The roughness of pyrite exposed to *A. ferrooxidans* as calculated by Ra (●) and Rq (○), and HH medium as calculated by Ra (▲) and Rq (Δ).

As can be seen in the plot above, in the presence of the bacteria, both the Ra and Rq of the pyrite surface increases linearly, with correlation coefficients of 0.953 and 0.948, respectively. It should also be noticed that as the exposure time increases, the standard deviation of the roughness values for both methods increases, indicating that there is more variation in roughness across the surface at advanced exposure times compared to those of shorter exposures. This is unsurprising, as the leaching of the surface is heterogeneous, and may have a significant impact on the contact angle of the pyrite surface. The pyrite exposed to the HH medium also showed high correlation coefficients in the calculated Ra and Rq values of 0.9318 and 0.9822 respectively. The sample roughness of the pyrite exposed to *A. ferrooxidans* for 2 to 72 h does not differ significantly from the controls. As the SEM images bare polished pyrite (Chapter 4, section 4.3.2, Figure 4.26) are visually identical to those exposed to abiotic medium for 2 h, and the difference in roughness for the shortest periods of exposure to *A. ferrooxidans* and abiotic medium are statistically insignificant, it can be assumed that the roughness of bare polished pyrite coincides with these values. After 168 h of exposure, this difference in roughness is significantly increased between pyrite exposed to *A. ferrooxidans* and the

control. This agrees with the initial observations of decreasing pH, increasing Eh and increasing concentrations of both ferric iron and soluble sulfur species in solution as mineral leaching is accelerated by *A. ferrooxidans*, which correlate with the increasing surface roughness measured here and observed using SEM.

Gehrke *et al* showed *A. ferrooxidans* cells prefer cracks and grain boundaries of pyrite using AFM and SEM, although our samples show they are also found on smoother regions of the surface [65]. Studies by Rohwerder *et al* and Sand *et al* investigating cell preference for defect sites on pyrite, suggest not only mechanical reasons, such as imperfections in the lattice increasing contact area for cell adhesion, as reason for adhesion alone [31, 66]. This agrees with the results observed in this study. They suggest low crystallization areas have higher levels of ferrous iron and thiosulfate ions going into solutions, which create local anodes and cathodes that attract cells via electrostatic interactions [31, 66].

No previous studies have been found on the bioleaching and bioflotation capabilities of *A. ferrooxidans* that have successfully compared mineral surface roughness in relation to the hydrophobicity of the sample and the presence and spread of cells on the surface. The above results suggest that the presence of *A. ferrooxidans* makes the pyrite surface significantly rougher in comparison with the HH medium control pyrite surface, and that this increase in roughness is proportional to the time spent in live culture. This agrees with previous studies that have observed via SEM that the mineral surface does appear to become rougher and covered in more leaching residue at longer exposure times [8, 15, 39, 41, 52, 56, 67]. Rohwerder *et al* specified that areas of low crystallization, which also favour dissolution of the mineral, are not limited to defects, but also on "clear" areas, which coincides with the formation of etch pits that have been observed with SEM in this study [66].

These results would suggest that the hydrophobicity of the pyrite exposed to HH medium would be similar to pyrite exposed to *A. ferrooxidans* for short exposure times (less than 24 h), as their measured roughness over this period is not significantly different [64]. These observations of the nature of the mineral surface must be compared to the measured hydrophobicity of the sample, to fully understand how *A. ferrooxidans* impacts the mineral surface in terms of its ability to depress or float pyrite.

4.3.4 Contact Angle

As was explored in Chapter 2, section 2.5.3, the hydrophobicity indicates whether a particle will be depressed or floated in a flotation cell, and how the presence of bacterial cells impacts the

hydrophobicity of a mineral and the time frame over which any changes occur is necessary for determining the nature of the interactions of the bacteria with the surface and relating to the suitability of their application to flotation. Two different methods of measuring contact angle, sessile drop and captive bubble, respectively, were applied to samples exposed to *A. ferrooxidans*, as was described in Chapter 3.

4.3.4.1 Sessile Drop Contact Angle

Sessile drop contact angle is commonly used to measure the hydrophobicity of surfaces, and as such was the first method explored as a means of measuring this property of pyrite upon exposure to *A. ferrooxidans*. The initial indicative results obtained using sessile drop contact angle, along with images of typical drops obtained using this technique, can be found in Figure 4.32, along with the hydrophobicity of polished pyrite.

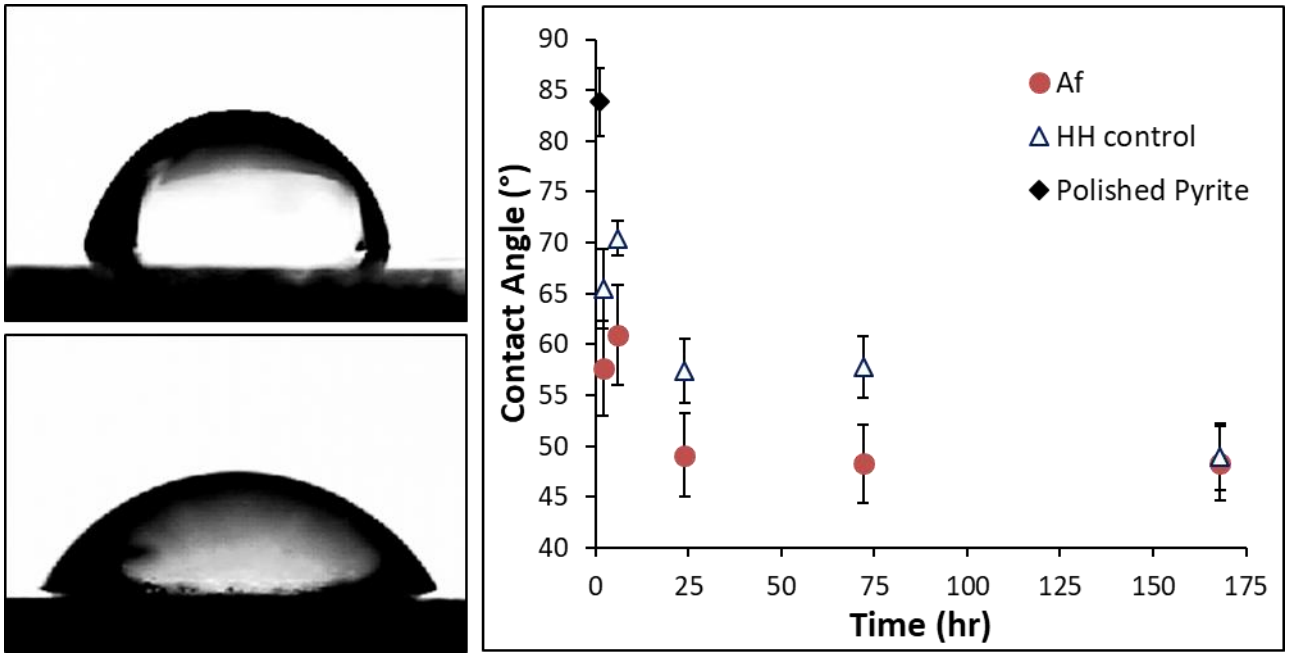

Figure 4.32: Water droplet on pyrite exposed to *A. ferrooxidans* for 6 h (Top left) and 168 h (Bottom left), Sessile drop contact angle of pyrite exposed to *A. ferrooxidans* (●), HH medium control (△), and polished pyrite (♦).

The sessile drop method gave a clear indication that at the early exposure times (less than 72 h) there was likely to be a significant difference in the hydrophobicity of pyrite exposed to *A. ferrooxidans* compared to the pyrite exposed to HH medium, although both showed a major decrease of over 15° in hydrophobicity compared to the polished pyrite.

However, there were found to be severe limitations with the application of sessile drop contact angle to this system, the most important of which is that the samples must be dried before being measured via this method. By drying the samples out before analysis, measurements are no longer representative of how the mineral surface will behave during flotation, where air is interacting with

minerals in solution as opposed to water being dropped onto dry mineral [68]. There is also the possibility that any bacterial cells or excretions are altered by the drying process, with cells lysing upon being dried, which may be resulting in a false positive result in the extension to which the hydrophobicity is altered, and confusing whether it is the cells or the cell excretions altering the contact angle [69]. To gain a more *in situ* measurement of how *A. ferrooxidans* is altering the hydrophobicity of the mineral, the captive bubble method of obtaining contact angle data was employed.

4.3.4.2 Captive Bubble Contact Angle

Captive bubble contact angle is a method by which the hydrophobicity of the mineral surface can be measured without drying the samples out between exposure and analysis. This allows any adhered cells to remain on the surface without lysing, and for any excretions to maintain their hydrated states during measurement. This means that the changes in hydrophobicity measured by this method will more closely resemble the behaviour of air bubble interactions with mineral in a flotation cell, giving a more realistic impression of the effect microorganisms and their excretions in altering mineral surface properties. Figure 4.33 shows the average five advancing and receding contact angles each pyrite sample, performed in triplicate, with the error bars representing the standard deviation of the samples measured.

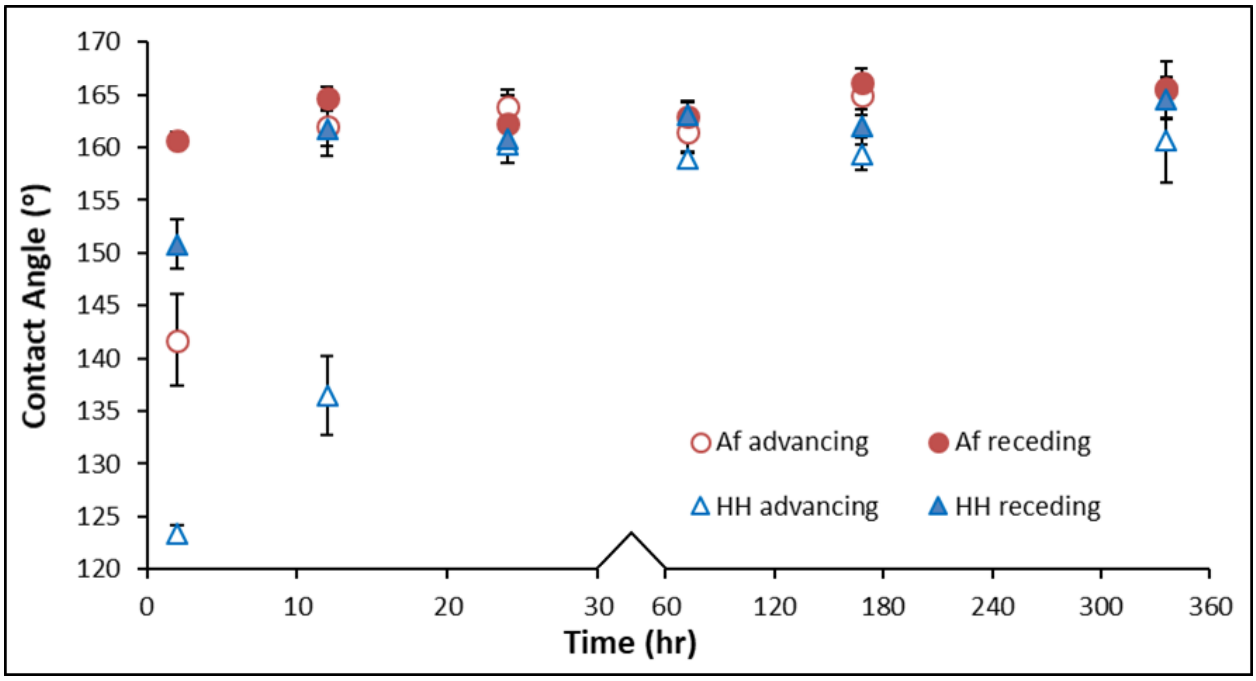

Figure 4.33: Advancing captive bubble contact angle of pyrite exposed to *A. ferrooxidans* (○) and HH medium (△). Receding captive bubble contact angle of pyrite exposed to *A. ferrooxidans* (●) and HH medium (▲). Error bars represent sample standard deviation in the contact angle measurements.

Pyrite samples exposed to *A. ferrooxidans* are less hydrophobic than the HH medium control at early stages of exposure, showing the most a significant decrease in hydrophobicity at 2 h of 9° to 18°. After 12 h, the pyrite exposed to *A. ferrooxidans* shows similar receding angle values to the HH control, however the advancing angle is over 25° greater. This indicates the pyrite exposed to *A. ferrooxidans* is more homogenous at this period of exposure, as indicated by the decreased hysteresis over a period with no significant difference in roughness, as determined by AFM in the previous section (section 4.3.3). After 24 h, the contact angles are similar for both biotic and abiotic pyrite, with the contact angle appearing to remain stable for 336 h.

Although the mineral recovery in a flotation system is dependent on particle size, a measured difference contact angle of as little as 3° can indicate an increase in recovery of up to 18% [70]. These results suggest that an exposure of as little as 2 h could promote the depression of pyrite by *A. ferrooxidans*, while longer periods of exposure showed no significant separation of contact angle compared to the control sample. This suggests the hydrophobicity is improved by the chemistry on the surface rather than the roughness, which the AFM results suggest is identical between biotic and abiotic samples at early exposures. This also suggests the presence of thick biofilm is not necessary for significant changes in hydrophobicity of the pyrite, as the SEM showed little cell coverage after 2 h. This suggests the interaction of *A. ferrooxidans* may be driven by either the indirect or indirect contact mechanisms, or potentially a combination of both, and that the nature of the interaction may be changing over the course of exposure. More research in this area is required to determine the optimal period of exposure for the highest degree of wettability of the pyrite surface, and to apply this optimised exposure period to microflotation studies on pure and more complex ores.

The literature in this area varies from noting the importance of hydrophobicity to flotation practices, and measuring the wettability of cells themselves, with very little presented linking the mineral surface properties to the presence of the bacteria. Studies that have analysed cells in isolation have used air-dried cells [71-73], or used organic solvents and looked at phase preference, although this is not usually accompanied by evidence that the cells survive the process [72, 74, 75].

Several previous studies have also found *A. ferrooxidans* reduces the hydrophobicity of pyrite, providing evidence as flotation results, or on air-dried samples [4, 15, 71, 75]. While these studies agree with the results presented here, none present control experiments or explore the chemical properties of the surface or remove the effects of topography or particle size to relate the surface chemistry to the wettability. Only Liu *et al* provide some images of their pyrite, but not of the surfaces examined by contact angle; only air-dried powdered samples were examined [15].

No previous studies have been found that comprehensively compares chemical analysis with physical properties of pyrite under exposure to *A. ferrooxidans*, and apply captive bubble to this system. For more detailed analysis of the impact of *A. ferrooxidans* on the hydrophobicity of the surface, the surface chemical composition must be investigated. This will enable the determination of why the contact angle results do not reflect the surface imaging and topography results obtained previously. This chemical analysis will be explored using PEEM and ToF-SIMS in the following sections.

4.3.5 Photoelectron Emission Microscopy

Photoelectron Emission Microscopy (PEEM) is a surface-sensitive spectromicroscopy technique that provides surface topography as well as chemical images taken at specific energies. Combining the images collected using PEEM with Near-edge X-ray Absorption Fine Structure (NEXAFS) spectra provides qualitative information on chemical bonding and element oxidation sates of the elements on the surface by taking images of the same sample at different energies. PEEM allows the use of a range of different energy X-rays to collect images of the surface at discrete energies, giving this technique a great advantage where one incident X-ray energy value must be set. A summary of signal assignment for Fe L-edge and C K-edge NEXAFS can be found in Table 3.5 and Table 3.6, respectively, in Chapter 3.

In the pyrite Fe L-edge NEXAFS spectra in Figure 4.34, the Fe L_3 peak is the most prominent feature, seen as two overlapping peaks due to transitions to the Fe 3*d* eg at 707.6 eV (A) and to Fe 3*d* states hybridized with S 3*p* at 708.5 eV (B) [76, 77]. Two characteristic peaks at 712-715 eV (C) are due to transitions to S 3*p* states hybridized with Fe 4*s* and 4*p* states in pyrite, while the intense Fe L_2 peak resides at 719.9 eV (D) [76-79]. Iron oxidation products including hematite [80-82], magnetite [81], goethite [81, 82], and wüstite [81] result in transitions of Fe 2*p* to Fe 3*d* states hybridized with O 2*p* states that overlap the pyrite Fe-S contributions between 707.8-710.5 eV. For the pyrite samples exposed to HH medium control shown in Figure 4.34, there is no discernible change in the features of the Fe L-edge spectra, from 2 to 168 h.

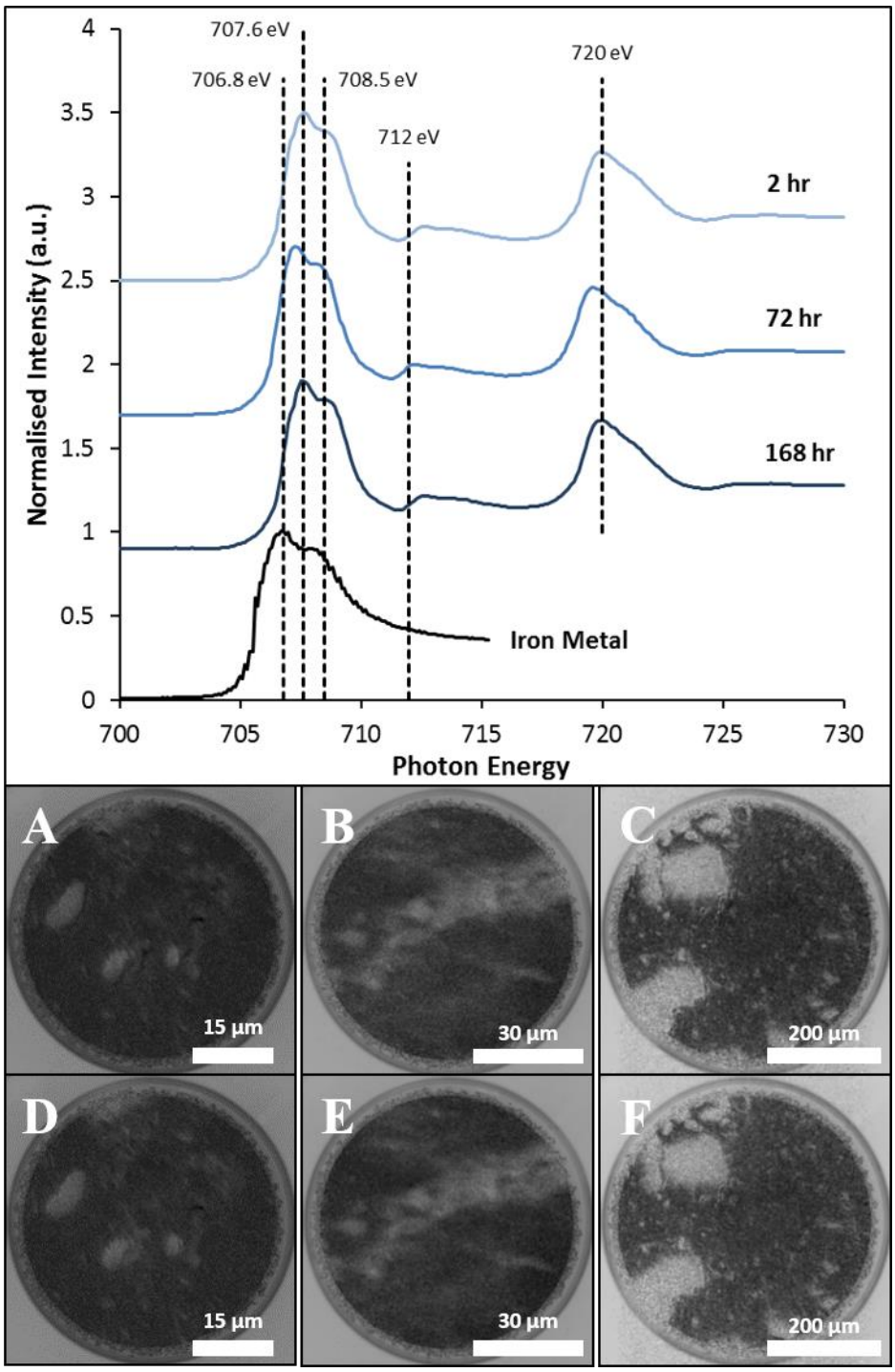

Figure 4.34: Fe L-edge NEXAFS spectra of pyrite exposed to HH medium control solutions (top), and single energy PEEM images of pyrite. After 2 h of exposure (A) unaltered pyrite, 707.6 eV; (D) iron (oxy)hydroxides, 708.5 eV; after 72 h (B) unaltered pyrite; (E) iron (oxy)hydroxides; and after 168 h (C) unaltered pyrite; (F) iron (oxy)hydroxides.

The pyrite surface after exposure to HH medium appears heterogeneous over the course of exposure, indicating areas differ in iron concentration. The lighter regions indicate a higher concentration of iron species, while the dark regions are iron deficient. These dark regions are likely due to the formation of sulfur-rich and oxygen-rich species that form when pyrite is exposed to both air and acidic media, obscuring the bulk pyrite iron [83-85]. The 707.6 eV and 708.5 eV images at both periods of exposure are identical, indicating no iron oxide or (oxy)hydroxide species have

formed on the surface, with both the 707.6 eV and 708.5 eV signals due to pyrite rather than secondary mineral formation. There is no indication of increased oxidation of the control over the course of exposure, which supports the observations made using the NEXAFS spectra.

The NEXAFS spectra obtained for pyrite shown in Figure 4.34 agree with those obtained by Goh *et al* [82], and are consistent with previous studies that used synthetic and natural pyrite samples displaying unalter pyrite [76, 77].

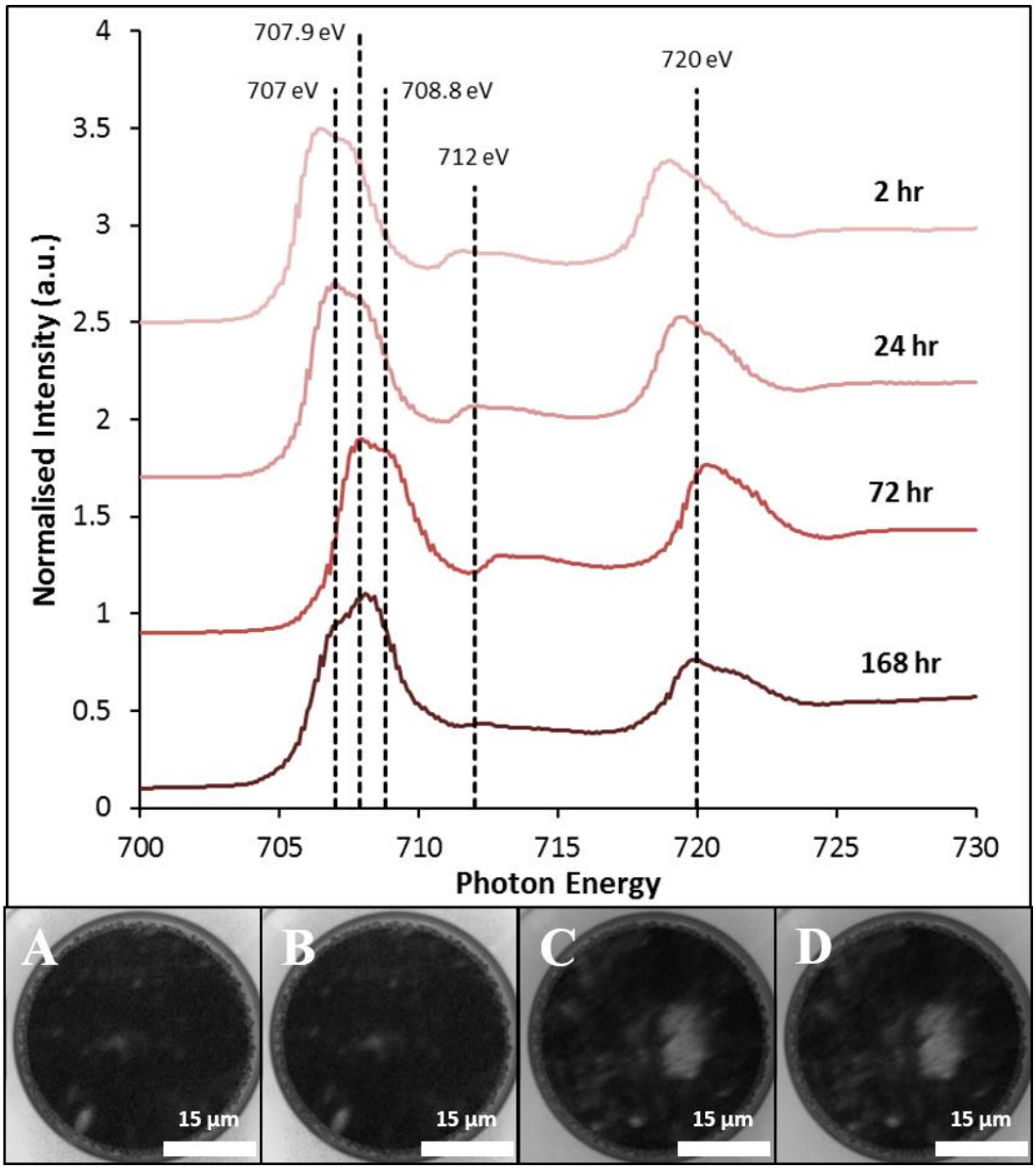

Figure 4.35: Fe L-edge NEXAFS spectra of pyrite exposed to *A. ferrooxidans* (top) and the corresponding single energy PEEM images of pyrite. After 2 h of exposure (A) unaltered pyrite, 706.5 eV; (B) iron (oxy)hydroxides, 707.5 eV. After 24 h of exposure (C) unaltered pyrite, 707 eV; (D) iron (oxy)hydroxides, 707.9 eV.

The pyrite that was exposed to bacteria, shown in Figure 4.35, show changes in spectral features between earlier exposure times and 168 h of exposure. The peak at (B) corresponding to the Fe 3*d* states hybridized with S 3*p* and the overlapping iron oxides and oxyhydroxides previously

mentioned, increases over the course of exposure [76-79]. The two peaks at 712-715 eV (C) corresponding to bulk pyrite decrease over time, indicating an increase in iron oxidation products occurring on the surface [82, 86]. The images shown in Figure 4.35 of pyrite at 2 and 24 h are all very dark, indicating that the iron is not a strong presence on the surface, and that both transitions appear in the same regions with little noticeable variation at all exposure times.

Figure 4.36 shows the C K-edge NEXAFS spectra of pyrite exposed to HH medium for 2, 72 and 168 h. The peak at 285.1 eV can be attributed to π* C=C and/or π* C-H [87, 88]. The large, broad peak at 292 eV can be attributed to π* C-C and σ* C-C, respectively [88]. Peaks at 287.6 eV and 288.8 are due to σ* C-H [89-91].

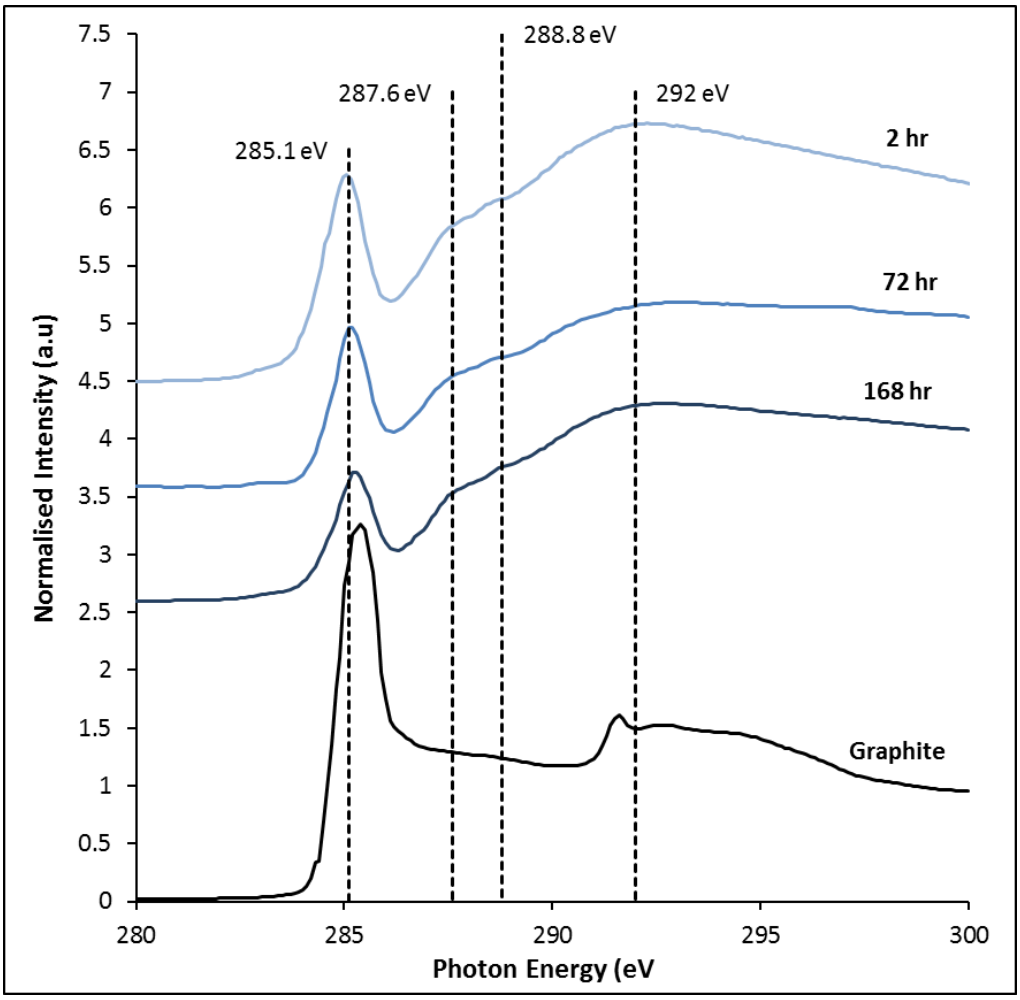

Figure 4.36: C K-edge NEXAFS spectra of pyrite exposed to HH medium for 2, 72 and 168 h, and the spectrum of graphite used for sample calibration. The transitions observed on pyrite exposed to HH medium are from C 1s to π* C=C and C-H at 285.1 eV, π* C=N and σ* C-H at 287.6 eV, carbonate 292 eV.

There are two main reasons why there is little change in the C K-edge spectra over time. Firstly, there is a possibility of radiation damage occurring on the surface, which has been documented in previous NEXAFS studies as characteristically intense C=C peaks at 285.1 eV, which occur as C-H bonds are dehydrogenated [92, 93]. Secondly, the other peaks are all indicative of aliphatic carbon,

which is highly likely to be adventitious due to the exposure to the atmosphere prior to loading the sample into the vacuum chamber, and is an unavoidable hazard of measuring carbon with this technique [94, 95].

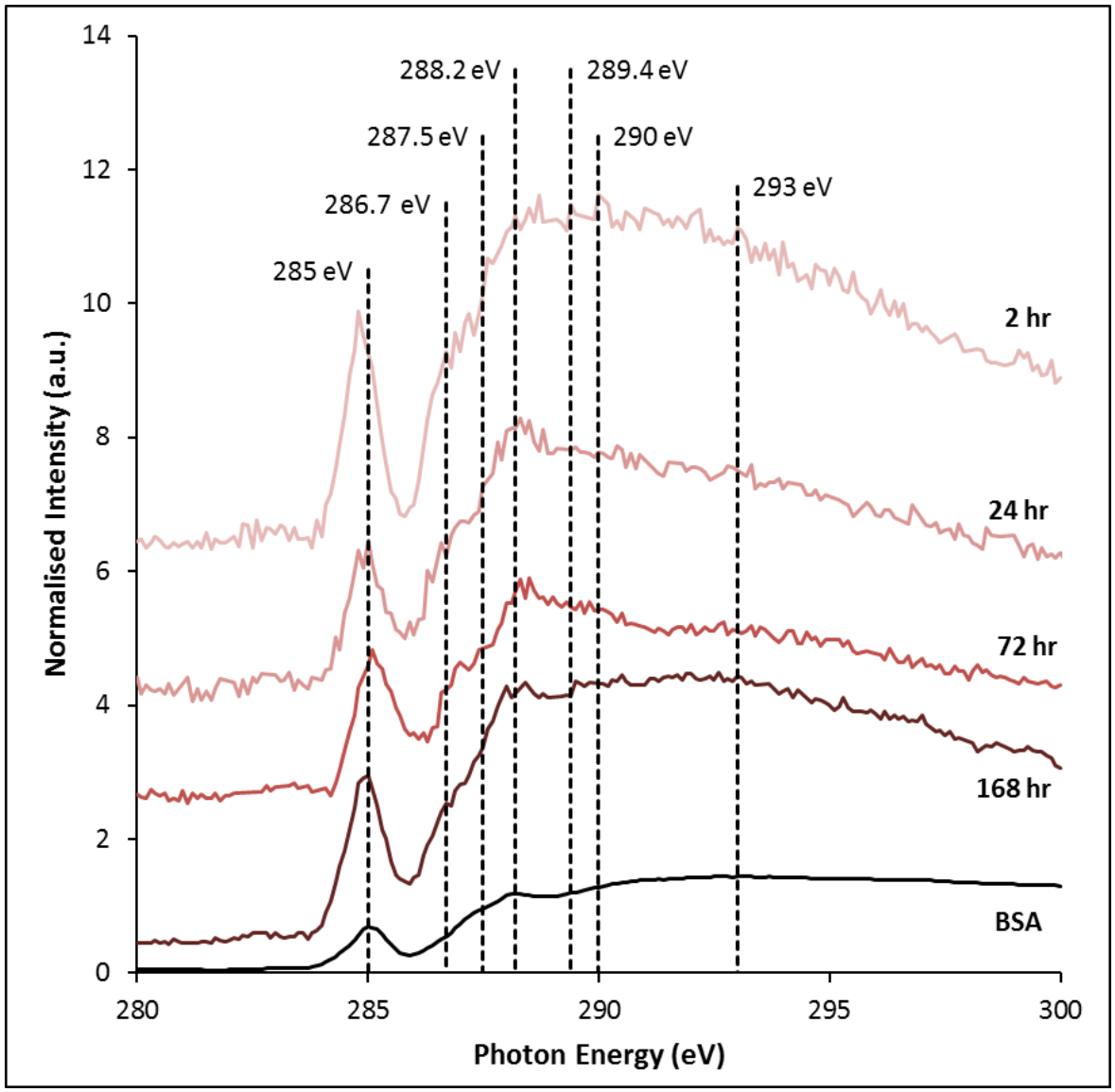

Figure 4.37: C K-edge NEXAFS spectra of pyrite exposed to *A. ferrooxidans* for 2, 24, 72 and 168 h, and the spectrum of bovine serum albumin (BSA) used for calibration. The transitions observed on pyrite exposed to *A. ferrooxidans* are from C 1s to π* C=C and C-H at 285 eV, π* C=N and σ* C-H at 286-287.7 eV, π* C=O at 288.2-288.7 eV, σ* CNH, σ* CH or π* C=N at 289.4 eV and σ* C-C at 292-294 eV.

Figure 4.37 shows the stacked C NEXAFS spectra of pyrite exposed to *A. ferrooxidans* for 2, 24, 72 and 168 h, and the changes in the carbon species occurring over those exposure times. Every C K-edge NEXAFS spectrum of the pyrite samples exposed to *A. ferrooxidans* exhibits a peak at 285 eV due to C 1s transitions to π* C=C. Peaks between 286 eV and 287.7 eV can be attributed to both the C 1s transitions to π* C=N and σ* C-H [87-90, 96-98]. The intensity of the π* C=C peak at 285 eV suggests that radiation damage may also be occurring, reducing the signal from C-H and C-C peaks between 286-287.7 eV and 292-294 eV [92, 93]. The presence of carbonate signal at 290 eV is also

an indicator of possible radiation damage, as carboxyl and carbonyl groups are reduced to form carbonate species on the surface, where there is no source of carbonate in the HH medium solution [90, 92, 93]. The π* C=O peak after 2 h occurs between 288.4-288.7 eV, suggesting that the peak is due to more carboxylic-type character common in lipids and biopolymer, that are likely to decrease the hydrophobicity of the surface at this stage [89, 97-100]. The π* C=O peak occurs at 288.2 eV after 24 h and remains there for the remainder of exposure, suggesting this is due to the π* C=O bonds in amides of protein [88-91, 96, 98, 100]. The protein-type π* C=O peak is commonly associated with the signal at 289.4 eV, which can be attributed to C 1s transitions to σ* CNH, σ* CH or π* C=N, amide functionality in proteins and nucleic acids [88, 89, 91]. After 168 h of exposure to bacteria, the shift in the π* C=O peak at 288.2 eV is also accompanied by an apparent increase in intensity in σ* C-C at 292-294 eV. This indicates a further shift towards polymeric substances, fatty acids and nucleic acids being more common on the surface as biofilm starts to build [88-90]. These components provide a reaction space in which ferrous iron can be oxidised to ferric iron without the need for bacterial attachment on the surface, suggesting a combination of the indirect and indirect contact mechanisms is likely to govern the interaction of *A. ferrooxidans* with the pyrite surface [30, 48, 101].

Several papers have previously studied bioleaching of minerals using *A. ferrooxidans*, although many of them only investigate the mineral surface using NEXAFS, neglecting the carbon of the cells themselves [39, 102-104]. Mitsunobu *et al* collected NEXAFS spectra of *A. ferrooxidans* cells using STXM that agree with the spectra collected in this study, noting that the protein signal at 288.2 eV was the most intense, with shoulders at approximately 287 eV and 289.4 eV [59]. Other studies have used the STXM technique to collect carbon NEXAFS of other types of cells, however the spectra indicate different composition to *A. ferrooxidans* cells, extracellular polymeric substances or background carbon, making direct comparison challenging [89, 100, 105]. This study shows significant shifts of over 288.4 eV to 288.2 eV in the π* C=O peak in the C K-edge NEXAFS of *A. ferrooxidans* over time, suggesting polysaccharide and fatty acid compounds are produced at early exposure stages, with protein and nucleic acid compounds being produced at longer exposure times. As biofilm begins to form on the surface, as was observed from the SEM images, more polymeric substances and fatty acids were again produced by the cells.

These changes do not correlate with the AFM results, which suggest that the hydrophobicity of the pyrite exposed to *A. ferrooxidans* should be greater than the hydrophobicity of the control, as correlates with the roughness increasing [64]. This suggests the effects of the chemical species on the surface are greater than those of the physical changes to the surface brought about by the bacteria.

4.3.6 Time of Flight – Secondary Ion Mass Spectrometry

Time of Flight – Secondary Ion Mass Spectrometry is semi-quantitative surface analysis that provides information of the surface chemistry by ablating atoms and molecular fragments from the surface and separating them by mass-to-charge ratio. The frequency with which an ion is detected is dependant not only on how much of that species there is on the surface, but also on the ability of the ion to leave the surface and the chemical environment of the surface [95]. While it is not possible to positively identify individual compounds in this mixture, a "fingerprint" can be obtained for each sample, and associations between fragments can be made by analysing the fragment images of the surface and assessing associations of the various species being released by the surface [95, 106-108]. This may lead to the identification of the types of molecules on the surface and relating these species to the physical effects on contact angle. The plots shown here are an indication of the proportion of each fragment on the mineral surface. As the samples were analysed using the same parameters, the intensities of the peaks can be used as a measure of the variation between samples. Figure 4.38 shows the positive ions on the surface of bare polished pyrite and pyrite exposed to *A. ferrooxidans* and HH medium for 2, 24, 72 and 168 h.

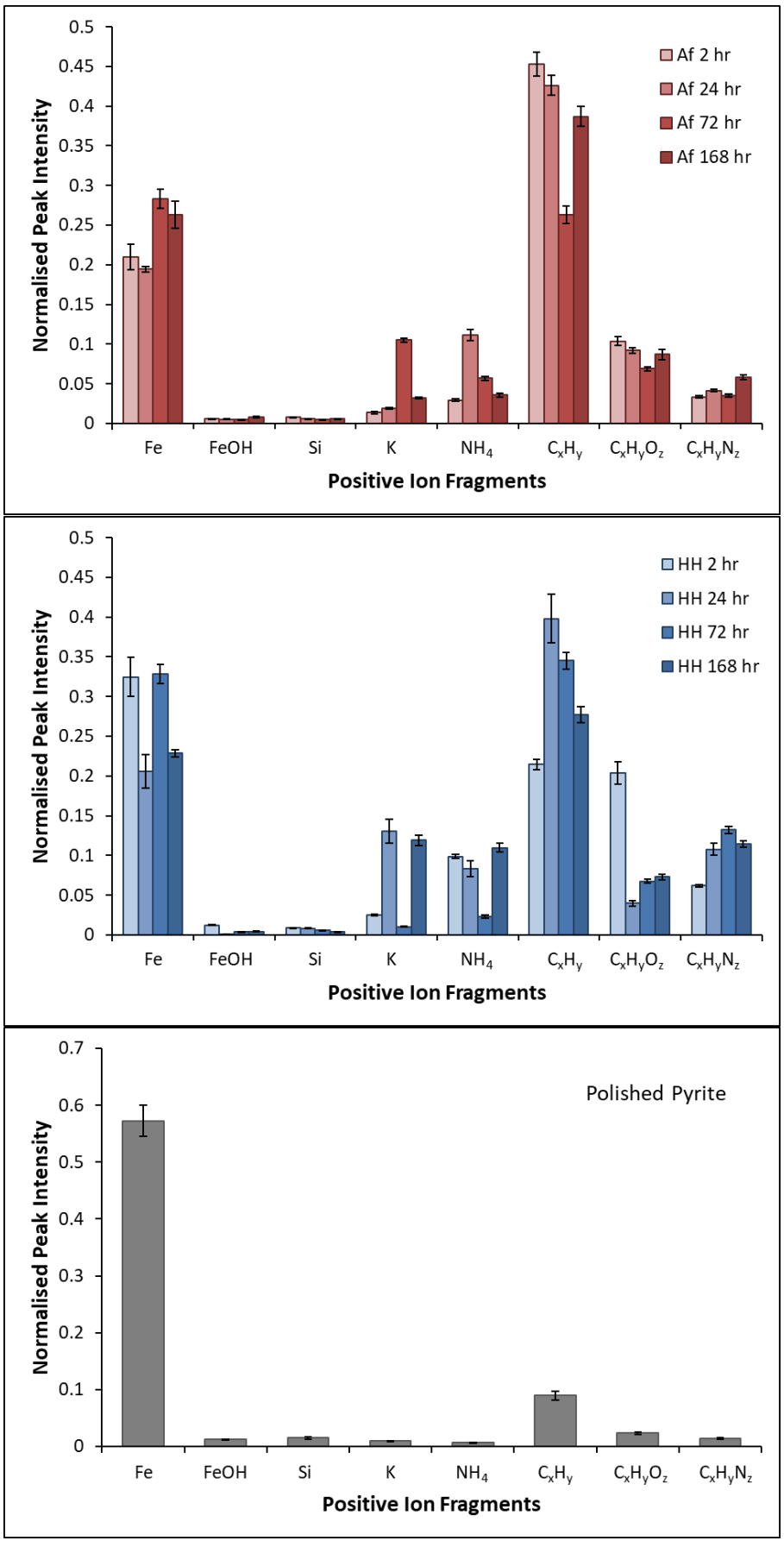

Figure 4.38: Average normalised peak intensities of positive fragments of pyrite exposed *A. ferrooxidans* (top) for 2, 24, 72 and 168 h, pyrite exposed to HH medium (middle) for 2, 24, 72 and 168 h, and bare polished pyrite (bottom).

The fragment profile of pyrite exposed to HH medium is dominated by Fe^+ and short chain $C_xH_y^+$ ($x \leq 6$) fragments over the course of the exposure. The proportion $C_xH_yN_z^+$ ($x \leq 5$, $z \leq 2$) fragments appears to increase over the course of exposure, but never as great in proportion as the Fe^+ and $C_xH_y^+$ fragments. There is an unexpectedly high proportion of $C_xH_yO_z^+$ ($x \leq 4$, $z \leq 2$) fragments after 2 h of exposure, which may be due to sample contamination, as the remaining samples are less than half as intense, increasingly only slightly over the course of exposure. The bare polished pyrite is dominated even more significantly by Fe^+, with the carbonaceous fragments consisting of less that 20% of the positive ions shown here. This is likely due to adventitious carbon, as the surface is exposed to the atmosphere both during the polishing process and prior to analysis.

The positive ion signals confirm that exposure of pyrite to *A. ferrooxidans* results in significant modification of the surface chemical speciation. The fragments dectected on pyrite exposed to *A. ferrooxidans* for are also dominated by the $C_xH_y^+$ and Fe^+ fragments. The Fe^+ significantly increases at 72 h and remains constant at 168 h when exposed to *A. ferrooxidans*, while the Fe^+ is variable for the controls. After 2 h, the proportion of $C_xH_y^+$ detected was significantly greater than the control at 2 h. A comparison of samples exposed to *A. ferrooxidans* over time indicates the formation N-containing organic species at 168 h. These results suggest the production of proteins in the biofilm at this time, and is supported by C K-edge NEXAFS results.

Because the medium contains the salts ammonium sulfate and potassium dihydrogen phosphate, the NH_4^+ and K^+ fragments can be expected on the surface, as HH medium salt precipitates. This is further supported by the very low amount of these species found on the surface of polished pyrite. The NH_4^+ fragment is therefore not on its own a reliable indicator of whether proteins are present on the surface. There is some variation of both the NH_4^+ and K^+ fragments between over the course of exposure, but this is likely due to variation in the amount of ammonium sulfate and potassium dihydrogen phosphate medium salts crystallising on the surface. Generally, the overall proportion of these fragments on the surface is lower on pyrite exposed to *A. ferrooxidans* compared to the controls. There are consistently low proportions of both Si^+ and $FeOH^+$ on the surface of all samples, indicating the presence of some silicate inclusions, and little to no jarosite formation on the surface for. This agrees with the SEM micrographs and the XRD data presented in sections 4.3.2 and 3.2, respectively.

To get a complete picture of the surface composition, and to complement the chemical species analysis that previous techniques were unable to fill, negative ions were also examined for all samples. Figure 4.39 shows the complementary negative fragments and elements of interest and significance collected by ToF-SIMS on pyrite exposed to *A. ferrooxidans* and HH medium for 2,

24, 72 and 168 h. The inset plots in Figure 4.39 show the sulfur species on the surface normalised to the total S^- detected on the surface, showing the proportion due to each sulfur species.

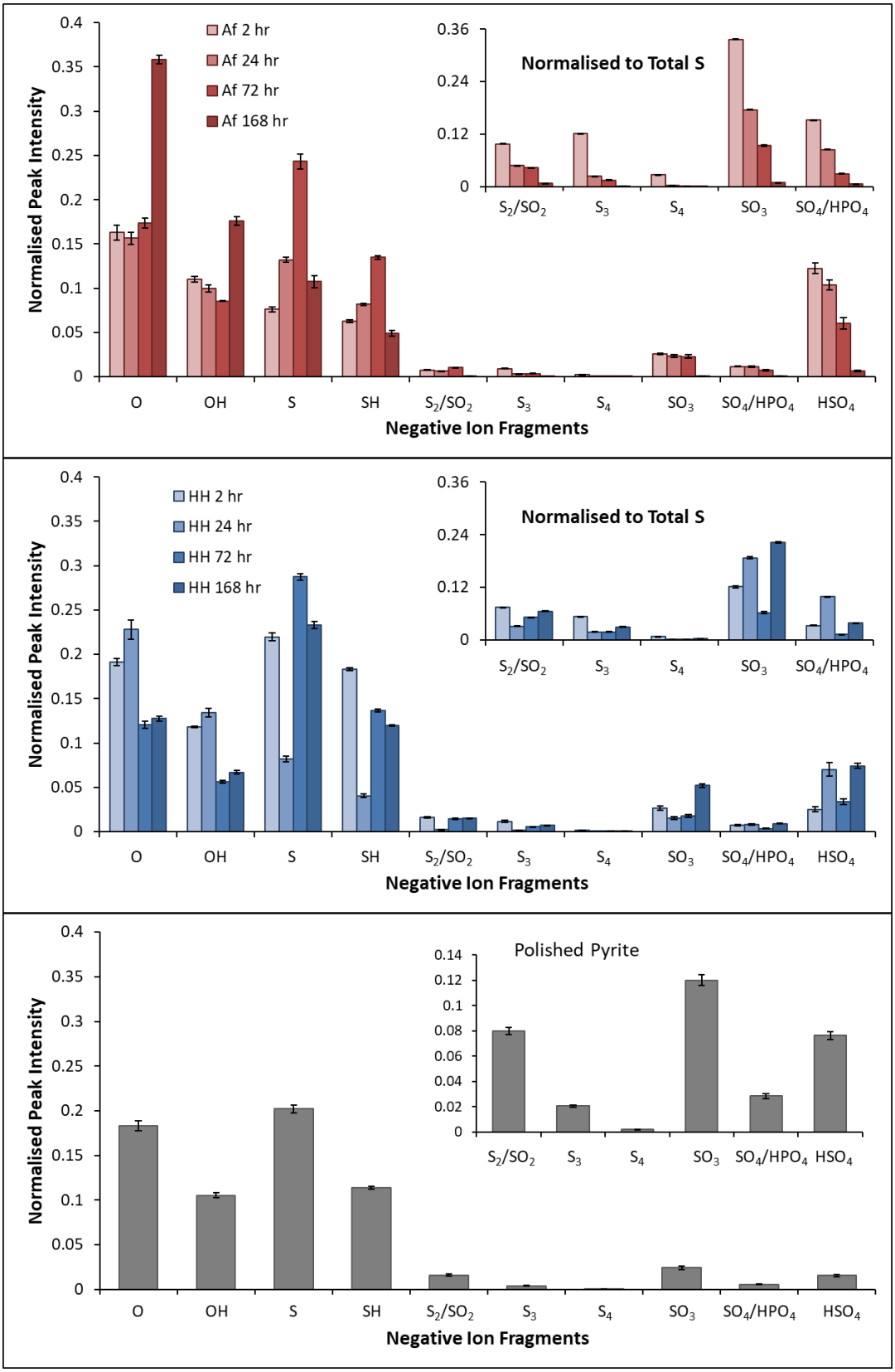

Figure 4.39: Average normalised peak intensities of negative fragments of pyrite exposed *A. ferrooxidans* (top) for 2, 24, 72 and 168 h, and pyrite exposed to HH medium (middle) for 2, 24, 72 and 168 h, and bare polished pyrite (bottom).

The negative ion fragments suggest that there is some oxidation of surface to form S_2, S_3 and sulfur-oxy species during exposure to HH medium and *A. ferrooxidans*. The S^- and SH^- fragments [109] occur with high frequency across all samples. Both SO_3^- and SO_2^- are known products of the oxidation process for sulfur in pyrite [110, 111]. The pyrite exposed to HH medium for 2 h shows the greatest proportion of hydrophobic polysulfide fragments, which agrees with the contact angle results that show this is the most hydrophobic surface. For longer periods of exposure, the pyrite is more sulfur-rich, which explains the slight decrease in contact angle after 24 h, however the high proportion of carbon-type fragments on the surface found in the positive spectra, and the decrease in proportion of polysulfide species are the reason the surface retains more hydrophilic character. The HSO_4^- and HPO_4^- / SO_4^- fragments follow the same trend as the K^+ fragment, with some similarity to the NH_4^+ fragment trend, agreeing with the positive ion results that show some ammonium sulfate and potassium dihydrogen phosphate crystals occurring on the surface. The bare polished pyrite shows lower proportions of polysulfide fragments and oxidised sulfur fragments that samples exposed to either abiotic medium or culture, however the high proportion of O^- and OH^- on the surface show the surface is still very reactive in air, oxidising rapidly, as has been observed in previous studies [112, 113].

The fragments detected on pyrite after exposure to *A. ferrooxidans* for 2 h have a much higher proportion of oxygenated sulfur species, O^- and OH^- on the surface compared to the control, agreeing with the contact angle results that suggest a less hydrophobic surface. Over the first 72 h of exposure to *A. ferrooxidans*, the proportion of S^- and SH^- increases. This agrees with the contact angle results that show the surface has become slightly more hydrophobic at this period, although the proportion of hydrophilic fragments still greatly outweighs the hydrophobic character of the surface at this point. It also aligns with the inflection point of the sulfur and ferrous iron concentrations in solution beginning to increase and decrease, respectively. This indicates a change in cell behaviour is occurring around this time, such as the change in preferred food source from S to Fe^{2+} postulated by Brunner *et al* [14]. After 168 h of exposure, the proportion of O^- and OH^- on the surface is the largest of any previous samples. This agrees with the Fe L-edge NEXAFS results that suggest the pyrite is most oxidised at this period of exposure. The lower detection of S species at the surface the samples exposed to *A. ferrooxidans* coupled with the higher $C_xH_y^+$ speciation indicates the formation of an organic over-layer due to biofilm formation. These results show that the O^- and OH^- ions dominate the negative spectra, and overlap strongly with hydrocarbons produced by bacteria, in agreement with the findings of Pradier *et al* [114].

Carbon signals of low molecular weight can be expected on the surface as adventitious carbon, and there is no way to isolate or remove this contamination from the analysis. This makes low

molecular weight fragments difficult to use for analytical purposes, and so the use of the larger molecular weight fragments is more diagnostic of bacteria and their excretions on the mineral surface. Larger molecular weight fragments could be used as a "fingerprint" region for biomaterials, as has been suggested in literature [95, 106-108], although identifying exact molecular structure from fragments of this size is not possible when analysing a complex matrix of compounds. Figure 4.40 shows the large molecular mass positive fragments collected by ToF-SIMS on pyrite exposed to *A. ferrooxidans* and HH medium for 2, 24, 72 and 168 h.

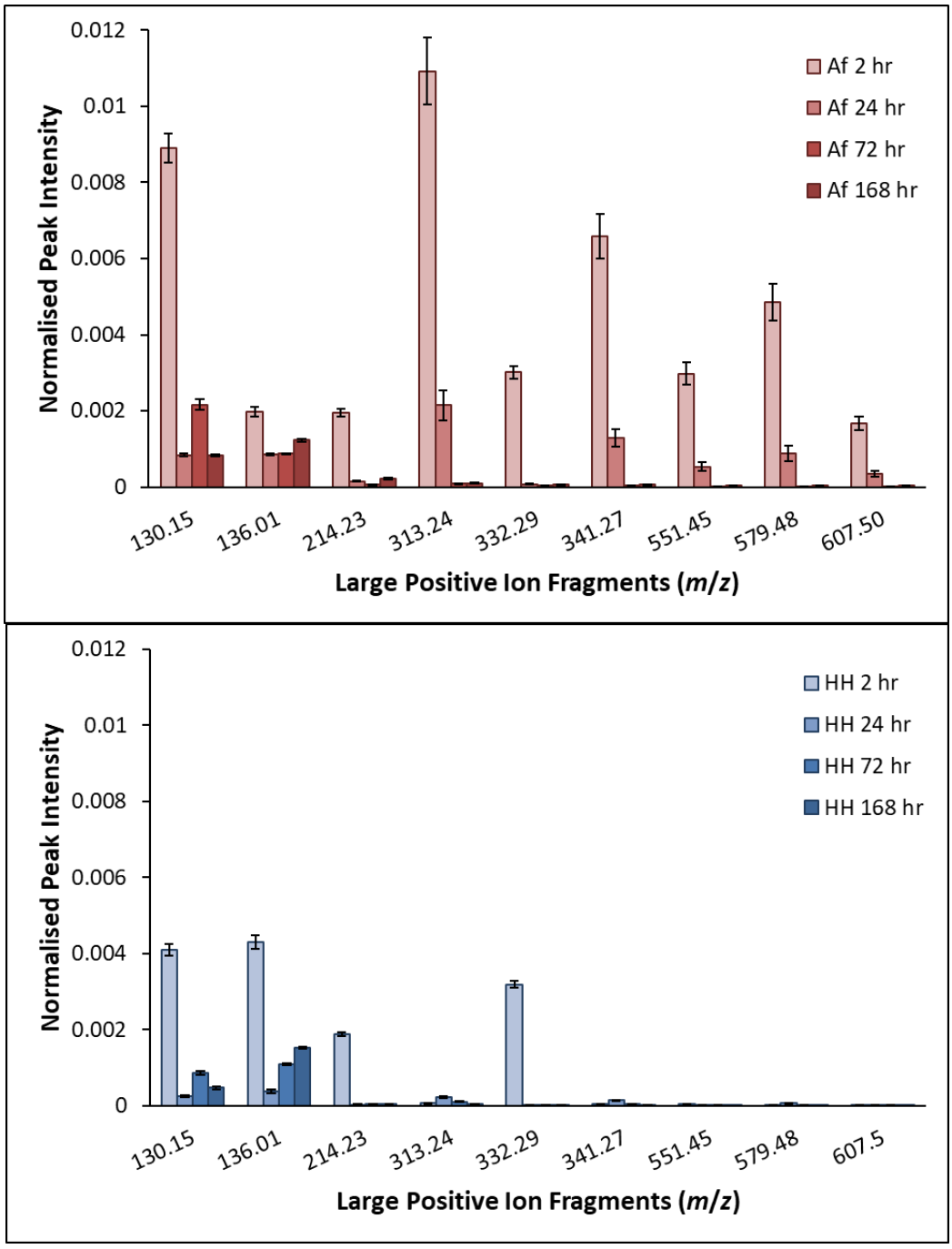

Figure 4.40: Average normalised peak intensities of large molecular weight positive fragments of pyrite exposed *A. ferrooxidans* (top) for 2, 24, 72 and 168 h, and pyrite exposed to HH medium (bottom) for 2, 24, 72 and 168 h.

As can be seen from this plot, initially, there are multiple large molecular weight fragments on the pyrite surface after exposure to *A. ferrooxidans* for 2 h. The fragment at 332.29 has been observed in previous lipid studies but not identified as a lipid fragment [115]. The remaining fragments have variously been identified as lipid or carbohydrate fragments by previous studies looking specifically at those structures, with many of these fragments identified as major components of several lipid and carbohydrate structures [106, 115-119]. The occurrence of these fragments indicates that large hydrophilic polysaccharide and lipid fragments are present and being produced very shortly after inoculation, which is consistent with both the PEEM and contact angle results presented in previous sections [9, 10, 120]. In contrast, the control pyrite shows little to no polysaccharide or lipid fragments over the course of the experiments, except for the fragment with a molecular weight of 332.29, the identity of which it is not possible to ascertain. The fragments at 130.15 and 136.01 have been identified as amino acid fragments [121-123], and may be adventitious, which is why the ion proportions follow the same trend for both biotic and abiotic experiments. This is consistent with the PEEM and low molecular weight ToF-SIMS which suggest the presence of some contamination after 2 h of exposure. The bare polished pyrite showed negligible larger molecular weight fragments, which is agrees with the previous results showing a clean pyrite surface. These results suggest the presence of EPS produced by *A. ferrooxidans* occurring on the pyrite surface after 2 h, in agreement with the results presented in the previous sections. This suggests the presence of functional groups in components of EPS that complex with ferrous iron, providing a reaction space for iron oxidation without the need for bacterial attachment to the surface in early stages of exposure [124, 125]. This suggests the indirect contact mechanism is occurring, with EPS coating the surface of the mineral prior to cell attachment and biofilm formation.

Large molecular weight negative fragments are not explored as extensively as positive fragments, but the those observed in this study support the conclusions of the positive ion fragments, indicating larger molecular weight molecules are present in early stages of attachment in statistically significant amounts and decrease as exposure continues. The average normalised peak intensity of large molecular weight negative fragments of pyrite exposed to *A. ferrooxidans* and HH medium for 2, 24, 72 and 168 h is shown in Figure 4.41. As was the case with the large molecular weight positive ion fragments, there were negligible large molecular weight negative ion fragments detected on the bare polished pyrite surface.

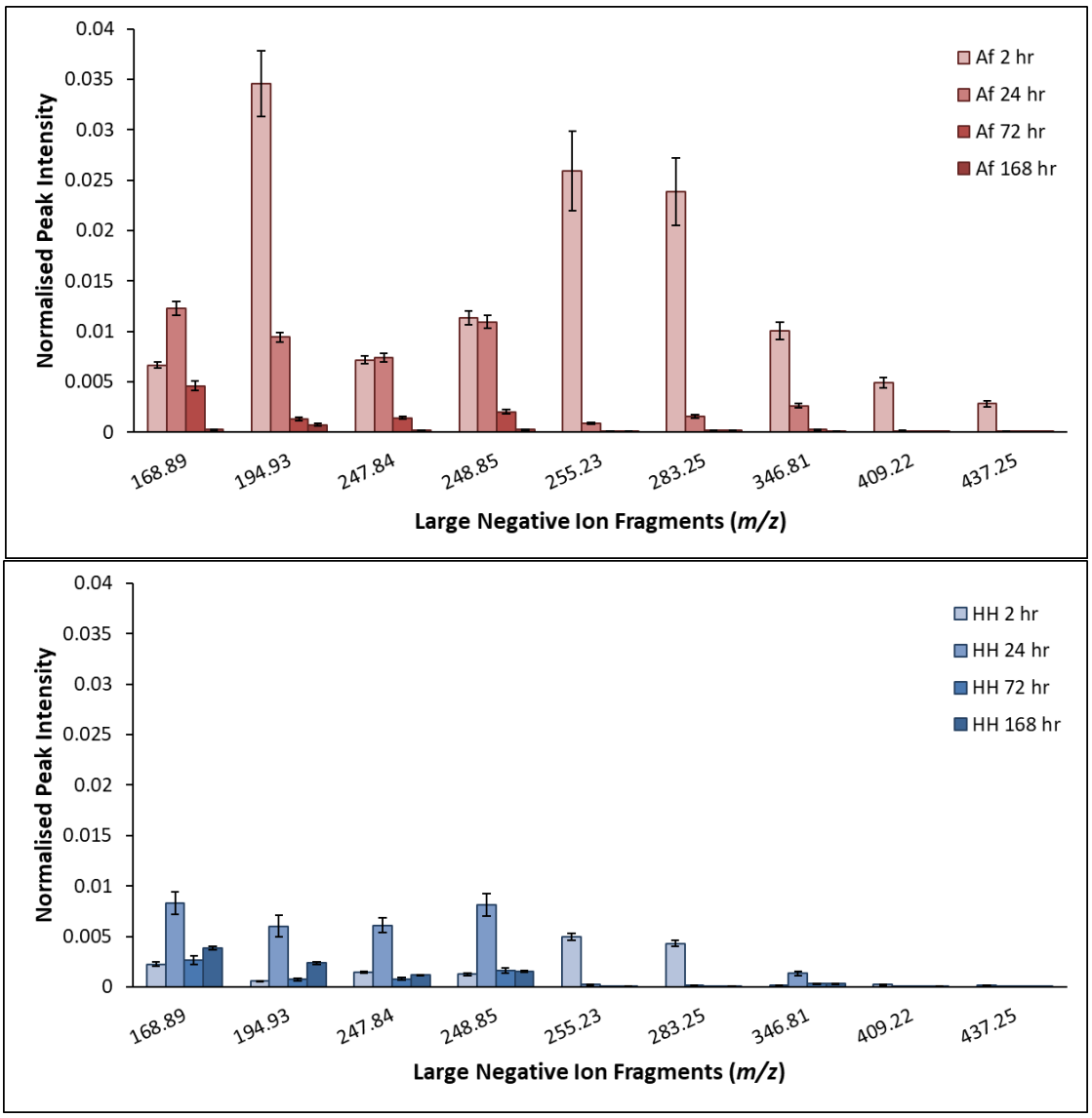

Figure 4.41: Average normalised peak intensities of large molecular weight negative fragments of pyrite exposed *A. ferrooxidans* (top) for 2, 24, 72 and 168 h, and pyrite exposed to HH medium (bottom) for 2, 24, 72 and 168 h.

As was seen in the positive ion spectra, initially there is a greater proportion of large molecular weight fragments after pyrite was exposed to *A. ferrooxidans* for 2 h, the frequency of which decreases after 24 h. The fragments with molecular masses 255.23 and 283.25 have both been identified as fatty acid or carbohydrate fragments in previous studies [115, 117-119, 126]. As the remaining fragments, which have not previously been identified, follow the same trend, it is not unreasonable to suggest that these fragments are also due to polysaccharides. The presence of the *m/z* 255.23 and 283.25 fragments on the control at 2 h is consistent with the potential contamination identified by the low molecular weight fragments identified in this study. These results concur with the positive ion spectra, suggesting a significant EPS presence on the pyrite surface after 2 h.

The association of the species on the surface is also possible with ToF-SIMS, and can be used to identify associations that are not apparent simply by looking at the collected spectra. Figure 4.42

shows examples of the positive ion images of pyrite exposed to *A. ferrooxidans* for 2 h. The ions were selected to show association of ions related to pyrite, medium salt precipitates, hydrocarbons and potential cell excretions on the pyrite surface.

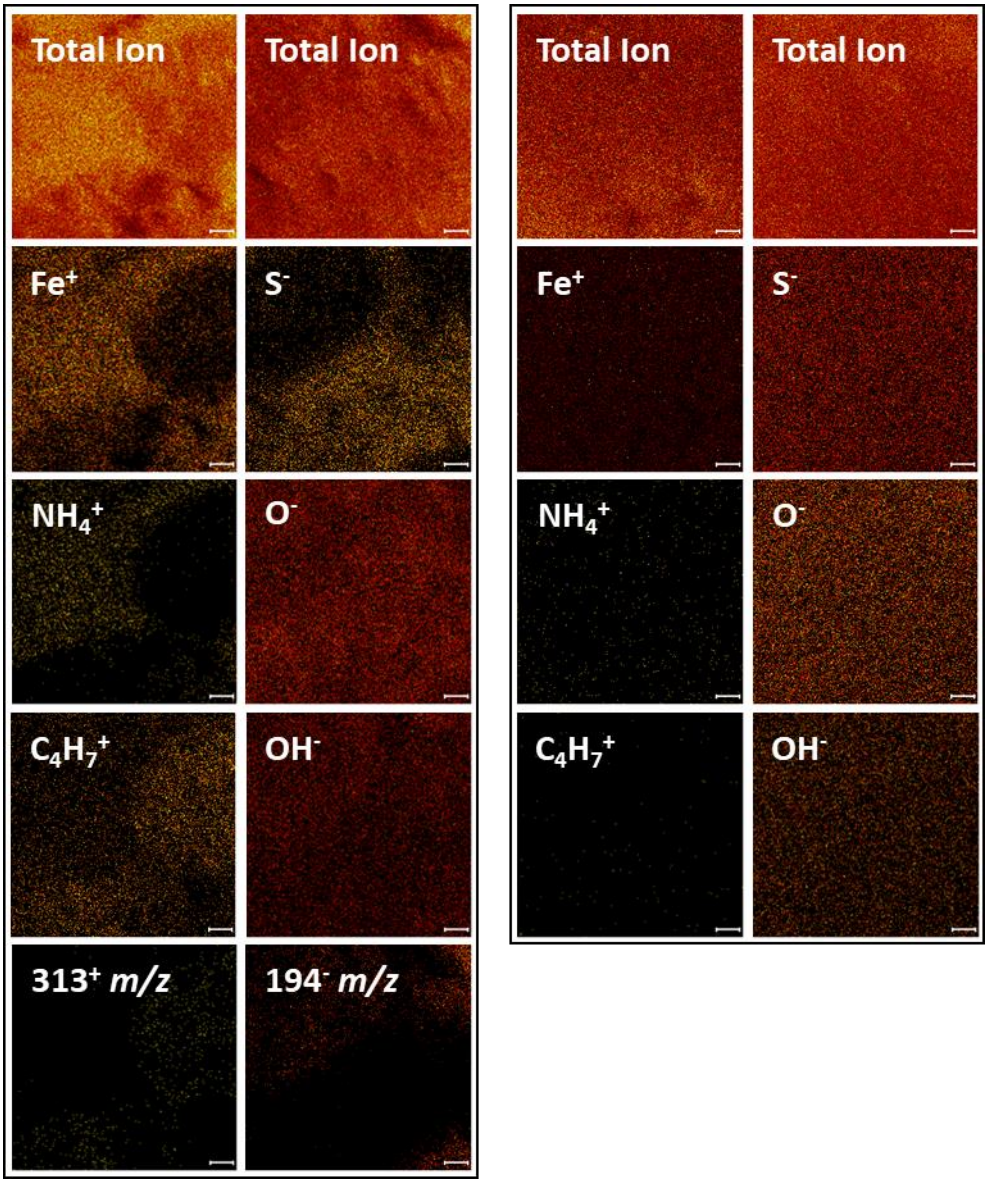

Figure 4.42: Positive (left column) and negative (right column) ion images of pyrite exposed to *A. ferrooxidans* for 2 h (left), and HH medium for 2 h (right) (scale bar 10 µm).

The pyrite exposed to *A. ferrooxidans* for 2 h shows two distinct domains on the surface. Though both are covered by O^- and OH^- fragments, the first region seems to be slightly richer in the O^- fragment, and is also covered by Fe^+ and S^-, with a not insignificant amount of NH_4^+. The other region is slightly richer in the OH^- fragment, and contains the most significant proportion of short chain carbon fragments, of which the $C_4H_7^+$ image is an example. It is also the region that contains the highest frequency of large molecular weight fragments, with images of the two most abundant fragments from the positive and negative SIMS shown as example.

The control pyrite surface shows a mostly uniform covering of each ion, with the suggestion of some clustering of NH_4^+ fragments, which suggest some of the NH_4^+ signal on the pyrite exposed to *A. ferrooxidans* may indeed have an organic source as well as an inorganic source.

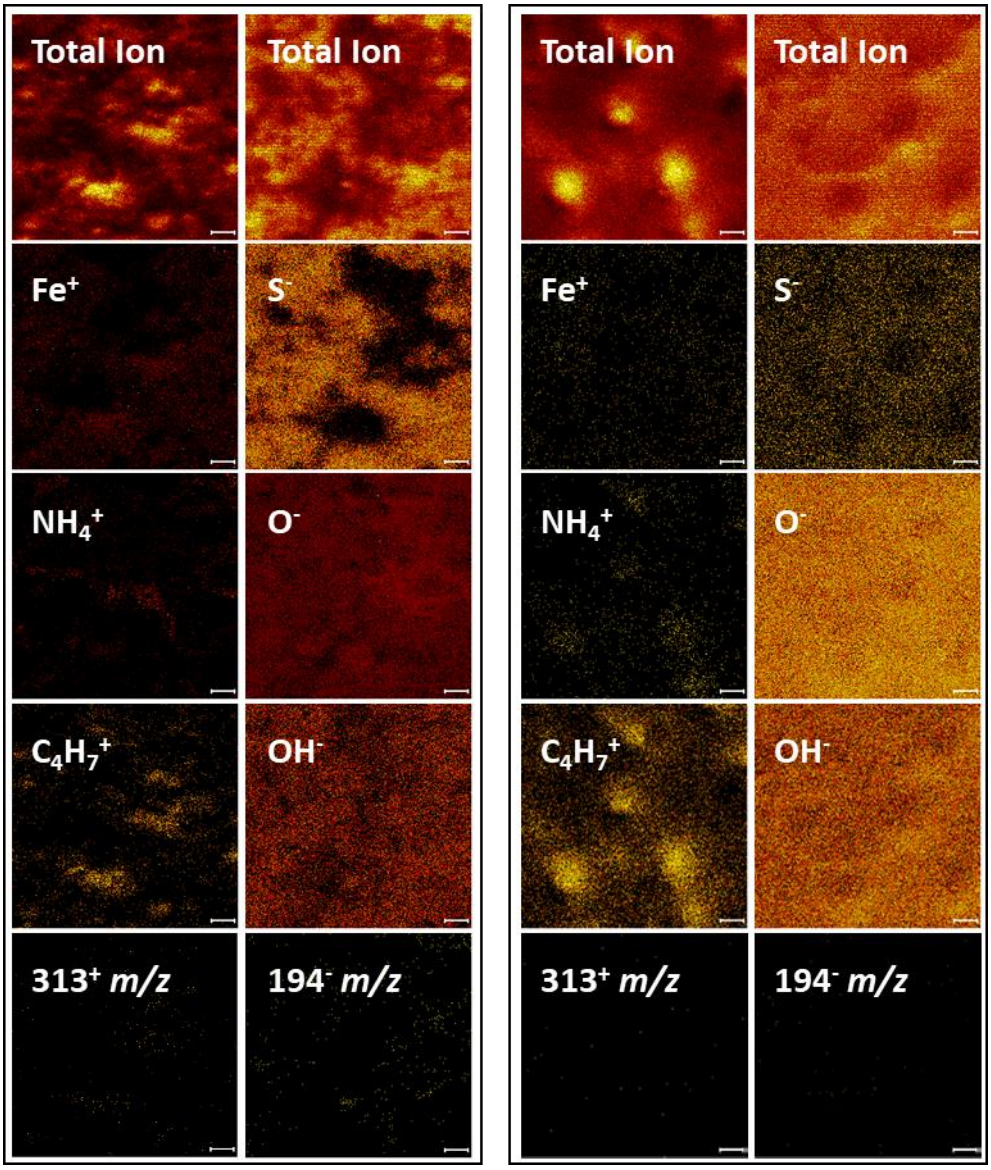

Figure 4.43: Positive (left column) and negative (right column) ion images of pyrite exposed to *A. ferrooxidans* for 24 h (left), and HH medium for 24 h (right) (scale bar 10 µm).

Figure 4.43 shows the positive and negative ion images collected from pyrite exposed to *A. ferrooxidans* and HH medium for 24 h. After 24 h of exposure, both samples remain dominated by the O^- and OH^- fragments, but islands of large molecular fragments and hydrocarbons and richer in OH^- appear to have formed on the surface of samples exposed to *A. ferrooxidans* that are too thick for Fe^+ and S^- to be seen on the surface. In contrast, the control pyrite remains uniform, and the carbon signals seem to be coming from surface defects, although not thick enough to obscure the Fe^+ and S^- fragments. Although larger fragments are detected on the surface, they appear much less frequently, and appear closely associated with surface defects, indicating contamination that was

possibly never eradicated by the initial polishing and cleaning processes detailed in Chapter 3, section 3.4.1.

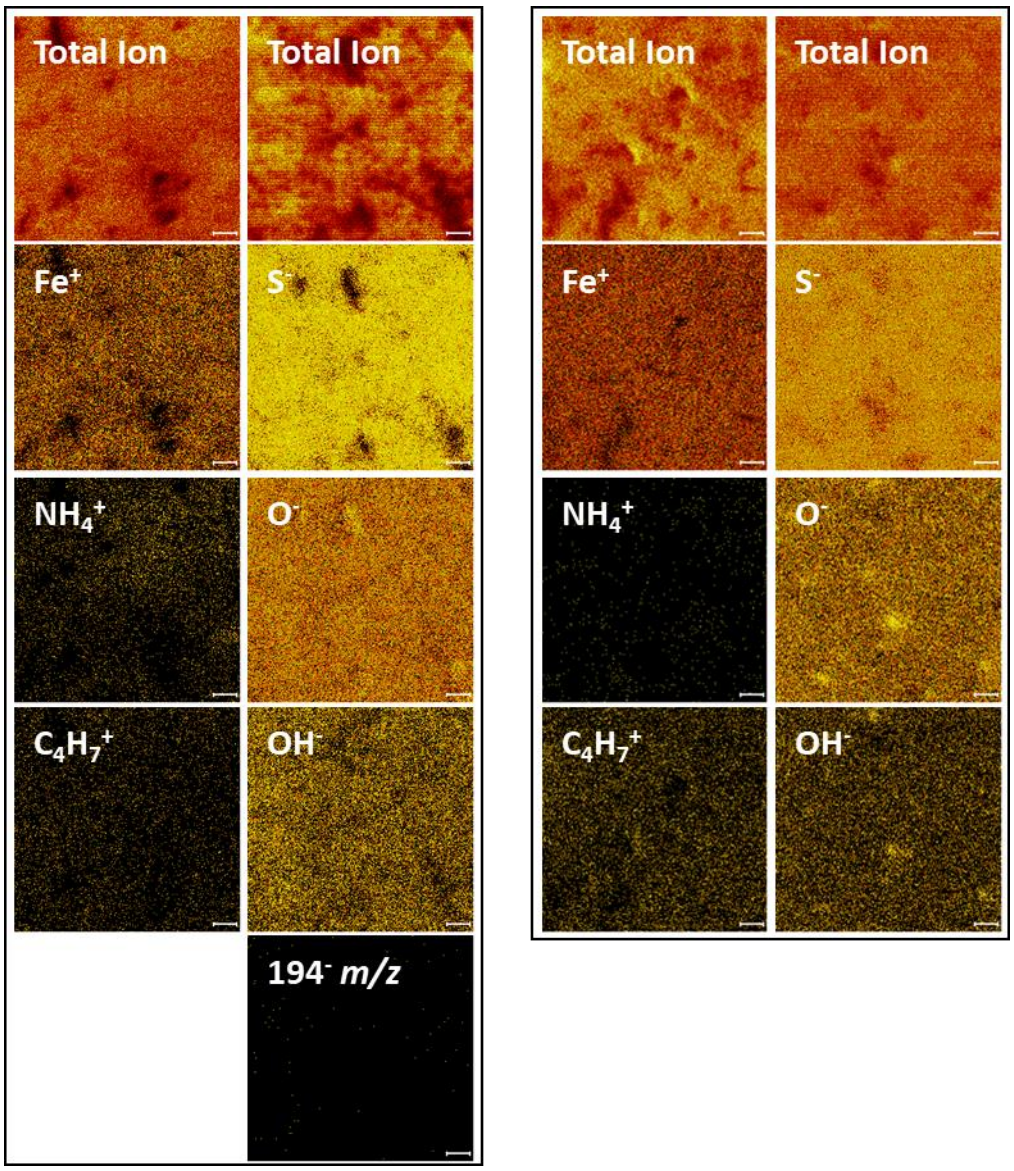

Figure 4.44: Positive (left column) and negative (right column) ion images of pyrite exposed to *A. ferrooxidans* for 72 h (left), and HH medium for 72 h (right) (scale bar 10 µm).

Figure 4.44 shows the positive and negative ion images collected from pyrite exposed to *A. ferrooxidans* and HH medium for 72 h. After 72 h of exposure pyrite exposed to *A. ferrooxidans*, the surface is uniformly covered in all ion species except for the large molecular weight fragments, with only the most frequently occurring fragment at 194.93 *m/z* able to be mapped. This fragment is notably not related to surface defects. The NH_4^+ fragment is also much thicker on the surface of pyrite exposed to the bacteria compared to the control at this stage. Apart from these differences, the control pyrite surface at this exposure time is also uniformly covered by the same ions. This agrees with the contact angle results that suggest there is little difference between pyrite exposed to HH medium and *A. ferrooxidans* at 72 h.

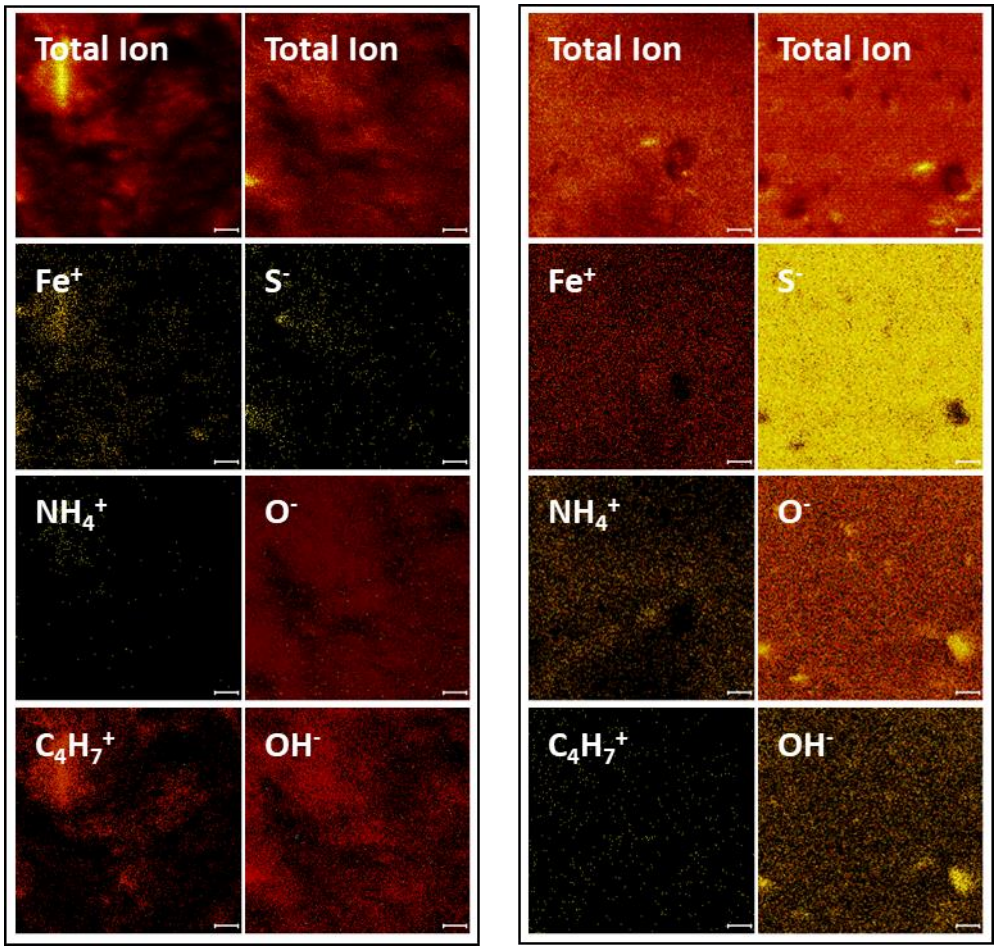

Figure 4.45: Positive (left column) and negative (right column) ion images of pyrite exposed to *A. ferrooxidans* for 168 h (left), and HH medium for 168 h (right) (scale bar 10 µm).

Figure 4.45 shows the positive and negative ion images collected from pyrite exposed to *A. ferrooxidans* and HH medium for 168 h. After 168 h of exposure, there is an indication of areas of high hydrocarbon concentration on the surface of pyrite exposed to *A. ferrooxidans*. This coincides with regions with the highest Fe^+ frequency. Most of the surface is dominated by the O^- and OH^- fragments. Again, the OH^- fragment appears to coincide with areas of high hydrocarbon abundancy, while the O^- appears uniform across the surface. This agrees with the NEXAFS Fe L-edge spectrum for pyrite exposed to *A. ferrooxidans* at this period, which shows the oxidation of the iron in pyrite after 168 h. As was mentioned earlier, these fragments coincide with a decrease in hydrophobicity of the surface. The pyrite exposed to HH medium appears much richer in sulfur, although still covered in a significant oxide layer. Like the previous control samples, the ions are seen to uniformly cover the surface.

Previous studies of pyrite surfaces using ToF-SIMS were focused mainly on identifying pyrite particles within a mixture of sulfide minerals, and on the ions associated with the pyrite surface and ions of interest to flotation. The results presented here for the control pyrite are much in agreement with previous studies that have observed, under a wide range of conditions, that the surface of pyrite

is iron-rich, which has been found to be unrelated to flotability [84, 85, 127-129]. Several ToF-SIMS studies have reported that samples richer in sulfur were more hydrophobic, while samples richer in O^-, OH^-, C^- and CH^- were likely to be less hydrophobic and remain in tailings [84, 85, 127-129]. These findings agree with the findings here, with the most sulfur rich sample, pyrite exposed to HH medium for 2 h, is also the most hydrophobic sample. The overall hydrophobicity of the sample is determined by a balance between surface species.

Previous studies that have utilised ToF-SIMS for the investigation of various microorganisms and their excretions have mainly focussed on the identification of known components such as proteins and monosaccharides by principle component analysis, however, it has yet to be successfully applied to complex samples [107, 130, 131]. Other studies have looked at specific types of compounds such as proteins or peptides on cells, and Dague *et al* specifically related protein fragments to increases in surface hydrophobicity, a contribution which is also observed in the results presented in this investigation [12, 132]. The EPS components produced by *A. ferrooxidans* have been observed in previous studies to contain a mixture of proteins, polysaccharides, uronic, humic and deoxyribonucleic acids [24, 37, 48, 66, 133], with the source of nutrients having been demonstrated to impact the composition and amount of EPS produced by cells [134]. The anionic functional groups from proteins and polysaccharides including carboxyl, sulfydryl, glycerae and phosphate, bind with metals including iron. This allows for initial oxidation of pyrite to Fe^{3+}-EPS complexes without bacterial attachment [124, 125]. The interaction of *A. ferrooxidans* can, therefore, be described as an indirect mechanism whereby EPS interacts with the pyrite surface, followed by an indirect contact mechanism as the cells irreversibly attach to the surface and biofilm develops [30, 48, 101]. As polysaccharides and fatty acids are produced at early exposure stages, cells or EPS harvested at this period of exposure to pyrite are likely to be more beneficial to the potential depression of pyrite than the more hydrophobic protein- and nucleic acid-rich EPS produced at longer periods of exposure. These findings suggest that biofilm formation is not required to significantly decrease the hydrophobicity of pyrite. EPS produced by *A. ferrooxidans* during initial attachment and at low cell coverage of the surface is adequate for surface modification.

4.4 Conclusions

Attachment of cells during the first hours of exposure was observed using SEM, with no obvious preference for surface defects. A biofilm develops after 168 h of exposure. The leaching of the pyrite is accelerated by the presence of bacteria, with the roughness of the surface as measured by AFM confirming that the mineral surface shows more significant pitting than is caused by acidic

medium alone. The difference in hydrophobicity is greatest between bacterial exposure and abiotic control after 2 h, which coincides with the presence of polysaccharide and fatty acid-type structures measured by PEEM. However, longer periods of exposure lead to inorganic oxidation of the pyrite surface, causing little difference in hydrophobicity of the samples until a biofilm begins to form after 168 h. These observations suggest that *A. ferrooxidans* preferentially produces polysaccharide and fatty acid compounds to assist with initial adhesion to pyrite, before beginning to produce more hydrophobic proteins as colonies begin to develop on the surface. This has important implications for the field of bioflotation, which would ideally require short-term exposure for the most efficient separation of minerals. This study suggests that the nature of bacterial excretions changes as the requirements of the cells change over time, and as such, the time cells are harvested and the length of exposure to the mineral is of crucial importance to effective separation of minerals.

4.5 References

1. Chandraprabha, M.N., Natarajan, K. A., Somasundaran, P., *Selective separation of pyrite from chalcopyrite and arsenopyrite by biomodulation using Acidithiobacillus ferrooxidans.* International Journal of Mineral Processing, 2005. **75**(1–2): p. 113-122.
2. Mehrabani, J.V., Mousavi, S. M., Noaparast, M., *Evaluation of the replacement of NaCN with Acidithiobacillus ferrooxidans in the flotation of high-pyrite, low-grade lead–zinc ore.* Separation and Purification Technology, 2011. **80**(2): p. 202-208.
3. Mehrabani, J.V., Noaparast, M., Mousavi, S. M., Dehghan, R., Rasooli, E., Hajizadeh, H., *Depression of pyrite in the flotation of high pyrite low-grade lead–zinc ore using Acidithiobacillus ferrooxidans.* Minerals Engineering, 2010. **23**(1): p. 10-16.
4. Nagaoka, T., Ohmura, N., Saiki, H., *A novel mineral processing by flotation using Thiobacillus ferrooxidans*, in *Process Metallurgy*, R. Amils and A. Ballester, Editors. 1999, Elsevier. p. 335-342.
5. Smith, R.W., Miettinen, M., *Microorganisms in flotation and flocculation: Future technology or laboratory curiosity?* Minerals Engineering, 2006. **19**(6–8): p. 548-553.
6. Somasundaran, P., Ren, Y., Rao, M. Y., *Applications of biological processes in mineral processing.* Colloids and Surfaces A: Physicochemical and Engineering Aspects, 1998. **133**(1): p. 13-23.
7. Cizaire, L., Martin, J. M., Le Mogne, Th., Gresser, E., *Chemical analysis of overbased calcium sulfonate detergents by coupling XPS, ToF-SIMS, XANES, and EFTEM.* Colloids and Surfaces A: Physicochemical and Engineering Aspects, 2004. **238**(1): p. 151-158.
8. Pacholewska, M., *Microbial leaching of blende flotation concentrate using Acidithiobacillus ferrooxidans and Acidithiobacillus thiooxidans.* Physicochemical Problems of Mineral Processing, 2003. **37**: p. 57-68.
9. Poorni, S., Natarajan, K. A., *Flocculation behaviour of hematite–kaolinite suspensions in presence of extracellular bacterial proteins and polysaccharides.* Colloids and Surfaces B: Biointerfaces, 2014. **114**(0): p. 186-192.
10. Vilinska, A., Hanumantha Rao, K., *Leptospirillum ferrooxidans-sulfide mineral interactions with reference to bioflotation and bioflocculation.* Transactions of Nonferrous Metals Society of China, 2008. **18**(6): p. 1403-1409.
11. La Vars, S.M., Newton, K., Quinton, J. S., Cheng, P.-Y., Wei, D.-H., Chan, Y.-L., Harmer, S. L., *Surface Chemical Characterisation of Pyrite Exposed to Acidithiobacillus*

ferrooxidans and Associated Extracellular Polymeric Substances. Minerals, 2018. **8**(4): p. 132.
12. Dague, E., Delcorte, A., Latgé, J.-P., Dufrêne, Y. F., *Combined Use of Atomic Force Microscopy, X-ray Photoelectron Spectroscopy, and Secondary Ion Mass Spectrometry for Cell Surface Analysis.* Langmuir, 2008. **24**(7): p. 2955-2959.
13. Hocheng, H., Chang, J. H., Hsu, H. S., Han, H. J., Chang, Y. L., Jadhav, U. U., *Metal removal by Acidithiobacillus ferrooxidans through cells and extra-cellular culture supernatant in biomachining.* CIRP Journal of Manufacturing Science and Technology, 2012. **5**(2): p. 137-141.
14. Brunner, B., Yu, J.-Y., Mielke, R. E., MacAskill, J. A., Madzunkov, S., McGenity, T. J., Coleman, M., *Different isotope and chemical patterns of pyrite oxidation related to lag and exponential growth phases of Acidithiobacillus ferrooxidans reveal a microbial growth strategy.* Earth and Planetary Science Letters, 2008. **270**(1–2): p. 63-72.
15. Liu, H., Gu, G., Xu, Y., *Surface properties of pyrite in the course of bioleaching by pure culture of Acidithiobacillus ferrooxidans and a mixed culture of Acidithiobacillus ferrooxidans and Acidithiobacillus thiooxidans.* Hydrometallurgy, 2011. **108**(1–2): p. 143-148.
16. Sampson, M.I., Phillips, C. V., Blake II, R. C., *Influence of the attachment of acidophilic bacteria during the oxidation of mineral sulphides.* Minerals Engineering, 2000. **13**(4): p. 373-389.
17. Yu, R.-L., Ou, Y., Tan, J.-X., Wu, F.-D., Sun, J., Miao, L., Zhong, D.-L., *Effect of EPS on adhesion of Acidithiobacillus ferrooxidans on chalcopyrite and pyrite mineral surfaces.* Transactions of Nonferrous Metals Society of China, 2011. **21**(2): p. 407-412.
18. Chandraprabha, M.N., Natarajan, K. A., *Surface chemical and flotation behaviour of chalcopyrite and pyrite in the presence of Acidithiobacillus thiooxidans.* Hydrometallurgy, 2006. **83**(1–4): p. 146-152.
19. Chandraprabha, M.N., Natarajan, K. A., *Role of outer membrane exopolymers of Acidithiobacillus ferrooxidans in adsorption of cells onto pyrite and chalcopyrite.* International Journal of Mineral Processing, 2013. **123**(0): p. 152-157.
20. Diao, M., Nguyen, T. A. H., Taran, E., Mahler, S., Nguyen, A. V., *Differences in adhesion of A. thiooxidans and A. ferrooxidans on chalcopyrite as revealed by atomic force microscopy with bacterial probes.* Minerals Engineering, 2014. **61**(0): p. 9-15.
21. Acharya, C., Sukla, L. B., Misra, V. N., *Biodepyritisation of coal.* Journal of Chemical Technology & Biotechnology, 2004. **79**(1): p. 1-12.
22. Duarte, J.C., Estrada, P. C., Pereira, P. C., Beaumont, H. P., *Thermophilic vs. mesophilic bioleaching process performance.* FEMS Microbiology Reviews, 1993. **11**(1–3): p. 97-102.
23. Felício, A.P., de Oliveira, E., Odena, M. A., Garcia Jr, O., Bertolini, M. C., Ferraz, L. F. C., Ottoboni, L. M. M., Novo, M. T. M., *Differential proteomic analysis of Acidithiobacillus ferrooxidans cells maintained in contact with bornite or chalcopyrite: Proteins involved with the early bacterial response.* Process Biochemistry, 2011. **46**(3): p. 770-776.
24. Kinzler, K., Gehrke, T., Telegdi, J., Sand, W., *Bioleaching—a result of interfacial processes caused by extracellular polymeric substances (EPS).* Hydrometallurgy, 2003. **71**(1–2): p. 83-88.
25. Mangold, S., Laxander, M., Harneit, K., Rohwerder, T. , Claus, G., Sand, W., *Visualization of Acidithiobacillus ferrooxidans biofilms on pyrite by atomic force and epifluorescence microscopy under various experimental conditions.* Hydrometallurgy, 2008. **94**(1–4): p. 127-132.
26. Schippers, A., *Microorganisms involved in bioleaching and nucleic acid-based molecular methods for their identification and quantification*, in *Microbial Processing of Metal Sulfides*, E.R.D.a.W. Sand, Editor. 2007, Springer: Dordrecht, Netherlands. p. 3-33.

27. Viera, M., Pogliani, C., Donati, E., *Recovery of zinc, nickel, cobalt and other metals by bioleaching*, in *Microbial Processing of Metal Sulfides*, W.S. Edgardo R. Donati, Editor. 2007, Springer: Dordrecht, The Netherlands. p. 103-119.
28. Yu, R.-L., Liu, J., Chen, A., Zhong, D.-L., Li, Q., Qin, W.-Q., Qiu, G.-Z., Gu, G.-H., *Interaction mechanism of Cu2+, Fe3+ ions and extracellular polymeric substances during bioleaching chalcopyrite by Acidithiobacillus ferrooxidans ATCC2370.* Transactions of Nonferrous Metals Society of China, 2013. **23**(1): p. 231-236.
29. Tan, S.N., Chen, M., *Early stage adsorption behaviour of Acidithiobacillus ferrooxidans on minerals I: An experimental approach.* Hydrometallurgy, 2012. **119–120**(0): p. 87-94.
30. Crundwell, F.K., *How do bacteria interact with minerals?* Hydrometallurgy, 2003. **71**(1–2): p. 75-81.
31. Sand, W., Gehrke, T., Jozsa, P.-G., Schippers, A., *(Bio)chemistry of bacterial leaching—direct vs. indirect bioleaching.* Hydrometallurgy, 2001. **59**(2): p. 159-175.
32. Wills, B.A., *Wills' Mineral Processing Technology*. 7th ed, ed. T.J. Napier-Munn. 2006, Oxford: Elsevier. 444.
33. Nagaraj, D.R., *Minerals Recovery and Processing*, in *Kirk-Othmer Encyclopedia of Chemical Technology*. 2000, John Wiley & Sons, Inc. p. 595-679.
34. Kawatra, S.K. *Flotation Fundamentals*. Mining Engineering Handbook, 2009. 30.
35. Mykytczuk, N.C.S., Trevors, J. T., Ferroni, G. D., Leduc, L. G., *Cytoplasmic membrane response to copper and nickel in Acidithiobacillus ferrooxidans.* Microbiological Research, 2011. **166**(3): p. 186-206.
36. Beard, S., Paradela, A., Albar, J. P., Jerez, C. A., *Growth of Acidithiobacillus Ferrooxidans ATCC 23270 in Thiosulfate Under Oxygen-Limiting Conditions Generates Extracellular Sulfur Globules by Means of a Secreted Tetrathionate Hydrolase.* Front Microbiol, 2011. **2**(79).
37. Sharma, P.K., Das, A., Hanumantha Rao, K., Forssberg, K. S. E., *Surface characterization of Acidithiobacillus ferrooxidans cells grown under different conditions.* Hydrometallurgy, 2003. **71**(1–2): p. 285-292.
38. Xia, J.-L., Yang, Y., He, H., Zhao, X.-J., Liang, C.-L., Zheng, L., Ma, C.-Y., Zhao, Y.-D., Nie, Z.-Y., Qiu, G.-Z., *Surface analysis of sulfur speciation on pyrite bioleached by extreme thermophile Acidianus manzaensis using Raman and XANES spectroscopy.* Hydrometallurgy, 2010. **100**(3–4): p. 129-135.
39. He, H., Xia, J.-L., Hong, F.-F., Tao, X.-X., Leng, Y.-W., Zhao, Y.-F., *Analysis of sulfur speciation on chalcopyrite surface bioleached with Acidithiobacillus ferrooxidans.* Minerals Engineering, 2012. **27–28**(0): p. 60-64.
40. Yu, J.-Y., McGenity, T. J., Coleman, M. L., *Solution chemistry during the lag phase and exponential phase of pyrite oxidation by Thiobacillus ferrooxidans.* Chemical Geology, 2001. **175**(3): p. 307-317.
41. Sasaki, K., Nakamuta, Y., Hirajima, T., Tuovinen, O. H., *Raman characterization of secondary minerals formed during chalcopyrite leaching with Acidithiobacillus ferrooxidans.* Hydrometallurgy, 2009. **95**(1–2): p. 153-158.
42. Zhu, J., Jiao, W., Li, Q., Liu, X., Qin, W., Qiu, G., Hu, Y., Chai, L., *Investigation of energy gene expressions and community structures of free and attached acidophilic bacteria in chalcopyrite bioleaching.* Journal of Industrial Microbiology & Biotechnology, 2012. **39**(12): p. 1833-1840.
43. Ralston, J., *Eh and its consequences in sulphide mineral flotation.* Minerals Engineering, 1991. **4**(7): p. 859-878.
44. Hayes, R.A., Ralston, J., *The collectorless flotation and separation of sulphide minerals by Eh control.* International Journal of Mineral Processing, 1988. **23**(1): p. 55-84.
45. Shen, W.Z., Fornasiero, D., Ralston, J., *Effect of collectors, conditioning pH and gases in the separation of sphalerite from pyrite.* Minerals Engineering, 1998. **11**(2): p. 145-158.

46. Petersen, J., Dixon, D. G., *Competitive bioleaching of pyrite and chalcopyrite.* Hydrometallurgy, 2006. **83**(1–4): p. 40-49.
47. Zhu, W., Xia, J.-L., Yang, Y., Nie, Z.-Y., Zheng, L., Ma, C.-Y., Zhang, R.-Y., Peng, A.-A., Tang, L., Qiu, G.-Z., *Sulfur oxidation activities of pure and mixed thermophiles and sulfur speciation in bioleaching of chalcopyrite.* Bioresource Technology, 2011. **102**(4): p. 3877-3882.
48. Watling, H.R., *The bioleaching of sulphide minerals with emphasis on copper sulphides — A review.* Hydrometallurgy, 2006. **84**(1–2): p. 81-108.
49. Deveci, H., Jordan, M. A., Powell, N., Alp, I., *Effect of salinity and acidity on bioleaching activity of mesophilic and extremely thermophilic bacteria.* Transactions of Nonferrous Metals Society of China, 2008. **18**(3): p. 714-721.
50. Dopson, M., Johnson, D. B., *Biodiversity, metabolism and applications of acidophilic sulfur-metabolizing microorganisms.* Environ Microbiol, 2012. **14**(10): p. 2620-31.
51. Larsson, L., Olsson, G., Hoist, O., Karlsson, H. T., *Oxidation of pyrite by Acidianus brierleyi: Importance of close contact between the pyrite and the microorganisms.* Biotechnology Letters, 1993. **15**(1): p. 99-104.
52. Mikkelsen, D., Kappler, U., Webb, R. I., Rasch, R., McEwan, A. G., Sly, L. I., *Visualisation of pyrite leaching by selected thermophilic archaea: Nature of microorganism–ore interactions during bioleaching.* Hydrometallurgy, 2007. **88**(1–4): p. 143-153.
53. Konishi, Y., Kogasaki, K., Asai, S., *Bioleaching of pyrite by Acidianus brierleyi in a continuous-flow stirred-tank reactor.* Chemical Engineering Science, 1997. **52**(24): p. 4525-4532.
54. Konishi, Y., Tokushige, M., Asai, S., Suzuki, T., *Copper recovery from chalcopyrite concentrate by acidophilic thermophile Acidianus brierleyi in batch and continuous-flow stirred tank reactors.* Hydrometallurgy, 2001. **59**(2–3): p. 271-282.
55. Konishi, Y., Matsui, M., Fujiwara, H., Nomura, T., Nakahara, K., *Zinc Leaching from Fly Ash in Municipal Waste Incineration by Thermophilic Archaean Acidianus brierleyi Growing on Elemental Sulfur.* Separation Science and Technology, 2003. **38**(16): p. 4117-4130.
56. Zhang, Y.-S., Qin, W.-Q., Wang, J., Zhen, S.-J., Yang, C.-R., Zhang, J.-W., Nai, S.-S., Qiu, G.-Z., *Bioleaching of chalcopyrite by pure and mixed culture.* Transactions of Nonferrous Metals Society of China, 2008. **18**(6): p. 1491-1496.
57. Gleisner, M., Herbert, R. B., Frogner Kockum, P. C., *Pyrite oxidation by Acidithiobacillus ferrooxidans at various concentrations of dissolved oxygen.* Chemical Geology, 2006. **225**(1): p. 16-29.
58. Karavaiko, G.I., Smolskaja, L. S., Golyshina, O. K., Jagovkina, M. A., Egorova, E. Y., *Bacterial pyrite oxidation: Influence of morphological, physical and chemical properties.* Fuel Processing Technology, 1994. **40**(2): p. 151-165.
59. Mitsunobu, S., Zhu, M., Takeichi, Y., Ohigashi, T., Suga, H., Jinno, M., Makita, H., Sakata, M., Ono, K., Mase, K., Takahashi, Y., *Direct Detection of Fe(II) in Extracellular Polymeric Substances (EPS) at the Mineral-Microbe Interface in Bacterial Pyrite Leaching*. Vol. 31. 2016.
60. Microanalysis, C.F.f.A.M.a. *Introduction to Energy Dispersive X-ray Spectrometry (EDS)*. 2015 [cited 2017; Available from: http://cfamm.ucr.edu/manuals.html.
61. Watling, H.R., Perrot, F. A., Shiers, D. W., *Comparison of selected characteristics of Sulfobacillus species and review of their occurrence in acidic and bioleaching environments.* Hydrometallurgy, 2008. **93**(1–2): p. 57-65.
62. *MyScope: training for advanced research*. 2014 April 15, 2014 [cited 2017 21/08]; Available from: ww.ammrf.org.au/myscope.
63. Swapp, S. *Geochemical Instrument Analysis: Scanning Electron Microscopy*. [Website] 2012 7/7/2012 [cited 2012 19/7/2012]; Available from: http://serc.carleton.edu/research_education/geochemsheets/techniques/SEM.html.

64. Chau, T.T., Bruckard, W. J., Koh, P. T. L., Nguyen, A. V., *A review of factors that affect contact angle and implications for flotation practice.* Advances in Colloid and Interface Science, 2009. **150**(2): p. 106-115.
65. Gehrke, T., Telegdi, J., Thierry, D., Sand, W., *Importance of Extracellular Polymeric Substances from Thiobacillus ferrooxidans for Bioleaching.* Appl Environ Microbiol, 1998. **64**(7): p. 2743-7.
66. Rohwerder, T., Sand, W., *Mechanisms and biochemical fundamentals of bacterial metal sulfide oxidation*, in *Microbial Processing of Metal Sulfides*, E.R.D.a.W. Sand, Editor. 2007 Springer. p. 35-58.
67. Smart, R.S.C., *Surface layers in base metal sulphide flotation.* Minerals Engineering, 1991. **4**(7–11): p. 891-909.
68. Fuerstenau, M.C., Chander, S., Woods, R., *Sulphide Mineral Flotation*, in *Froth Flotation: A Century of Innovation*, M.C. Fuerstenau, Jameson, G., Yoon, R.-H., Editor. 2007, Society for Mining, Metallurgy, and Exploration: Littleton, Colarado. p. 425-464.
69. Loeb, G.I., *The Properties of Nonbiological Surfaces and Their Characterization*, in *Bacterial Adhesion: Mechanisms and Physiological Significance*, D.C. Savage, Fletcher, M., Editor. 1985, Plenum Press: New York. p. 111-127.
70. Chipfunhu, D., Zanin, M., Grano, S., *Flotation behaviour of fine particles with respect to contact angle.* Chemical Engineering Research and Design, 2012. **90**(1): p. 26-32.
71. Ohmura, N., Kitamura, K., Saiki, H., *Selective Adhesion of Thiobacillus ferrooxidans to Pyrite.* Applied and Environmental Microbiology, 1993. **59**(12): p. 4044-4050.
72. Sharma, P.K., Hanumantha Rao, K., Forssberg, K. S. E., Natarajan, K. A., *Surface chemical characterisation of Paenibacillus polymyxa before and after adaptation to sulfide minerals.* International Journal of Mineral Processing, 2001. **62**(1–4): p. 3-25.
73. Zhu, J., Li, Q., Jiao, W., Jiang, H., Sand, W., Xia, J., Liu, X., Qin, W., Qiu, G., Hu, Y., Chai, L., *Adhesion forces between cells of Acidithiobacillus ferrooxidans, Acidithiobacillus thiooxidans or Leptospirillum ferrooxidans and chalcopyrite.* Colloids and Surfaces B: Biointerfaces, 2012. **94**: p. 95-100.
74. Jordan, M.A., Barr, D. W., Phillips, C. V., *Iron and sulphur speciation and cell surface hydrophobicity during bacterial oxidation of a complex copper concentrate.* Minerals Engineering, 1993. **6**(8–10): p. 1001-1011.
75. Vilinska, A., Hanumantha Rao, K., *Surface Thermodynamics and Extended DLVO Theory of Acidithiobacillus ferrooxidans Cells Adhesion on Pyrite and Chalcopyrite*. Vol. 2. 2009.
76. Womes, M., Karnatak, R. C., Esteva, J. M., Lefebvre, I., Allan, G., Olivier-Fourcades, J., Jumas, J. C., *Electronic structures of FeS and FeS2: X-ray absorption spectroscopy and band structure calculations.* Journal of Physics and Chemistry of Solids, 1997. **58**(2): p. 345-352.
77. Fleet, M.E., *XANES Spectroscopy of sulphur in Earth Materials*. Vol. 43. 2005. 1811-1838.
78. von Oertzen, G.U., Jones, R. T., Gerson, A. R., *Electronic and optical properties of Fe, Zn and Pb sulfides.* Physics and Chemistry of Minerals, 2005. **32**(4): p. 255-268.
79. Miedema, P.S., de Groot, F. M. F., *The iron L edges: Fe 2p X-ray absorption and electron energy loss spectroscopy.* Journal of Electron Spectroscopy and Related Phenomena, 2013. **187**(Supplement C): p. 32-48.
80. van Aken, P.A., Lauterbach, S., *Strong magnetic linear dichroism in Fe L23 and O K electron energy-loss near-edge spectra of antiferromagnetic hematite α-Fe2O3.* Physics and Chemistry of Minerals, 2003. **30**(8): p. 469-477.
81. van Aken, P.A., Liebscher, B., *Quantification of ferrous/ferric ratios in minerals: new evaluation schemes of Fe L 23 electron energy-loss near-edge spectra.* Physics and Chemistry of Minerals, 2002. **29**(3): p. 188-200.
82. Goh, S.W., Buckley, A. N., Lamb, R. N., Rosenberg, R. A., Moran, D., *The oxidation states of copper and iron in mineral sulfides, and the oxides formed on initial exposure of*

chalcopyrite and bornite to air. Geochimica et Cosmochimica Acta, 2006. **70**(9): p. 2210-2228.
83. Buckley, A.N., Woods, R., *An X-ray photoelectron spectroscopic study of the oxidation of chalcopyrite.* Australian Journal of Chemistry, 1984. **37**(12): p. 2403-2413.
84. Kalegowda, Y., Chan, Y.-L., Wei, D.-H., Harmer, S. L., *X-PEEM, XPS and ToF-SIMS characterisation of xanthate induced chalcopyrite flotation: Effect of pulp potential.* Surface Science, 2015. **635**: p. 70-77.
85. Kalegowda, Y., Harmer, S. L., *Classification of time-of-flight secondary ion mass spectrometry spectra from complex Cu–Fe sulphides by principal component analysis and artificial neural networks.* Analytica Chimica Acta, 2013. **759**: p. 21-27.
86. Doyle, C.S., Kendelewicz, T., Bostick, B. C., Brown, G. E., *Soft X-ray spectroscopic studies of the reaction of fractured pyrite surfaces with Cr(VI)-containing aqueous solutions.* Geochimica et Cosmochimica Acta, 2004. **68**(21): p. 4287-4299.
87. Kaznacheyev, K., Osanna, A., Jacobsen, C., Plashkevych, O., Vahtras, O., Ågren, H., Carravetta, V., Hitchcock, A. P., *Innershell Absorption Spectroscopy of Amino Acids.* The Journal of Physical Chemistry A, 2002. **106**(13): p. 3153-3168.
88. Stewart-Ornstein, J., Hitchcock, A. P., Hernandez Cruz, D., Henklein, P., Overhage, J., Hilpert, K., Hale, J. D., Hancock, R. E., *Using intrinsic X-ray absorption spectral differences to identify and map peptides and proteins.* J Phys Chem B, 2007. **111**(26): p. 7691-9.
89. Solomon, D., Lehmann, J., Harden, J., Wang, J., Kinyangi, J., Heymann, K., Karunakaran, C., Lu, Y., Wirick, S., Jacobsen, C., *Micro- and nano-environments of carbon sequestration: Multi-element STXM–NEXAFS spectromicroscopy assessment of microbial carbon and mineral associations.* Chemical Geology, 2012. **329**(0): p. 53-73.
90. Wan, J., Tyliszczak, T., Tokunaga, T. K., *Organic carbon distribution, speciation, and elemental correlations within soil microaggregates: Applications of STXM and NEXAFS spectroscopy.* Geochimica et Cosmochimica Acta, 2007. **71**(22): p. 5439-5449.
91. Miot, J., Benzerara, K., Morin, G., Kappler, A., Bernard, S., Obst, M., Férard, C., Skouri-Panet, F., Guigner, J.-M., Posth, N., Galvez, M., Brown Jr, G. E., Guyot, F., *Iron biomineralization by anaerobic neutrophilic iron-oxidizing bacteria.* Geochimica et Cosmochimica Acta, 2009. **73**(3): p. 696-711.
92. Rightor, E.G., Hitchcock, A. P., Ade, H., Leapman, R. D., Urquhart, S. G., Smith, A. P., Mitchell, G., Fischer, D., Shin, H. J., Warwick, T., *Spectromicroscopy of Poly(ethylene terephthalate): Comparison of Spectra and Radiation Damage Rates in X-ray Absorption and Electron Energy Loss.* The Journal of Physical Chemistry B, 1997. **101**(11): p. 1950-1960.
93. Zubavichus, Y., Fuchs, O., Weinhardt, L., Heske, C., Umbach, E., Denlinger, J. D., Grunze, M., *Soft X-Ray-Induced Decomposition of Amino Acids: An XPS, Mass Spectrometry, and NEXAFS Study.* Radiation Research, 2004. **161**(3): p. 346-358.
94. Watts, B., Thomsen, L., Dastoor, P. C., *Methods in carbon K-edge NEXAFS: Experiment and analysis.* Journal of Electron Spectroscopy and Related Phenomena, 2006. **151**(2): p. 105-120.
95. Briggs, D., Vickerman, J. C., *ToF-SIMS : surface analysis by mass spectrometry*. 2001, Chichester : IM ; Manchester: SurfaceSpectra
96. Dynes, J.J., Lawrence, J. R., Korber, D. R., Swerhone, G. D., Leppard, G. G., Hitchcock, A. P., *Morphological and biochemical changes in Pseudomonas fluorescens biofilms induced by sub-inhibitory exposure to antimicrobial agents.* Can J Microbiol, 2009. **55**(2): p. 163-78.
97. Boese, J., Osanna, A., Jacobsen, C., Kirz, J., *Carbon edge XANES spectroscopy of amino acids and peptides.* Journal of Electron Spectroscopy and Related Phenomena, 1997. **85**(1–2): p. 9-15.
98. Coker, V.S., Byrne, J. M., Telling, N. D., Van Der Laan, G., Lloyd, J. R., Hitchcock, A. P., Wang, J., Pattrick, R. A. D., *Characterisation of the dissimilatory reduction of Fe(III)-*

oxyhydroxide at the microbe – mineral interface: the application of STXM–XMCD. Geobiology, 2012. **10**(4): p. 347-354.
99. Morin, C., Hitchcock, A. P., Cornelius, R. M., Brash, J. L., Urquhart, S. G., Scholl, A., Doran, A., *Selective adsorption of protein on polymer surfaces studied by soft X-ray photoemission electron microscopy.* Journal of Electron Spectroscopy and Related Phenomena, 2004. **137–140**(0): p. 785-794.
100. Chan, C.S., Fakra, S. C., Edwards, D. C., Emerson, D., Banfield, J. F., *Iron oxyhydroxide mineralization on microbial extracellular polysaccharides.* Geochimica et Cosmochimica Acta, 2009. **73**(13): p. 3807-3818.
101. Harneit, K., Göksel, A., Kock, D., Klock, J. H., Gehrke, T., Sand, W., *Adhesion to metal sulfide surfaces by cells of Acidithiobacillus ferrooxidans, Acidithiobacillus thiooxidans and Leptospirillum ferrooxidans.* Hydrometallurgy, 2006. **83**(1–4): p. 245-254.
102. Yang, Y., Liu, W., Chen, M., *A copper and iron K-edge XANES study on chalcopyrite leached by mesophiles and moderate thermophiles.* Minerals Engineering, 2013. **48**(0): p. 31-35.
103. Yang, Y., Harmer, S., Chen, M., *Synchrotron X-ray photoelectron spectroscopic study of the chalcopyrite leached by moderate thermophiles and mesophiles.* Minerals Engineering, 2014. **69**: p. 185-195.
104. Yang, H.-Y., Liu, W., Chen, G.-B., Liu, Y.-Y., Tong, L.-L., Jin, Z.-N., Liu, Z.-L., *Function of microorganism and reaction pathway for carrollite dissolution during bioleaching.* Transactions of Nonferrous Metals Society of China, 2015. **25**(8): p. 2718-2754.
105. Kalirai, S.S., Lam, K. P., Bazylinski, D. A., Lins, U., Hitchcock, A. P., *Examining the chemistry and magnetism of magnetotactic bacterium Candidatus Magnetovibrio blakemorei strain MV-1 using scanning transmission X-ray microscopy.* Chemical Geology, 2012. **300–301**(0): p. 14-23.
106. Belu, A.M., Davies, M. C., Newton, J. M., Patel, N., *TOF-SIMS Characterization and Imaging of Controlled-Release Drug Delivery Systems.* Analytical Chemistry, 2000. **72**(22): p. 5625-5638.
107. Berman, E.S.F., Wu, L., Fortson, S. L., Kulp, K. S., Nelson, D. O., Wu, K. J., *Chemometric and statistical analyses of ToF-SIMS spectra of increasingly complex biological samples.* Surface and Interface Analysis, 2009. **41**(2): p. 97-104.
108. de Brouwer, J.F.C., Cooksey, K. E., Wigglesworth-Cooksey, B., Staal, M. J., Stal, L. J., Avci, R., *Time of Flight-Secondary Ion Mass Spectrometry on isolated extracellular fractions and intact biofilms of three species of benthic diatoms.* Journal of Microbiological Methods, 2006. **65**(3): p. 562-572.
109. Brito e Abreu, S., Brien, C., Skinner, W., *ToF-SIMS as a New Method to Determine the Contact Angle of Mineral Surfaces.* Langmuir, 2010. **26**(11): p. 8122-8130.
110. Brandl, H., *Microbial Leaching of Metals*, in *Biotechnology Set*. 2008, Wiley-VCH Verlag GmbH. p. 191-224.
111. Rimstidt, J.D., Vaughan, D. J., *Pyrite oxidation: a state-of-the-art assessment of the reaction mechanism.* Geochimica et Cosmochimica Acta, 2003. **67**(5): p. 873-880.
112. Schaufuß, A.G., Nesbitt, H. W., Kartio, I., Laajalehto, K., Bancroft, G. M., Szargan, R., *Incipient oxidation of fractured pyrite surfaces in air.* Journal of Electron Spectroscopy and Related Phenomena, 1998. **96**(1–3): p. 69-82.
113. Chandra, A.P., Gerson, A. R., *The mechanisms of pyrite oxidation and leaching: A fundamental perspective.* Surface Science Reports, 2010. **65**(9): p. 293-315.
114. Pradier, C.M., Rubio, C., Poleunis, C., Bertrand, P., Marcus, P., Compère, C., *Surface Characterization of Three Marine Bacterial Strains by Fourier Transform IR, X-ray Photoelectron Spectroscopy, and Time-of-Flight Secondary-Ion Mass Spectrometry, Correlation with Adhesion on Stainless Steel Surfaces.* The Journal of Physical Chemistry B, 2005. **109**(19): p. 9540-9549.

115. Heim, C., Sjövall, P., Lausmaa, J., Leefmann, T., Thiel, V., *Spectral characterisation of eight glycerolipids and their detection in natural samples using time-of-flight secondary ion mass spectrometry.* Rapid Communications in Mass Spectrometry, 2009. **23**(17): p. 2741-2753.
116. Vaidyanathan, S., Fletcher, J. S., Jarvis, R. M., Henderson, A., Lockyer, N. P., Goodacre, R., Vickerman, J. C., *Explanatory multivariate analysis of ToF-SIMS spectra for the discrimination of bacterial isolates.* Analyst, 2009. **134**(11): p. 2352-2360.
117. Biesinger, M.C., Miller, D. J., Harbottle, R. R., Possmayer, F., McIntyre, N. S., Petersen, N. O., *Imaging lipid distributions in model monolayers by ToF-SIMS with selectively deuterated components and principal components analysis.* Applied Surface Science, 2006. **252**(19): p. 6957-6965.
118. Baldwin, P.M., Melia, C. D., Davies, M. C., *The Surface Chemistry of Starch Granules Studied by Time-of-Flight Secondary Ion Mass Spectrometry.* Journal of Cereal Science, 1997. **26**(3): p. 329-346.
119. Robinson, M.A., Graham, D. J., Morrish, F., Hockenbery, D., Gamble, L. J., *Lipid analysis of eight human breast cancer cell lines with ToF-SIMS.* Biointerphases, 2016. **11**(2): p. 02A303.
120. Behera, S.K., Mulaba-Bafubiandi, A. F., *Microbes Assisted Mineral Flotation a Future Prospective for Mineral Processing Industries: A Review.* Mineral Processing and Extractive Metallurgy Review, 2017. **38**(2): p. 96-105.
121. Sanni, O.D., Wagner, M. S., Briggs, D., Castner, D. G., Vickerman, J. C., *Classification of adsorbed protein static ToF-SIMS spectra by principal component analysis and neural networks.* Surface and Interface Analysis, 2002. **33**(9): p. 715-728.
122. Schilke, K.F., McGuire, J., *Detection of nisin and fibrinogen adsorption on poly(ethylene oxide) coated polyurethane surfaces by time-of-flight secondary ion mass spectrometry (TOF-SIMS).* Journal of Colloid and Interface Science, 2011. **358**(1): p. 14-24.
123. Breitenstein, D., Rommel, C. E., Stolwijk, J., Wegener, J., Hagenhoff, B., *The chemical composition of animal cells reconstructed from 2D and 3D ToF-SIMS analysis.* Applied Surface Science, 2008. **255**(4): p. 1249-1256.
124. Beech, I.B., Sunner, J., *Biocorrosion: towards understanding interactions between biofilms and metals.* Current Opinion in Biotechnology, 2004. **15**(3): p. 181-186.
125. Rojas-Chapana, J.A., Tributsch, H., *Bio-leaching of pyrite accelerated by cysteine.* Process Biochemistry, 2000. **35**(8): p. 815-824.
126. Tervahattu, H., Juhanoja, J., Kupiainen, K., *Identification of an organic coating on marine aerosol particles by TOF-SIMS.* Journal of Geophysical Research: Atmospheres, 2002. **107**(D16): p. ACH 18-1-ACH 18-7.
127. Khmeleva, T.N., Georgiev, T. V., Jasieniak, M., Skinner, W. M., Beattie, D. A., *XPS and ToF-SIMS study of a chalcopyrite–pyrite–sphalerite mixture treated with xanthate and sodium bisulphite.* Surface and Interface Analysis, 2005. **37**(8): p. 699-709.
128. Boulton, A., Fornasiero, D., Ralston, J., *Characterisation of sphalerite and pyrite flotation samples by XPS and ToF-SIMS.* International Journal of Mineral Processing, 2003. **70**(1–4): p. 205-219.
129. Hart, B., Biesinger, M., Smart, R. St. C., *Improved statistical methods applied to surface chemistry in minerals flotation.* Minerals Engineering, 2006. **19**(6–8): p. 790-798.
130. Berman, E.S.F., Kulp, K. S., Knize, M. G., Wu, L., Nelson, E. J., Nelson, D. O., Wu, K. J., *Distinguishing Monosaccharide Stereo- and Structural Isomers with TOF-SIMS and Multivariate Statistical Analysis.* Analytical Chemistry, 2006. **78**(18): p. 6497-6503.
131. Jungnickel, H., Jones, E. A., Lockyer, N. P., Oliver, S. G., Stephens, G. M., Vickerman, J. C., *Application of TOF-SIMS with Chemometrics To Discriminate between Four Different Yeast Strains from the Species Candida glabrata and Saccharomyces cerevisiae.* Analytical Chemistry, 2005. **77**(6): p. 1740-1745.

132. Vaidyanathan, S., Fletcher, J. S., Lockyer, N. P., Vickerman, J. C., *TOF-SIMS investigation of Streptomyces coelicolor, a mycelial bacterium.* Applied Surface Science, 2008. **255**(4): p. 922-925.
133. Comte, S., Guibaud, G., Baudu, M., *Relations between extraction protocols for activated sludge extracellular polymeric substances (EPS) and EPS complexation properties: Part I. Comparison of the efficiency of eight EPS extraction methods.* Enzyme and Microbial Technology, 2006. **38**(1–2): p. 237-245.
134. Li, Q., Wang, Q., Zhu, J., Zhou, S., Gan, M., Jiang, H., Sand, W., *Effect of Extracellular Polymeric Substances on Surface Properties and Attachment Behavior of Acidithiobacillus ferrooxidans.* Minerals, 2016. **6**(4): p. 100.

5 Characterisation of *Leptospirillum ferrooxidans* and Pyrite: Growth Behaviour and Mineral Surface Properties.

5.1 Introduction

The bacterial strain *Leptospirillum ferrooxidans* has been applied in many leaching investigations due to its ability to oxidise Fe(II) to Fe(III), as was explored in Chapter 2, section 2.2.3 [1-8]. The pure strain of this microorganism is currently not as commonly used for bioflotation, although many studies use it as part of mixed cultures, leaving is application as a flotation reagent largely unexplored [2-6]. Bioflotation investigations using *L. ferrooxidans* have focussed mainly on the mineral recovery of chalcopyrite, sphalerite, pyrrhotite and pyrite, with no investigation of the cells or the sulfide mineral surfaces [9-11].

Unlike the bacterium *A. ferrooxidans* investigated in the previous chapter, *L. ferrooxidans* is unable to use sulfur as a source of nutrients, potentially creating a different chemical environment on the surface of sulfide minerals [1, 12, 13]. This bacterial strain is widely recognised as a major producer of extracellular polymeric substances (EPS), which would suggest it would be ideal for flotation studies, where large amounts of biomass are required for industrial applications [1, 3, 14]. It has also been identified as a more efficient oxidiser of pyrite than *A. ferrooxidans*, suggesting any surface effects due to oxidation on the surface may be accelerated in comparison [15].

The flotation studies conducted using *L. ferrooxidans* have focussed on chalcopyrite in comparison with other sulfide minerals, with inconsistent condition and often contradictory findings making comparison challenging [9-11]. These studies perform flotation experiments using chemical collector, which has been shown to negatively impact cell activity, and thus is likely to interfere with mineral-cell interactions and EPS production [16]. They also involve processing of the cells, including washing and artificially concentrating the cells by centrifugation before exposing the cells to the mineral which may be altering natural cell behaviour and changing the nature of their excretions [9-11].

A thorough study of a pure strain of *L. ferrooxidans*, in the absence of synthetic flotation reagent and other forms of pre-processing, for its potential application to bioflotation has yet to be explored. In this chapter, pyrite is exposed to *L. ferrooxidans* and the surface of the mineral will be analysed for signs of EPS and bacterial attachment, with special interest taken in the time-frame over which attachment occurs and how the chemical species on the surface are changed by the presence of the bacteria. No previous study has been found on the bioleaching or bioflotation capabilities of *L.*

ferrooxidans that successfully compares mineral surface roughness in relation to the hydrophobicity of the sample and the presence and spread of cells on the surface.

5.2 Experimental

5.2.1 Mineral Preparation

The bulk pyrite for culture growth is described in in Chapter 3, section 3.2, Table 3.4. The cubic pyrite used for this investigation and the preparation of mineral tile samples are described in Chapter 3, sections 3.2 and 3.4, respectively.

Tiles were either snap frozen in HH medium for AFM and ToF-SIMS analysis or stored in fixative for dehydration and sputtering coating for SEM by methods described in Chapter 3, section 3.9.

5.2.2 Cell Growth and Monitoring

Cultures of *L. ferrooxidans* (DSM 2705) were received live from the DSMZ (Deutsche Sammlung von Mikroorganismen und Zellkulturen) and inoculated into HH medium and continuously subcultured as described in Chapter 3, section 3.3.1. Cultures were monitored by direct cell counting, as described in Chapter 3, section 3.8.

5.2.3 Surface Characterisation

Surface analysis of pyrite control and those exposed to *L. ferrooxidans* were performed using Scanning Electron Microscope (SEM), Energy Dispersive X-ray spectroscopy (EDX), Atomic Force Microscopy (AFM), captive bubble contact angle, Scanning Transmission X-ray Microscopy (STXM) and Near-edge X-ray Absorption Fine Structure (NEXAFS), and Time of Flight – Secondary Ion Mass Spectroscopy (ToF-SIMS). Details for these techniques can be found in Chapter 3, sections 3.9, 3.10, 3.11, 3.13, 3.14 and 3.16.

5.3 Results and Discussion

5.3.1 Growth of *Leptospirillum ferrooxidans* on Pyrite and Chalcopyrite

5.3.1.1 Cell Growth

The live culture of *L. ferrooxidans* was first cultured on HH medium containing ferrous sulfate, with growth of this culture monitored by titrating against cerium(IV) sulfate to determine the concentration of Fe(II), from which the bacteria obtain their energy as it oxidises to Fe(III) [17, 18]. Figure 5.46 shows a typical concentration curve of the *L. ferrooxidans* base culture at 5% inoculum.

The control solution of HH medium containing ferrous sulfate is identical to that presented for *A. ferrooxidans* in the previous chapter, section 4.3.1.

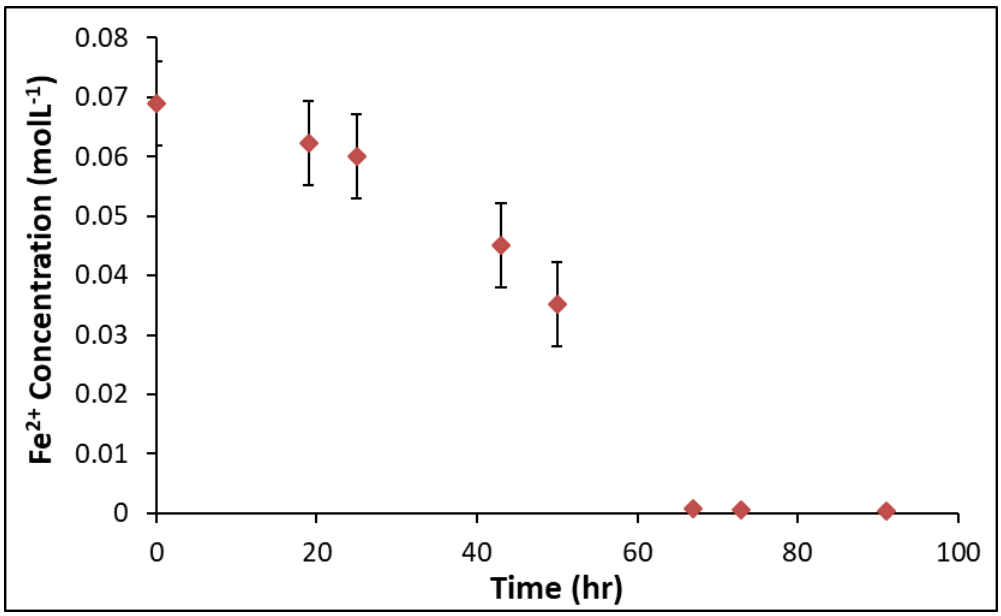

Figure 5.46: Ferrous iron titration curves of *L. ferrooxidans* in HH medium at 5% inoculum.

The ferrous iron concentration in *L. ferrooxidans* grown on HH medium containing ferrous sulfate reaches exponential phase at the same period as *A. ferrooxidans*, with cultures at the same inocula volumes reaching stationary phase after 72 h. This suggests that when ferrous iron is the sole source of nutrients, the two strains show identical cell activity. As such, the 5% inoculum base culture was suitable for subculturing for the adaptation to ground pyrite, with comparable conditions to the *A. ferrooxidans* culture in the previous chapter. *L. ferrooxidans* was adapted to grow on pyrite by subculturing from cultures grown on soluble ferrous sulfate into HH medium with 20 g of UV sterilised pyrite replacing the ferrous sulfate as described in Chapter 3, section 3.3.1. Cultures were inoculated at 10% with *L. ferrooxidans*. Growth curves on pyrite were determined by counting, and a typical growth curve is shown in Figure 5.47.

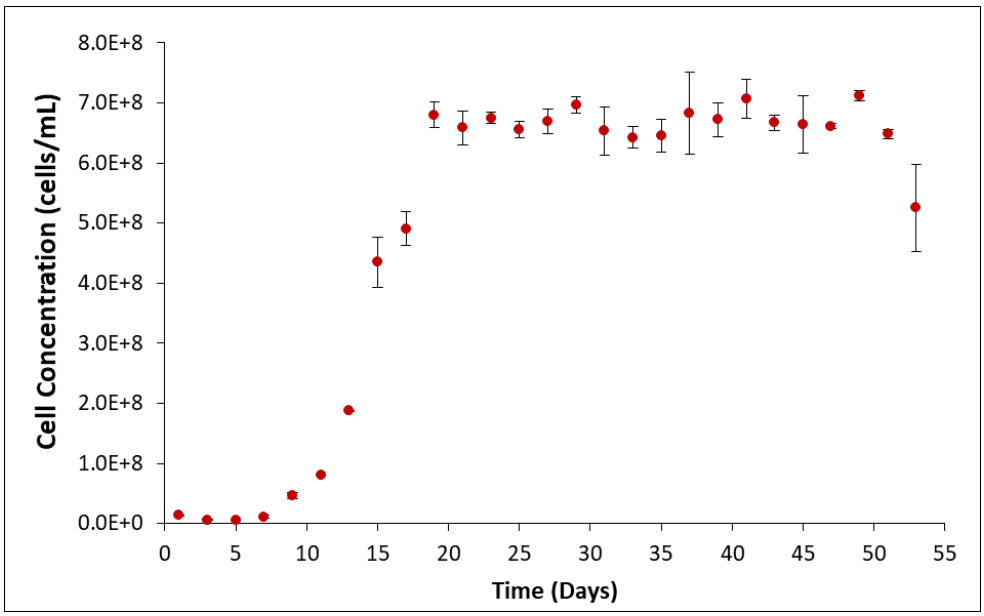

Figure 5.47: Typical growth curve of *L. ferrooxidans* on pyrite (+38, -75 um) at 10% inoculum.

When grown on a solution that contains soluble ferrous iron, *L. ferrooxidans* typically reach the exponential phase between 20-40 hours, completing a growth cycle in approximately 96 hours (Figure 5.46). When grown on pyrite, the *L. ferrooxidans* culture typically reaches the exponential phase between 11-19 days, completing a growth cycle in approximately 7 weeks (Figure 5.47). Final cell concentrations of *L. ferrooxidans* on pyrite were found to be over 6.5×10^8 cells/mL.

The results presented here agree with the final cell concentrations previously described growth of *L. ferrooxidans* on pyrite. Previous studies of *L. ferrooxidans* on a variety of substrates ranges between 10^7 and 10^{10} cells/mL, with stationary phase reached typically between 4-16 days on mineral or ore sources and 10-40 hours on a variety of media solutions [3, 6-8, 10, 19-21]. As was the case for *A. ferrooxidans*, inocula volume, growth rates and mineral adaptability can vary greatly with each new growth cycle, and individual lab strains might behave differently, making direct comparison challenging.

The growth of *L. ferrooxidans* is not very well characterised in the literature, with most previous work being performed on mixed cultures or other sulfidic ores [3, 6-8, 10, 20, 21]. Other studies have investigated cell population by counting cell adhesion to mineral [3, 8, 10, 21]. This involves pre-concentration of cells to a known number, followed by exposure to ground mineral for a short period, after which the decrease in cell population in solution is attributed to cell adhesion to the surface [3, 8, 10, 20, 21].

5.3.1.2 Eh and pH Monitoring

The pyrite HH medium control pH and Eh presented here is identical to that shown in Chapter 4, section 4.3.1.2. The pH of the *L. ferrooxidans* culture grown on pyrite starts at 1.8, dropping to pH 0.9 at its lowest point on day 49, where sits below for the remainder of the exposure. The Eh values for *L. ferrooxidans* exposed to pyrite are reported relative to an Ag/AgCl electrode at 1 atm, with an average temperature of 21.6 ± 1.3 °C. The Eh and pH curves of the HH medium and *L. ferrooxidans* pyrite leachate is shown in Figure 5.48.

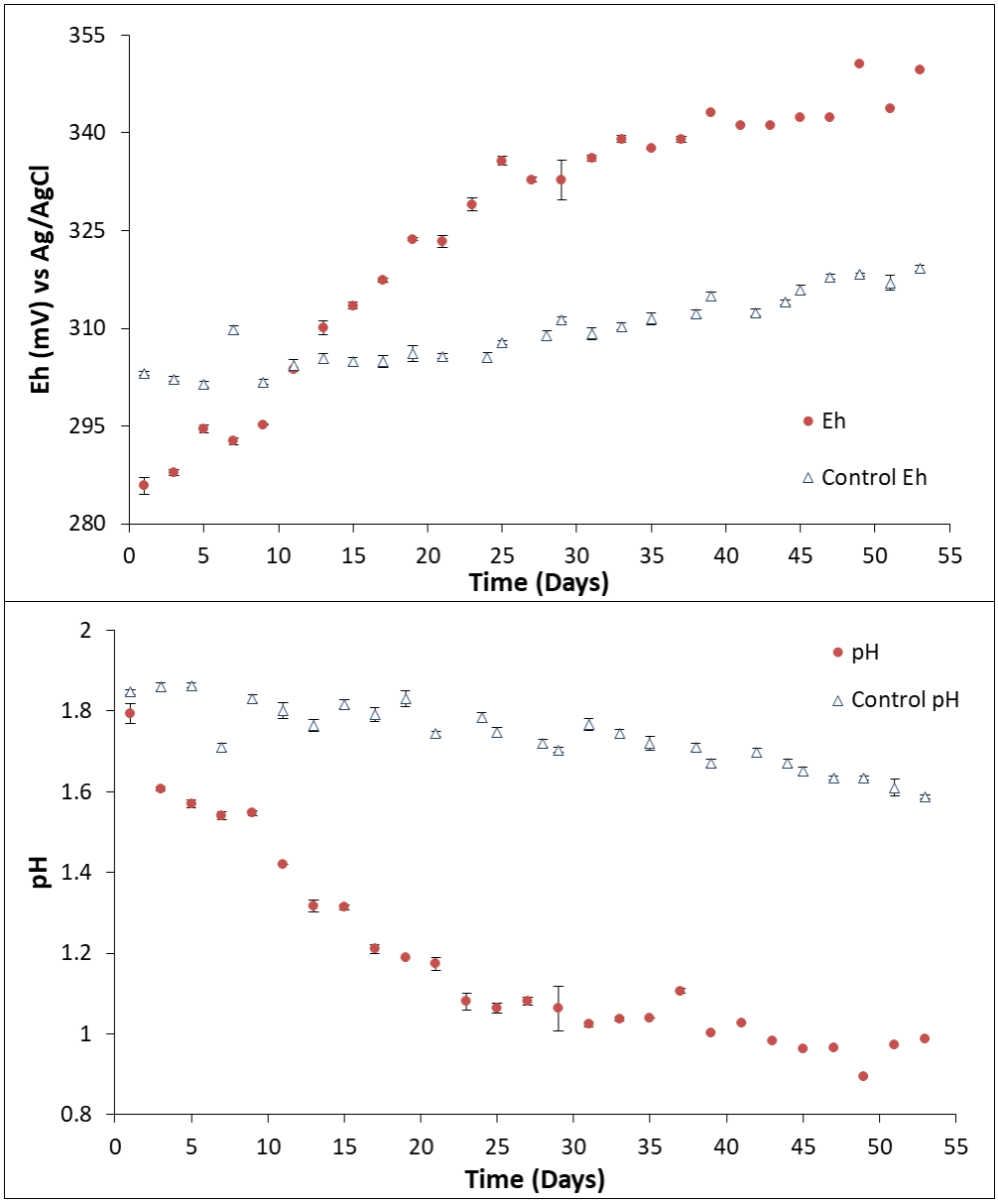

Figure 5.48: Typical Eh (top) and pH (bottom) curves of *L. ferrooxidans* on pyrite (+38, -75 um) at 10% inoculum (●), and HH medium (Δ).

The pH values measured over the course of these experiments suggests that the consumption of sulfuric acid is outweighed by production, with the pH never greater than the initial value measured for the medium solution. This suggests the surface of the mineral is leaching at an accelerated rate

when exposed to *L. ferrooxidans*, promoting the production of soluble iron and sulfur species in solution, and iron oxidise and elemental sulfur on the surface of the mineral to a greater extent than on the control surface (see Equations 4.37-4.43, Chapter 4, section 4.3.1.2) [22-31]. Lower pH is also less conducive to the formation of jarosite [32]. The Eh of the *L. ferrooxidans* culture grown on pyrite steadily increases from just over 285 mV to over 349 mV over the course of the natural growth cycle. The Eh values in the pyrite mineral culture increases over time, suggesting oxidative conditions are occurring, promoting the formation of hydrophilic oxidation species such as sulfates and iron hydroxides (Equations 4.37-4.39, 4.41 and 4.43) and on the surface and increasing the concentration of ferric iron and soluble sulfur species in solution [22-31].

Previous studies have measured the Eh and pH of leachate of a variety of substrates using *L. ferrooxidans*, a summary of which can be found in Table 5.8. All potentials reported here have been converted to Ag/AgCl reference electrode values where appropriate.

Table 5.8: Previous Eh and pH studies of *L. ferrooxidans* bioleaching on a variety of substrates.

Substrate	Duration (days)	Eh $_{init.}$ (mV)	Eh $_{fin.}$ (mV)	pH $_{init.}$	pH $_{fin.}$	Reference
Ferrous sulfate	0.02		540-650	-	-	[33]
Pyrite [a]	80	600	750	3	2	[19]
Pyrite [b]	20	270	420	1.5	1.7	[34]
Pyrite [b]	29	380	380	1.8	1.6	[35]
Pyrite [b]	24	-	-	2.05	1.92	[36]
Pyrite and Chalcopyrite [a]	40	400	700	-	-	[4]
Chalcopyrite [a]	30	375	650	-	-	[6]
Chalcopyrite [b]	30	375	375	-	-	[6]

[a] Mixed culture, [b] Abiotic control

The Eh and pH of the pyrite leachate presented in Figure 5.48 agree with the trends observed in the literature, however due to the mixture of cultures, pure culture studies like the one presented here are necessary to isolate the effects of each individual strain on select minerals [4, 6, 19]. Xia *et al* observed that the starting Eh of the HH medium control was lower than that of pyrite culture Eh, but the Eh measured after 20 days was higher in the culture than the control, a result which is observed in this study, over a longer time frame [34].

The difference between the Eh of the pyrite culture and the abiotic control is most pronounced at longer exposure stages, suggesting the pyrite surface becomes more oxidised as cell population increases. These results suggest initial contact with the surface may be necessary for *L. ferrooxidans*

to impact the leaching of the mineral surface, indicating either the direct or indirect contact mechanisms may govern the interaction. The soluble iron and sulfur species that contribute to Eh in the leaching of pyrite are investigated in the following section using titration and Inductively Coupled Plasma Optical Emission Spectroscopy (ICPOES).

5.3.1.3 Inductively Coupled Plasma Optical Emission Spectroscopy, Cerium(IV) Sulfate Titration

Ferrous iron concentration and ferric iron concentration were determined by colorimetric titration against cerium(IV) sulfate and ICPOES, respectively, with the methods described in Chapter 3, sections 3.6 and 3.7. The sulfur concentration represented here describes all soluble sulfur species. The ferrous iron, ferric iron and soluble sulfur concentrations of the leachate of pyrite exposed to HH medium and *L. ferrooxidans* culture are shown in Figure 5.49. The HH medium iron and sulfur concentrations are identical to those discussed in Chapter 4, section 4.3.1.3.

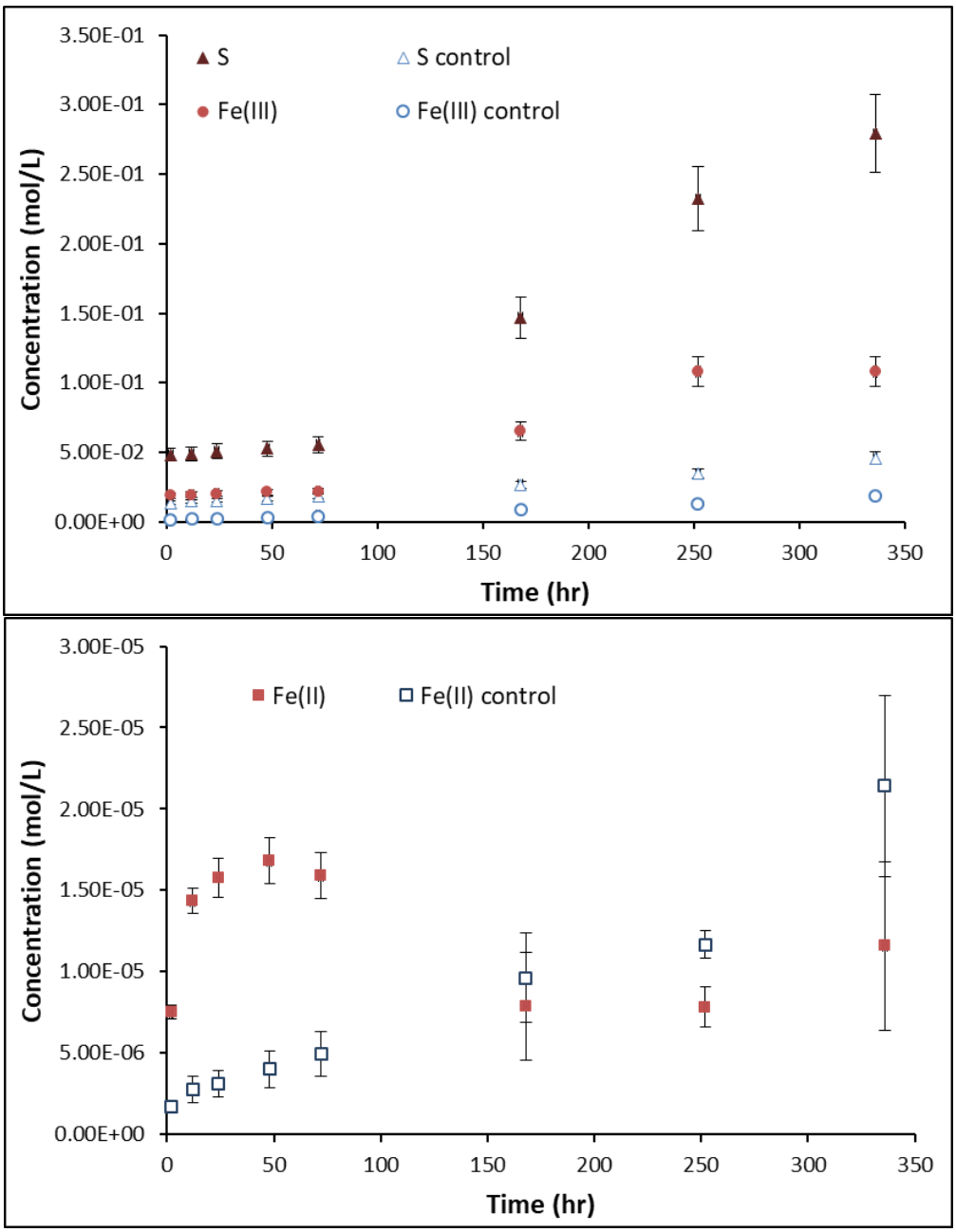

Figure 5.49: Typical concentration curves of (top) of *L. ferrooxidans* on pyrite (●), and HH medium (○). and solubilised sulfur in *L. ferrooxidans* on pyrite (▲), and HH medium (Δ). Typical concentration curves of ferrous iron (bottom) of *L. ferrooxidans* on pyrite (■), and HH medium (□).

The concentration in solution of Fe^{3+} of pyrite exposed to *L. ferrooxidans* remains between $1.9x10^{-2}$ and $2.2x10^{-2}$ mol/L for the first 72 h, then increases to 0.11 mol/L by 250 h, and remains unchanged by 336 h. The concentration of Fe^{2+} increases from an initial concentration of $7.0x10^{-6}$ mol/L to a maximum of $1.7x10^{-5}$ mol/L over the first 168 h, after which the concentration decreases to $7.9x10^{-6}$ mol/L at 168-250 h, then increases to a final concentration of $1.2x10^{-5}$ mol/L at 336 h. The concentration of dissolved sulfur in solution follows a similar trend to that of Fe^{3+}, remaining between $4.8x10^{-2}$-$5.5x10^{-2}$ mol/L for the first 72 h, then increasing to 0.28 mol/L by 336 h. Unlike the Fe^{3+} curve, which remains the same between 250 and 336 h, the dissolved sulfur concentration continues to increase.

Any increase in ferric iron concentration could lead to greater ferric iron leaching of the surface, in turn producing more Fe^{2+} ions, while both ferric iron and bacterial leaching may produce soluble sulfur species, meaning the concentration of dissolved sulfur is seen to continue to increase [19, 21]. The ferrous iron concentration increases initially, suggesting that the acid is being consumed and releasing Fe^{2+} into solution early on in exposure as per Equation 4.40 (Chapter 4, section 4.3.1.2), when bacterial numbers are at their lowest. As bacterial numbers start to increase, the Fe^{2+} in solution begins to be oxidised by the cells, causing the concentration in Fe^{2+} to decrease, coinciding with an increase Fe^{3+} concentration. This corresponds to the beginning of the *L. ferrooxidans* exponential phase [19, 21]. These results agree with the Eh curves, that show ferric iron and soluble sulfur concentrations are increasing over the period of exposure as surface oxidation continues, with the control Eh and ion concentrations increasing very little. This suggests the surface is likely to be rich in iron oxides, elemental sulfur and oxygenated sulfur species [22-31].

Few previous studies have analysed the iron concentration leached from pyrite by pure *L. ferrooxidans* cultures, and those that do report the total iron yielded after leaching experiments have been conducted [3, 37]. Previous investigations have monitored the iron concentrations on pyrite leached by *L. ferrooxidans* in mixed cultures, however there is no uniform method for reporting iron concentrations in solution [19, 21]. No previous sterile control measurements were found in the literature for comparison with total dissolved sulfur concentration measured here. As was the case in the previous chapter, the lack of abiotic experiments performed in previous studies prevents an effective comparison of biotic leaching to abiotic leaching. The studies into solution component concentrations show a wide variation in initial and final iron concentrations, making direct comparison difficult and highly dependent of culture conditions and nutrient sources. However, the values presented here are within the ranges of values found by other investigations, suggesting they are not unreasonable, and may provide insight into how *L. ferrooxidans* interacts with pyrite mineral.

The lack of pure culture and pure mineral investigations in this area, coupled with no uniform methods of data reporting has created a gap in understanding how *L. ferrooxidans* behaves upon exposure to pyrite, and shows that more rigorous culture monitoring is needed in leaching experiments using this microorganism. Many of these studies are linking the results of solution analysis to surface effects on the mineral such as the formation of inhibitory Fe^{2+} layers [21], cell adhesion [19] and oxidation species [4, 20] without presenting surface analysis that can confirm these proposed relationships. To relate the solution ion content, Eh and pH to the behaviour of *L. ferrooxidans* on the surface of pyrite, and to identify secondary mineral formation and leaching progression, it is necessary to investigate the surface using imaging techniques.

5.3.2 Scanning Electron Microscopy and Energy Dispersive X-ray Spectroscopy

To relate solution conditions to the mineral leaching and cell interaction with the mineral surface, scanning electron microscopy (SEM) is used to provide images of the pyrite and *L. ferrooxidans*. Typical SEM images obtained for pyrite upon exposure to HH medium control in comparison to pyrite exposed to *L. ferrooxidans* are shown in Figure 5.50.

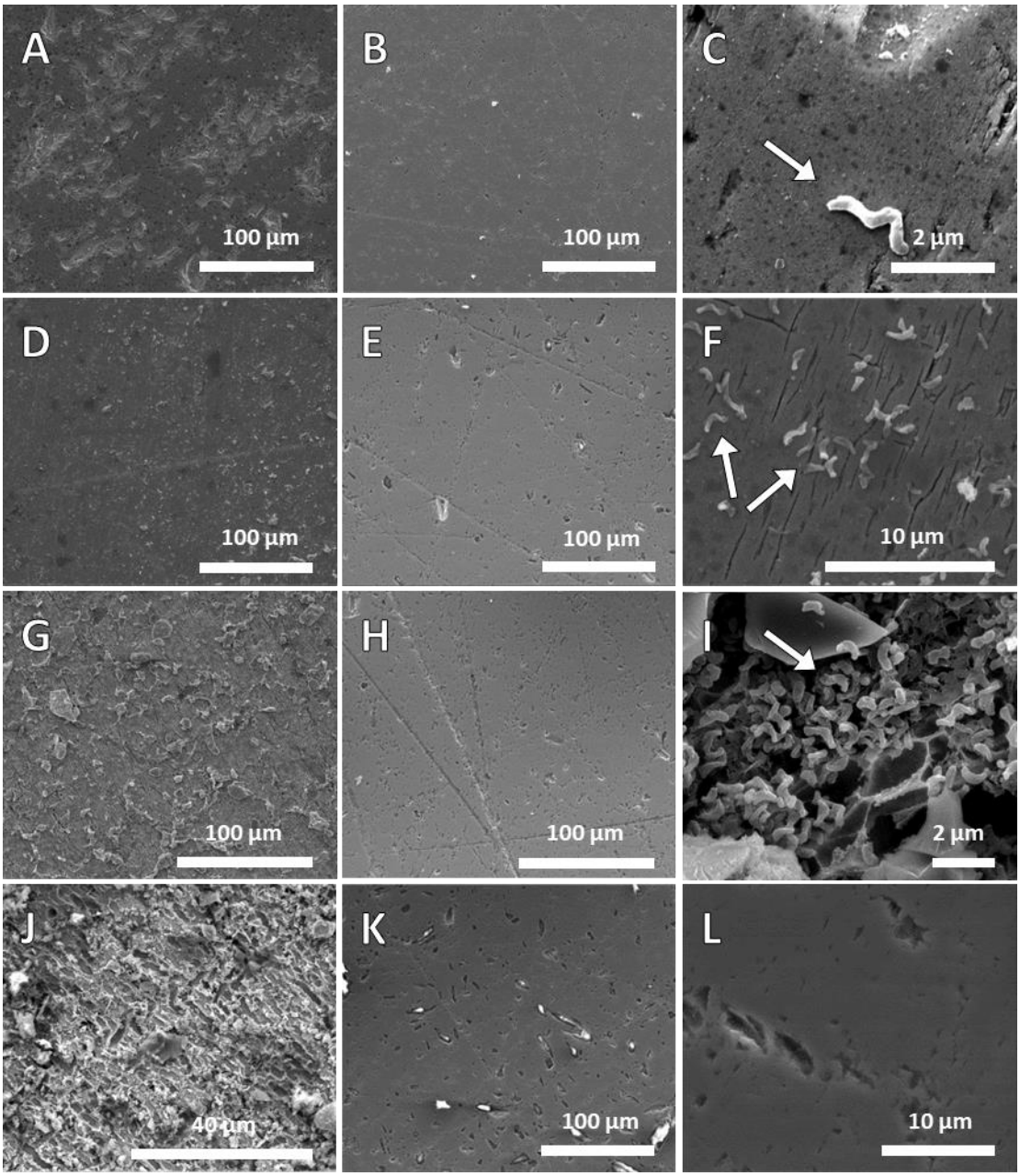

Figure 5.50: Pyrite tiles exposed to *L. ferrooxidans* for 2 h (A), 24 h (D), 72 h (G) and 168 h (J), pyrite tiles exposed to HH medium for 2 h (B), 24 h (E), 72 h (H) and 168 h (K), *L. ferrooxidans* cells, indicated by arrows (C), leaching rivers (F), *L. ferrooxidans* biofilm (I) etch pits (L).

The surface of pyrite exposed to HH medium has been described previously in Chapter 4, section 4.3.2. In summary, for each period of exposure (Figure 5.50(B, E, H, and K)), the pyrite shows some pitting, typically regularly orientated and 0.8-1.8 µm in length and 0.2-0.8 µm wide, with

some scratches remaining on the surface from the polishing process. Etch pits increase in number on the surface after 168 h. The pyrite exposed to the medium for 2 h is all but identical to the bare polished pyrite shown in Figure 4.26 in the previous chapter (chapter 4, section 4.3.2).

After 2 h exposure to pyrite (see Figure 5.50(L)), *L. ferrooxidans* cells are observed on the surface with no apparent preference for surface defects as cells were found on smooth areas of the surface (see Figure 5.50(C)). Etch pits on the surface are comparable in size to those observed on the control mineral at this period of exposure. *L. ferrooxidans cells* were found to be average of 0.76 μm^2 in area, with cell coverage at this stage of exposure calculated at 0.57 ± 0.14 %. This level of coverage is similar to that observed for *A. ferrooxidans* at 2 h of exposure (Chapter 4, section 4.3.2). After 24 h of exposure of the pyrite surface to *L. ferrooxidans*, the cell population has dramatically increased. There is still no apparent preference for surface defects of the cells on the surface, and the cells appear to be uniformly distributed across the surface with random orientation, shown in Figure 5.50(F). There is a greater amount of loose debris on the surface compared with the HH medium control (Figure 5.50(D)). The sample exposed to the *L. ferrooxidans* also appears to have fine cracks appearing in the mineral surface, a pattern which was also observed on pyrite exposed to *A. ferrooxidans* at this exposure period (Figure 5.50(F)) The cell coverage at this stage of exposure has been calculated at approximately 3.32 ± 0.40 %. After 72 h of exposure to *L. ferrooxidans*, the pyrite is covered in debris in a wide range of shapes and sizes, visible in Figure 5.50(G). The surface is showing deeper rivers along crystal boundaries, than the cracks observed at 24 h. These rivers have been identified by previous investigation to be caused by ferric iron leaching and not direct bacterial action [38]. Cells cover the surface in random orientation, and are also seen adhered to the mineral debris, with cell coverage measured at 10.7 ± 3.94 %. This coverage is more than double the coverage observed at 24 h, and significantly greater than the coverage measured for *A. ferrooxidans* after the longest period of exposure (Chapter 4, section 4.3.2). After 168 h of exposure to *L. ferrooxidans*, the pyrite sample is heavily leached and covered in cells and biofilm, the extent of which is difficult to quantify due to the number of particles coated in cells that have adhered to the surface, as are observed in Figure 5.50(I). The surface shows signs of advanced leaching (Figure 5.50(J)), with some areas of the surface exhibited a great deal of charging due to the thick carbon layer due to the biofilm coating the surface, making clear images hard to obtain in these areas. Advanced pitting in regularly arranged shapes in sizes ranging from 3-9 μm long and 2.5-3.5 μm wide cover the surface, and appear coated in strand-like material, the identity of which was investigated using EDX.

The results found here agree with previous studies, which suggest that this strain has been found to adhere more significantly to pyrite than other microorganisms [3], and dominates adhered cell

populations over longer periods of exposure [8]. The number of cells on the surface is seen to increase, which agrees with many adhesion studies performed on *L. ferrooxidans* [3, 8, 10]. The amount of debris on the surface appears to be increasing at a significantly greater rate and in greater size than those observed on pyrite exposed to *A. ferrooxidans*, with etching of the surface appearing more advanced. These results suggest initial attachment takes place prior to the significant mineral leaching observed in the Eh/pH and ICPOES, indicating cell attachment and/or EPS production is necessary for *L. ferrooxidans* to impact the pyrite surface. This further suggests either the direct contact mechanism, the indirect contact mechanism, or a combination of both determines the interaction of this strain with the pyrite surface.

Very few papers were identified performed abiotic control leaching experiments for the purposes of SEM compare to biotic leaching experiments. Studies by Xia *et al* and Mitsunobu *et* al observed a smooth mineral surface on pyrite after extended periods of exposure (≥20 days), both of which agrees with the comparatively smooth control surfaces observed in this study [34, 39]. Several studies air-dry their samples, which makes any comparison to attachment of cells on the surface impossible [32, 34]. The lack of control images being collected in biotic leaching studies, combined with the lack of consistency in sample preparation and pH of leaching solutions, makes comparing results challenging, and isolating bacterial action from chemical leaching more difficult. The information on the propagation of this microorganism on mineral surfaces provided by this study fills an important gap in the literature, showing an unexpected lack of preference of this strain for defect sites, and the much-accelerated biofilm formation compared to other more heavily studied strains.

The elemental composition of surface artefacts, and the identification of cellular material as distinct from secondary mineral precipitates was determined using EDX analysis. The EDX analysis of the pyrite surface exposed to *L. ferrooxidans* are shown in Figure 5.51 as average atomic percentage. The elements Si, Al and Na were detected at levels below 2%.

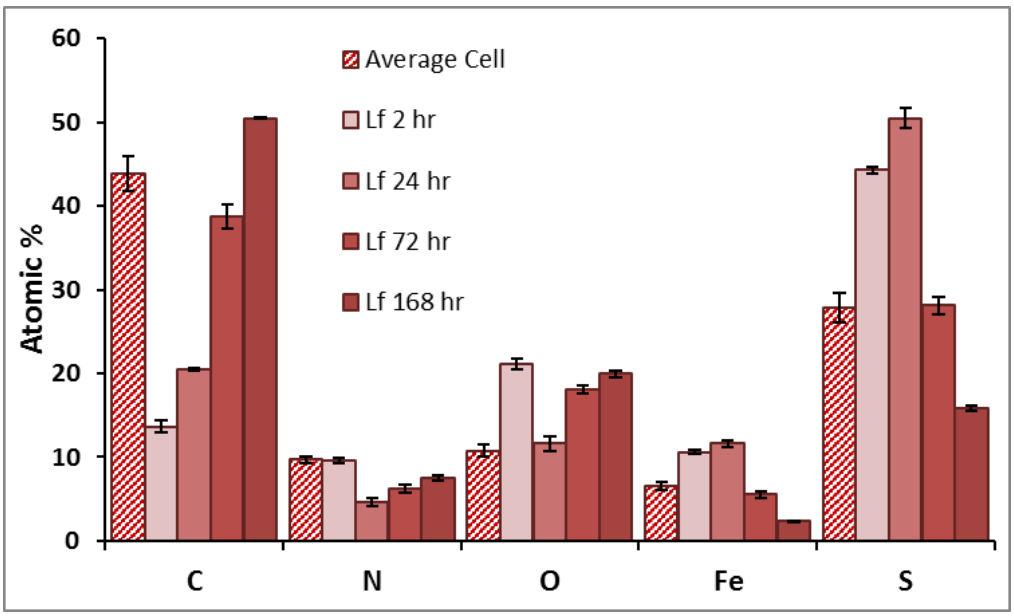

Figure 5.51: Average atomic percentage of pyrite exposed to *L. ferrooxidans* for 2, 24, 72 and 168 h, and the average atomic percentage of individual *L. ferrooxidans* cells (pattern), as determined by EDX

The individual cells of *L. ferrooxidans* present a significant carbon signal compared to bare spots mineral measured, however cells are typically not thick enough to block all signal from the bulk mineral beneath, which is why typical pyrite signals of Fe and S are still observed [40]. The pyrite surface exposed to *L. ferrooxidans* displays significant changes in elemental composition over time. Over the course of exposure, the amount of carbon, nitrogen and oxygen detected on the surface increases, agreeing with the significant biofilm coverage of *L. ferrooxidans* on the surface, a phenomenon not observed in the *A. ferrooxidans* culture over this period.

The EDX analysis of the pyrite surface exposed to HH medium are shown in Figure 5.52 as average atomic percentage. The elements Al and Si were detected at levels below 2.5%. These values are the same as those described and discussed in Chapter 4, section 4.3.2, shown here for comparison. Briefly, these results suggest the control surface is sulfur-rich, which agrees with the Eh results that show greater concentration of iron leaching into solution than sulfur, with no change occurring over the course of exposure.

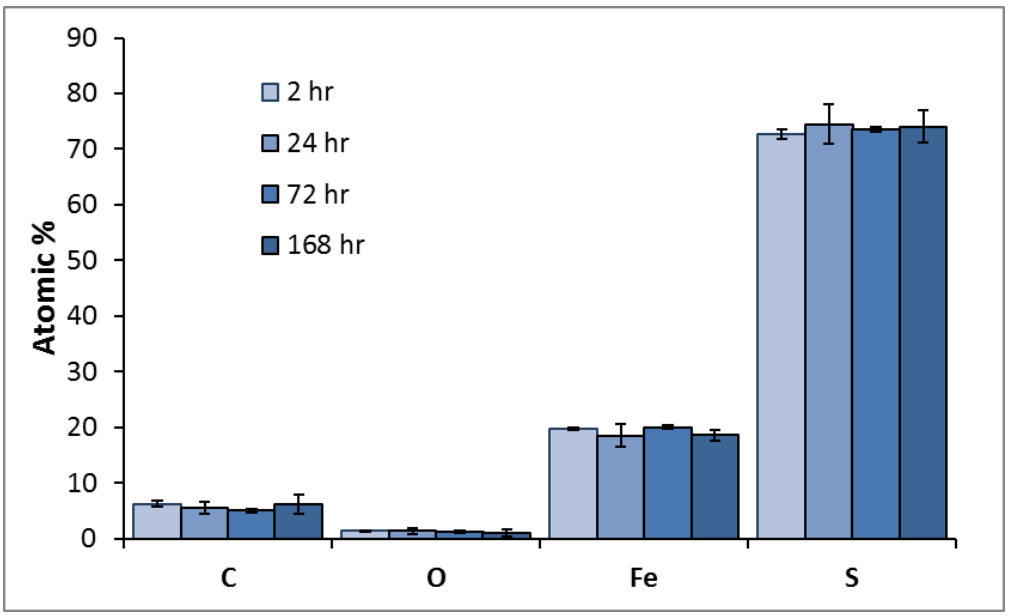

Figure 5.52: Average atomic percentage of pyrite exposed to HH medium for 2, 24, 72 and 168 h, as determined by EDX

As EDX penetrates the surface up to 5 µm, other experiments will be needed to investigate the outermost atomic layers with minimal bulk pyrite contribution, and to relate the physical properties to chemical species on the surface [41-43].

5.3.3 Atomic Force Microscopy

As the topography of the surface has the potential to impact the wettability of a surface, the effects of surface leaching and pitting observed in the SEM images need to be isolated from the chemical changes on the mineral surface [44]. To assess the changes in the pyrite surface topography and isolate these effects from the chemical alterations brought about by *L. ferrooxidans*, atomic force microscopy (AFM) is used to quantify the physical impact of pyrite leaching.

Typical AFM images obtained for pyrite after different periods of exposure to *L. ferrooxidans* are shown in Figure 5.53. At least four images like those shown in Figure 5.53 were obtained per sample, always over an area of 10 µm, to calculate the average roughness of the sample.

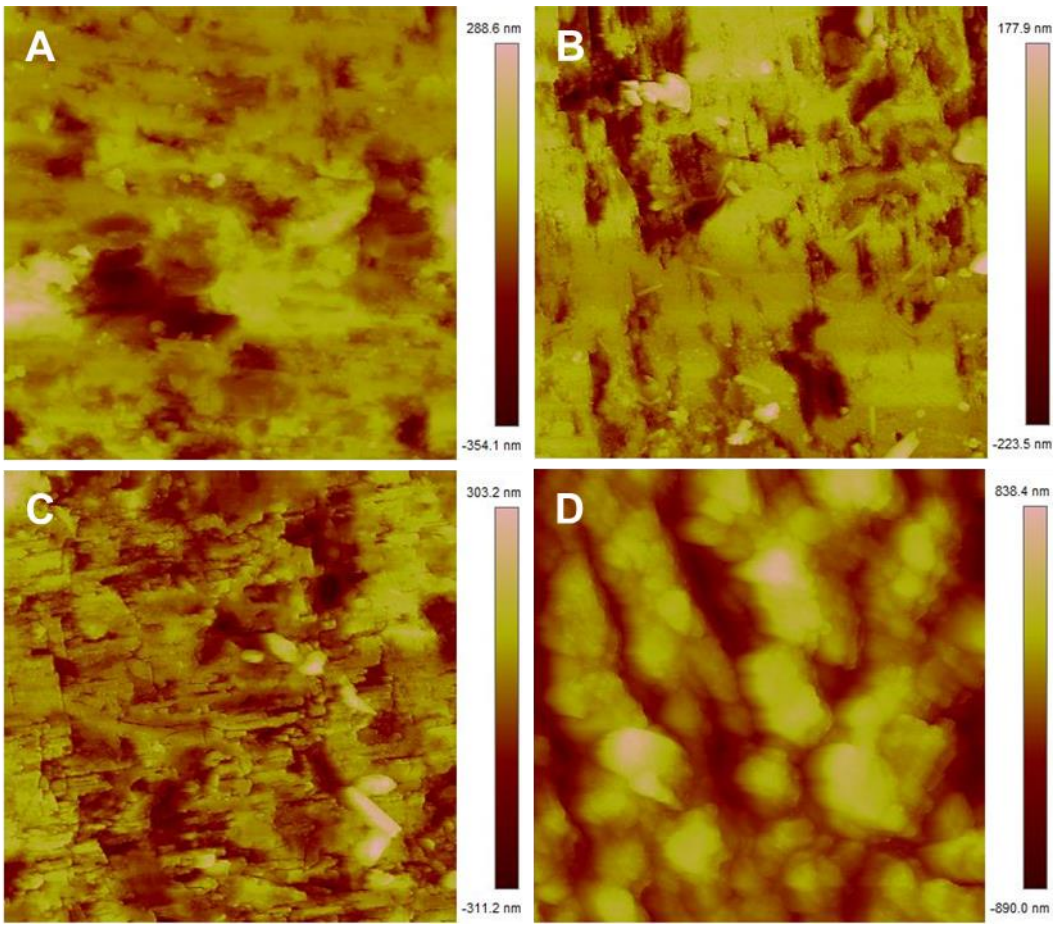

Figure 5.53: 10 x 10 µm AFM height images of pyrite exposed to *L. ferrooxidans* for 2 h (A); 24 h (B); 72 h (C); 168 h (D).

The roughness of the pyrite surface exposed to *L. ferrooxidans* and HH medium as calculated by Ra and Rq are shown in Figure 5.54, with the error bars representing the 95% confidence interval. The HH medium control measurements are the same as those described in Chapter 4, section 4.3.3. The two different methods used to calculate the average roughness of the pyrite surface was described in Chapter 3, section 3.10.2.

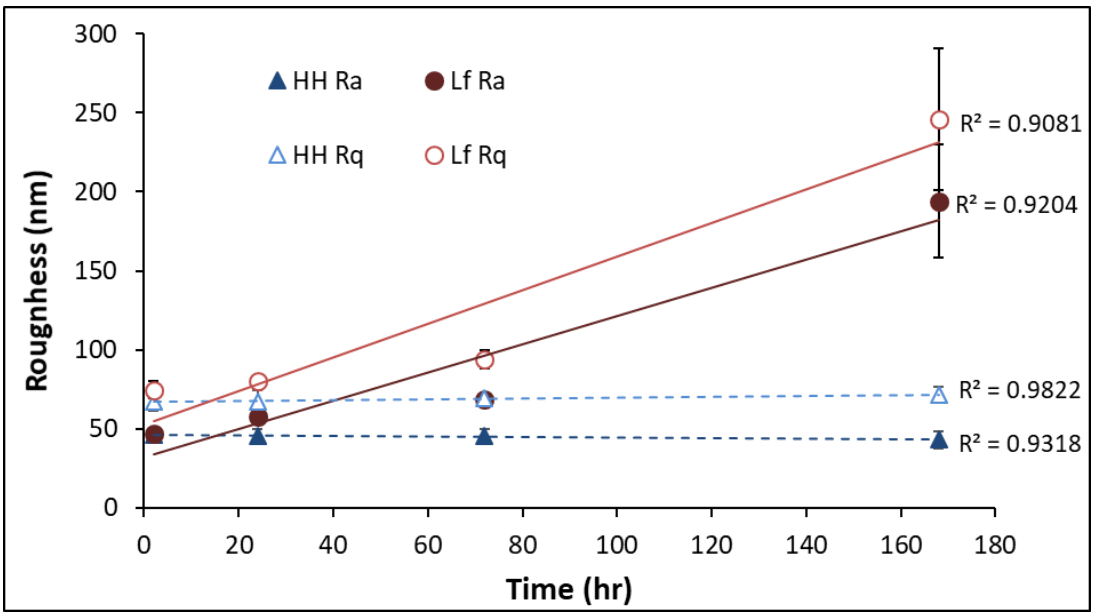

Figure 5.54: The roughness of pyrite exposed to *L. ferrooxidans* as calculated by Ra (●) and Rq (○), and HH medium as calculated by Ra (▲) and Rq (△).

As was also observed in the previous chapter, the Ra and Rq of the pyrite surface increases linearly in the presence of bacterial cells, with correlation coefficients of 0.9204 and 0.9081, respectively. The increase in the standard deviation of samples over the course of exposure suggests there is more variation in roughness across the surface at advanced exposure times compared to those of shorter exposures. This agrees with the amount of uneven debris and pitting observed on the surface of the pyrite using SEM. The sample roughness of the pyrite exposed to *L. ferrooxidans* for 2 and 24 h does not differ significantly from the controls, however after 72 h, the pyrite surface is quantifiably rougher after exposure to *L. ferrooxidans*. After 168 h of exposure, this difference in roughness is even more significant, agreeing with the initial observations made using SEM. As was noted in the previous chapter (Chapter 4, section 4.3.3), the SEM images of bare polished pyrite (Chapter 4, section 4.3.2, Figure 4.26) are visually identical to those exposed to abiotic medium for 2 h. As was observed for *A. ferrooxidans*, the difference in roughness for the shortest periods of exposure to *L. ferrooxidans* and abiotic medium are statistically insignificant, and as such it can be assumed that the roughness of bare polished pyrite coincides with these values.

Previous studies that have applied AFM to studying *L. ferrooxidans* on the surface of pyrite have focussed on cell morphology, sometimes coupling AFM with epifluorescence to observe cell adhesion and EPS production [2, 3, 8]. While more extensive studies have been performed on *A. ferrooxidans*, as was discussed in the previous chapter (Chapter 4, section 4.3.3), very few have investigated any cell preference for defect sites by *L. ferrooxidans*. Although preference for surface defects has been observed for other strains by previous investigations, this does not appear to be the case for *L. ferrooxidans* [14, 45, 46]. Other studies have suggested low crystallization areas have

higher levels of ferrous iron and thiosulfate ions going into solution [14, 45]. This suggests that *L. ferrooxidans* would have ready access to iron nutrients on smooth areas of the surface.

The above results suggest that the presence of *L. ferrooxidans* is making the pyrite surface significantly rougher in comparison to the pyrite surface exposed to HH medium, and that this increase in roughness is proportional to the time spent in live culture. These results would suggest that the hydrophobicity of the HH medium pyrite control would be similar to pyrite exposed to *L. ferrooxidans* for short exposure times (less than 24 h), as their morphology over this period is not significantly different . These observations of the nature of the mineral surface must be compared to the measured hydrophobicity of the sample, to fully understand how *L. ferrooxidans* impacts the mineral surface in terms of its ability to depress or float pyrite.

5.3.4 Captive Bubble Contact Angle

The measure of wettability by captive bubble contact angle provides insight into the suitability of *L. ferrooxidans* as a potential flotation reagent. Contact angle provides an indication of how the microorganisms impact mineral wettability. Although some studies have measured the hydrophobicity of pyrite exposed to *A. ferrooxidans* (Chapter 4, section 4.3.4), few have measured this aspect of pyrite exposed to *L. ferrooxidans*. Investigations into *L. ferrooxidans* in relation to mineral wettability have either measured mineral recovery by flotation in the presence of synthetic collector, or the contact angle of air-dried cells [8, 11]. This leaves the impact of untreated cells on pyrite surface wettability unexplored. Figure 5.55 shows the average five advancing and receding contact angles each pyrite sample, performed in triplicate, with the error bars representing the standard deviation of the samples measured.

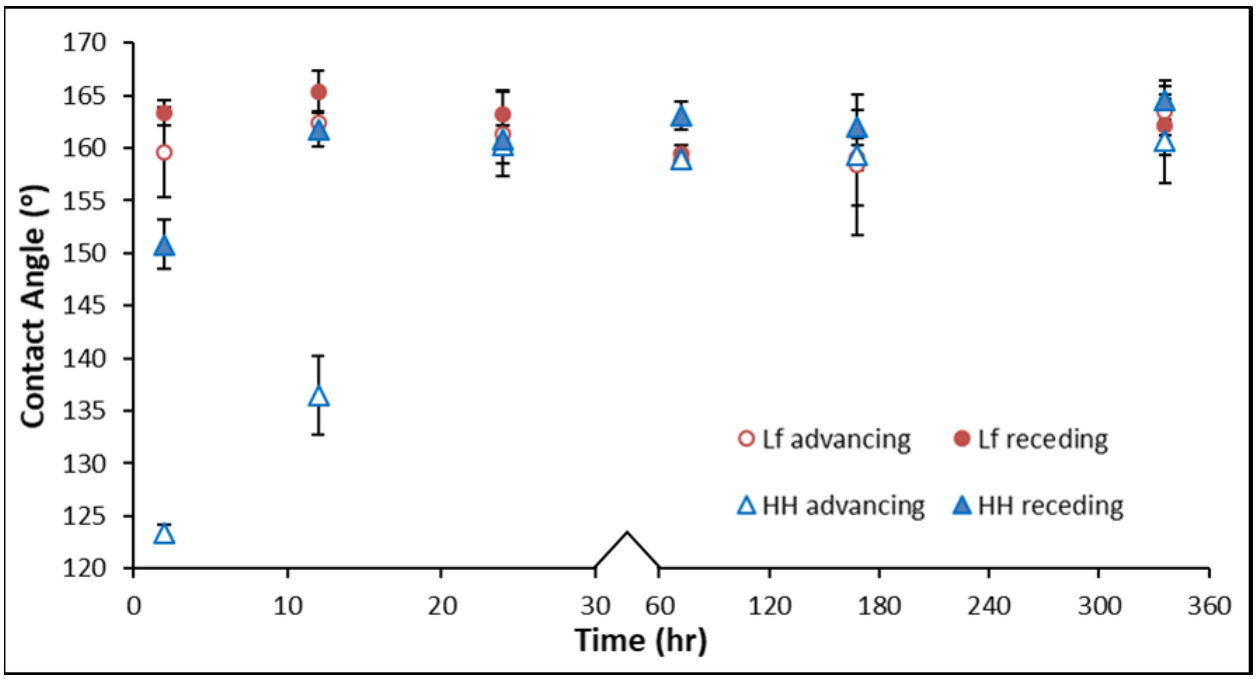

Figure 5.55: Advancing captive bubble contact angle of pyrite exposed to *L. ferrooxidans* (○) and HH medium (Δ). Receding captive bubble contact angle of pyrite exposed to *L. ferrooxidans* (●) and HH medium (▲). Error bars represent sample standard deviation.

Pyrite samples exposed to *L. ferrooxidans* are less hydrophobic than the HH medium control at early stages of exposure, showing the most a significant decrease in hydrophobicity at 2 h of 12.5° to 36°. After 24 h, the pyrite exposed to *L. ferrooxidans* is still slightly less hydrophobic than the pyrite exposed to the HH medium, with advancing and receding angles greater by 3° and 25°, respectively. The pyrite exposed to *L. ferrooxidans* is more homogenous at early periods of exposure compared to the control, suggesting decreased hysteresis when cells are present. After 72 h, the contact angles are similar for both control and bacteria-exposed pyrite, with the contact angle appearing to remain stable for 336 h.

As was mentioned in the previous chapter, a difference in contact angle of as little as 3° can alter mineral recovery by up to 18%, depending on the size fraction of the particles [47]. These results suggest that an exposure of as little as 2 h could promote the depression of pyrite by *L. ferrooxidans*, while longer periods of exposure showed no significant separation of contact angle compared to the HH medium control sample. This suggests the hydrophobicity is improved by the chemistry on the surface rather than the roughness, which the AFM results suggest is identical between biotic and abiotic samples at early exposures. This also suggests the presence of thick biofilm is not necessary for significant changes in hydrophobicity of the pyrite, as the SEM showed little cell coverage after 2 h.

As was observed for *A. ferrooxidans*, the biggest impact *L. ferrooxidans* has on the hydrophobicity of the pyrite in comparison to the HH medium control is in the early stages of exposure. This may in part be due to the larger population of *L. ferrooxidans* on the mineral surface compared to *A. ferrooxidans*, observed using SEM. At this stage, it is still not possible to determine whether the direct contact or indirect contact mechanism dominates the bacterial interaction with the pyrite surface. To separate physical changes on the surface such as roughness from potential chemical effects on the surface, surface chemical analysis must be performed on the system. This chemical analysis will be explored using STXM and ToF-SIMS in the following sections.

5.3.5 Scanning Transmission X-ray Microscopy

Scanning Transmission X-ray Microscopy (STXM) is used on the fine particles of pyrite that are used to grow the bacteria in culture. This technique provides *in situ* physicochemical analysis of the ground mineral that would be necessary for flotation, an advantage over techniques that rely on flat and smooth samples that are less representative of flotation systems. As has been discussed, NEXAFS spectra provide information on the chemical bonding and oxidation states of the elements on the surface. A summary of signal assignments for Fe L-edge and C K-edge NEXAFS can be found in Chapter 3, section 3.11, Table 3.5 and Table 3.6, respectively.

The Fe L-edge NEXAFS spectra obtained for pyrite exposed to *L. ferrooxidans* for 24 and 336 h are shown in Figure 5.56. The samples were prepared by drop casting and air drying, as described in Chapter 3, section 3.9.1. The behaviour of pyrite exposed to the HH medium control solution was investigated using Fe L-edge NEXAFS in the previous chapter, and showed no significant change over time (Chapter 4, section 4.3.5).

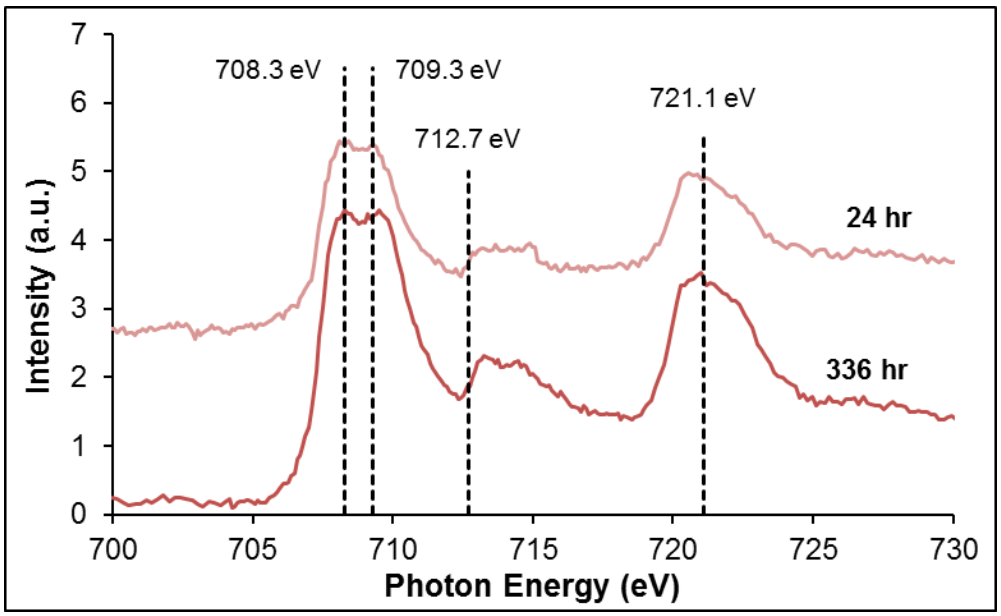

Figure 5.56: Fe L-edge NEXAFS spectra of pyrite exposed to *L. ferrooxidans* for 24 and 336 h. The transitions observed are to Fe 3*d* states hybridized with S 3*p* at 708.5 eV (overlapping with Fe 2*p* to Fe 3*d* states hybridized with O 2*p* states at 707.8-710.5 eV), S 3*p* states hybridized with Fe 4*s* and 4*p* states at 712-715 eV, and the Fe L_2 peak at 719.9 eV.

The transitions that cause the peaks present in the pyrite Fe L-edge NEXAFS spectra have been described in the previous chapter (Chapter 4, section 4.3.5) [48-50]. The spectrum for pyrite exposed to *L. ferrooxidans* for 336 h shows the Fe L_3 transitions corresponding to the Fe 3*d* states hybridized with S 3*p* and iron oxides and (oxy)hydroxides at 707.9-708.8 eV [48-51] increasing, and the S 3*p* to Fe 4*s* and 4*p* transitions at 712-715 eV [52, 53] decreasing. This indicates an increase in iron oxidation products occurring on the surface that obscures the bulk pyrite signal. The increased surface area of particles compared to flat coupons is likely to be at least partially responsible for this increased oxidation. The NEXAFS spectra obtained for pyrite shown above agree heavily with those obtained by Goh *et al* [52], and generally agree with studies that used synthetic pyrite or pyrite samples that was not exposed to air, although they did not have the resolution to observe the two overlapping peaks, they infer the existence of the structure seen by Goh *et al* and in this study [48, 49].

The behaviour of pyrite exposed to the HH medium control solution was investigated using C K-edge NEXAFS in the previous chapter, and showed no significant change over time (Chapter 4, section 4.3.5). Briefly, the signals indicated potential radiation damage [54, 55], and the presence of adventitious carbon [56, 57]. Figure 5.57 shows the stacked C K-edge NEXAFS spectra of pyrite exposed to *L. ferrooxidans* for 2, 24, and 336 h, and the changes in the carbon species occurring over those exposure times, as well as both DNA and sodium alginate standard spectra. All spectra

were corrected to the 285.1 eV of the aromatic π* C=C peak of DNA, with details described in Chapter 3, section 3.13.2.

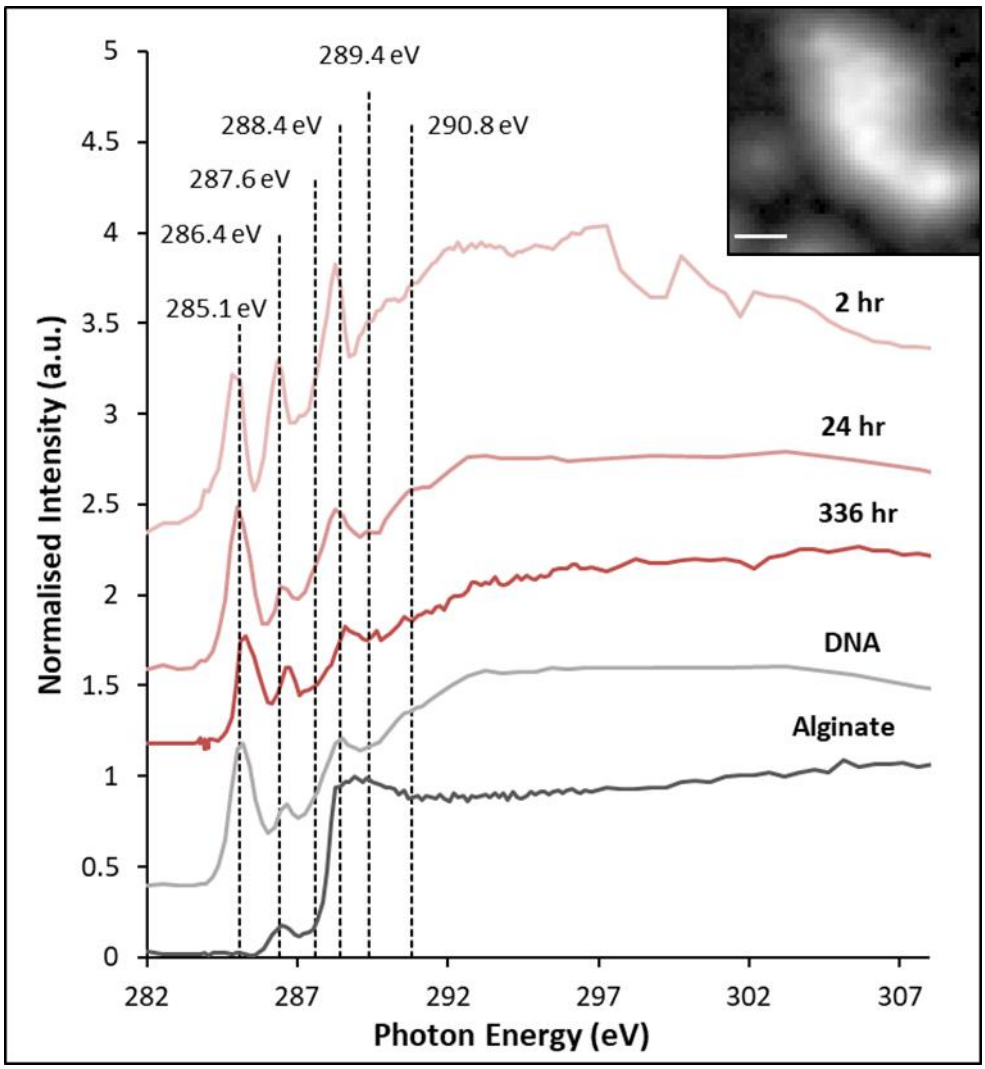

Figure 5.57: C K-edge NEXAFS spectra of chalcopyrite exposed to *L. ferrooxidans* for 2, 24 and 336 h, bovine serum albumin (DNA) and sodium alginate (used for calibration) Inset: Carbon image stack (scale 1 µm). The transitions observed on pyrite exposed to *L. ferrooxidans* are from C 1s to π* C=C and C-H at 285.1 eV, π* C=N and π* C=C at 286.4 eV, π* C=O at 288.4 eV, σ* CNH, σ* CH or π* C=N at 289.4 eV and σ* C-C at 292-294 eV.

The C K-edge NEXAFS spectra of pyrite exposed to *L. ferrooxidans* were collected over the total area of the carbon stack image, an example of which is shown above (Inset). The NEXAFS spectra were collected over an area of the sample to improve the signal, which was very weak. The spectra collected of DNA and sodium alginate display peak in expected areas, with sodium alginate not displaying signal at 285.1 eV due to no aromatic C=C functionalities occurring within its structure, shown in Figure 5.58.

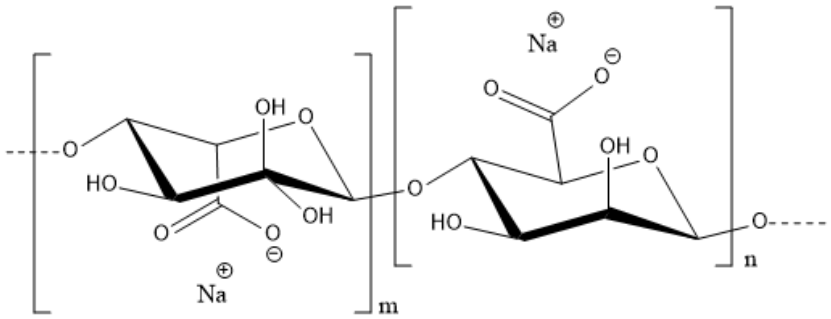

Figure 5.58: Chemical structure of sodium alginate

Every C K-edge NEXAFS spectra each of the pyrite samples exposed to *L. ferrooxidans* is showing the π* C=C peak at 285 eV, and second intense signals at 286.4 eV, which have been associated with both π* C=N and π* C=C peaks [58-64]. All spectra are also showing broad signal in the 292-294 eV region that can be attributed to σ* C-C [58, 60, 62]. The π* C=O peak after 2 h occurs between 288.4-288.7 eV, suggesting that the peak is due to more carboxylic-type character common in lipids and biopolymer [60, 63-66]. After 24 h, the π* C=O peak appears broader, suggesting an increase in signal due to the π* C=O bonds in amides of protein, which typically occur at 288.2 eV [58-60, 62, 64, 66, 67]. The protein-type π* C=O peak is associated with the increase in the peak at 289.4 eV, which can be attributed to σ* CNH, σ* CH or π* C=N amide functionality in proteins and nucleic acids [58, 60, 67]. After 336 h, the protein contributions have decreased, while the π*C=O at 288.4 eV of polysaccharides remains strong. The π* C=C peak at 285.1 eV may also be indicative of radiation damage as C-H and C-C bonds are reduced, however, as the sodium alginate spectrum is displaying no signal in this area, radiation damage appears to be unlikely in these samples [54, 55].

Several papers have previously studied bioleaching of minerals using *L. ferrooxidans*, although many of them investigating the mineral surface using NEXAFS, as the investigation of carbon of the cells themselves is challenging in most UHV techniques [6, 68, 69]. Other studies have used the STXM technique to collect carbon NEXAFS of other types of cells, and although they have identified similar functionalities, the spectra do not have the same shape, indicating different EPS composition to *L. ferrooxidans* [60, 66, 70].

These samples provide evidence for why the difference in hydrophobicity of pyrite exposed to *L. ferrooxidans* at 2 h is decreased compared to the sample exposed to the HH medium control; hydrophilic polysaccharide-type species [11, 71, 72] produced by the bacteria are detected at this stage of exposure, creating a less hydrophobic surface compared to the pyrite exposed to HH medium. As cells start to colonise the surface and oxidation of the mineral progresses, the sample becomes slightly less hydrophobic after 24 h compared to the control. After 336 h of exposure to *L.*

ferrooxidans, the pyrite surface appears to be slightly more oxidised than that at 24 h, and there seems to be little change in biofilm composition between 24 and 336 h. As was observed in the previous chapter, the anionic function groups in EPS components are present at early stages of exposure, providing binding sites for iron and promoting pyrite oxidation without the need for cell attachment to the surface [73, 74]. Due to the presents of iron-complexing EPS on the pyrite surface, it is likely that the indirect contact mechanism most accurately describes the interaction of *L. ferrooxidans* with pyrite over the early periods of exposure [20, 23, 75].

These changes do not correlate with the AFM results, which suggest that the hydrophobicity of the pyrite exposed to *L. ferrooxidans* should be greater than the hydrophobicity of the control, as correlates with the roughness increasing [44]. As was the case for *A. ferrooxidans*, these results suggest that the effects of the chemical species on the surface are greater than those of the physical changes to the surface brought about by the bacteria. This indicates the indirect contact mechanism, which relies on EPS for the alteration of the mineral surface, may dominate the interaction of *L. ferrooxidans* with pyrite.

5.3.6 Time of Flight – Secondary Ion Mass Spectrometry

ToF-SIMS provides chemical and elemental information on the outermost atomic layers of the surface, providing semi-quantitative information on the chemistry contributing to the hydrophobicity of the mineral surface compared to X-ray techniques that penetrate the surface. Although individual compounds in a mixture are not yet able to be individually identified, a "fingerprint" can be obtained of the fragments identified on the surface of the pyrite exposed to *L. ferrooxidans*, which may lead to the identification of the types of molecules on the surface that impact contact angle [57, 76-78].

The plots shown here are an indication of the proportion of each fragment on the mineral surface, and are only comparable with other fragments of the same sample. Figure 5.59 shows the positive ions on the surface of pyrite exposed to *L. ferrooxidans* and HH medium for 2, 24, 72 and 168 h. Although the peaks selected for the total fragment profile is slightly different to that of *A. ferrooxidans* on pyrite, the proportions of ions are unaffected for the control pyrite samples. As such, the description of the positive and negative ion fragments of the pyrite exposed to HH medium presented in this graph can be found in Chapter 4, section 4.3.6. The ToF-SIMS analysis of bare polished pyrite was also discussed in the previous section (Chapter 4, section 4.3.6); briefly, the positive ion spectra were dominated by Fe^{+}, with very low proportions of carbonaceous fragments, while the negative ion fragments indicated surface oxidation through exposure to the atmosphere. Negligible amounts of large molecular weight fragments were detected.

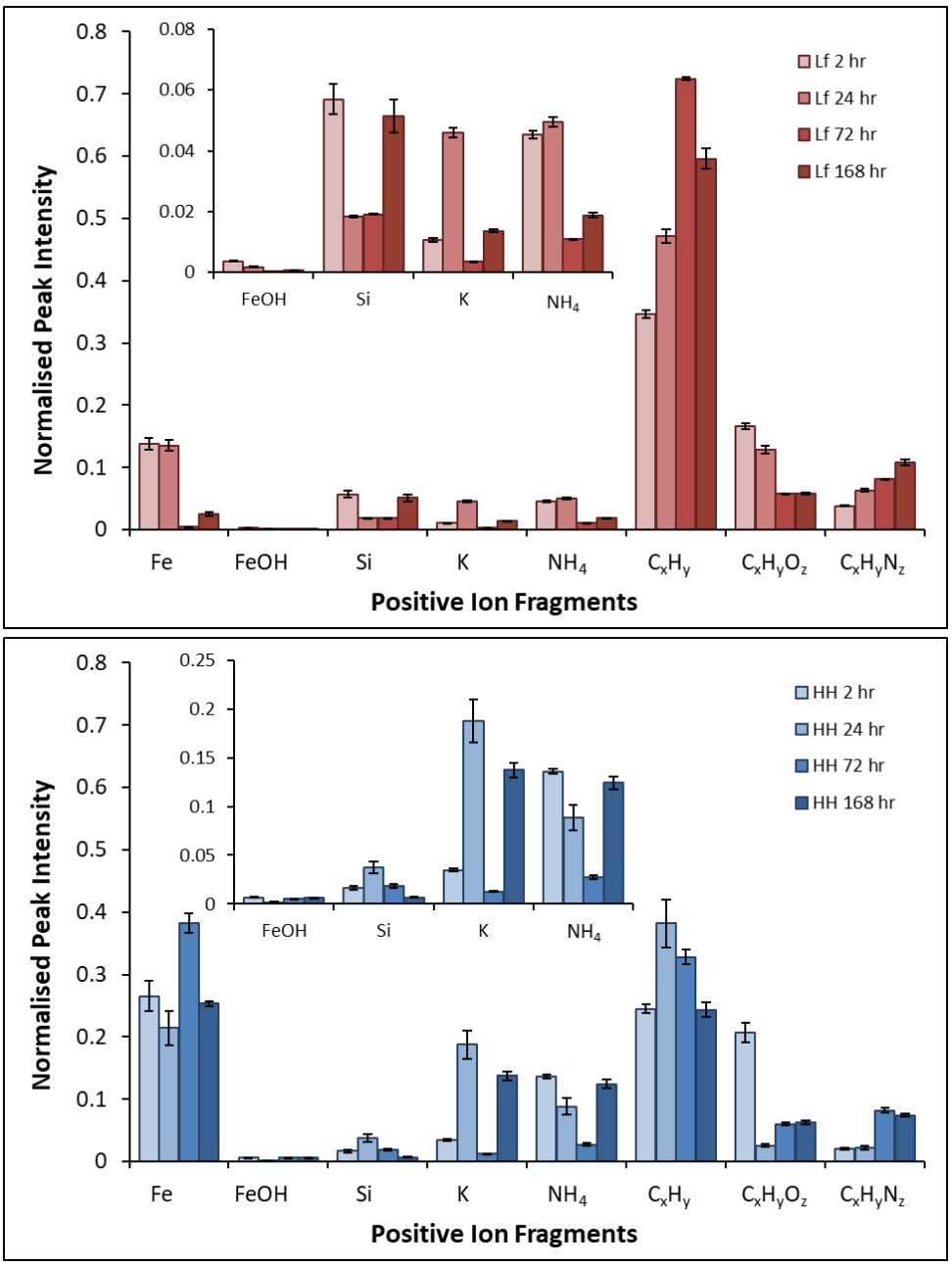

Figure 5.59: Average normalised peak intensities of positive fragments of pyrite exposed *L. ferrooxidans* (top) for 2, 24, 72 and 168 h, and pyrite exposed to HH medium (bottom) for 2, 24, 72 and 168 h.

The fragment profile of pyrite exposed to *L. ferrooxidans* is dominated by short chain $C_xH_y^+$ ($x \leq 6$) fragments for every period of exposure, with the $C_xH_yO_z^+$ ($x \leq 4$, $z \leq 2$) fragments are in high proportions at early periods of exposure. The high proportion of hydrophilic $C_xH_y^+$ and $C_xH_yO_z^+$ fragments at these early periods of exposure compared to the more iron-rich control samples suggest that the *L. ferrooxidans* cells are producing polysaccharides, making the surface less hydrophobic [11, 71, 72]. This agrees with the results presented in both the STXM and contact angle studies that suggest the presence of polysaccharides during early periods of exposure, making the pyrite surface significantly less hydrophobic than the control. This also shows the pyrite surface

exposed to *L. ferrooxidans* is less hydrophobic than the pyrite surface exposed to *A. ferrooxidans* over the same time periods (Chapter 4, section 4.3.4).

After longer periods of exposure, the proportion of $C_xH_yN_z^+$ ($x \leq 5$, $z \leq 2$) fragments increases significantly. The increase in proportion of hydrophobic protein-type signals [79] is likely to be partially responsible for the increase in hydrophobicity observed at this point in the contact angle results, with a more complete picture possible by analysis of the negative ion fragments and larger molecular weight fragments that will come later in this chapter. These results also suggest that *L. ferrooxidans* produces more protein-type compounds as biofilm begins to build up on the mineral surface as was observed by SEM. However, as *L. ferrooxidans* is known EPS producer, the proportion of organic fragments observed on the pyrite surface upon exposure is much greater than that observed for *A. ferrooxidans*, and causes the decreased hydrophobicity of the pyrite at shorter exposure times [1, 3, 14].

The proportion of Fe^+ detected on the surface decreases over the course of exposure, suggesting the layer of bacterial cells that was shown to spread over time are obscuring the mineral below, resulting in the dramatic decrease in proportion. Due to medium salt precipitates on the surface, both NH_4^+ and K^+ are expected to be detected on the surface. As was specified in the previous chapter, these salt prcipitates mean the NH_4^+ fragment is not a reliable indicator proteins on the surface. There are very small amounts of Si^+ and $FeOH^+$ on the surface, indicating little to no jarosite formation on the surface and some silicate inclusions, which is expected from the XRD data. The proportions of these fragments remain low over the course of exposure. This agrees with the NEXAFS results that also suggested little jarosite or secondary minerals formation.

Figure 5.60 shows the complementary negative fragments and elements of interest and significance collected by ToF-SIMS on pyrite exposed to *L. ferrooxidans* and HH medium for 2, 24, 72 and 168 h. The inset plots in Figure 5.60 show the sulfur species on the surface normalised to the total S^- detected on the surface, showing the proportion due to each sulfur species. The fragments detected on pyrite after exposure to *L. ferrooxidans* for are dominated by the O^- and OH^- fragments for all samples. Over earlier periods of exposure, the proportion of hydrophobic sulfur species is much lower compared to the control. This agrees with the contact angle data results that show the pyrite exposed to *L. ferrooxidans* is less hydrophobic than the control after 2 h. Oxygenated sulfur species such as SO_3^- and SO_4^- are in greater proportion on the surface than polysulfide species such as S_3^- and S_4^-, although the overall proportion of sulfur species on the surface is much smaller than that observed on the control pyrite for the duration of exposure.

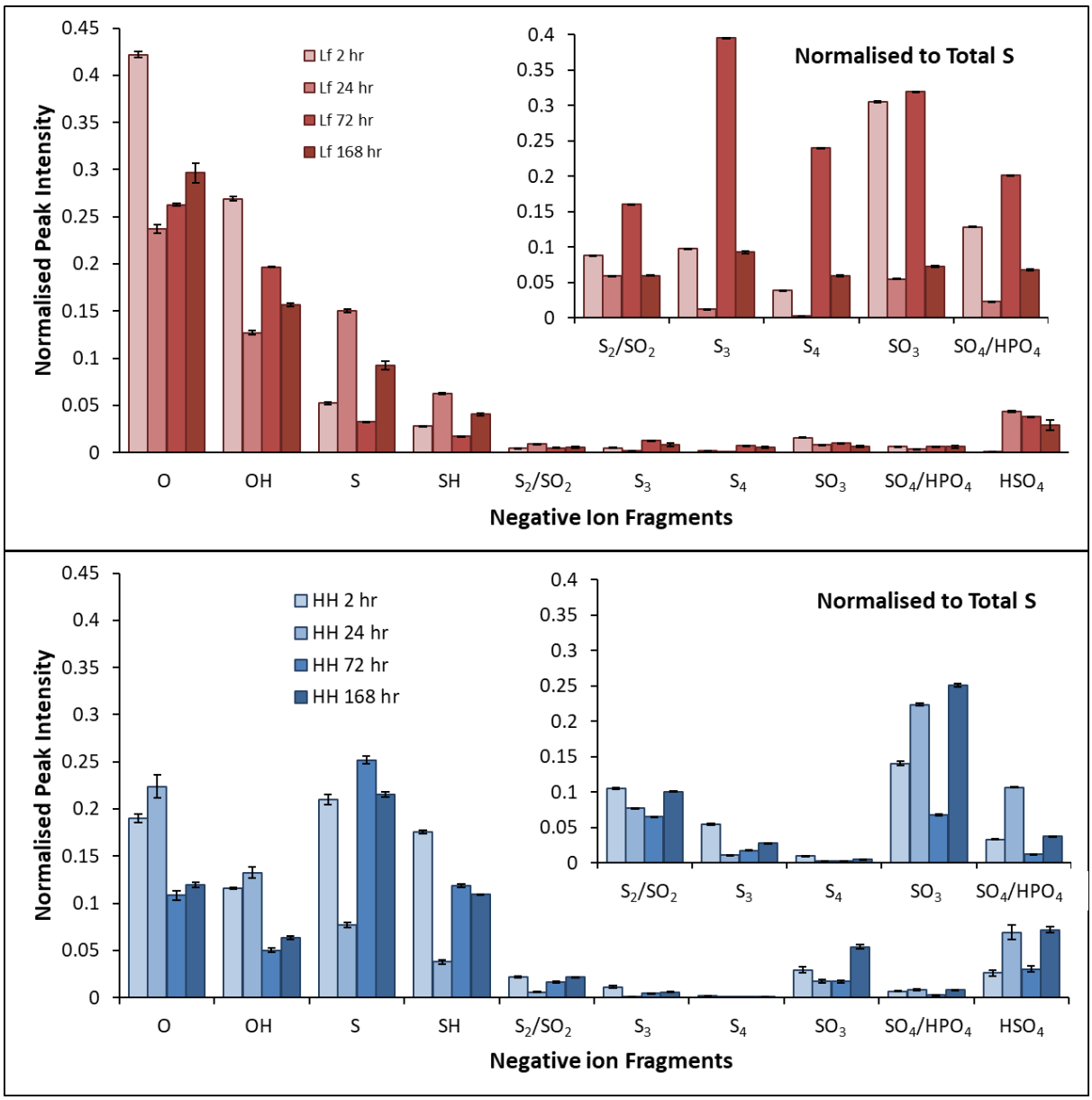

Figure 5.60: Average normalised peak intensities of negative fragments of pyrite exposed *L. ferrooxidans* (top) for 2, 24, 72 and 168 h, and pyrite exposed to HH medium (bottom) for 2, 24, 72 and 168 h.

Over longer periods of exposure the proportion of polysulfide species on the pyrite exposed to *L. ferrooxidans* increases, with longer periods of exposure resulting in larger proportions of polysulfide on the surface than the control for the same periods. This increase in polysulfides coincides with an increase in ferric iron in solution, indicating the surface has become more sulfur-rich as iron is leached from the surface of the mineral and consumed by the bacteria. This agrees with the contact angle results that show a slight increase in hydrophobicity of the pyrite over 72 h of exposure to *L. ferrooxidans*, however, as biofilm grows, the surface remains hydrophilic overall.

As was the case with pyrite exposed to *A. ferrooxidans*, larger molecular weight fragments associated with the production of EPS were detected on the surface of pyrite exposed to *L.*

ferrooxidans. Figure 5.61 shows the large molecular mass positive fragments collected by ToF-SIMS on pyrite exposed to *L. ferrooxidans* and HH medium for 2, 24, 72 and 168 h.

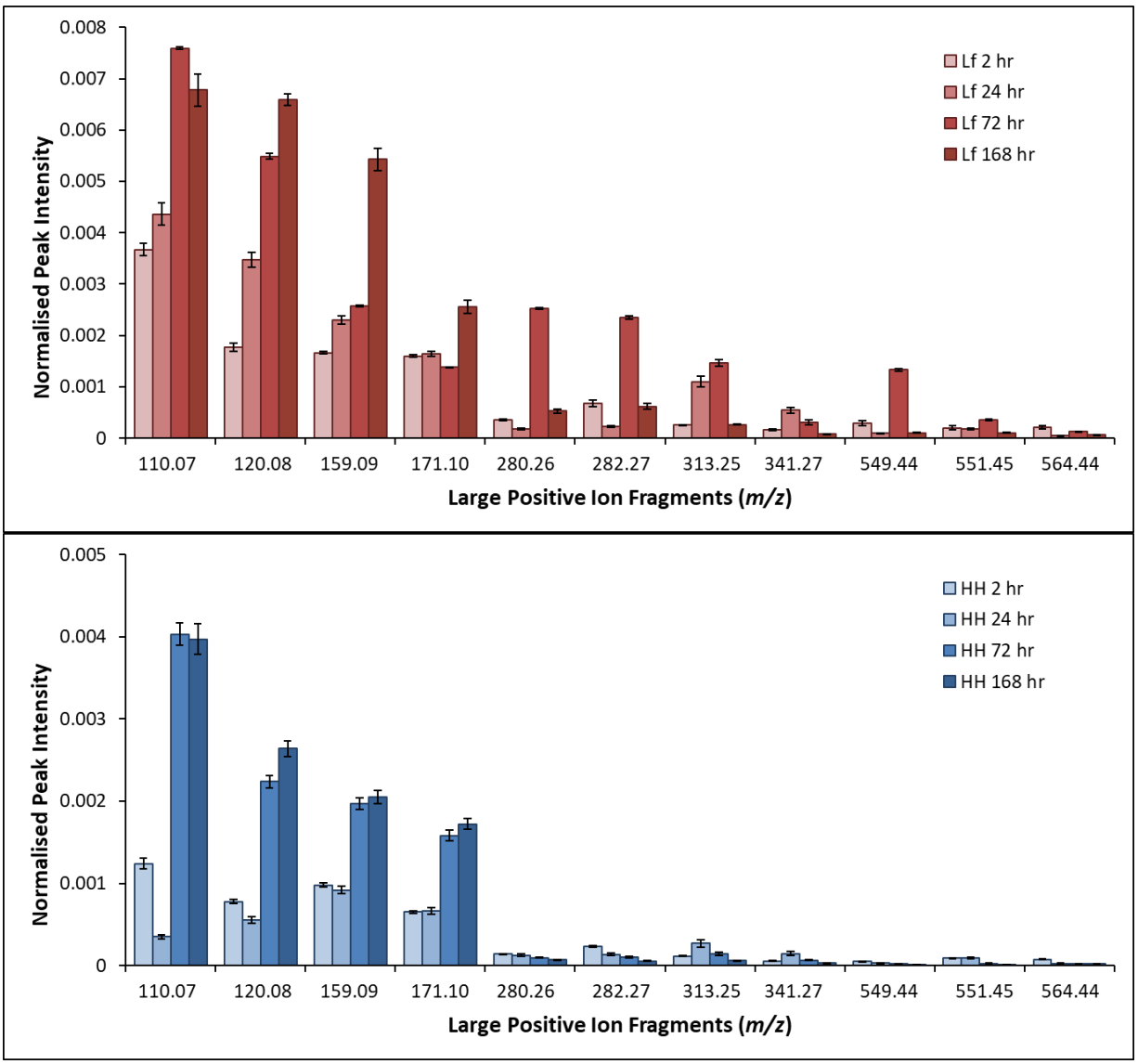

Figure 5.61: Average normalised intensity of large positive fragments of pyrite exposed to HH medium (bottom) and *L. ferrooxidans* (top) 2, 24, 72 and 168 h.

Initially, there are multiple large molecular weight fragments on the pyrite surface after exposure to *L. ferrooxidans*, with the proportion increasing significantly by 168 h for most of the fragments. The fragments that follow this increasing frequency trend are of *m/z* 110.07, 120.08 and 159.09 and have been identified as amino acid fragments by several previous studies, which may indicate DNA or protein on the surface increasing in frequency over time as biofilm increases on the surface [77, 80-83]. The remaining fragments have variously been identified as lipid or carbohydrate fragments by previous studies looking specifically at those structures, with many of these fragments identified as major components of several lipid and carbohydrate structures [76, 78, 81, 84-87]. The fragment with *m/z* 280.26 follows the same trend as other polysaccharide-type fragments, indicating that it is

also likely to be a large polysaccharide fragment, although the accurate identity is not possible to ascertain. The proportion of these fragments are significantly greater in pyrite samples exposed to *L. ferrooxidans* compared to the pyrite exposed to HH medium, with the polysaccharide-type fragments having larger proportions at earlier exposure times, with the amino-acid fragments becoming more frequent at 72-168 h. The occurrence of these fragments indicates that large hydrophilic polysaccharide and lipid fragments are present and being produced very shortly after inoculation, which is consistent with both the NEXAFS and contact angle results presented in previous sections. These results support the indirect contact mechanism as describing the interaction of *L. ferrooxidans* with pyrite over early periods of exposure, however the build-up of biofilm and the increase in high mass fragments due to EPS components and cellular material make it impossible to determine whether the direct or indirect contact mechanism dominates in longer periods of exposure.

The negative ion fragments of large molecular weight are less well understood than the positive fragments, but can be used to compliment the positive ion spectra. Unique EPS fragments can also be identified in the negative ion spectra. The average normalised peak intensity of large molecular weight negative fragments of pyrite exposed to *L. ferrooxidans* and HH medium for 2, 24, 72 and 168 h is shown in Figure 5.62.

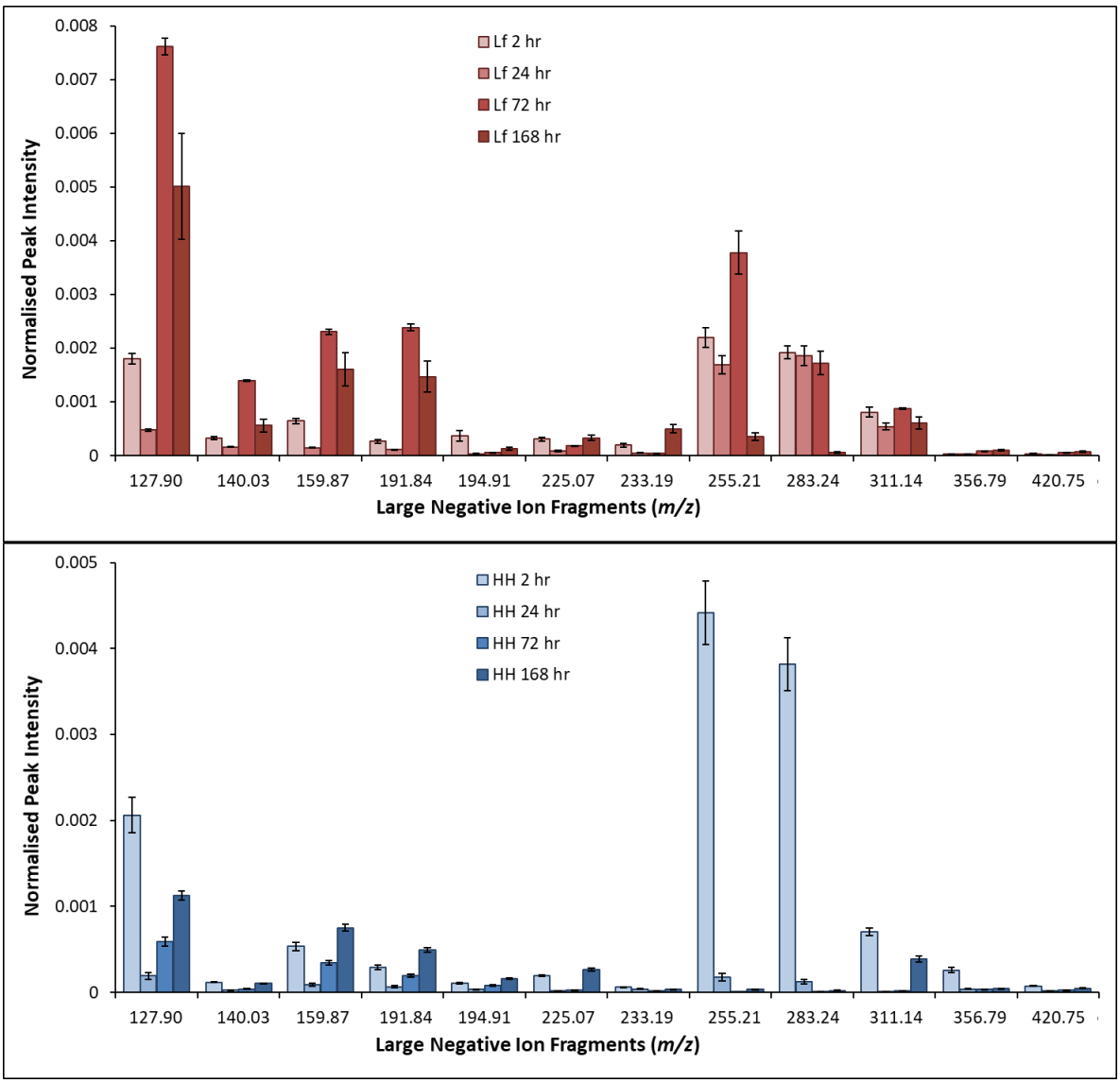

Figure 5.62: Average normalised intensity of large negative fragments of pyrite exposed to HH medium (bottom) and *L. ferrooxidans* (top) 2, 24, 72 and 168 h.

Large molecular weight negative fragments are not explored as extensively as positive fragments, but the those observed in this study support the conclusions of the positive ion fragments, indicating larger molecular weight molecules are present in early stages of attachment in statistically significant amounts and decrease as exposure continues. The fragments with *m/z* 127.90, 140.03, 194.91, 255.23, 283.25 and 311.14 have both been identified as fatty acid or carbohydrate fragments in previous studies [84-86, 88, 89]. As the fragments at *m/z* 159.87, 191.84, 225.07, 233.19, 356.79 and 420.75 follow the same trend, it is not unreasonable to suggest that these fragments are also due to polysaccharides and/or lipids.

Previous investigations of pyrite surfaces using ToF-SIMS were focused mainly on identifying pyrite particles within a mixture of sulfide minerals, and on the ions associated with the pyrite surface and ions of interest to flotation. The results presented here for the control pyrite are much in

agreement with previous studies that have observed, under a wide range of conditions, that the surface of pyrite is iron-rich; with hydrophilic iron hydroxides leading to pyrite depression while hydrophobic sulfur-rich surfaces lead to flotation [90-94].

Previous studies that have utilised ToF-SIMS for the investigation of microorganisms and their excretions have mainly focussed on the separation of known components such as proteins and monosaccharides by principle component analysis, however, it has yet to be successfully applied to complex samples [77, 95, 96]. Our results agree with those obtained by Pradier *et al*, who observed that the negative spectra of bacteria are dominated by the O^- and OH^- fragments, which agrees with the strong overlap of those ions with hydrocarbons caused by bacteria observed here [97]. They also found that bacterial species rich in carbohydrates and proteins, which they concluded by summing oxygenated and nitrogenated carbon signals respectively, achieved the highest adhesion to steel surfaces, with carbohydrate rich cells adhering most effectively [97]. Other studies have looked at specific types of compounds such as proteins or peptides on cells, and Dague *et al* specifically related protein fragments as being hydrophobic, a contribution which is also observed here [79, 81].

5.4 Conclusions

It was observed using SEM that attachment of cells occurs at very early stages of exposure, with no obvious preference for surface defects, and that this initial attachment develops into uniform, monolayered biofilm by 168 h of exposure. Leaching of the pyrite is accelerated by the presence of *L. ferrooxidans*, with the roughness of the surface as measured by AFM confirming advanced pitting compared to acidic the medium alone. The difference in hydrophobicity is greatest between bacterial exposure and abiotic control at the early exposure stages of 2 h, which coincides with the presence of polysaccharide and fatty acid-type structures measured by both NEXAFS and ToF-SIMS. Longer periods of exposure lead to inorganic oxidation of the pyrite surface exposed to HH medium, and increased production of hydrophobic proteins and sulfur-rich passivation layers on pyrite exposed to cells, causing little difference in hydrophobicity of the samples by the time full biofilm forms at 168 h.

These observations suggest that *L. ferrooxidans* preferentially produces polysaccharide and fatty acid compounds to assist with initial adhesion to pyrite, before beginning to produce more hydrophobic proteins as colonies begin to develop on the surface. They also produce significantly more of these products that the *A. ferrooxidans* studied in the previous chapter, providing a greater difference in hydrophobicity compared to pyrite exposed to HH medium. These results suggest both mesophiles interact through the indirect contact mechanism during early periods of exposure to the

surface of pyrite, however the development of biofilm over longer periods of exposure to *L. ferrooxidans* means it is not possible to differentiate the indirect contact and the direct mechanisms over longer periods of exposure. This has important implications for the field of bioflotation, which would ideally require short-term exposure for the most efficient separation of minerals and a larger amount of the product required to affect the desired changes. This study suggests that not only is the nature of bacterial excretions changing, but that similar changes may be occurring across strains and that strains that produce more EPS are potentially more efficient at providing the means of mineral separation. As was found in the previous chapter, when cells are harvested and the length of exposure to the mineral is of crucial importance to effective separation of minerals.

5.5 References

1. Ban, J.-R., Gu, G.-H., Hu, K.-T., *Bioleaching and electrochemical property of marmatite by Leptospirillum ferrooxidans.* Transactions of Nonferrous Metals Society of China, 2013. **23**(2): p. 494-500.
2. Florian, B., Noël, N., Sand, W., *Visualization of initial attachment of bioleaching bacteria using combined atomic force and epifluorescence microscopy.* Minerals Engineering, 2010. **23**(6): p. 532-535.
3. Florian, B., Noël, N., Thyssen, C., Felschau, I., Sand, W., *Some quantitative data on bacterial attachment to pyrite.* Minerals Engineering, 2011. **24**(11): p. 1132-1138.
4. Petersen, J., Dixon, D. G., *Competitive bioleaching of pyrite and chalcopyrite.* Hydrometallurgy, 2006. **83**(1–4): p. 40-49.
5. Petersen, J., Dixon, D. G., *Thermophilic heap leaching of a chalcopyrite concentrate.* Minerals Engineering, 2002. **15**(11): p. 777-785.
6. Yang, Y., Liu, W., Chen, M., *A copper and iron K-edge XANES study on chalcopyrite leached by mesophiles and moderate thermophiles.* Minerals Engineering, 2013. **48**(0): p. 31-35.
7. Yang, H.-Y., Liu, W., Chen, G.-B., Liu, Y.-Y., Tong, L.-L., Jin, Z.-N., Liu, Z.-L., *Function of microorganism and reaction pathway for carrollite dissolution during bioleaching.* Transactions of Nonferrous Metals Society of China, 2015. **25**(8): p. 2718-2754.
8. Zhu, J., Li, Q., Jiao, W., Jiang, H., Sand, W., Xia, J., Liu, X., Qin, W., Qiu, G., Hu, Y., Chai, L., *Adhesion forces between cells of Acidithiobacillus ferrooxidans, Acidithiobacillus thiooxidans or Leptospirillum ferrooxidans and chalcopyrite.* Colloids and Surfaces B: Biointerfaces, 2012. **94**: p. 95-100.
9. Govender, Y., Gericke, M,, *Extracellular polymeric substances (EPS) from bioleaching systems and its application in bioflotation.* Minerals Engineering, 2011. **24**(11): p. 1122-1127.
10. Pecina, E.T., Rodríguez, M., Castillo, P., Díaz, V., Orrantia, E., *Effect of Leptospirillum ferrooxidans on the flotation kinetics of sulphide ores.* Minerals Engineering, 2009. **22**(5): p. 462-468.
11. Vilinska, A., Hanumantha Rao, K., *Leptospirillum ferrooxidans-sulfide mineral interactions with reference to bioflotation and bioflocculation.* Transactions of Nonferrous Metals Society of China, 2008. **18**(6): p. 1403-1409.
12. Hippe, H., *Leptospirillum gen. nov. (ex Markosyan 1972), nom. rev., including Leptospirillum ferrooxidans sp. nov. (ex Markosyan 1972), nom. rev. and Leptospirillum thermoferrooxidans sp. nov. (Golovacheva et al. 1992).* International Journal of Systematic and Evolutionary Microbiology, 2000. **50**(2): p. 501-503.

13. Johnson, D.B., *Biomining — biotechnologies for extracting and recovering metals from ores and waste materials.* Current Opinion in Biotechnology, 2014. **30**(0): p. 24-31.
14. Rohwerder, T., Sand, W., *Mechanisms and biochemical fundamentals of bacterial metal sulfide oxidation*, in *Microbial Processing of Metal Sulfides*, E.R.D.a.W. Sand, Editor. 2007 Springer. p. 35-58.
15. Boon, M., Brasser, H. J., Hansford, G. S., Heijnen, J. J., *Comparison of the oxidation kinetics of different pyrites in the presence of Thiobacillus ferrooxidans or Leptospirillum ferrooxidans.* Hydrometallurgy, 1999. **53**(1): p. 57-72.
16. Jafari, M., Shafaei, S., Abdollahi, H., Gharabaghi, M., Chehreh Chelgani, S., *A Comparative Study on the Effect of Flotation Reagents on Growth and Iron Oxidation Activities of Leptospirillum ferrooxidans and Acidithiobacillus ferrooxidans.* Minerals, 2017. **7**(1): p. 2.
17. Pacholewska, M., *Microbial leaching of blende flotation concentrate using Acidithiobacillus ferrooxidans and Acidithiobacillus thiooxidans.* Physicochemical Problems of Mineral Processing, 2003. **37**: p. 57-68.
18. Mykytczuk, N.C.S., Trevors, J. T., Ferroni, G. D., Leduc, L. G., *Cytoplasmic membrane response to copper and nickel in Acidithiobacillus ferrooxidans.* Microbiological Research, 2011. **166**(3): p. 186-206.
19. Sand, W., Rohde, K., Sobotke, B., Zenneck, C., *Evaluation of Leptospirillum ferrooxidans for Leaching*. Vol. 58. 1992. 85-92.
20. Harneit, K., Göksel, A., Kock, D., Klock, J. H., Gehrke, T., Sand, W., *Adhesion to metal sulfide surfaces by cells of Acidithiobacillus ferrooxidans, Acidithiobacillus thiooxidans and Leptospirillum ferrooxidans.* Hydrometallurgy, 2006. **83**(1–4): p. 245-254.
21. Rodríguez, Y., Ballester, A., Blázquez, M. L., González, F., Muñoz, J. A., *New information on the pyrite bioleaching mechanism at low and high temperature.* Hydrometallurgy, 2003. **71**(1–2): p. 37-46.
22. Zhu, W., Xia, J.-L., Yang, Y., Nie, Z.-Y., Zheng, L., Ma, C.-Y., Zhang, R.-Y., Peng, A.-A., Tang, L., Qiu, G.-Z., *Sulfur oxidation activities of pure and mixed thermophiles and sulfur speciation in bioleaching of chalcopyrite.* Bioresource Technology, 2011. **102**(4): p. 3877-3882.
23. Watling, H.R., *The bioleaching of sulphide minerals with emphasis on copper sulphides — A review.* Hydrometallurgy, 2006. **84**(1–2): p. 81-108.
24. Deveci, H., Jordan, M. A., Powell, N., Alp, I., *Effect of salinity and acidity on bioleaching activity of mesophilic and extremely thermophilic bacteria.* Transactions of Nonferrous Metals Society of China, 2008. **18**(3): p. 714-721.
25. Dopson, M., Johnson, D. B., *Biodiversity, metabolism and applications of acidophilic sulfur-metabolizing microorganisms.* Environ Microbiol, 2012. **14**(10): p. 2620-31.
26. Larsson, L., Olsson, G., Hoist, O., Karlsson, H. T., *Oxidation of pyrite by Acidianus brierleyi: Importance of close contact between the pyrite and the microorganisms.* Biotechnology Letters, 1993. **15**(1): p. 99-104.
27. Mikkelsen, D., Kappler, U., Webb, R. I., Rasch, R., McEwan, A. G., Sly, L. I., *Visualisation of pyrite leaching by selected thermophilic archaea: Nature of microorganism–ore interactions during bioleaching.* Hydrometallurgy, 2007. **88**(1–4): p. 143-153.
28. Sharma, P.K., Das, A., Hanumantha Rao, K., Forssberg, K. S. E., *Surface characterization of Acidithiobacillus ferrooxidans cells grown under different conditions.* Hydrometallurgy, 2003. **71**(1–2): p. 285-292.
29. Konishi, Y., Kogasaki, K., Asai, S., *Bioleaching of pyrite by Acidianus brierleyi in a continuous-flow stirred-tank reactor.* Chemical Engineering Science, 1997. **52**(24): p. 4525-4532.
30. Konishi, Y., Tokushige, M., Asai, S., Suzuki, T., *Copper recovery from chalcopyrite concentrate by acidophilic thermophile Acidianus brierleyi in batch and continuous-flow stirred tank reactors.* Hydrometallurgy, 2001. **59**(2–3): p. 271-282.

31. Konishi, Y., Matsui, M., Fujiwara, H., Nomura, T., Nakahara, K., *Zinc Leaching from Fly Ash in Municipal Waste Incineration by Thermophilic Archaean Acidianus brierleyi Growing on Elemental Sulfur.* Separation Science and Technology, 2003. **38**(16): p. 4117-4130.
32. Zhang, Y.-S., Qin, W.-Q., Wang, J., Zhen, S.-J., Yang, C.-R., Zhang, J.-W., Nai, S.-S., Qiu, G.-Z., *Bioleaching of chalcopyrite by pure and mixed culture.* Transactions of Nonferrous Metals Society of China, 2008. **18**(6): p. 1491-1496.
33. van Scherpenzeel, D.A., Boon, M., Ras, C., Hansford, G. S., Heijnen, J. J., *Kinetics of Ferrous Iron Oxidation by Leptospirillum Bacteria in Continuous Cultures.* Biotechnology Progress, 1998. **14**(3): p. 425-433.
34. Xia, J.-L., Yang, Y., He, H., Zhao, X.-J., Liang, C.-L., Zheng, L., Ma, C.-Y., Zhao, Y.-D., Nie, Z.-Y., Qiu, G.-Z., *Surface analysis of sulfur speciation on pyrite bioleached by extreme thermophile Acidianus manzaensis using Raman and XANES spectroscopy.* Hydrometallurgy, 2010. **100**(3–4): p. 129-135.
35. Liu, H., Gu, G., Xu, Y., *Surface properties of pyrite in the course of bioleaching by pure culture of Acidithiobacillus ferrooxidans and a mixed culture of Acidithiobacillus ferrooxidans and Acidithiobacillus thiooxidans.* Hydrometallurgy, 2011. **108**(1–2): p. 143-148.
36. Yu, J.-Y., McGenity, T. J., Coleman, M. L., *Solution chemistry during the lag phase and exponential phase of pyrite oxidation by Thiobacillus ferrooxidans.* Chemical Geology, 2001. **175**(3): p. 307-317.
37. Boon, M., Heijnen, J. J., *Chemical oxidation kinetics of pyrite in bioleaching processes.* Hydrometallurgy, 1998. **48**(1): p. 27-41.
38. Karavaiko, G.I., Smolskaja, L. S., Golyshina, O. K., Jagovkina, M. A., Egorova, E. Y., *Bacterial pyrite oxidation: Influence of morphological, physical and chemical properties.* Fuel Processing Technology, 1994. **40**(2): p. 151-165.
39. Mitsunobu, S., Zhu, M., Takeichi, Y., Ohigashi, T., Suga, H., Jinno, M., Makita, H., Sakata, M., Ono, K., Mase, K., Takahashi, Y., *Direct Detection of Fe(II) in Extracellular Polymeric Substances (EPS) at the Mineral-Microbe Interface in Bacterial Pyrite Leaching*. Vol. 31. 2016.
40. Watling, H.R., Perrot, F. A., Shiers, D. W., *Comparison of selected characteristics of Sulfobacillus species and review of their occurrence in acidic and bioleaching environments.* Hydrometallurgy, 2008. **93**(1–2): p. 57-65.
41. Microanalysis, C.F.f.A.M.a. *Introduction to Energy Dispersive X-ray Spectrometry (EDS)*. 2015 [cited 2017; Available from: http://cfamm.ucr.edu/manuals.html.
42. *MyScope: training for advanced research*. 2014 April 15, 2014 [cited 2017 21/08]; Available from: ww.ammrf.org.au/myscope.
43. Swapp, S. *Geochemical Instrument Analysis: Scanning Electron Microscopy*. [Website] 2012 7/7/2012 [cited 2012 19/7/2012]; Available from: http://serc.carleton.edu/research_education/geochemsheets/techniques/SEM.html.
44. Chau, T.T., Bruckard, W. J., Koh, P. T. L., Nguyen, A. V., *A review of factors that affect contact angle and implications for flotation practice.* Advances in Colloid and Interface Science, 2009. **150**(2): p. 106-115.
45. Sand, W., Gehrke, T., Jozsa, P.-G., Schippers, A., *(Bio)chemistry of bacterial leaching—direct vs. indirect bioleaching.* Hydrometallurgy, 2001. **59**(2): p. 159-175.
46. Gehrke, T., Telegdi, J., Thierry, D., Sand, W., *Importance of Extracellular Polymeric Substances from Thiobacillus ferrooxidans for Bioleaching.* Appl Environ Microbiol, 1998. **64**(7): p. 2743-7.
47. Chipfunhu, D., Zanin, M., Grano, S., *Flotation behaviour of fine particles with respect to contact angle.* Chemical Engineering Research and Design, 2012. **90**(1): p. 26-32.
48. Womes, M., Karnatak, R. C., Esteva, J. M., Lefebvre, I., Allan, G., Olivier-Fourcades, J., Jumas, J. C., *Electronic structures of FeS and FeS2: X-ray absorption spectroscopy and*

band structure calculations. Journal of Physics and Chemistry of Solids, 1997. **58**(2): p. 345-352.
49. Fleet, M.E., *XANES Spectroscopy of sulphur in Earth Materials*. Vol. 43. 2005. 1811-1838.
50. von Oertzen, G.U., Jones, R. T., Gerson, A. R., *Electronic and optical properties of Fe, Zn and Pb sulfides.* Physics and Chemistry of Minerals, 2005. **32**(4): p. 255-268.
51. Miedema, P.S., de Groot, F. M. F., *The iron L edges: Fe 2p X-ray absorption and electron energy loss spectroscopy.* Journal of Electron Spectroscopy and Related Phenomena, 2013. **187**(Supplement C): p. 32-48.
52. Goh, S.W., Buckley, A. N., Lamb, R. N., Rosenberg, R. A., Moran, D., *The oxidation states of copper and iron in mineral sulfides, and the oxides formed on initial exposure of chalcopyrite and bornite to air.* Geochimica et Cosmochimica Acta, 2006. **70**(9): p. 2210-2228.
53. Doyle, C.S., Kendelewicz, T., Bostick, B. C., Brown, G. E., *Soft X-ray spectroscopic studies of the reaction of fractured pyrite surfaces with Cr(VI)-containing aqueous solutions.* Geochimica et Cosmochimica Acta, 2004. **68**(21): p. 4287-4299.
54. Zubavichus, Y., Fuchs, O., Weinhardt, L., Heske, C., Umbach, E., Denlinger, J. D., Grunze, M., *Soft X-Ray-Induced Decomposition of Amino Acids: An XPS, Mass Spectrometry, and NEXAFS Study.* Radiation Research, 2004. **161**(3): p. 346-358.
55. Rightor, E.G., Hitchcock, A. P., Ade, H., Leapman, R. D., Urquhart, S. G., Smith, A. P., Mitchell, G., Fischer, D., Shin, H. J., Warwick, T., *Spectromicroscopy of Poly(ethylene terephthalate): Comparison of Spectra and Radiation Damage Rates in X-ray Absorption and Electron Energy Loss.* The Journal of Physical Chemistry B, 1997. **101**(11): p. 1950-1960.
56. Watts, B., Thomsen, L., Dastoor, P. C., *Methods in carbon K-edge NEXAFS: Experiment and analysis.* Journal of Electron Spectroscopy and Related Phenomena, 2006. **151**(2): p. 105-120.
57. Briggs, D., Vickerman, J. C., *ToF-SIMS : surface analysis by mass spectrometry*. 2001, Chichester : IM ; Manchester: SurfaceSpectra
58. Stewart-Ornstein, J., Hitchcock, A. P., Hernandez Cruz, D., Henklein, P., Overhage, J., Hilpert, K., Hale, J. D., Hancock, R. E., *Using intrinsic X-ray absorption spectral differences to identify and map peptides and proteins.* J Phys Chem B, 2007. **111**(26): p. 7691-9.
59. Dynes, J.J., Lawrence, J. R., Korber, D. R., Swerhone, G. D., Leppard, G. G., Hitchcock, A. P., *Morphological and biochemical changes in Pseudomonas fluorescens biofilms induced by sub-inhibitory exposure to antimicrobial agents.* Can J Microbiol, 2009. **55**(2): p. 163-78.
60. Solomon, D., Lehmann, J., Harden, J., Wang, J., Kinyangi, J., Heymann, K., Karunakaran, C., Lu, Y., Wirick, S., Jacobsen, C., *Micro- and nano-environments of carbon sequestration: Multi-element STXM–NEXAFS spectromicroscopy assessment of microbial carbon and mineral associations.* Chemical Geology, 2012. **329**(0): p. 53-73.
61. Kaznacheyev, K., Osanna, A., Jacobsen, C., Plashkevych, O., Vahtras, O., Ågren, H., Carravetta, V., Hitchcock, A. P., *Innershell Absorption Spectroscopy of Amino Acids.* The Journal of Physical Chemistry A, 2002. **106**(13): p. 3153-3168.
62. Wan, J., Tyliszczak, T., Tokunaga, T. K., *Organic carbon distribution, speciation, and elemental correlations within soil microaggregates: Applications of STXM and NEXAFS spectroscopy.* Geochimica et Cosmochimica Acta, 2007. **71**(22): p. 5439-5449.
63. Boese, J., Osanna, A., Jacobsen, C., Kirz, J., *Carbon edge XANES spectroscopy of amino acids and peptides.* Journal of Electron Spectroscopy and Related Phenomena, 1997. **85**(1–2): p. 9-15.
64. Coker, V.S., Byrne, J. M., Telling, N. D., Van Der Laan, G., Lloyd, J. R., Hitchcock, A. P., Wang, J., Pattrick, R. A. D., *Characterisation of the dissimilatory reduction of Fe(III)-oxyhydroxide at the microbe – mineral interface: the application of STXM–XMCD.* Geobiology, 2012. **10**(4): p. 347-354.

65. Morin, C., Hitchcock, A. P., Cornelius, R. M., Brash, J. L., Urquhart, S. G., Scholl, A., Doran, A., *Selective adsorption of protein on polymer surfaces studied by soft X-ray photoemission electron microscopy.* Journal of Electron Spectroscopy and Related Phenomena, 2004. **137–140**(0): p. 785-794.
66. Chan, C.S., Fakra, S. C., Edwards, D. C., Emerson, D., Banfield, J. F., *Iron oxyhydroxide mineralization on microbial extracellular polysaccharides.* Geochimica et Cosmochimica Acta, 2009. **73**(13): p. 3807-3818.
67. Miot, J., Benzerara, K., Morin, G., Kappler, A., Bernard, S., Obst, M., Férard, C., Skouri-Panet, F., Guigner, J.-M., Posth, N., Galvez, M., Brown Jr, G. E., Guyot, F., *Iron biomineralization by anaerobic neutrophilic iron-oxidizing bacteria.* Geochimica et Cosmochimica Acta, 2009. **73**(3): p. 696-711.
68. Yang, Y., Harmer, S., Chen, M., *Synchrotron X-ray photoelectron spectroscopic study of the chalcopyrite leached by moderate thermophiles and mesophiles.* Minerals Engineering, 2014. **69**: p. 185-195.
69. Yang, Y., Liu, W., Chen, M., *XANES and XRD study of the effect of ferrous and ferric ions on chalcopyrite bioleaching at 30°C and 48°C.* Minerals Engineering, 2015. **70**: p. 99-108.
70. Kalirai, S.S., Lam, K. P., Bazylinski, D. A., Lins, U., Hitchcock, A. P., *Examining the chemistry and magnetism of magnetotactic bacterium Candidatus Magnetovibrio blakemorei strain MV-1 using scanning transmission X-ray microscopy.* Chemical Geology, 2012. **300–301**(0): p. 14-23.
71. Behera, S.K., Mulaba-Bafubiandi, A. F., *Microbes Assisted Mineral Flotation a Future Prospective for Mineral Processing Industries: A Review.* Mineral Processing and Extractive Metallurgy Review, 2017. **38**(2): p. 96-105.
72. Poorni, S., Natarajan, K. A., *Flocculation behaviour of hematite–kaolinite suspensions in presence of extracellular bacterial proteins and polysaccharides.* Colloids and Surfaces B: Biointerfaces, 2014. **114**(0): p. 186-192.
73. Beech, I.B., Sunner, J., *Biocorrosion: towards understanding interactions between biofilms and metals.* Current Opinion in Biotechnology, 2004. **15**(3): p. 181-186.
74. Rojas-Chapana, J.A., Tributsch, H., *Bio-leaching of pyrite accelerated by cysteine.* Process Biochemistry, 2000. **35**(8): p. 815-824.
75. Crundwell, F.K., *How do bacteria interact with minerals?* Hydrometallurgy, 2003. **71**(1–2): p. 75-81.
76. Belu, A.M., Davies, M. C., Newton, J. M., Patel, N., *TOF-SIMS Characterization and Imaging of Controlled-Release Drug Delivery Systems.* Analytical Chemistry, 2000. **72**(22): p. 5625-5638.
77. Berman, E.S.F., Wu, L., Fortson, S. L., Kulp, K. S., Nelson, D. O., Wu, K. J., *Chemometric and statistical analyses of ToF-SIMS spectra of increasingly complex biological samples.* Surface and Interface Analysis, 2009. **41**(2): p. 97-104.
78. de Brouwer, J.F.C., Cooksey, K. E., Wigglesworth-Cooksey, B., Staal, M. J., Stal, L. J., Avci, R., *Time of Flight-Secondary Ion Mass Spectrometry on isolated extracellular fractions and intact biofilms of three species of benthic diatoms.* Journal of Microbiological Methods, 2006. **65**(3): p. 562-572.
79. Dague, E., Delcorte, A., Latgé, J.-P., Dufrêne, Y. F., *Combined Use of Atomic Force Microscopy, X-ray Photoelectron Spectroscopy, and Secondary Ion Mass Spectrometry for Cell Surface Analysis.* Langmuir, 2008. **24**(7): p. 2955-2959.
80. Breitenstein, D., Rommel, C. E., Stolwijk, J., Wegener, J., Hagenhoff, B., *The chemical composition of animal cells reconstructed from 2D and 3D ToF-SIMS analysis.* Applied Surface Science, 2008. **255**(4): p. 1249-1256.
81. Vaidyanathan, S., Fletcher, J. S., Lockyer, N. P., Vickerman, J. C., *TOF-SIMS investigation of Streptomyces coelicolor, a mycelial bacterium.* Applied Surface Science, 2008. **255**(4): p. 922-925.

82. Schilke, K.F., McGuire, J., *Detection of nisin and fibrinogen adsorption on poly(ethylene oxide) coated polyurethane surfaces by time-of-flight secondary ion mass spectrometry (TOF-SIMS).* Journal of Colloid and Interface Science, 2011. **358**(1): p. 14-24.
83. Sanni, O.D., Wagner, M. S., Briggs, D., Castner, D. G., Vickerman, J. C., *Classification of adsorbed protein static ToF-SIMS spectra by principal component analysis and neural networks.* Surface and Interface Analysis, 2002. **33**(9): p. 715-728.
84. Baldwin, P.M., Melia, C. D., Davies, M. C., *The Surface Chemistry of Starch Granules Studied by Time-of-Flight Secondary Ion Mass Spectrometry.* Journal of Cereal Science, 1997. **26**(3): p. 329-346.
85. Heim, C., Sjövall, P., Lausmaa, J., Leefmann, T., Thiel, V., *Spectral characterisation of eight glycerolipids and their detection in natural samples using time-of-flight secondary ion mass spectrometry.* Rapid Communications in Mass Spectrometry, 2009. **23**(17): p. 2741-2753.
86. Robinson, M.A., Graham, D. J., Morrish, F., Hockenbery, D., Gamble, L. J., *Lipid analysis of eight human breast cancer cell lines with ToF-SIMS.* Biointerphases, 2016. **11**(2): p. 02A303.
87. Vaidyanathan, S., Fletcher, J. S., Jarvis, R. M., Henderson, A., Lockyer, N. P., Goodacre, R., Vickerman, J. C., *Explanatory multivariate analysis of ToF-SIMS spectra for the discrimination of bacterial isolates.* Analyst, 2009. **134**(11): p. 2352-2360.
88. Biesinger, M.C., Miller, D. J., Harbottle, R. R., Possmayer, F., McIntyre, N. S., Petersen, N. O., *Imaging lipid distributions in model monolayers by ToF-SIMS with selectively deuterated components and principal components analysis.* Applied Surface Science, 2006. **252**(19): p. 6957-6965.
89. Tervahattu, H., Juhanoja, J., Kupiainen, K., *Identification of an organic coating on marine aerosol particles by TOF-SIMS.* Journal of Geophysical Research: Atmospheres, 2002. **107**(D16): p. ACH 18-1-ACH 18-7.
90. Boulton, A., Fornasiero, D., Ralston, J., *Characterisation of sphalerite and pyrite flotation samples by XPS and ToF-SIMS.* International Journal of Mineral Processing, 2003. **70**(1–4): p. 205-219.
91. Khmeleva, T.N., Georgiev, T. V., Jasieniak, M., Skinner, W. M., Beattie, D. A., *XPS and ToF-SIMS study of a chalcopyrite–pyrite–sphalerite mixture treated with xanthate and sodium bisulphite.* Surface and Interface Analysis, 2005. **37**(8): p. 699-709.
92. Hart, B., Biesinger, M., Smart, R. St. C., *Improved statistical methods applied to surface chemistry in minerals flotation.* Minerals Engineering, 2006. **19**(6–8): p. 790-798.
93. Kalegowda, Y., Harmer, S. L., *Chemometric and Multivariate Statistical Analysis of Time-of-Flight Secondary Ion Mass Spectrometry Spectra from Complex Cu–Fe Sulfides.* Analytical Chemistry, 2012. **84**(6): p. 2754-2760.
94. Kalegowda, Y., Harmer, S. L., *Classification of time-of-flight secondary ion mass spectrometry spectra from complex Cu–Fe sulphides by principal component analysis and artificial neural networks.* Analytica Chimica Acta, 2013. **759**: p. 21-27.
95. Berman, E.S.F., Kulp, K. S., Knize, M. G., Wu, L., Nelson, E. J., Nelson, D. O., Wu, K. J., *Distinguishing Monosaccharide Stereo- and Structural Isomers with TOF-SIMS and Multivariate Statistical Analysis.* Analytical Chemistry, 2006. **78**(18): p. 6497-6503.
96. Jungnickel, H., Jones, E. A., Lockyer, N. P., Oliver, S. G., Stephens, G. M., Vickerman, J. C., *Application of TOF-SIMS with Chemometrics To Discriminate between Four Different Yeast Strains from the Species Candida glabrata and Saccharomyces cerevisiae.* Analytical Chemistry, 2005. **77**(6): p. 1740-1745.
97. Pradier, C.M., Rubio, C., Poleunis, C., Bertrand, P., Marcus, P., Compère, C., *Surface Characterization of Three Marine Bacterial Strains by Fourier Transform IR, X-ray Photoelectron Spectroscopy, and Time-of-Flight Secondary-Ion Mass Spectrometry, Correlation with Adhesion on Stainless Steel Surfaces.* The Journal of Physical Chemistry B, 2005. **109**(19): p. 9540-9549.

6 Characterisation of *Acidianus brierleyi* and Pyrite: Growth Behaviour and Mineral Surface Properties.

6.1 Introduction

A. brierleyi was one of the first acidophilic archaea to be isolated, first discovered and described by Brierleyi *et al* in Yellowstone hot springs [1]. As was explored in Chapter 2, section 2.2.4, *A. brierleyi* has been used in bioleaching investigations, but is not as commonly used for bioflotation, where it has only been used in a mixture with other archaea [2]. This bioflotation study focussed mainly on mineral recovery measurements, with no investigation of the cells, their mechanism of attachment, or the mineral surface physicochemical properties [2]. This microorganism has mainly been applied to the bioleaching of a wide variety of substrates, including hydrotreating catalyst [3, 4], sphalerite [5, 6], enargite [7, 8] and molybdenite [9]. *A. brierleyi* has also been used to leach pyrite and chalcopyrite, and have been shown to grow on these substrates in the literature [10-18]. Most of these studies are limited to observing recovery of metals of interest from leaching processes, with little if any surface characterisation or chemical analysis of the mineral [5, 6, 10-13, 16-18].

Unlike the bacterial strains investigated in the previous chapters, which grow under mesophilic conditions, *A. brierleyi* is an extreme thermophile used by previous studies in temperatures between 60-75 °C [7, 8, 10-12, 19]. *A. brierleyi* is capable of oxidizing both ferrous iron and elemental sulfur to ferric iron and sulfate, respectively, with the increase of ideal growth temperature of 30-40°C compared to mesophilic strains shown to accelerate bioleaching and surface oxidation [1, 10-12, 20-24]. This accelerated surface oxidation might promote the formation of oxygen-rich species on the mineral surface, creating a less hydrophobic surface ideal for depression in mineral flotation.

Govender *et al* used *Acidianus sp* mixed with other thermophilic archaea grown on chalcopyrite to pre-treat and successfully float chalcopyrite, focussing on process optimization rather than the chemical species and microorganisms involved [2]. This study did find that the mixed culture of extreme thermophiles provided the highest recovery for chalcopyrite [2]. These results, coupled with the ability of *A. brierleyi* to tolerate higher temperatures and high metal ion concentrations make it a prime candidate for bioflotation applications [2, 10-12, 25, 26].

A thorough study of a pure strain of *A. brierleyi* and the potential use it has in future studies for bioflotation has yet to be explored. In this chapter, pyrite is exposed to *A. brierleyi* and the surface of the mineral is analysed for signs of EPS and bacterial attachment. Special interest is taken in the

time-frame over which attachment occurs and how the chemical species on the surface are changed by the presence of *A. brierleyi*. No previous study has been found that comprehensively compares chemical analysis with physical properties of pyrite under exposure to *A. brierleyi*.

6.2 Experimental

6.2.1 Mineral Preparation

The bulk pyrite for culture growth is described in in Chapter 3, section 3.2, Table 3.4. The cubic pyrite used for this investigation and the preparation of mineral tile samples are described in Chapter 3, sections 3.2 and 3.4, respectively.

Tiles were either snap frozen in DSM 150 medium for AFM and ToF-SIMS analysis or stored in fixative for dehydration and sputtering coating for SEM by methods described in Chapter 3, section 3.9.

6.2.2 Cell Growth and Monitoring

Cultures of *A. brierleyi* (DSM 1651) were received live from the DSMZ (Deutsche Sammlung von Mikroorganismen und Zellkulturen) and a base culture was inoculated into DSM 150 medium and continuously subcultured as described in Chapter 3, section 3.3.2. Cultures were monitored by direct cell counting, as described in Chapter 3, section 3.8.

6.2.3 Surface Characterisation

Surface analysis of pyrite control and those exposed to *A. brierleyi* were performed using Scanning Electron Microscope (SEM), Energy Dispersive X-ray spectroscopy (EDX), Atomic Force Microscopy (AFM), captive bubble contact angle, and Time of Flight – Secondary Ion Mass Spectroscopy (ToF-SIMS). Details for these techniques can be found in Chapter 3, sections 3.9, 3.10, 3.14, and 3.16.

6.3 Results and Discussion

6.3.1 Growth of *Acidianus brierleyi* on Pyrite

6.3.1.1 Cell Growth

The live culture of *A. brierleyi* was first cultured in DSM 150 medium using sulfur flowers powder as a source of nutrients. Growth of this base culture was monitored by direct counting; however, it should be noted that cell behaviour altered significantly after removal from culture, with live cells

ceasing movement as sample temperature dropped, making direct monitoring challenging. This was minimised by maintaining culture samples at 60 °C prior to counting to reduce cooling as much as possible. An example of *A. brierleyi* growth curve on sulfur flowers powder is show in Figure 6.63. When cultures reached an excess of 10^8 cells/mL, samples had to be diluted by a factor of 2 or 10 to allow for effective counting. This resulted in larger error being introduced for larger cell populations. This culture was continually subcultured at 10% inoculum, with a growth cycle completing every three weeks.

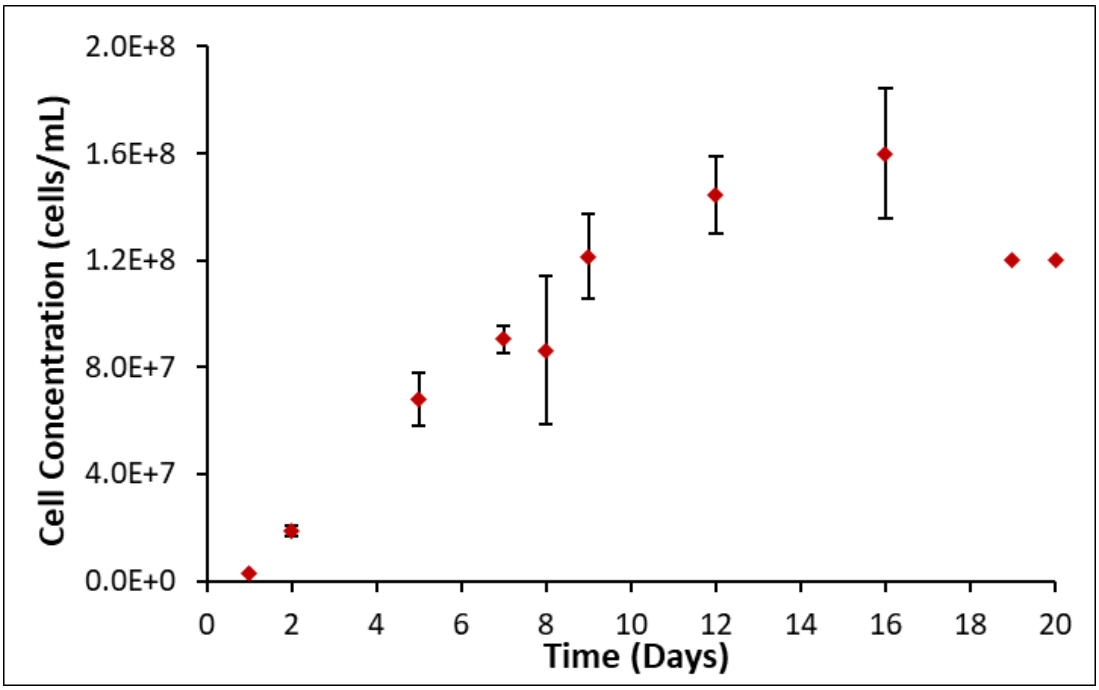

Figure 6.63: Typical growth curve of *A. brierleyi* on sulfur flowers at 10% inoculum in DSM 150 medium.

A. brierleyi was adapted to grow on pyrite by subculturing from cultures grown on sulfur flowers powder into DSM 150 medium with 20 g of UV sterilised pyrite. Cultures were inoculated at 10% with *A. brierleyi*. Growth curves were determined by counting, and a typical growth curve is shown in Figure 6.64.

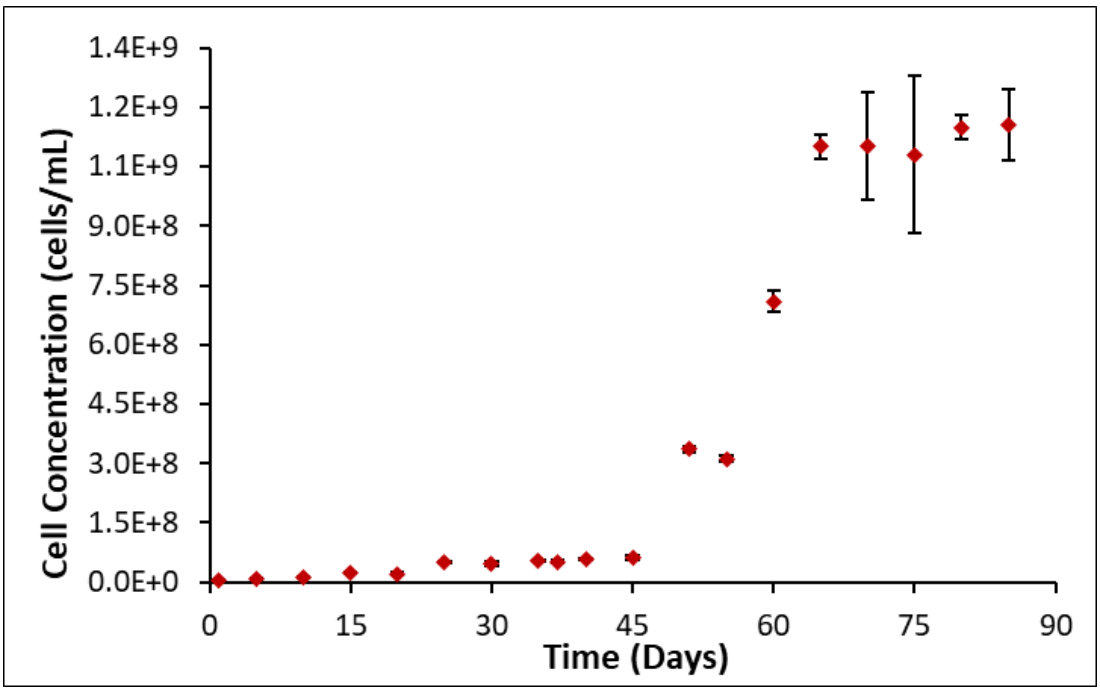

Figure 6.64: Typical growth curve of *A. brierleyi* on pyrite (+38, -75 um) at 10% inoculum in DSM 150 medium.

When grown on sulfur flower, the cultures typically reach the exponential phase within the first week, completing a growth cycle in 21 days (Figure 6.63). *A. brierleyi* grown on pyrite stabilized to a 90-day growth cycle, with the cells reaching the exponential phase between 45-60 days (Figure 6.64).

Final cell concentrations previously described of *A. brierleyi* on a variety of substrates ranges between 10^7 and 10^{15} cells/mL, with stationary phase reached typically between 2 to 20 days [3, 7, 8, 12-15, 19, 21, 23, 25]. Several previous studies have grown *A. brierleyi* on elemental sulfur on the prescribed medium, but concentrate the cells prior to bioleaching experiments without reporting base culture growth curves, or grow cells in a different media prior to leaching experiments [7, 8, 14, 15, 23]. As has been stated in previous chapters, the variation of inoculation and growth conditions makes direct comparison with previous studies challenging.

6.3.1.2 Eh and pH Monitoring

The Eh and pH of *A. brierleyi* on pyrite was measured with reference to a Ag/AgCl electrode at 1 atm with an average temperature of 24.3 ± 0.9 °C, while the average temperature of the control DSM 150 medium exposed to pyrite was measured with an average temperature of 24.5 ± 1.1 °C. The Eh and pH curves of the DSM 150 medium and *A. brierleyi* pyrite leachate are shown in Figure 6.65. The pH of the *A. brierleyi* culture grown on pyrite starts at 1.56, decreasing steadily to pH 0.49 day 85, while the Eh steadily increases from 320 mV to over 389 mV over the course of the natural growth cycle. In contrast, the pH of the control solution starts at 2.25, but has decreased

consistently at a great rate the *A. brierleyi* culture to a final pH of 0.6 by day 75, converging on the pH of the *A. brierleyi* culture. The Eh of the control solution starts at 208 mV, well below that of the archaea culture, increasing steadily to a final Eh of just over 383 mV by day 75, also converging on the Eh of the culture solution.

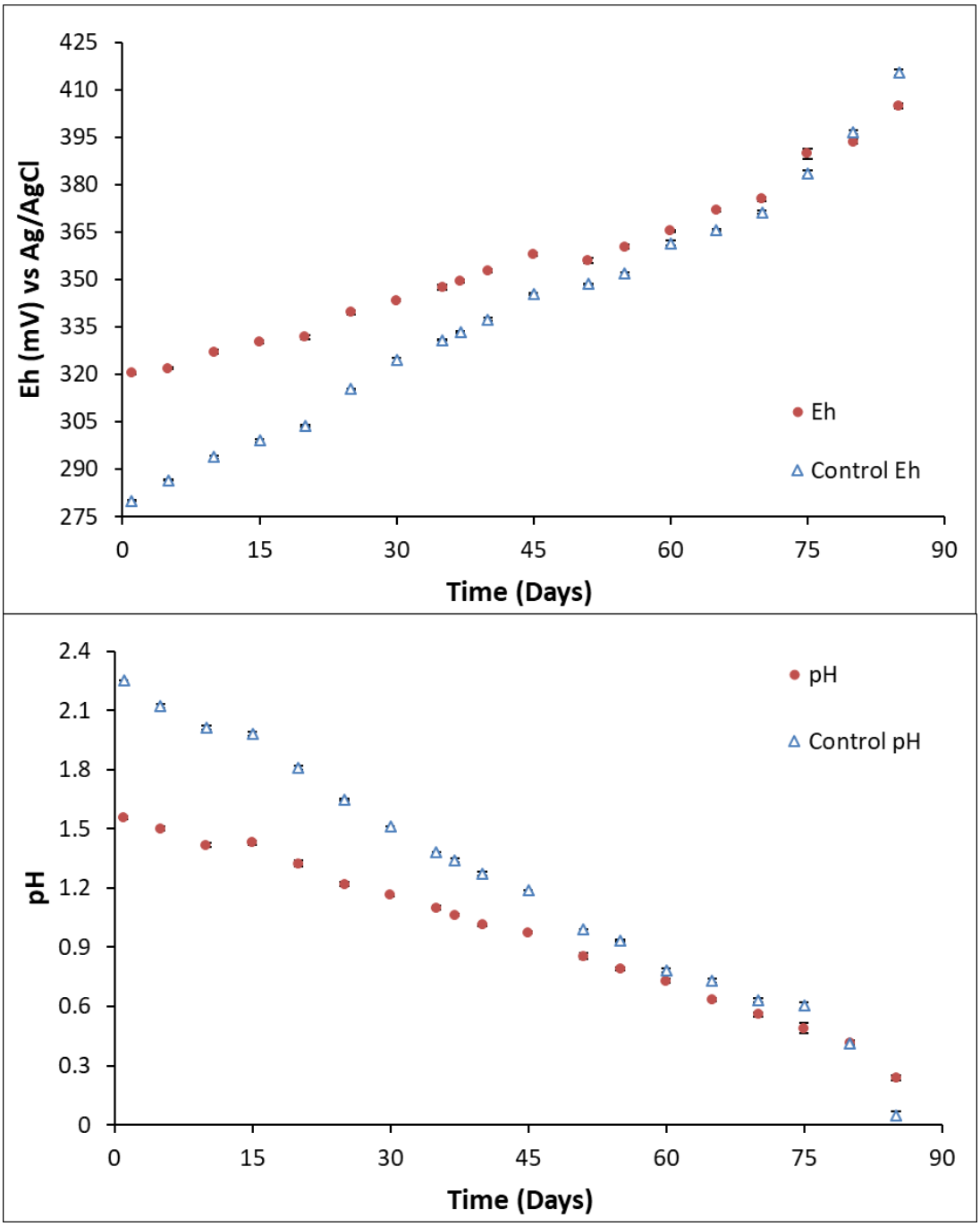

Figure 6.65: Typical Eh (top) and pH (bottom) curves of *A. brierleyi* on pyrite (+38, -75 um) at 10% inoculum (●), and DSM 150 medium (Δ).

Previous studies have measured the Eh and pH of leachate of a variety of substrates using *A. brierleyi*, a summary of which can be found in Table 6.9. All potentials reported here have been converted to Ag/AgCl reference electrode values where appropriate.

Table 6.9: Previous Eh and pH studies of *A. brierleyi* bioleaching various substrates.

Substrate	Duration (days)	Eh $_{init.}$ (mV)	Eh $_{fin.}$ (mV)	pH $_{init.}$	pH $_{fin.}$	Reference
S^0	6	-	-	2.3	1.0	[23]
S^0	20	-	-	2-1.5	0.66	[3]
Decoked catalyst [a]	14	320	440	1.6	2.0	[4]
Enargite	30	295	595	1.5	1.3-1.1	[7]
Enargite	25	295	645	1.5	1.3	[8]
Molybdenite	28	467	699	≥2.0	≤1.0	[9]
Chalcopyrite	14	315	395	1.5	0.8	[14, 15]
Chalcopyrite (abiotic)	14	315	355	1.5	1.45	[14, 15]

[a] No reported reference electrode

Several of the studies listed in this table performed no control experiments for comparison of their bioleaching results [3, 7-9, 23]. The Eh and pH data recorded in this study agree with strongly with the results obtained by Zhu *et al*, however, all the studies on mineral leaching and sulfur-grown cultures observed a decrease in pH between 2.5 and 0.5, which agrees with the range of values observed over the leaching of pyrite in this study [14, 15]. The results of this study show the pH decreases as the pyrite oxidises and produces H^+, per Equations 4.37, 4.38 and 4.41, promoting higher concentrations of soluble sulfur species such as sulfates, and ferric iron in solution. The pH values measured over the course of these experiments suggests that the consumption of sulfuric acid is outweighed by production, with the pH never greater than the initial value measured for the medium solution. Lower pH is also less conducive to the formation of jarosite, as per Equation 4.44 [27].

The Eh values observed in this study are increasing over time, suggesting oxidative conditions which will impact the surface species forming on the surface. These conditions promote the oxidation of the pyrite surface to produce soluble sulfur oxidation products and ferric iron in solution, which in turn result in elemental sulfur and iron oxidation products forming on the mineral surface [6, 10, 12, 15-17, 19, 23, 28, 29]. Unlike the mesophilic strains investigated in the previous chapters, the difference between the Eh of the culture and the abiotic control is most pronounced at early exposure stages, suggesting the oxidation of the pyrite surface is accelerated by the presence of cells. Titration and Inductively Coupled Plasma Optical Emission Spectroscopy (ICPOES) are applied in the following section to determine the ionic iron and sulfur species present in solution that contribute to the Eh measured over the course of exposure to pyrite.

6.3.1.3 *Inductively Coupled Plasma Optical Emission Spectroscopy, Cerium(IV) Sulfate Titration*

The methods through which ferrous iron, ferric iron and total soluble sulfur were determined by ICPOES, and colorimetric titration against cerium(IV) sulfate as described in Chapter 3, sections 3.6 and 3.7, respectively. The ferrous iron, ferric iron and soluble sulfur concentrations of the leachate of pyrite exposed to DSM 150 medium and *A. brierleyi* culture are shown in Figure 6.66.

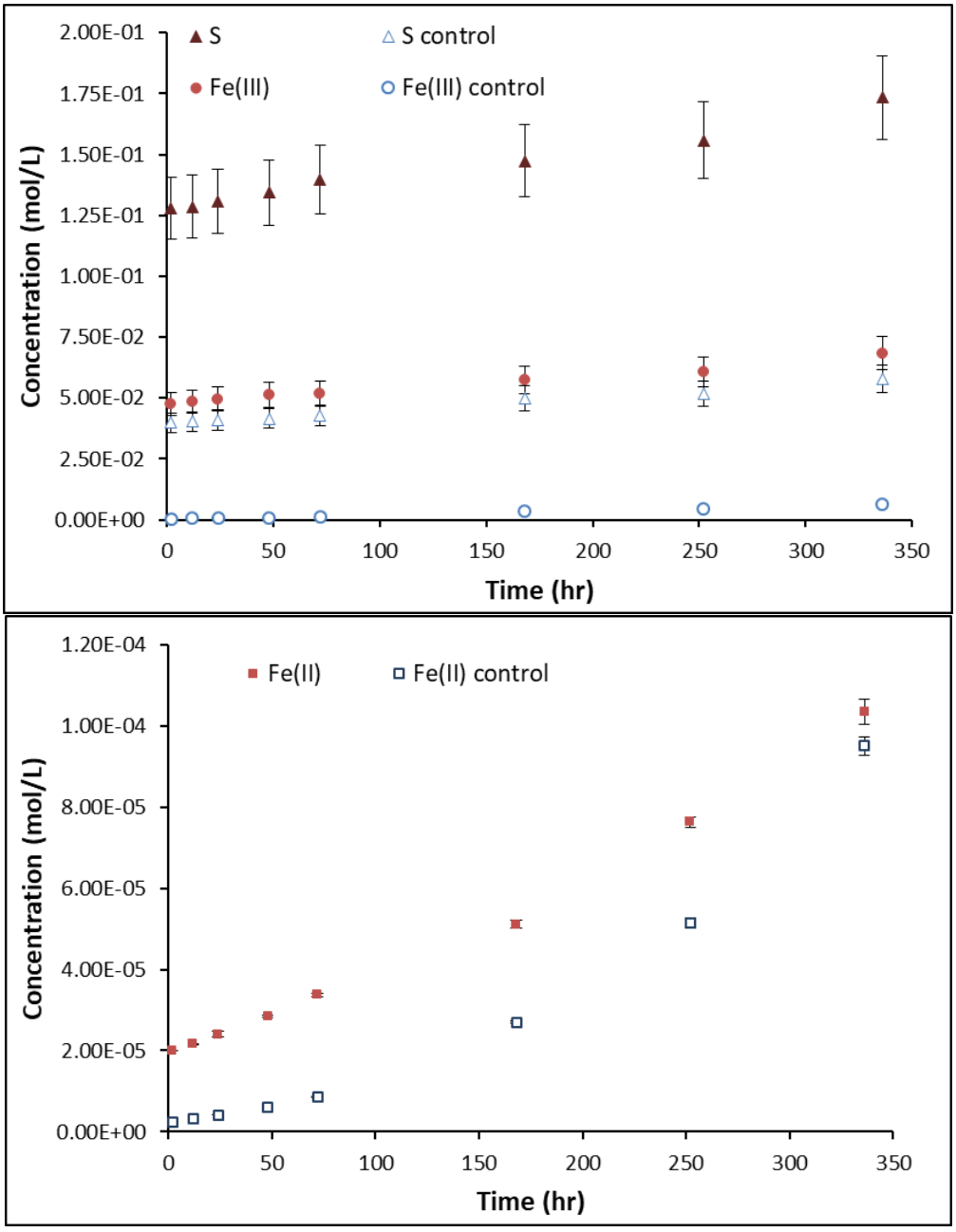

Figure 6.66: Typical concentration curves of ferric iron (top) of *A. brierleyi* on pyrite (●), and DSM 150 medium (○). and solubilised sulfur (top) in *A. brierleyi* on pyrite (▲), and DSM 150 medium (△). Typical concentration curves of ferrous iron (bottom) of *A. brierleyi* on pyrite (■), and DSM 150 medium (□).

The concentration of Fe^{2+} ions in the medium leaching solution increases almost linearly from $2.28x10^{-6}$ mol/L at 2 h up to $9.51x10^{-5}$ mol/L by 336 h, with this linear increase repeated by the Fe^{3+} ions, the concentration of which increases from $4.16x10^{-2}$ mol/L up to $6.33x10^{-2}$ mol/L over 336 h. The total S measured in solution also displays a linear increase from $3.98x10^{-2}$ mol/L up to $5.79x10^{-2}$ mol/L over the same period. In each case, the initial concentration of the respective ions is greater in the *A. brierleyi* cultures than the medium solution, which also increase in concentration linearly. The *A. brierleyi* culture leaching solution displays an increase in Fe^{2+} ions of $2.0x10^{-5}$ mol/L up to $1.04x10^{-4}$ mol/L, an increase in Fe^{3+} ions of $4.76x10^{-2}$ mol/L up to $6.83x10^{-2}$ mol/L, and an increase in total S also of $1.28x10^{-1}$ mol/L up to $1.73x10^{-1}$ mol/L over the course of 336 h.

Previous studies have measured the iron and sulfur concentrations in the leachate of a variety of substrates using *A. brierleyi*. The ferrous iron concentrations reported in in the literature range between 0 mol/L and $6.27x10^{-3}$ mol/L, with the ferrous iron reported in this study falling within this range [16, 19]. The ferric iron concentrations previously reported range between $8.95x10^{-8}$ mol/L and $2.81x10^{-2}$ mol/L, with the concentrations reported in this study falling within that range [13-16, 19]. The sulfate concentrations previously reported in studies are limited to chalcopyrite leaching, with a range between $1.97x10^{-3}$ and 0.45 mol/L, which agrees with the total soluble sulfur measured in this study [12, 14, 15]. Many previous investigations into ion concentration in solution measured either total or ferrous iron and sulfate concentration in solution. Several studies on a variety of substrates add ferric or ferrous iron to their leaching solutions, making direct comparison of results challenging [7, 8, 19, 24].

The results of this study show the concentration of all ions is greater in *A. brierleyi* culture compared to the control DSM 150 medium, and that both total S and Fe^{3+} are leaching at a greater rate in the *A. brierleyi* culture. This suggests microbial action is oxidising the elemental sulfur in the surface to create a greater concentration of oxidised sulfur species in solution. However, it appears that while the Fe^{2+} concentration is greater in the culture solution, Fe^{2+} is leaching at a greater rate in the DSM 150 medium solution. This may be due to the formation of secondary minerals precipitates observed in previous studies removing ferrous iron from solution more effectively in culture [7, 8]. The difference between the control and the culture ion concentrations may be due to less oxidising activity in the control.

The increased rate of ions leaching into solution in the biotic experiments, and the higher concentration of both soluble sulfur and ferric iron species in solution, agrees with the Eh results which suggest more oxidative conditions and higher concentration of ions in when *A. brierleyi* is in contact with the pyrite [30]. These results suggest the presence of *A. brierleyi* is accelerating the

production of ferric irons in solution, which in turn leach the pyrite surface via Equations 4.37 and 4.42. This indicates that *A. brierleyi* may be interacting with the surface via the indirect or indirect contact mechanisms, by catalysing the oxidation of ferrous iron rather than by direct action on the mineral surface, as discussed in Chapter 2, section 2.3.2.

Although the exponential phase of *A. brierleyi* does not begin until day 45 of exposure to pyrite, the leaching of iron and sulfur-species from the mineral appears immediate, accompanied by a decrease in pH and an increase in Eh as sulfuric acid is produced and ferrous iron is oxidised to ferric iron and the leaching of the mineral is perpetuated. To relate the solution ion content, Eh and pH to the behaviour of *L. ferrooxidans* on the surface of pyrite, and to identify secondary mineral formation and leaching progression, it is necessary to investigate the surface using imaging techniques.

6.3.2 Scanning Electron Microscopy and Energy Dispersive X-ray Spectroscopy

Energy Dispersive X-ray (EDX) analysis was performed on the surface of the pyrite exposed to *A. brierleyi*, and on the artefacts observed on the surface using Scanning Electron Microscopy (SEM). This was done to enable the identification of the elements present and their atomic ratios, which be used to identify cellular material from secondary mineral precipitates. The EDX analysis of the pyrite surface exposed to *A. brierleyi* are shown in Figure 6.67 as average atomic percentage. The elements Al, Si, Na and K were detected at levels below 2%. EDX spectra were also collected for the large microscale aggregates observed on the surface shown in Figure 6.69(L). The polyp-type structures display only carbon and oxygen. Silicate crystal inclusions were highly visible in the pyrite samples, and these regions were avoided.

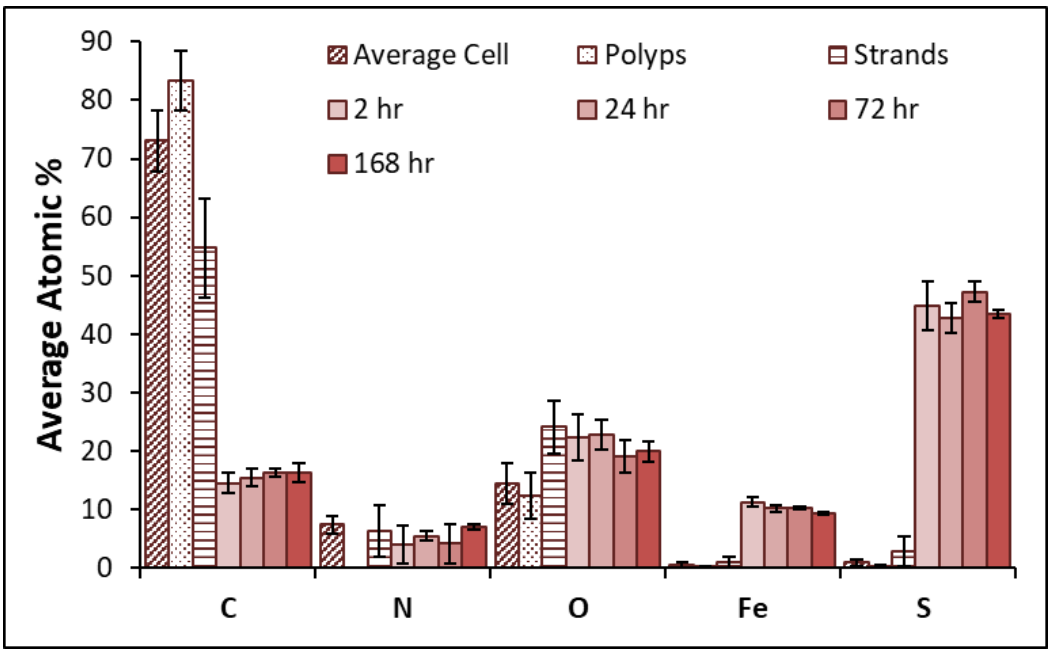

Figure 6.67: Average atomic percentage of pyrite exposed to *A. brierleyi* for 2, 24, 72 and 168 h, and the average atomic percentage of individual *A. brierleyi* cells (diagonal stripes), organic matter polyps (dots) and organic aggregate strands (horizontal stripes) as determined by EDX

The EDX atomic percentages of the pyrite surface exposed to *A. brierleyi* are relatively stable and within standard deviation, but this could be due in part to the fact that EDX penetrates the surface up to 5 μm, and presents significant bulk pyrite signal [31]. The cells of *A. brierleyi* present a significant carbon signal compared to the mineral spots measured, however cells are typically not thick enough to block all signal from the bulk mineral beneath, which is why typical pyrite signals of Fe and S are still observed [32]. Some carbon signal is observed on the pyrite surface that show no significant change over time, potentially due to the EDX having lack of sensitivity to the thin layers of carbon than do not have a large surface coverage [32].

The EDX analysis of the pyrite surface exposed to DSM 150 medium are shown in Figure 6.68 as average atomic percentage. The elements Al, Si and Na were detected at levels below 1%. The atomic percentages of pyrite exposed to DSM 150 medium control display a consistently lower amount of oxygen present on the surface as every period of exposure than pyrite exposed to *A. brierleyi*. The atomic percentage of carbon increases over the first 72 h of exposure, which coincides with a decrease in iron and a slight increase in sulfur. This suggests a build-up of carbon compounds on the surface, coating and potentially partially obscuring the mineral, coupled with the iron leaching from the pyrite, leaving the surface sulfur-rich.

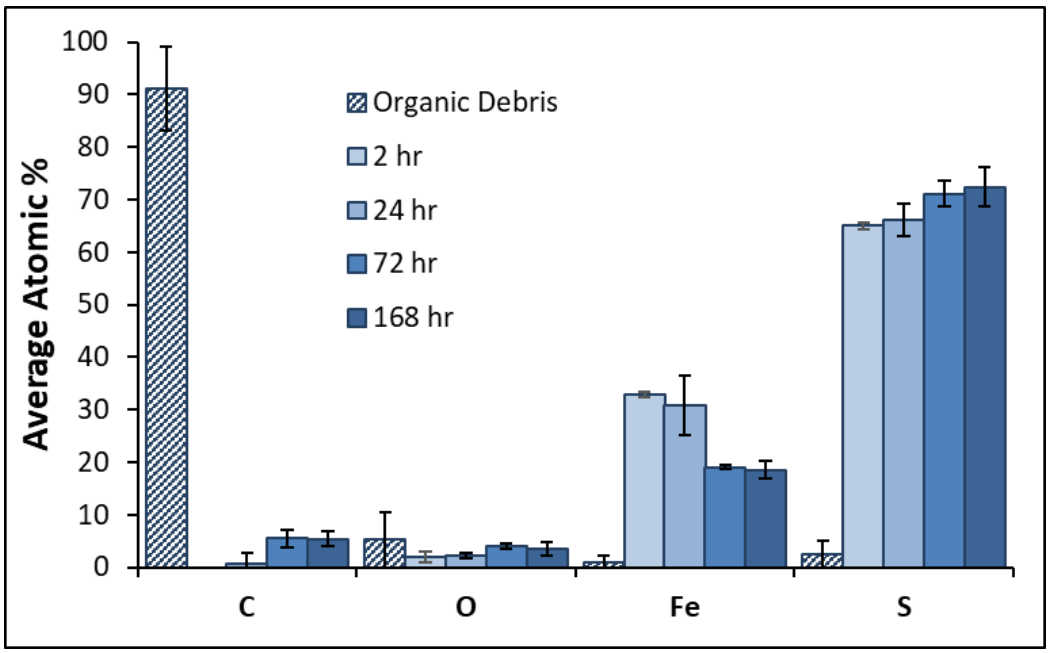

Figure 6.68: Average atomic percentage of pyrite exposed to DSM 150 medium for 2, 24, 72 and 168 h, and the average atomic percentage of organic debris (diagonal stripes), as determined by EDX.

Organic debris was also observed on the surface of the pyrite, and displayed high carbon signal, however, unlike the cells measured on the surface, no nitrogen was detected, with a detection limit of 0.1% [31]. The inorganic debris, shown on the surface next to *A. brierleyi* cells in Figure 6.69(C), was also examined by EDX, with the spectra of 27 individual pieces of debris analysed from several samples. The average atomic percentages are presented in Table 6.10.

Table 6.10: Average atomic percentage EDX data of inorganic precipitates

Element	*Atomic %*
C	5.8 ± 3.4
O	58.7 ± 8.9
Fe	9.4 ± 1.2
S	19.3 ± 6.0
K	4.1 ± 0.8
Si, Al, P, Na, N	< 1%

This results in atomic ratios of $K_1Fe_{2.3}S_{4.7}O_{14.3}$, which agrees closely with the chemical formula for potassium jarosite ($KFe_3(SO_4)_2.(OH)_6$), a commonly occurring secondary mineral precipitate [7, 8, 16]. The elevated atomic percentage of sulfur may be due to polysulfide precipitates and bulk pyrite signal from the underlying mineral [31].

Few studies have applied EDX to the analysis of surfaces bioleached by *A. brierleyi* or to the identification of *A. brierleyi* cells on mineral substrates. The results for the pyrite surface presented in this study agree with those of Mikkelsen *et al* and Takatsugi *et al*, who used EDX to characterise bulk pyrite leached by *A. brierleyi*, and identified sub-micron precipitates as iron sulfates, iron phosphates, and secondary minerals such as jarosite and scorodite ($FeAsO_4.2H_2O$) [8, 16].

Scanning electron microscopy (SEM) provides images that allow the identification of secondary mineral precipitates, the assessment of cell attachment to the mineral surface, and relation of mineral leaching to the solution conditions. Typical SEM images obtained for pyrite upon exposure to the DSM 150 medium control in comparison to pyrite exposed to *A. brierleyi* are shown in Figure 6.69. After 2 hours of exposure to *A. brierleyi* (see Figure 6.69(A)), the pyrite surface is covered with sub-micron debris, and is showing some surface leaching in the form of pits and cracks across the surface, which have been observed in a previous study and identified as leaching related to the crystal faces of the pyrite [33]. Scratches from the polishing process are also visible on the surface at all periods of exposure. The sub-micron debris observed in this study agrees with similar artefacts reported by Mikkelsen *et al* during pyrite leaching by *A. brierleyi* [16]. Large organic material aggregates (Figure 6.69(L)) were also found on the surface, showing strand-like structures and polyps between 3-10 μm in length, similar to structures formed by interactions between yeast extract and elemental sulfur observed by Cosmidis *et al* [34]. Larger inorganic particles are also observed on the surface, with more found in voids in the surface rather than on smoother regions, such as those pictured in Figure 6.69(C). These larger particles, determined by EDX to be jarosite crystals, typically appear in size range of 1-2 μm^2, the morphology and size of which is similar to crystals presented by Sasaki *et al*, and were formed biotically and abiotically [35]. The cells observed on the surface are spheroidal, with an average diameter of 3.11 ± 0.78 μm. This agrees with Segerer *et al*, who describes cell width of the genus *Acidianus* within a range of 0.5-2 μm, depending on growth conditions [20].

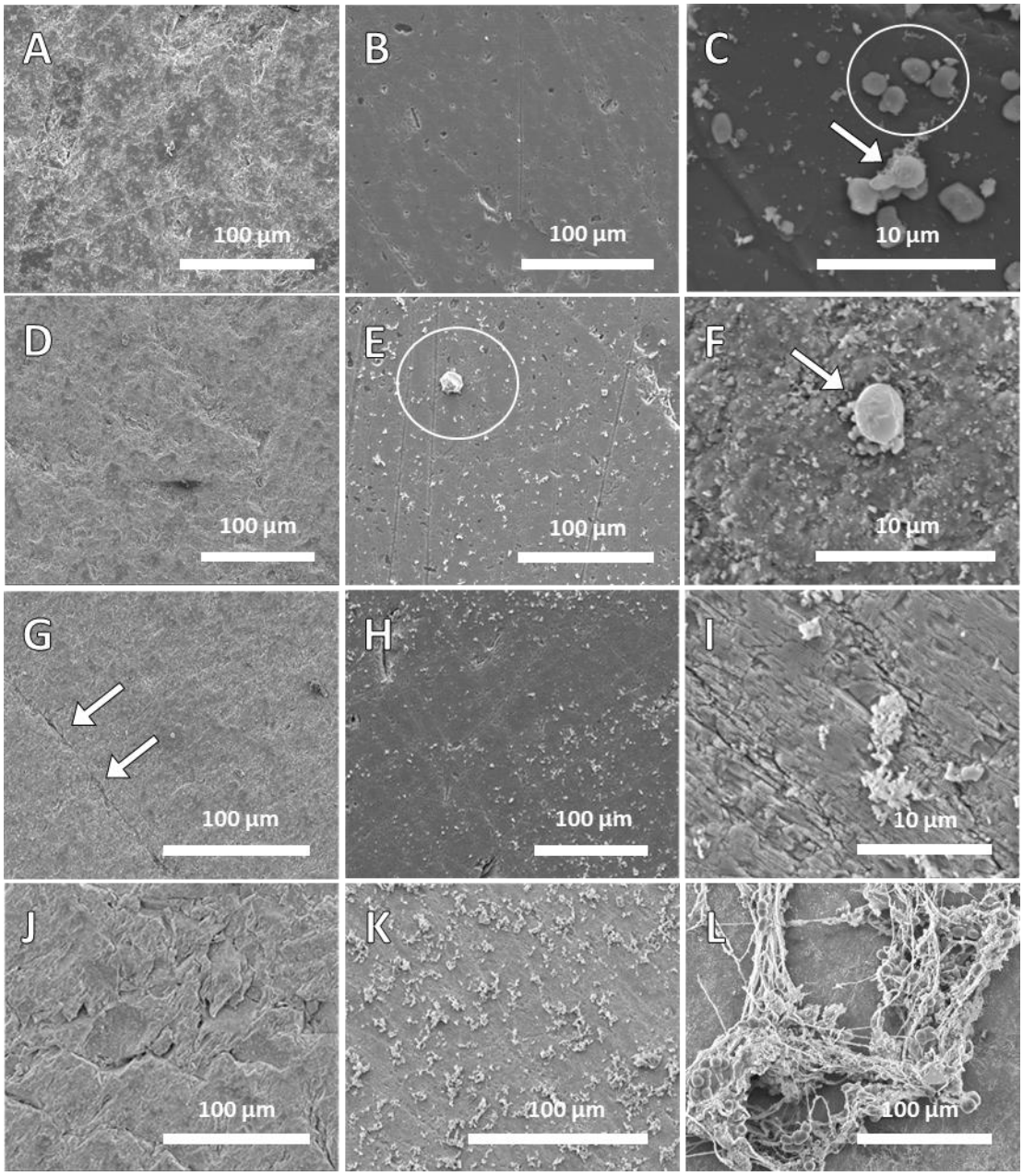

Figure 6.69: Pyrite tiles exposed to *A. brierleyi* for 2 h (A), 24 h (D), 72 h (G) and 168 h (J), jarosite precipitates, indicated by circle (2 h) and *A. brierleyi* cells (2h, 72 h), indicated by arrows (C, F), pyrite tiles exposed to DSM 150 medium for 2 h (B), 24 h (E), 72 h (H) and 168 h (K), close-up of scratches, rivers and submicron debris (168 h) (I), typical large organic aggregates (2 h) (L).

Between 24 and 72 h (see Figure 6.69(D) and (G), respectively), pyrite exposed to *A. brierleyi* does not appear to be significantly more leached than the pyrite exposed for 2 h, with the surface covered uniformly in sub-micron debris of the kind shown indicated by circles in Figure 6.69(C). Cells are occurring on the surface with similar frequency, and show no preference for voids or cracks, with cells not appearing near each other. After 72 h of larger cracks have appeared in the surface such as those seen indicated by arrows in Figure 6.69(G). Large organic aggregates were also observed on the pyrite surface, pictured in Figure 6.69(L). After 168 h of exposure, *A. brierleyi* cells do not occur frequently on the surface, with an average of less than 0.1 cells/mm^2 measured for every period of exposure, which is equivalent to a surface coverage of less than 0.04%. By this stage, the

surface is showing advanced leaching, with large cracks and sub-micron debris across the surface of the pyrite, shown in Figure 6.69(J).

The pyrite exposed to DSM 150 medium for 2 h (see (Figure 6.69(B)) was found to have pits and scratches, with the etch pits 1-4 μm in length, and 0.5-1.5 μm in width, similar in size to those observed on the pyrite exposed to *A. brierleyi* and more significant that observed on bare polished pyrite shown in Chapter 4, section 4.3.2, Figure 4.26. After 24 h, the pyrite shows sub-micron inorganic debris on the surface, as well as organic aggregates such as the one shown indicated by a circle in Figure 6.69(E). Etch pits on the surface are of the same dimensions as those observed on pyrite exposed to medium for 2 h. Pyrite exposed to DSM 150 medium for 72 h (see Figure 6.69(H)), has etch pits that have not significantly increased in size or frequency, and the surface is covered in sub-micron debris. The formation of larger, irregular-shaped particles on the surface, typically between 1-3 μm in length, may be the formation of jarosites or other precipitates. The pyrite exposed to DSM 150 medium for 168 hours (see Figure 6.69(K)) shows rivers of cracks along crystal boundaries caused by the chemical leaching process, shown up close in Figure 6.69(I), and appear deeper than the finer cracks observed at 24 h. These rivers and finer cracks have been identified by previous investigation to be caused by ferric iron leaching and not direct bacterial action [36]. The surface of the pyrite is covered in secondary mineral precipitates.

The results for *A. brierleyi* on pyrite are in stark contrast to the coverage measured for the mesophilic bacteria in the previous chapters for equivalent exposure times (Chapters 4 and 5), or coverage found by Tan *et al* of *A. ferrooxidans* on chalcopyrite of less than 0.8% after 1 h of exposure [37]. There is no appearance of colonisation by cells or the formation of biofilm, and no suggestion of cell division taking place on the surface as this period of exposure. This suggests that the cells may not be attracted to the surface or reproducing on the surface as the other two strains have done; it is very possible that the cells that are attaching to the surface are being mostly caught up in surface defects in the process of routine mixing, and irreversible attachment takes place. With no motile ability, it is these cells are unable to actively seek out the mineral for a food source [20]. These observations agree with the Eh and ICPOES results that suggest *A. brierleyi* may be promoting the production of ferric iron in solution, interacting with the pyrite via the indirect mechanism or indirect contact mechanism rather than by direct attachment to the surface. The aggregates observed on the surface bear strong resemblance to structures observed in a study by Cosmidis *et al*, who observed yeast extract forming nanometre and micrometre scale strand-like and spherical structures with elemental sulfur that mimic the appearance of cellular and extracellular structures [34].

SEM has previously been applied to the bioleaching a variety of substrates by *A. brierleyi*, however, few investigations have been able to provide images of the cells or corroborating evidence to prove cell identity, with the majority focussing on substrate morphology. Several studies have used SEM to investigate substrates exposed to *A. brierleyi*, however the sample preparation methods involved no steps to preserve cells, and as such they show no images of cells attached to particles [3, 4, 11]. The secondary mineral precipitates agree with the findings of Takatsugi *et al*, who found jarosite and scorodite ($FeAsO_4.2H_2O$) secondary mineral particles precipitated on the surface of enargite particles bioleached by *A. brierleyi* [8]. The images presented in Figure 6.69 strongly resemble those found in a study by Mikkelsen *et al* of pyrite leached by *A. brierleyi*, which showed a significant amount of debris and sub-micron leach residues on the surface, along with significant surface leaching [16].

These results suggest that secondary minerals are much more prolific on the surface of pyrite compared exposed to *A. brierleyi* and DSM 150 medium compared to the mesophilic bacteria and medium explored previously. It is also apparent that organic aggregates are occurring on the surface across both biotic and abiotic samples, suggesting the medium may be providing unwanted contamination of the surface. Although SEM and EDX provide important visualisation of the pyrite surface, and the secondary minerals and *A. brierleyi* cells that appear on the surface, these techniques are not sufficient to provide information on the physical and chemical properties of the surface. As EDX penetrates up to 5 µm into the surface, other experiments will be needed to investigate the outermost atomic layers with minimal bulk pyrite contribution, and to relate physical properties to chemical species on the surface [31, 38, 39].

6.3.3 Atomic Force Microscopy

Atomic force microscopy (AFM) is used to quantify the roughness of the pyrite surface, due to the topographical impact the surface leaching and pitting observed in using SEM may have on the hydrophobicity of the pyrite surface [40]. Any changes in the wettability of the pyrite may be caused by both physical changes in surface topography and surface chemistry, and as such the surface roughness must be considered. This will enable the isolation of any chemical alterations induced by presence of *A. brierleyi* on the surface of the pyrite. Typical AFM images of pyrite exposed to *A. brierleyi* in the presence of yeast extract are shown in Figure 6.70. At least four images were obtained per sample, always over an area of 10 µm, to calculate the average roughness of the sample.

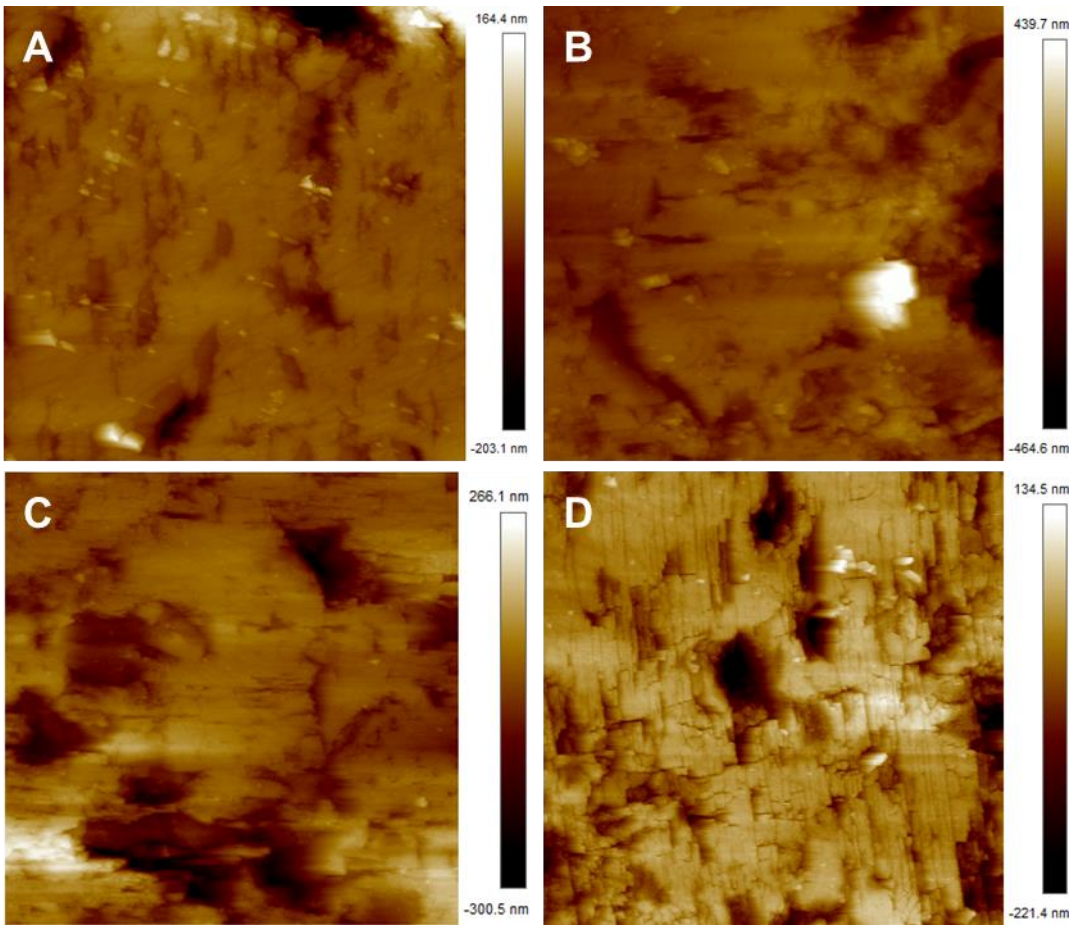

Figure 6.70: 10 x 10 µm AFM height images of pyrite exposed to *A. brierleyi* for 2 h (A); 24 h (B); 72 h (C); 168 h (D).

The roughness of the pyrite surface exposed to *A. brierleyi* and DSM 150 medium as calculated by Ra and Rq are shown in Figure 6.71, with the error bars representing the 95% confidence interval. The two different methods used to calculate the average roughness of the pyrite surface was described in Chapter 3, section 3.10.2.

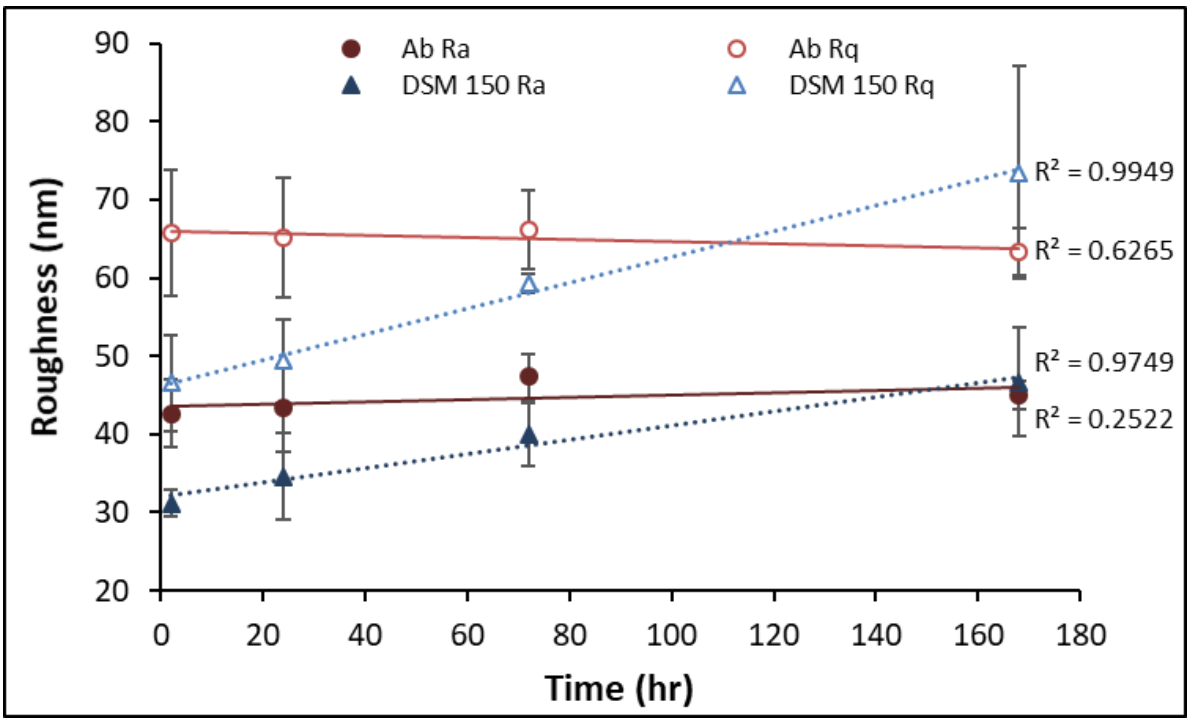

Figure 6.71: The roughness of pyrite exposed to *A. brierleyi* as calculated by Ra (●) and Rq (○), and DSM 150 medium as calculated by Ra (▲) and Rq (Δ).

The sample exposed to the medium control solution increased linearly over 168 h. Both the Ra and Rq values of the pyrite surfaces showing the same trend, with correlation coefficients of 0.9749 and 0.9949, respectively. The roughness of pyrite samples exposed to *A. brierleyi* show no such trend, and the values obtained are not significantly different from each other by either Ra or Rq calculation method over the course of exposure, nor are they distinguishable from the values obtained from the controls. This agrees with the SEM results, which show a large amount of debris and surface leaching of the pyrite exposed to *A. brierleyi* and to DSM 150 medium solution at all periods of exposure. As has been previously discussed (Chapter 4, section 4.3.3), it can safely be assumed that the roughness of bare polished pyrite is statistically insignificant from the roughness of pyrite exposed to the mesophiles and abiotic HH medium for 2 h. These roughness values fall within the range of roughness values measured for pyrite exposed to *A. brierleyi* and abiotic DSM 150 medium.

Previous studies have not yet investigated this strain of archaea using AFM, however, this technique has been applied to other bioleaching microorganisms, as have been discussed in Chapter 2, section 2.5.2. The AFM measurements made here suggest the hydrophobicity of the surfaces are likely to be similar or identical between pyrite samples exposed to the DSM 150 medium and *A. brierleyi*, regardless of the length of exposure. Chau *et al* noted that an increase in roughness would correlated with an increase in the hydrophobicity of the mineral surface, but as no significant difference in roughness is observed here, it could be expected that the contact angle would remain

static [40]. The visualisation of the surface and the quantification of surface roughness must be compared to the measured hydrophobicity of the sample, to fully understand how *A. brierleyi* impacts the mineral surface in terms of its ability to depress or float pyrite. This will enable the separation of the physical properties from the chemical properties of the surface.

6.3.4 Captive Bubble Contact Angle

Captive bubble contact angle enables an *in-situ* measurement of the wettability of the pyrite surface exposed to *A. brierleyi* without unwanted surface oxidation or contamination that can be induced through drying the surface prior to analysis. Contact angle measurements provide an indication of how both the growth medium and *A. brierleyi* impact the hydrophobicity of pyrite, and allow the suitability of this archaea as a flotation reagent to be assessed. Figure 6.72 shows the average five advancing and receding contact angles each pyrite sample, performed in triplicate, with the error bars representing the standard deviation of the samples measured.

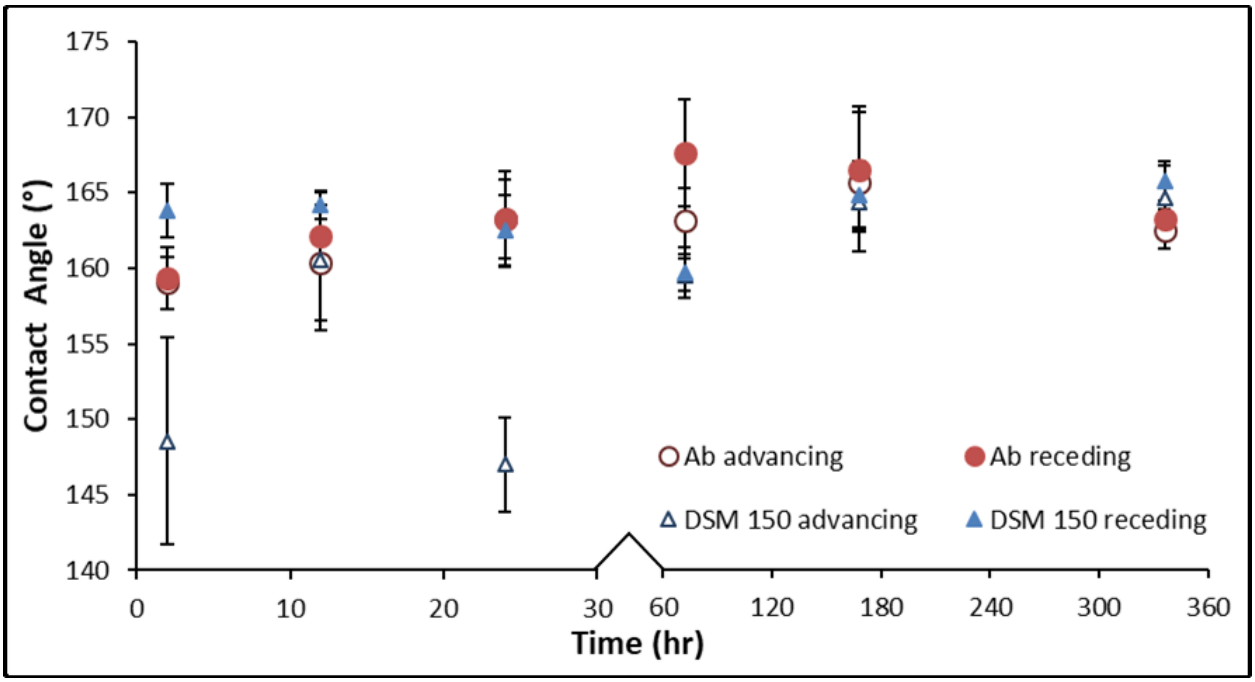

Figure 6.72: Advancing captive bubble contact angle of pyrite exposed to *A. brierleyi* (○) and DSM 150 medium (△). Receding captive bubble contact angle of pyrite exposed to *A. brierleyi* (●) and DSM 150 medium (▲). Error bars represent sample standard deviation.

A. brierleyi culture displayed a much greater heterogeneity of the surfaces compared to the medium alone over the first 24 h of exposure, where there is up to 15° difference in advancing and receding angle values. After 168 hours of exposure, both biotic and abiotic contact angle values show the surfaces appear much more heterogeneous. The pyrite exposed to *A. brierleyi* does not appear to significantly alter the hydrophobicity of the surface until after 72 h, where the advancing and receding contact angles are increased compared to the medium controls by 4° and 8°, respectively.

After longer periods of exposure (over 168 h), the hydrophobicity of the medium control samples and those exposed to *A. brierleyi* are indistinguishable from each other.

The DSM 150 medium control captive bubble presented here shows much lower hydrophobicity at shorter exposure times than the mesophilic medium presented in Chapters 4 and 5, by over 20° difference in receding angles after 2 h of exposure. The initial lack of heterogeneity and fluctuations in hydrophobicity of pyrite exposed to DSM 150 medium could be due to interactions between the surface and the yeast extract in the medium, which was seen aggregating on the surface using SEM in section 6.3.2.

Small differences in contact angle (3°) can have a significant impact on flotation recovery, depending on the size fraction of mineral particles used [41]. These results suggest that an exposure of 72 h could promote the depression of pyrite *by A. brierleyi*, while other periods of exposure may be impacted by poor sample hysteresis and no significant separation of contact angle compared to the DSM 150 medium control sample. This may be in part due to the increased carbon presence in the DSM 150 medium impacting the surface chemistry, suggested by the presence of organic aggregates and increasing carbon atomic percentage found by SEM and EDX. These results suggest little difference is surface chemistry between biotic and abiotic samples, which further supports the indirect mechanism as the mechanism through which *A. brierleyi* interacts with the pyrite surface; promoting ferric iron production for indirect oxidation, rather than direct action on the surface.

While *A. brierleyi* has been heavily researched as a bioleaching microorganism, there is little application of this strain to flotation studies. Most previous studies have analysed mineral hydrophobicity upon exposure to mesophiles, as was previously discussed in chapters 4 and 5 [33, 42-45]. Of the studies that have investigated the impact on the hydrophobicity of minerals by *A. brierleyi* either a mixture of cell cultures was applied, or the hydrophobicity of cells lawns rather than minerals was reported [2, 46]. These studies suggest that the surface of *A. brierleyi* is hydrophilic, and that extreme thermophilic cells can provide equivalent recovery of minerals compared to moderate thermophiles [2, 46]. There has yet to be a study into the impact of *A. brierleyi* on the hydrophobicity of pyrite, and the impact of the medium composition to the mineral wettability has yet to be properly considered.

These results suggest *A. brierleyi* may be much less effective at separating pyrite under the current growth conditions, as there may be interference from the growth medium itself on the pyrite surface. To separate physical changes from potential chemical effects on the surface, and to identify potential growth medium contaminants, surface chemical analysis must be performed on the system. This chemical analysis will be explored using ToF-SIMS in the following section.

6.3.5 Time of Flight – Secondary Ion Mass Spectrometry

The SEM results have shown a lack of cell adhesion to the pyrite surface, and little relation with changes in surface roughness to the contact angles measured here, although it is observed that both the DSM 150 medium and the *A. brierleyi* are impacting the pyrite surface hydrophobicity. To separate physical changes on the surface such as roughness from potential chemical effects on the surface, surface chemical analysis was performed. This chemical analysis will be explored using ToF-SIMS. The ToF-SIMS analysis of bare polished pyrite was discussed in Chapter 4, section 4.3.6; briefly, the positive ion spectra were dominated by Fe^{+}, with very low proportions of carbonaceous fragments, while the negative ion fragments indicated surface oxidation through exposure to the atmosphere. Negligible amounts of large molecular weight fragments were detected. Figure 6.73 shows the positive ions on the surface of pyrite exposed to *A. brierleyi* and DSM 150 medium for 2, 24, 72 and 168 h.

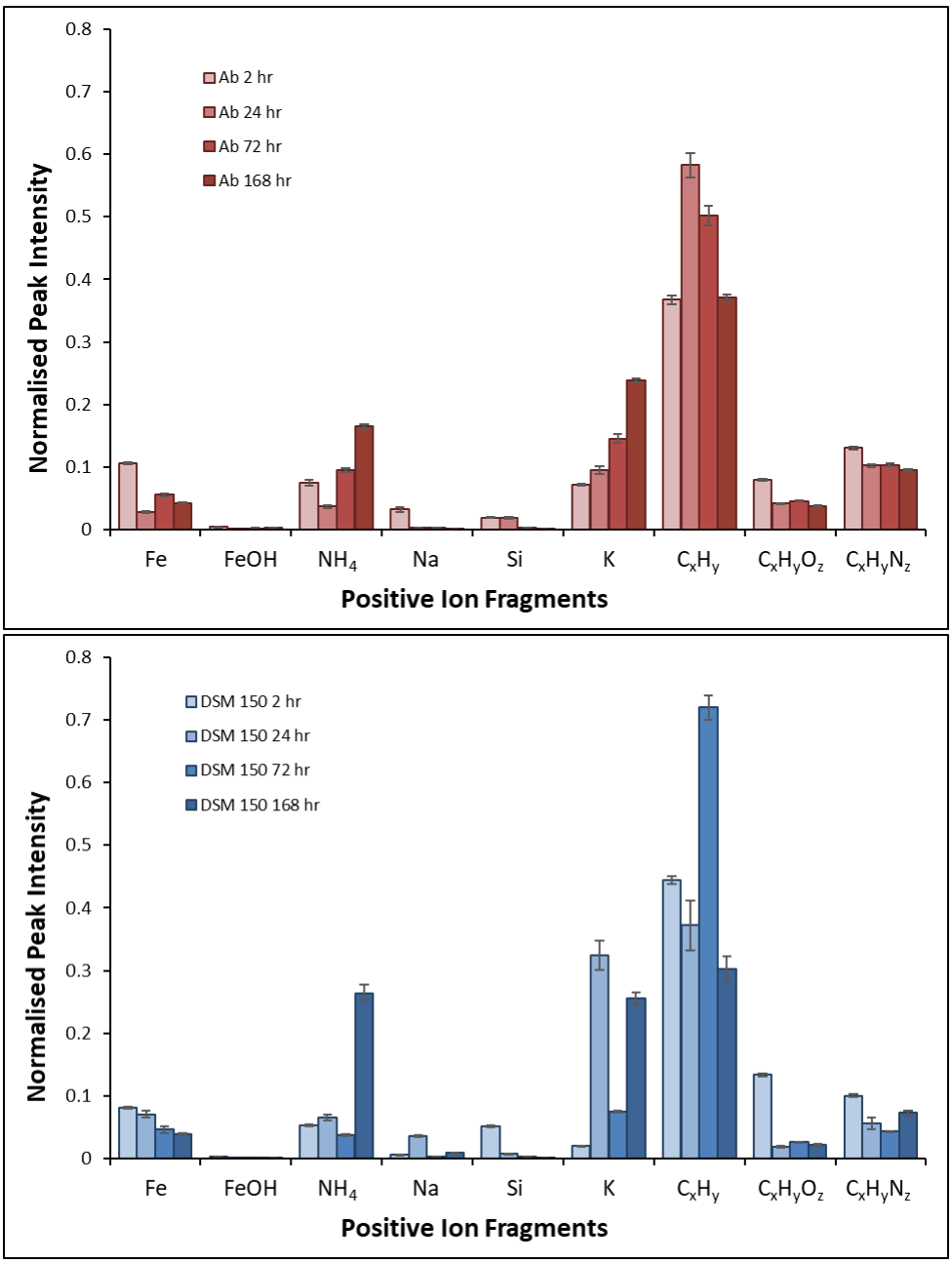

Figure 6.73: Average normalised peak intensities of positive fragments of pyrite exposed *A. brierleyi* (top) for 2, 24, 72 and 168 h, and pyrite exposed to DSM 150 medium (bottom) for 2, 24, 72 and 168 h.

The fragment profiles of pyrite exposed to both *A. brierleyi* and DSM 150 medium display similar trends. Every positive ion spectrum is dominated by short chain $C_xH_y^+$ ($x \leq 6$) fragments, with the proportions Fe^+, Si^+, $C_xH_yN_z^+$ ($x \leq 5$, $z \leq 2$) and $C_xH_yO_z^+$ ($x \leq 4$, $z \leq 2$) appearing high initially, decreasing over the course of exposure. The proportion of Si^+ and Na^+ detected decreases over the first 72 h, remaining in similar proportion at 168 h. The proportions of both K^+ and NH_4^+ fragments increase on the surface over the course of exposure for both biotic and abiotic samples, however the proportion is more variable over the course of exposure to the DSM 150 medium. The $FeOH^+$ fragment remains in low proportion on every pyrite surface over the course of the exposure. These fragments could be due to jarosite formation, as was seen in the SEM and EDX results, or could be

attributed to medium salt precipitates, and coincides with the increase in inorganic debris on the surface observed in the SEM results.

The medium solution contains ammonium sulfate and potassium chloride, and as such the NH_4^+ and K^+ fragments can be expected on the surface. This means the NH_4^+ fragment alone is not a reliable indicator of proteins on the surface. The medium solution also contains yeast extract, which is also a potential source of K^+ and Na^+, although the presence of $FeOH^+$ on all samples suggests the formation of iron hydroxide species and jarosite precipitations, the structure of which may include NH_4^+, K^+ and Na^+ ions (see Equation 4.44, Chapter 4, section 4.3.1.2). The presence of Si^+ on all samples in relatively low proportions indicated silicate inclusions, which are expected from the EDX analysis. These results suggest a large amount of carbonaceous material on the surface, with possible organic and inorganic sources for the K^+ and NH_4^+, as was seen in the SEM results that showed large organic aggregates, sub-micron debris and jarosite precipitates on the surface. These results are consistent with the heterogeneous distribution of medium salt precipitates, yeast extract contamination of the surface and secondary mineral formation.

To complement the positive ion mass spectra, the negative ion mass spectra were also examined for all samples. Figure 6.74 shows the negative fragments and elements of interest and significance collected by ToF-SIMS on pyrite exposed to *A. brierleyi* and DSM 150 medium for 2, 24, 72 and 168 h.

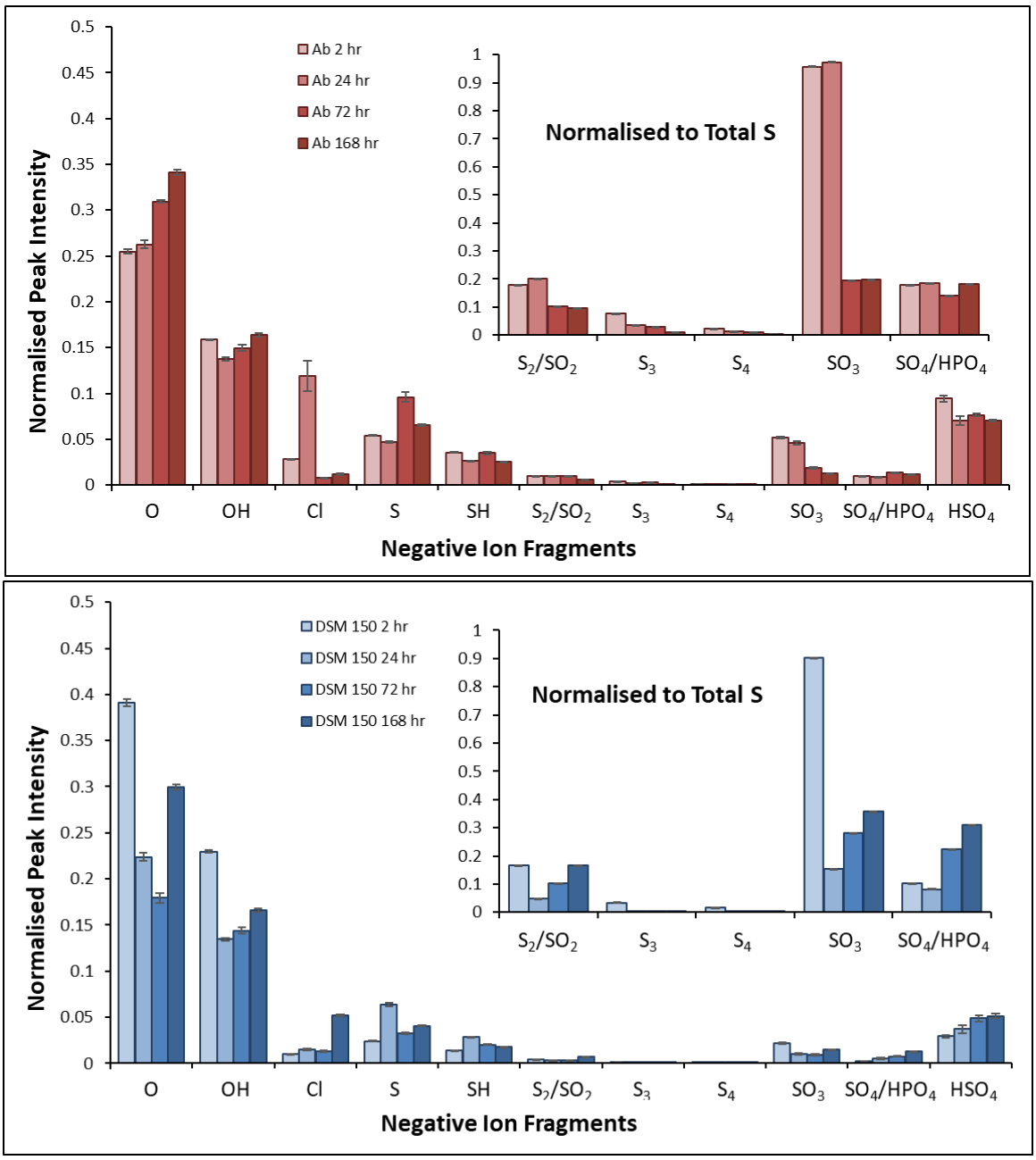

Figure 6.74: Average normalised peak intensities of negative fragments of pyrite exposed *A. brierleyi* (top) for 2, 24, 72 and 168 h, and pyrite exposed to DSM 150 medium (bottom) for 2, 24, 72 and 168 h.

The fragments detected on pyrite after exposure to both DSM 150 medium and *A. brierleyi* are dominated by the O^- and OH^- fragments for every period of exposure, while the proportions of S^- and SH^- are variable across the samples. For all periods of exposure, oxygenated sulfur species such as SO_3^- and SO_4^- are in greater proportion on the surface than polysulfide species such as S_3^- and S_4^-. This is confirmed when the sulfur species are normalised to total sulfur, shown inset in Figure 6.74 (top and bottom), with most of the sulfur on the surface at this period of exposure is due to oxygenated sulfur fragments. For both biotic and abiotic samples, the surfaces are richer in polysulfides in early periods of exposure, the proportions of oxygenated sulfur fragments show reverse trends; increasing over time on pyrite exposed to DSM 150 medium, and decreasing when

exposed to *A. brierleyi*. The proportion of Cl^- on the pyrite exposed to *A. brierleyi* is variable, in contrast to the abiotic experiments that show Cl^- on the surface also increases over the course of exposure. This may be expected on the surface as it is present in the medium solution in both yeast extract and potassium chloride. After 168 h of exposure, the increase in proportion of Cl^- corresponds with the increase in proportion of K^+ and NH_4^+ fragments in the positive ion results.

These results agree with the contact angle results that show the pyrite surface is very heterogeneous over the course of exposure, with the overall contact angle remaining hydrophilic for all samples due to the larger proportion of oxygenated species covering the surface. The similar trends in surface species between biotic and abiotic samples, and the high proportion of carbonaceous material observed in the positive ion mass spectra, suggests that yeast extract and secondary mineral precipitates are impacting the wettability of the surface. This contamination is potentially masking the action of the *A. brierleyi* and associated EPS, creating the potentially false impression that cells act on the surface by the indirect or indirect contact mechanisms.

To assess potential EPS production by *A. brierleyi*, and to distinguish EPS from potential yeast extract contamination, larger molecular weight fragments were also investigated. Figure 6.75 shows the large molecular mass positive fragments collected by ToF-SIMS on pyrite exposed to *A. brierleyi* and DSM 150 medium for 2, 24, 72 and 168 h. Compared to the large molecular weight fragment patterns obtained from pyrite exposed to the mesophilic cultures in Chapters 4 and 5, there appears to be a much lower proportion of large molecular weight fragments across all periods of exposure, and much lower size range in which these large fragments are seen to occur (*m/z* 400-600 in mesophilic cultures compared to $\leq$ 400 for *A. brierleyi*).

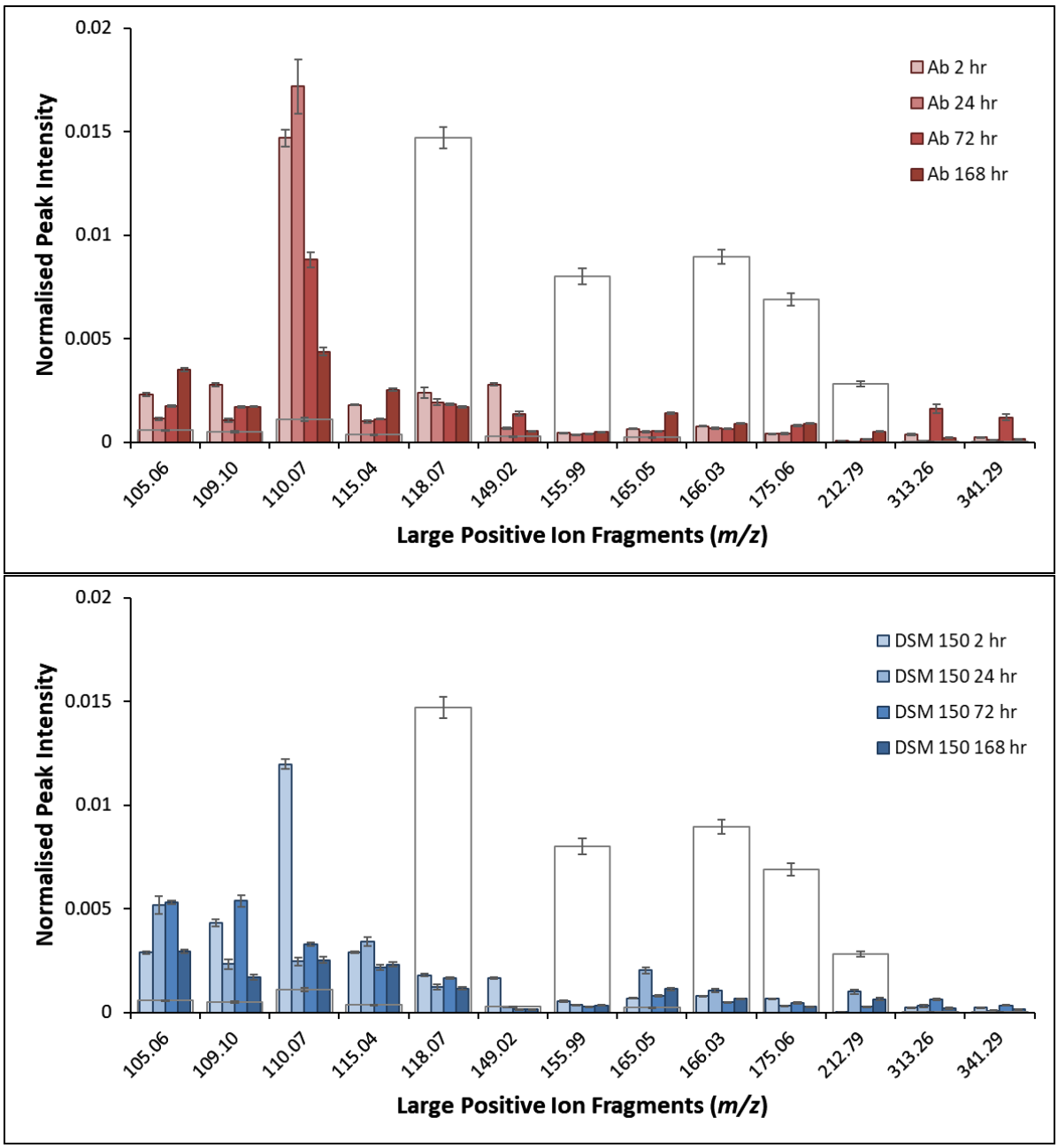

Figure 6.75: Average normalised peak intensities of large molecular weight positive fragments of pyrite exposed *A. brierleyi* (top) for 2, 24, 72 and 168 h, and pyrite exposed to DSM 150 medium (bottom) for 2, 24, 72 and 168 h, and yeast extract (outline).

As can be seen in this plot, many of the larger molecular weight fragments observed on pyrite exposed to both DSM 150 medium and *A. brierleyi* are also observed in the fragment pattern of dry yeast extract, except for the peaks with *m/z* ratios of 313.26 and 341.29. These fragments have been identified as major components of several lipid and fatty acid structures by previous studies looking specifically at those structures [47-51]. The fragment at mass 110.07 has been identified in previous studies as a characteristic fragment of histidine, an amino acid that occurs in yeast extract, while the fragment with *m/z* 165.05 has been identified as an organic molecule fragment containing a sodium atom in a lipid ToF-SIMS study by Heim *et al* [50, 52-56]. The fragments at *m/z* 105.06, 115.04,

118.07, 155.99, 166.03, 175.06 have been observed in other ToF-SIMS biomolecule studies, mostly in carbohydrate structures. However, the Vitamin B complexes present in yeast extract are not well-characterised by ToF-SIMS, and these may also be contributing to the fragment profile of the pyrite exposed to the medium and the culture. There are few investigations that have characterised biomolecules under a variety of conditions, and a positive identification of fragments in a complex mixture is not currently possible [47-50, 52, 54, 57-59]. The fragments with *m/*z 109.1 and 212.79 were unable to be identified. As most of these fragments may be found in yeast extract as well as cell-produced biomolecules, it is not possible to separate potential EPS from the influence of yeast extract on the pyrite surface.

As was the case for the positive ions of large molecular weight, many of the negative ion fragments observed on pyrite exposed to both DSM 150 medium and *A. brierleyi* are also observed in the fragment pattern of dry yeast extract. The average normalised peak intensity of large molecular weight negative fragments of pyrite exposed to *A. brierleyi* and DSM 150 medium for 2, 24, 72 and 168 h is shown in Figure 6.76.

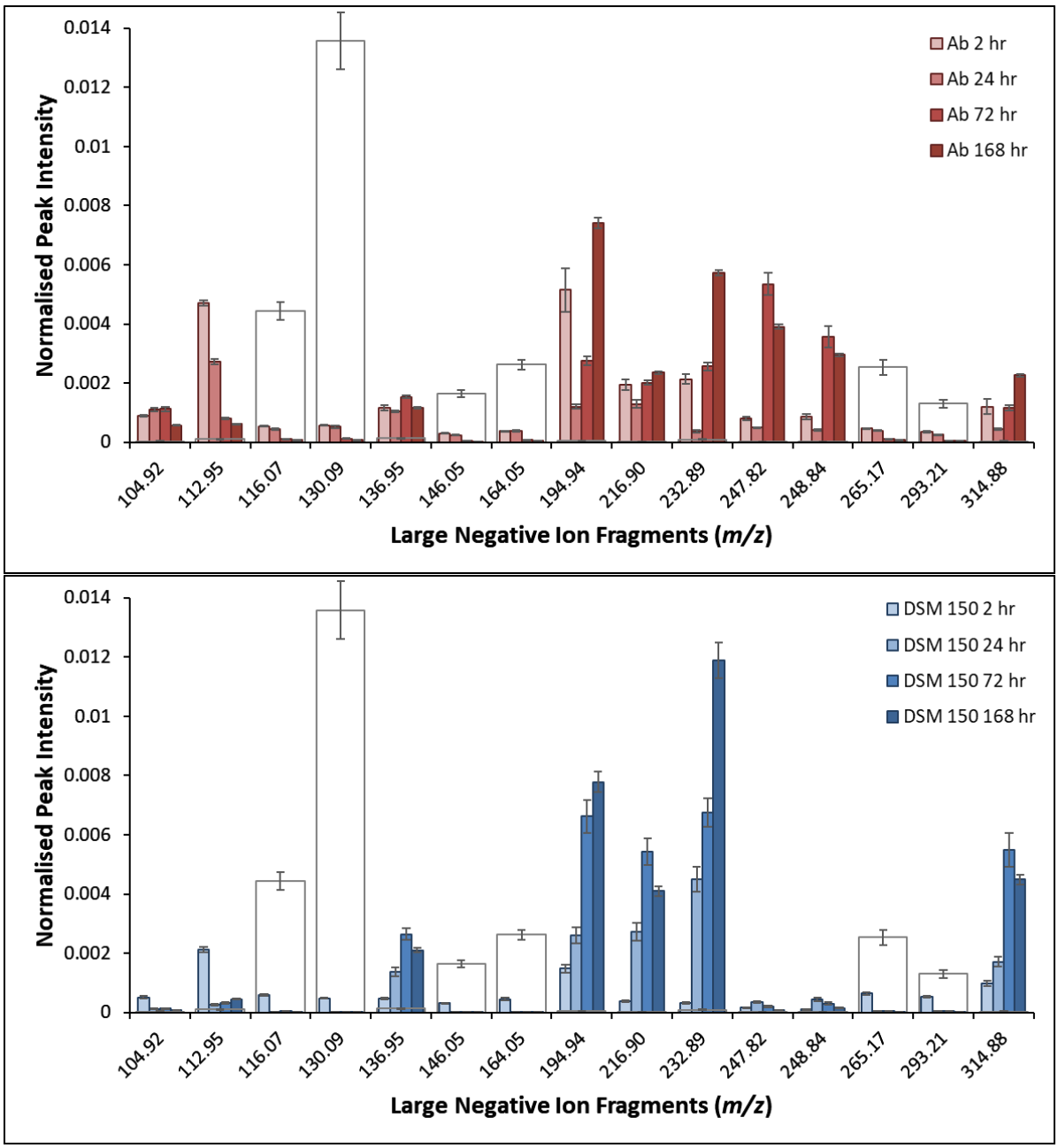

Figure 6.76: Average normalised peak intensities of large molecular weight negative fragments of pyrite exposed *A. brierleyi* (top) for 2, 24, 72 and 168 h, and pyrite exposed to DSM 150 medium (bottom) for 2, 24, 72 and 168 h, and yeast extract (outline).

The fragments of *m/z* 136.09, 194.94, 216.90, 232.89, 247.82, 248.84 and 314.88 appear to be increasing in proportion on the pyrite exposed to both the DSM 150 medium and the *A. brierleyi* as the period of exposure progresses, with the medium showing the largest proportion of these fragments after 168 h. The fragments at *m/z* 216.9 and 232.89 are potential glucoside fragments, with yeast extract being a source of sugars from which these fragments may originate [60]. The fragment at *m/z* 136.95 has been identified in a previous study as a phospholipid fragment [50]. The fragment at *m/z* 112.95 has been identified in a previous study as a carbohydrate fragment [49].

The fragments identified in yeast extract of *m/z* 112.95, 116.07, 130.09, 146.05, 164.05, 265.17, 293.21 appear in greater proportion on the pyrite surface after 2 h of exposure to both the DSM 150 medium and the *A. brierleyi*, with the proportions decreasing on the surface after 72 h in the culture. These fragments were found to decrease in frequency after 24 h in the DSM 150 medium control and remain low for the longer periods of exposure. While these fragments were detected in the yeast extract spectra, the frequency of occurence is much lower, which could be due to the difference in sample preparation between dry-mounted, whole yeast extract powder and the solubilized yeast extract exposed to the pyrite surface in the medium. The study by Cosomidis *et al* suggests that the complex mixture that is yeast extract reacts with elemental sulfur, and as such it is possible new organic molecules are forming upon exposure of yeast extract to the sulfide mineral surface [34].

The only fragments observed on the pyrite surface that do not follow similar trends in both the DSM 150 medium and *A. brierleyi* culture are the fragments *m/z* 247.82 and 248.84. These two fragments appear in lower proportion on the pyrite exposed to *A. brierleyi* at 2 and 24 h to become the third and fourth most frequently occurring large molecular weight fragments on the pyrite surface, respectively, after 72 and 168 h. They are seen only at much lower proportion over the course of exposure to DSM 150 medium. These two fragments were also found on the pyrite surface after exposure to *A. ferrooxidans* as possible EPS components (see Chapter 4, section 4.3.6), however they were unable to be positively identified. The fragment of *m/z* 194.94 was also unidentifiable, but like the fragments of *m/z* 247.82 and 248.84, was observed on the pyrite exposed to *A. ferrooxidans*. This suggests that these fragments may be solely due to cells and their excretions rather than yeast extract or adventitious carbon.

Analysis of complex biological samples using ToF-SIMS has yet to successfully identify all individual components, with many previous studies focusing on specific proteins and carbohydrates in the sample matrix [57, 58, 61]. Our results, which show little cell attachment and little indication of EPS on the biotic samples, agree with those obtained by Pradier *et al*, who suggest low carbohydrate surface contributions result little cell attachment to solid surfaces [62]. Other studies have looked at specific types of compounds such as proteins or peptides on cells, and Dague *et al* specifically related protein fragments as being hydrophobic, a contribution which is also observed here [53, 63].

Previous studies of pyrite surfaces using ToF-SIMS were focused mainly on identifying pyrite particles within a mixture of sulfide minerals, and focussed mainly on the ions associated with the pyrite surface and ions of interest to flotation. These investigations were discussed in detail in

Chapter 4, section 4.3.6, with the findings supporting the argument that surfaces richer in sulfur species are more hydrophobic, as is observed here.

The results observed here suggest yeast extract interacts with the surface, in a way that prevents the elucidation of microbial action on the surface from the impact of the prescribed medium solution. This makes it impossible to determine whether the indirect or indirect contact mechanism is the most accurate description of the interaction of *A. brierleyi* with pyrite. This finding is something very few papers have suggested [19]. There is debate in the literature as to the role yeast extract plays in the growth of *A. brierleyi* and its impact on the mineral surface [5, 19, 20, 24]. Differentiation of the interaction of *A. brierleyi* from yeast extract with the mineral surface is necessary to understand the mechanism behind archaea leaching and flotation of pyrite.

6.4 Conclusions

Unlike the mesophilic bacteria investigated in the previous chapters, very little attachment of *A. brierleyi* cells occurs on the pyrite surface over the period of 168 h, as observed using SEM. Leaching of the pyrite surface appeared to be enhanced by *A. brierleyi*, with cells preventing the formation of sub-micron debris, however they did not increase the size of the etch pits observed in the surface. This resulted in initial increases in surface roughness of pyrite exposed to *A. brierleyi* compared to the control, however longer periods of exposure display similar roughness, as measured by AFM. The lack of attachment observed, coupled with the initial increase in leaching of the surface suggests that *A. brierleyi* may be acting on the surface via the indirect or indirect contact mechanisms by supplying significantly greater concentrations of ferric iron to solution to leach the surface compared to the control.

Organic microaggregates were observed on the pyrite surface over the course exposure to *A. brierleyi* and the abiotic controls, with the structures appearing larger when cells were present in solution. These organic aggregates, coupled with the identification of similar surface species over the surface of all pyrite samples, both biotic and abiotic, suggest that the yeast extract in the medium is acting on the pyrite surface. Although several fragments were identified by ToF-SIMS that are likely to be due to *A. brierleyi* rather than the yeast extract, the mixture of complex organic molecules found in yeast extract, such as proteins and vitamins, make it impossible to separate the impact of cells from yeast extract. This in turn means there is no way to positively state which mechanism is the most accurate description of the *A. brierleyi* interaction with pyrite, and obstructs the identification of the potential microbial compounds impacting the hydrophobicity of the surface.

6.5 References

1. Brierley, J.A., *Acdidophilic thermophilic archaebacteria: potential application for metals recovery.* FEMS Microbiology Reviews, 1990. **6**(2-3): p. 287-291.
2. Govender, Y., Gericke, M,, *Extracellular polymeric substances (EPS) from bioleaching systems and its application in bioflotation.* Minerals Engineering, 2011. **24**(11): p. 1122-1127.
3. Bharadwaj, A., Ting, Y.-P., *Bioleaching of spent hydrotreating catalyst by acidophilic thermophile Acidianus brierleyi: Leaching mechanism and effect of decoking.* Bioresource Technology, 2013. **130**(0): p. 673-680.
4. Gerayeli, F., Ghojavand, F., Mousavi, S. M., Yaghmaei, S., Amiri, F., *Screening and optimization of effective parameters in biological extraction of heavy metals from refinery spent catalysts using a thermophilic bacterium.* Separation and Purification Technology, 2013. **118**: p. 151-161.
5. Deveci, H., Akcil, A., Alp, I., *Bioleaching of complex zinc sulphides using mesophilic and thermophilic bacteria: comparative importance of pH and iron.* Hydrometallurgy, 2004. **73**(3–4): p. 293-303.
6. Deveci, H., Jordan, M. A., Powell, N., Alp, I., *Effect of salinity and acidity on bioleaching activity of mesophilic and extremely thermophilic bacteria.* Transactions of Nonferrous Metals Society of China, 2008. **18**(3): p. 714-721.
7. Sasaki, K., Takatsugi, K., Hirajima, T., *Effects of initial Fe2+ concentration and pulp density on the bioleaching of Cu from enargite by Acidianus brierleyi.* Hydrometallurgy, 2011. **109**(1–2): p. 153-160.
8. Takatsugi, K., Sasaki, K., Hirajima, T., *Mechanism of the enhancement of bioleaching of copper from enargite by thermophilic iron-oxidizing archaea with the concomitant precipitation of arsenic.* Hydrometallurgy, 2011. **109**(1–2): p. 90-96.
9. Rastegar, S.O., Mousavi, S. M., Rezaei, M., Shojaosadati, S. A., *Statistical evaluation and optimization of effective parameters in bioleaching of metals from molybdenite concentrate using Acidianus brierleyi.* Journal of Industrial and Engineering Chemistry, 2014. **20**(5): p. 3096-3101.
10. Konishi, Y., Kogasaki, K., Asai, S., *Bioleaching of pyrite by Acidianus brierleyi in a continuous-flow stirred-tank reactor.* Chemical Engineering Science, 1997. **52**(24): p. 4525-4532.
11. Konishi, Y., Asai, S., Tokushige, M., Suzuki, T., *Kinetics of the bioleaching of chalcopyrite concentrate by acidophilic thermophile acidianus brierleyi.* Biotechnol Prog, 1999. **15**(4): p. 681-8.
12. Konishi, Y., Tokushige, M., Asai, S., Suzuki, T., *Copper recovery from chalcopyrite concentrate by acidophilic thermophile Acidianus brierleyi in batch and continuous-flow stirred tank reactors.* Hydrometallurgy, 2001. **59**(2–3): p. 271-282.
13. Meng, C., Shi, X., Lin, H. , Chen, J., Guo, Y., *UV induced mutations in Acidianus brierleyi growing in a continuous stirred tank reactor generated a strain with improved bioleaching capabilities.* Enzyme and Microbial Technology, 2007. **40**(5): p. 1136-1140.
14. Zhu, W., Xia, J.-L., Peng, A.-A., Nie, Z.-Y., Qiu, G,-Z., *Characterization of apparent sulfur oxidation activity of thermophilic archaea in bioleaching of chalcopyrite.* Transactions of Nonferrous Metals Society of China, 2013. **23**(8): p. 2383-2388.
15. Zhu, W., Xia, J.-L., Yang, Y., Nie, Z.-Y., Zheng, L., Ma, C.-Y., Zhang, R.-Y., Peng, A.-A., Tang, L., Qiu, G.-Z., *Sulfur oxidation activities of pure and mixed thermophiles and sulfur speciation in bioleaching of chalcopyrite.* Bioresource Technology, 2011. **102**(4): p. 3877-3882.

16. Mikkelsen, D., Kappler, U., Webb, R. I., Rasch, R., McEwan, A. G., Sly, L. I., *Visualisation of pyrite leaching by selected thermophilic archaea: Nature of microorganism–ore interactions during bioleaching.* Hydrometallurgy, 2007. **88**(1–4): p. 143-153.
17. Watling, H.R., *The bioleaching of sulphide minerals with emphasis on copper sulphides — A review.* Hydrometallurgy, 2006. **84**(1–2): p. 81-108.
18. Brierley, J.A., *A perspective on developments in biohydrometallurgy.* Hydrometallurgy, 2008. **94**(1–4): p. 2-7.
19. Larsson, L., Olsson, G., Hoist, O., Karlsson, H. T., *Oxidation of pyrite by Acidianus brierleyi: Importance of close contact between the pyrite and the microorganisms.* Biotechnology Letters, 1993. **15**(1): p. 99-104.
20. Segerer, A., Neuner, A., Kristjansson, J. K., Stetter, K. O., *Acidianus infernus gen. nov., sp. nov., and Acidianus brierleyi comb. nov.: Facultatively Aerobic, Extremely Acidophilic Thermophilic Sulfur-Metabolizing Archaebacteria.* International Journal of Systematic Bacteriology, 1986. **36**(4): p. 559-564.
21. Shiers, D.W., Ralph, D. E., Watling, H. R., *A comparative study of substrate utilisation by Sulfobacillus species in mixed ferrous ion and tetrathionate growth medium.* Hydrometallurgy, 2010. **104**(3–4): p. 363-369.
22. Rohwerder, T., Sand, W., *Mechanisms and biochemical fundamentals of bacterial metal sulfide oxidation*, in *Microbial Processing of Metal Sulfides*, E.R.D.a.W. Sand, Editor. 2007 Springer. p. 35-58.
23. Konishi, Y., Matsui, M., Fujiwara, H., Nomura, T., Nakahara, K., *Zinc Leaching from Fly Ash in Municipal Waste Incineration by Thermophilic Archaean Acidianus brierleyi Growing on Elemental Sulfur.* Separation Science and Technology, 2003. **38**(16): p. 4117-4130.
24. Konishi, Y., Nishimura, H., Asai, S., *Bioleaching of sphalerite by the acidophilic thermophile Acidianus brierleyi.* Hydrometallurgy, 1998. **47**(2–3): p. 339-352.
25. Nemati, M., Harrison, S. T. L., *A comparative study on thermophilic and mesophilic biooxidation of ferrous iron.* Minerals Engineering, 2000. **13**(1): p. 19-24.
26. Norris, P.R., Burton, N. P., Clark, D. A., *Mineral sulfide concentrate leaching in high temperature bioreactors.* Minerals Engineering, 2013. **48**(0): p. 10-19.
27. Zhang, Y.-S., Qin, W.-Q., Wang, J., Zhen, S.-J., Yang, C.-R., Zhang, J.-W., Nai, S.-S., Qiu, G.-Z., *Bioleaching of chalcopyrite by pure and mixed culture.* Transactions of Nonferrous Metals Society of China, 2008. **18**(6): p. 1491-1496.
28. Dopson, M., Johnson, D. B., *Biodiversity, metabolism and applications of acidophilic sulfur-metabolizing microorganisms.* Environ Microbiol, 2012. **14**(10): p. 2620-31.
29. Sharma, P.K., Das, A., Hanumantha Rao, K., Forssberg, K. S. E., *Surface characterization of Acidithiobacillus ferrooxidans cells grown under different conditions.* Hydrometallurgy, 2003. **71**(1–2): p. 285-292.
30. Xia, J.-L., Yang, Y., He, H., Zhao, X.-J., Liang, C.-L., Zheng, L., Ma, C.-Y., Zhao, Y.-D., Nie, Z.-Y., Qiu, G.-Z., *Surface analysis of sulfur speciation on pyrite bioleached by extreme thermophile Acidianus manzaensis using Raman and XANES spectroscopy.* Hydrometallurgy, 2010. **100**(3–4): p. 129-135.
31. Microanalysis, C.F.f.A.M.a. *Introduction to Energy Dispersive X-ray Spectrometry (EDS).* 2015 [cited 2017; Available from: http://cfamm.ucr.edu/manuals.html.
32. Watling, H.R., Perrot, F. A., Shiers, D. W., *Comparison of selected characteristics of Sulfobacillus species and review of their occurrence in acidic and bioleaching environments.* Hydrometallurgy, 2008. **93**(1–2): p. 57-65.
33. Liu, H., Gu, G., Xu, Y., *Surface properties of pyrite in the course of bioleaching by pure culture of Acidithiobacillus ferrooxidans and a mixed culture of Acidithiobacillus ferrooxidans and Acidithiobacillus thiooxidans.* Hydrometallurgy, 2011. **108**(1–2): p. 143-148.

34. Cosmidis, J., Templeton, A. S., *Self-assembly of biomorphic carbon/sulfur microstructures in sulfidic environments.* 2016. **7**: p. 12812.
35. Sasaki, K., Konno, H., *Morphology of jarosite-group compounds precipitated from biologically and chemically oxidized Fe ions.* The Canadian Mineralogist, 2000. **38**(1): p. 45-56.
36. Karavaiko, G.I., Smolskaja, L. S., Golyshina, O. K., Jagovkina, M. A., Egorova, E. Y., *Bacterial pyrite oxidation: Influence of morphological, physical and chemical properties.* Fuel Processing Technology, 1994. **40**(2): p. 151-165.
37. Tan, S.N., Chen, M., *Early stage adsorption behaviour of Acidithiobacillus ferrooxidans on minerals I: An experimental approach.* Hydrometallurgy, 2012. **119–120**(0): p. 87-94.
38. *MyScope: training for advanced research*. 2014 April 15, 2014 [cited 2017 21/08]; Available from: ww.ammrf.org.au/myscope.
39. Swapp, S. *Geochemical Instrument Analysis: Scanning Electron Microscopy*. [Website] 2012 7/7/2012 [cited 2012 19/7/2012]; Available from: http://serc.carleton.edu/research_education/geochemsheets/techniques/SEM.html.
40. Chau, T.T., Bruckard, W. J., Koh, P. T. L., Nguyen, A. V., *A review of factors that affect contact angle and implications for flotation practice.* Advances in Colloid and Interface Science, 2009. **150**(2): p. 106-115.
41. Chipfunhu, D., Zanin, M., Grano, S., *Flotation behaviour of fine particles with respect to contact angle.* Chemical Engineering Research and Design, 2012. **90**(1): p. 26-32.
42. Ohmura, N., Kitamura, K., Saiki, H., *Selective Adhesion of Thiobacillus ferrooxidans to Pyrite.* Applied and Environmental Microbiology, 1993. **59**(12): p. 4044-4050.
43. Nagaoka, T., Ohmura, N., Saiki, H., *A novel mineral processing by flotation using Thiobacillus ferrooxidans*, in *Process Metallurgy*, R. Amils and A. Ballester, Editors. 1999, Elsevier. p. 335-342.
44. Zhu, J., Li, Q., Jiao, W., Jiang, H., Sand, W., Xia, J., Liu, X., Qin, W., Qiu, G., Hu, Y., Chai, L., *Adhesion forces between cells of Acidithiobacillus ferrooxidans, Acidithiobacillus thiooxidans or Leptospirillum ferrooxidans and chalcopyrite.* Colloids and Surfaces B: Biointerfaces, 2012. **94**: p. 95-100.
45. Vilinska, A., Hanumantha Rao, K., *Surface Thermodynamics and Extended DLVO Theory of Acidithiobacillus ferrooxidans Cells Adhesion on Pyrite and Chalcopyrite*. Vol. 2. 2009.
46. Jordan, M.A., Barr, D. W., Phillips, C. V., *Iron and sulphur speciation and cell surface hydrophobicity during bacterial oxidation of a complex copper concentrate.* Minerals Engineering, 1993. **6**(8–10): p. 1001-1011.
47. Biesinger, M.C., Miller, D. J., Harbottle, R. R., Possmayer, F., McIntyre, N. S., Petersen, N. O., *Imaging lipid distributions in model monolayers by ToF-SIMS with selectively deuterated components and principal components analysis.* Applied Surface Science, 2006. **252**(19): p. 6957-6965.
48. Belu, A.M., Davies, M. C., Newton, J. M., Patel, N., *TOF-SIMS Characterization and Imaging of Controlled-Release Drug Delivery Systems.* Analytical Chemistry, 2000. **72**(22): p. 5625-5638.
49. Baldwin, P.M., Melia, C. D., Davies, M. C., *The Surface Chemistry of Starch Granules Studied by Time-of-Flight Secondary Ion Mass Spectrometry.* Journal of Cereal Science, 1997. **26**(3): p. 329-346.
50. Heim, C., Sjövall, P., Lausmaa, J., Leefmann, T., Thiel, V., *Spectral characterisation of eight glycerolipids and their detection in natural samples using time-of-flight secondary ion mass spectrometry.* Rapid Communications in Mass Spectrometry, 2009. **23**(17): p. 2741-2753.
51. Robinson, M.A., Graham, D. J., Morrish, F., Hockenbery, D., Gamble, L. J., *Lipid analysis of eight human breast cancer cell lines with ToF-SIMS.* Biointerphases, 2016. **11**(2): p. 02A303.

52. Vaidyanathan, S., Fletcher, J. S., Jarvis, R. M., Henderson, A., Lockyer, N. P., Goodacre, R., Vickerman, J. C., *Explanatory multivariate analysis of ToF-SIMS spectra for the discrimination of bacterial isolates.* Analyst, 2009. **134**(11): p. 2352-2360.
53. Vaidyanathan, S., Fletcher, J. S., Lockyer, N. P., Vickerman, J. C., *TOF-SIMS investigation of Streptomyces coelicolor, a mycelial bacterium.* Applied Surface Science, 2008. **255**(4): p. 922-925.
54. Breitenstein, D., Rommel, C. E., Stolwijk, J., Wegener, J., Hagenhoff, B., *The chemical composition of animal cells reconstructed from 2D and 3D ToF-SIMS analysis.* Applied Surface Science, 2008. **255**(4): p. 1249-1256.
55. Schilke, K.F., McGuire, J., *Detection of nisin and fibrinogen adsorption on poly(ethylene oxide) coated polyurethane surfaces by time-of-flight secondary ion mass spectrometry (TOF-SIMS).* Journal of Colloid and Interface Science, 2011. **358**(1): p. 14-24.
56. Sanni, O.D., Wagner, M. S., Briggs, D., Castner, D. G., Vickerman, J. C., *Classification of adsorbed protein static ToF-SIMS spectra by principal component analysis and neural networks.* Surface and Interface Analysis, 2002. **33**(9): p. 715-728.
57. Berman, E.S.F., Kulp, K. S., Knize, M. G., Wu, L., Nelson, E. J., Nelson, D. O., Wu, K. J., *Distinguishing Monosaccharide Stereo- and Structural Isomers with TOF-SIMS and Multivariate Statistical Analysis.* Analytical Chemistry, 2006. **78**(18): p. 6497-6503.
58. Berman, E.S.F., Wu, L., Fortson, S. L., Kulp, K. S., Nelson, D. O., Wu, K. J., *Chemometric and statistical analyses of ToF-SIMS spectra of increasingly complex biological samples.* Surface and Interface Analysis, 2009. **41**(2): p. 97-104.
59. Urquhart, A.J., Taylor, M., Anderson, D. G., Langer, R., Davies, M. C., Alexander, M. R., *TOF-SIMS Analysis of a 576 Micropatterned Copolymer Array To Reveal Surface Moieties That Control Wettability.* Analytical Chemistry, 2008. **80**(1): p. 135-142.
60. Pikulski, M., Brodbelt, J. S., *Differentiation of flavonoid glycoside isomers by using metal complexation and electrospray ionization mass spectrometry.* Journal of the American Society for Mass Spectrometry, 2003. **14**(12): p. 1437-1453.
61. Jungnickel, H., Jones, E. A., Lockyer, N. P., Oliver, S. G., Stephens, G. M., Vickerman, J. C., *Application of TOF-SIMS with Chemometrics To Discriminate between Four Different Yeast Strains from the Species Candida glabrata and Saccharomyces cerevisiae.* Analytical Chemistry, 2005. **77**(6): p. 1740-1745.
62. Pradier, C.M., Rubio, C., Poleunis, C., Bertrand, P., Marcus, P., Compère, C., *Surface Characterization of Three Marine Bacterial Strains by Fourier Transform IR, X-ray Photoelectron Spectroscopy, and Time-of-Flight Secondary-Ion Mass Spectrometry, Correlation with Adhesion on Stainless Steel Surfaces.* The Journal of Physical Chemistry B, 2005. **109**(19): p. 9540-9549.
63. Dague, E., Delcorte, A., Latgé, J.-P., Dufrêne, Y. F., *Combined Use of Atomic Force Microscopy, X-ray Photoelectron Spectroscopy, and Secondary Ion Mass Spectrometry for Cell Surface Analysis.* Langmuir, 2008. **24**(7): p. 2955-2959.

7 Characterisation of *Acidianus brierleyi* and Pyrite without Yeast Extract Enhancement: Growth Behaviour and Mineral Surface Properties.

7.1 Introduction

The investigation in the previous chapter concluded that the inclusion of yeast extract in the growth medium, which most studies have done [1-19], is likely to interfere with the mineral surface. This makes the isolation of cell action on the surface impossible.

Most previous investigations have not investigated the impact of yeast extract on the recovery of bioleaching products, nor have they included media control measurements for comparison [1-5, 9-14]. Studies by Konishi *et al* and Deveci *et al* observes that growth of *A. brierleyi* is enhanced by yeast extract, and therefore their bio-oxidation rate is improved, however they make no observations on the action of yeast extract in the bioleaching system [20, 21]. This disagrees with results presented by Larsson *et al*, who found the addition of yeast extract to *A. brierleyi* culture did not enhance the leaching rate of pyrite, and in control experiments reduced the oxidation of pyrite upon addition to solution [22].

In this chapter, *A. brierleyi* will be grown first on elemental sulfur, then on pyrite, without the inclusion of yeast extract in the medium. The growing cultures and the pyrite surface will be explored using the same analytical techniques applied in the previous chapter (Chapter 6). This will enable the assessment of the impact of yeast extract on the mineral surface chemistry, and the isolation of the impact of *A. brierleyi* on pyrite to fully explore the application of this archaea to the bioflotation of sulfide minerals.

7.2 Experimental

7.2.1 Mineral Preparation

The bulk pyrite for culture growth is described in in Chapter 3, section 3.2, Table 3.4. The cubic pyrite used for this investigation and the preparation of mineral tile samples are described in Chapter 3, sections 3.2 and 3.4, respectively.

Tiles were either snap frozen in modified DSM 150 medium for AFM and ToF-SIMS analysis or stored in fixative for dehydration and sputtering coating for SEM by methods described in Chapter 3, section 3.9.

7.2.2 Cell Growth and Monitoring

Cultures of *A. brierleyi* (DSM 1651) were received live from the DSMZ (Deutsche Sammlung von Mikroorganismen und Zellkulturen) and a base culture was inoculated into modified DSM 150 medium, made by omitting the yeast extract from the prescribed recipe and continuously subcultured as described in Chapter 3, section 3.3.2. Cultures were monitored by direct cell counting, as described in Chapter 3, section 3.8.

7.2.3 Surface Characterisation

Surface analysis of pyrite control and those exposed to *A. brierleyi* were performed using Scanning Electron Microscope (SEM), Energy Dispersive X-ray spectroscopy (EDX), Atomic Force Microscopy (AFM), captive bubble contact angle, and Time of Flight – Secondary Ion Mass Spectroscopy (ToF-SIMS). Details for these techniques can be found in Chapter 3, sections 3.9, 3.10, 3.14, and 3.16.

7.3 Results and Discussion

7.3.1 Growth of *Acidianus brierleyi* on Pyrite without Yeast Extract

7.3.1.1 Cell Growth

The live culture of *A. brierleyi* was first cultured on sulfur flowers powder as a nutrient source, and continually subcultured at 10% inoculum, with a cycle completing every three weeks. After several complete growth cycles on the recommended medium, cultures were inoculated at 10% inoculum into DSM 150 medium on sulfur flowers powder without the inclusion of yeast extract. This modified media recipe will hereafter be denoted as DSMny 150 medium. An example of *A. brierleyi* growth curve on sulfur without yeast extract is show in Figure 7.77. *A. brierleyi* was adapted to grow on pyrite by subculturing from cultures with sulfur flowers powder as a nutrient source into DSMny 150 medium with 20 g of UV sterilised pyrite. Cultures were inoculated at 10% with *A. brierleyi*. Growth curves were determined by counting, and a typical growth curve is shown in Figure 7.78.

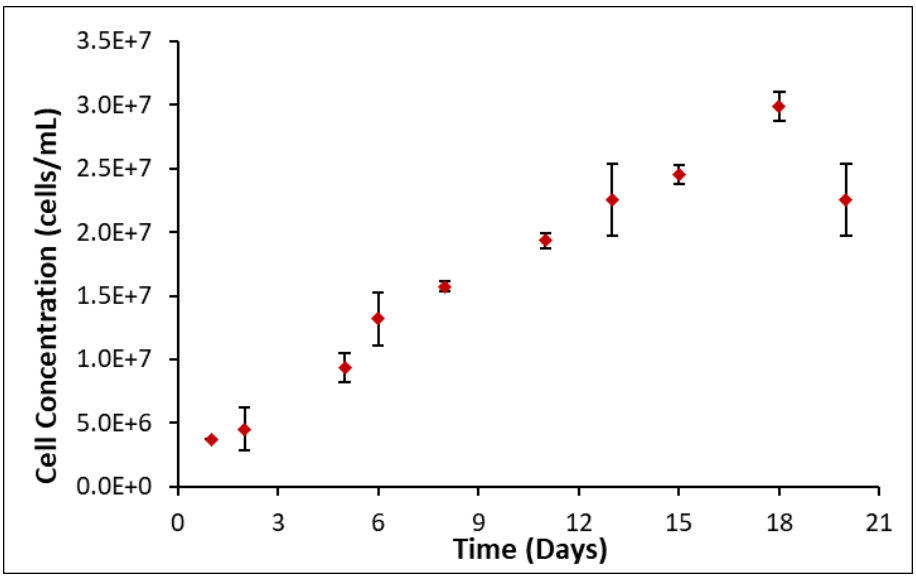

Figure 7.77: Typical growth curve of *A. brierleyi* on sulfur flowers at 10% inoculum in DSMny 150 medium.

Although *A. brierleyi* growth is enhanced by the presence of yeast extract, the culture without yeast extract still shows growth from an initial cell concentration of 3.6 x 10^6 cells/mL to over 2.9 x 10^7 cells per mL within a three-week growth cycle.

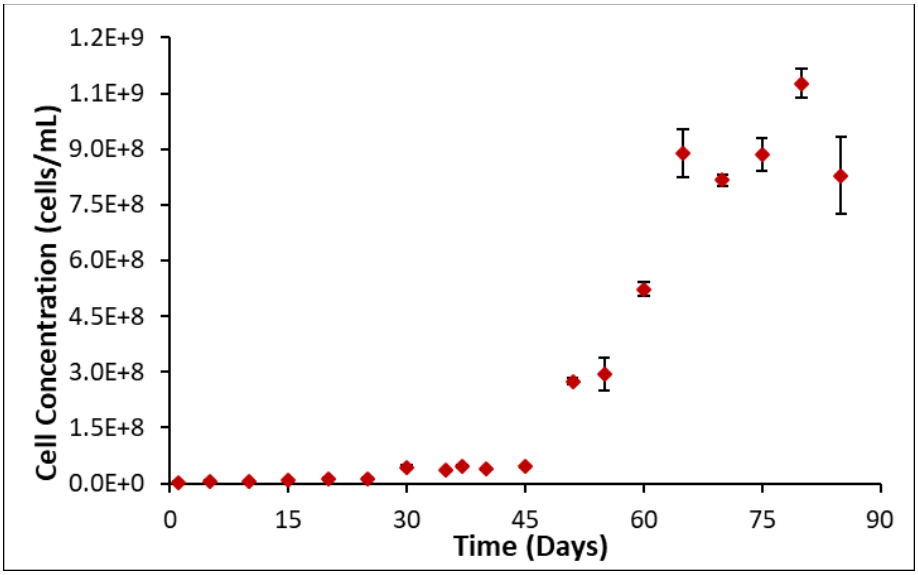

Figure 7.78: Typical growth curve of *A. brierleyi* on pyrite (+38, -75 um) at 10% inoculum in DSMny 150 medium.

When grown on sulfur flowers powder, the cultures typically reach the exponential phase within the first week, completing a growth cycle in 21 days (Figure 7.77). *A. brierleyi* grown on pyrite stabilized to a 90-day growth cycle, with the cell reaching the exponential phase between 45-60 days.

The previous studies that investigated the growth of *A. brierleyi* on a variety of substrates are summarised in Chapter 6, section 6.3.1.1. Final cell concentrations previously described of *A. brierleyi* on a variety of substrates ranges between 10^7 and 10^{15} cells/mL, with stationary phase reached typically between 2 to 20 days [1, 3, 4, 8-11, 16, 19, 22, 23]. The final cell concentrations agree with those studies, however the growth cycle on pyrite in the present study is considerably longer.

7.3.1.2 Comparison to A. brierleyi *Enhanced with Yeast Extract*

The *A. brierleyi* reach exponential phase at the same time as culture containing yeast extract, however final cell concentration was not as high, with final cell concentration around $8.5x10^8$ cells/mL, compared to $1.1x10^9$ cells/mL. The results here suggest the yeast extract does enhance growth, as observed in previous studies [20, 21]. This appears to result in an increased cell concentration compared to culture without yeast extract, however, there is little difference in the length of the growth cycles between cultures with or without yeast extract.

7.3.1.3 Eh and pH Monitoring

The Eh and pH of *A. brierleyi* on pyrite in the absence of yeast extract was measured with reference to a Ag/AgCl electrode at 1 atm at an average temperature of 24.3 ± 1.1 °C, while the average temperature of the DSMny 150 medium exposed to pyrite was found to have an average temperature of 24.3 ± 1.8 °C. The Eh and pH curves of the DSMny 150 medium and *A. brierleyi* pyrite leachate are shown in Figure 7.79. The pH of the *A. brierleyi* culture grown on pyrite starts at 1.61, decreasing steadily to pH 0.43 day 65 before dropping sharply to below 0 over the next 10 days, while the Eh steadily increases from 318 mV to 398 mV by day 70, where it remains static for the remainder of the natural growth cycle. In contrast, the pH of the control solution starts at 2.32, and decreases steadily to a final pH of 0.54 by day 75, never going below the corresponding *A. brierleyi* pH at the same period of exposure. The Eh of the control solution starts at 277 mV, well below that of the archaea culture, increasing steadily to a final Eh of just over 374 mV by day 75, converging on the Eh of the culture solution at day 30, but never rising above the Eh of the culture solution.

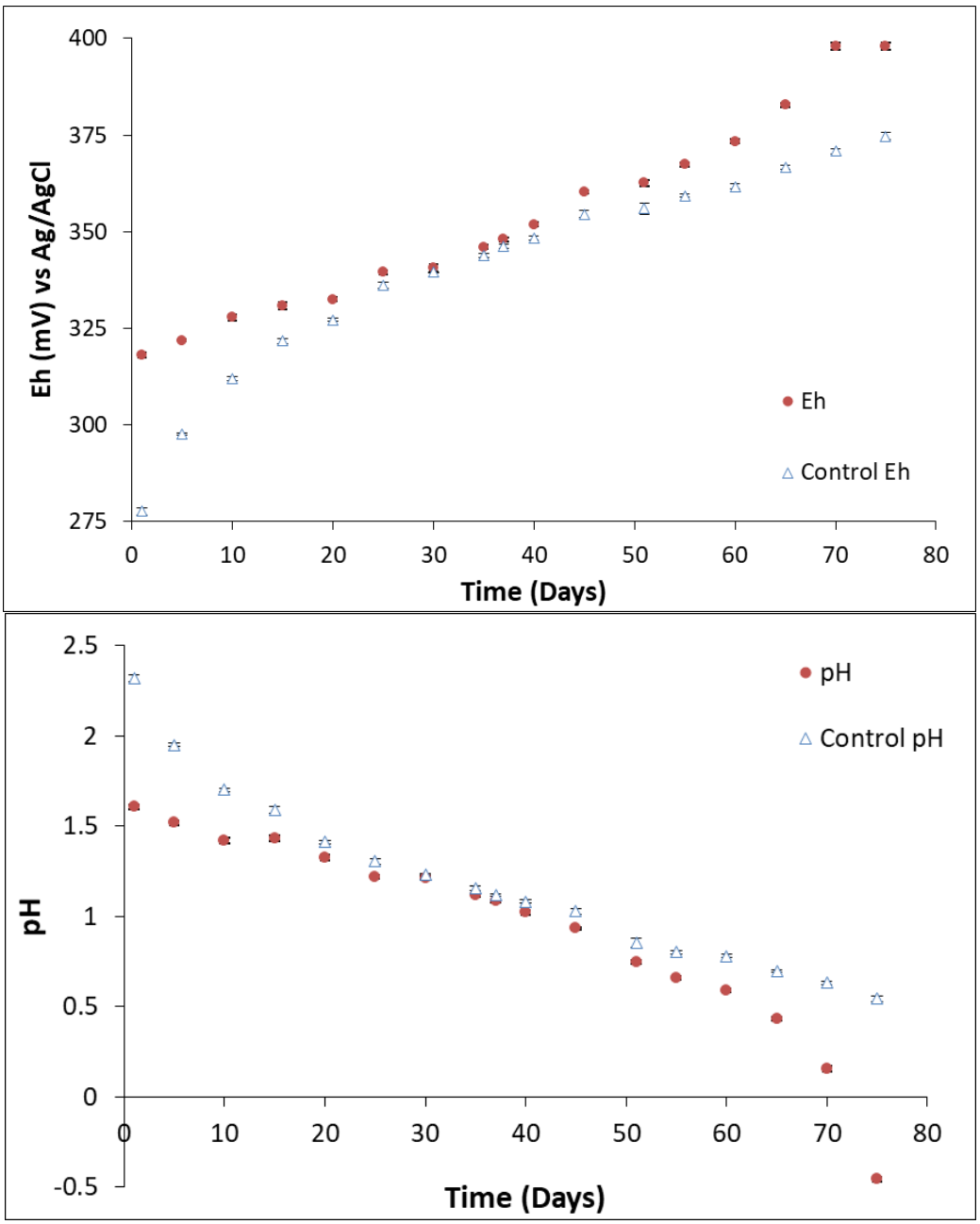

Figure 7.79: Typical Eh (top) and pH (bottom) curves of *A. brierleyi* on pyrite (+38, -75 um) at 10% inoculum (●), and DSM 150 medium (Δ).

The previous studies that investigated the Eh and pH of *A. brierleyi* on a variety of substrates are summarised in Chapter 6, section 6.3.1.2, and the reactions that occur in the leaching of pyrite are discussed in Chapter 4, section 4.3.1.2, in Equations 4.37-4.44. The previous studies on mineral leaching and sulfur-grown cultures observed a decrease in pH between 2.5 and 0.5, which agrees with the range of values observed over the leaching of pyrite in this study [1-5, 10, 11, 23]. The Eh values found is this study fall within the Eh values reported in previous studies, which showed increasing values over a range of 315-850 mV, depending on the substrate [2-5, 10, 11].

The decrease in pH appears accelerated by the presence of *A. brierleyi* cells over longer periods of exposure, which coincides with the exponential phase of the culture, indicating the increase in cell population is contributing to the oxidation of the mineral. As was the case in previous chapters, the Eh values increase over time, suggesting oxidative conditions are occurring, promoting the formation of hydrophilic oxidation species on the surface. This suggests the presence of a greater concentration of ferric iron and soluble sulfur species may be expected in the leachate of *A. brierleyi* on pyrite compared to the abiotic controls. The difference between the Eh of the culture and the abiotic control is most pronounced at both the early and late exposure stages, suggesting the oxidation of the pyrite surface is accelerated in the presence of cells early in exposure, as well as over longer periods of exposure (≥50 days).

7.3.1.4 Comparison to A. brierleyi *Enhanced with Yeast Extract*

The Eh values of *A. brierleyi* grown with and without yeast extract are similar until after day 45, where the Eh of the culture with yeast extract becomes greater than the culture without yeast extract by between 7-22 mV. This suggest the culture with yeast extract has more oxidative conditions over longer periods of exposure. The pH values are also similar until after day 45, where the culture without yeast extract becomes lower than the culture with yeast extract by between 0.1-0.4. This suggests that in the absence of yeast extract, *A. brierleyi* is potentially promoting the formation of acid in solution by either the oxidation of elemental sulfur (Equation 4.43) or production of jarosites and iron oxides/hydroxides (Equations 4.41 and 4.44) on the surface, rather than the oxidation of ferrous iron to ferric iron (Equation 4.40) [6, 8, 10, 13, 14, 22-26].

Importantly, the two media control solutions show also different Eh curves. The Eh values are initially the same, however by the end of the first week the Eh is higher in DSMny 150 medium compared to DSM 150 medium, and remains higher by between 8.5-23.5 mV until day 60, where the Eh values converge. A difference of 50 mV or less could, depending on pH, promote the formation of iron hydroxides and/or elemental sulfur (Equations 4.41 and 4.42) on the surface of pyrite that impact hydrophobicity [6, 8, 10, 13, 14, 22-27]. This suggests the yeast extract may be preventing mineral surface oxidation over earlier periods on exposure. The pH is lower in DSMny 150 medium by between 0.14-0.39, and remains lower until day 60 where the pH values converge.

These results suggest yeast extract in the medium controls may be slowing leaching early in exposure, and that the action of *A. brierleyi* culture is altered by the presence of yeast extract in solution, leading to potentially different oxidation products being promoted. A comparison must be made to assess the ions and the potential impact of the yeast extract contributing to the Eh using titration and Inductively Coupled Plasma Optical Emission Spectroscopy (ICPOES).

7.3.1.5 *Inductively Coupled Plasma Optical Emission Spectroscopy, Cerium(IV) Sulfate Titration*

As has been described in previous chapters, the ferrous iron, ferric iron and total soluble sulfur were determined using a combination of ICPOES and colorimetric titration using cerium(IV) sulfate. The methods used to determine the concentrations of these species is described in Chapter 3, sections 3.6 and 3.7. The ferrous iron, ferric iron and soluble sulfur concentrations of the leachate of pyrite exposed to DSMny 150 medium and *A. brierleyi* culture are shown in Figure 7.80.

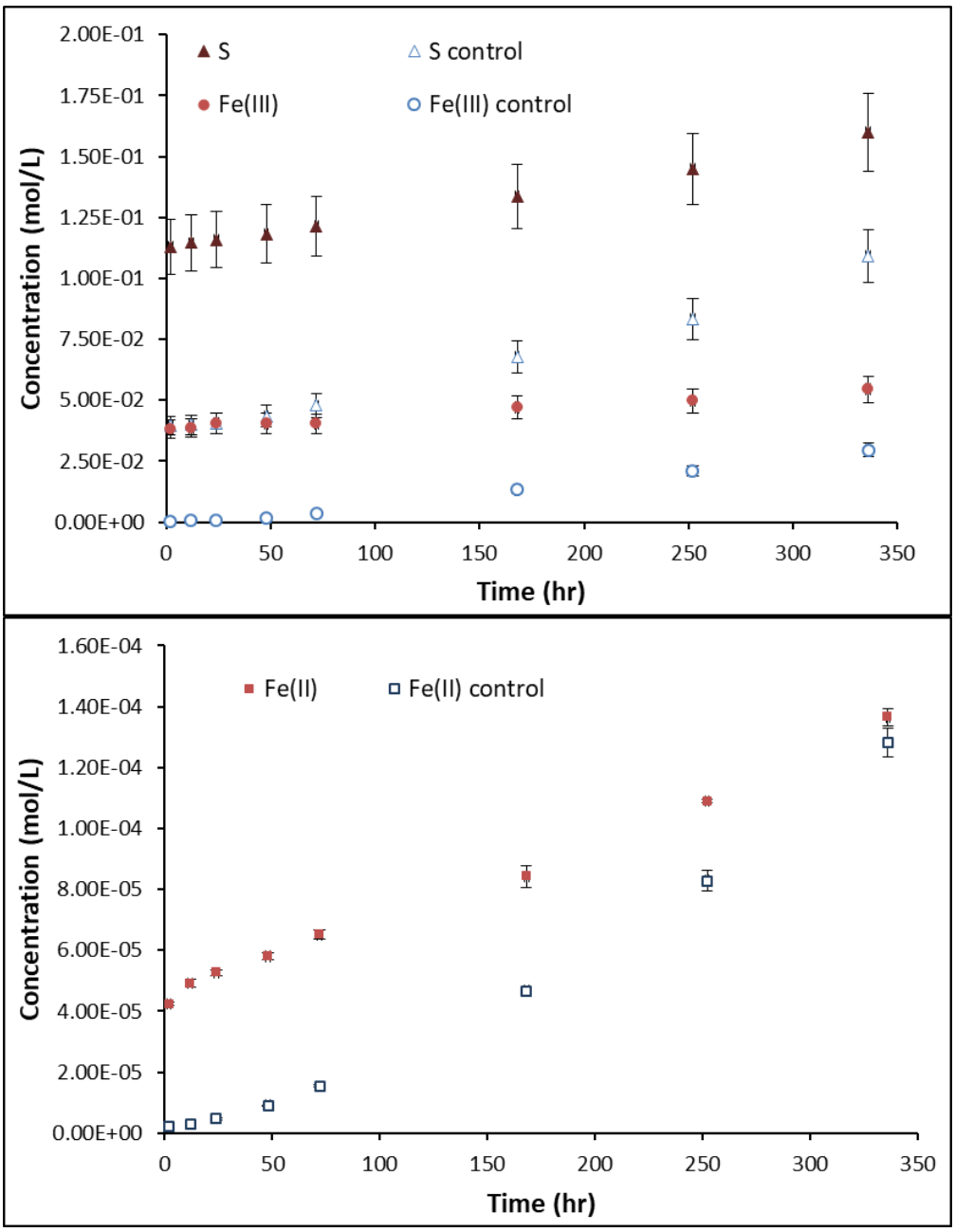

Figure 7.80: Typical concentration curves of ferric iron (top) of *A. brierleyi* on pyrite (●), and DSMny 150 medium (○). and solubilised sulfur (top) in *A. brierleyi* on pyrite (▲), and DSMny 150 medium (Δ). Typical concentration curves of ferrous iron (bottom) of *A. brierleyi* on pyrite (■), and DSMny 150 medium (□).

The concentration of Fe^{2+} ions in the DSMny 150 medium leaching solution increases almost linearly from $2.06x10^{-6}$ mol/L at 2 h to $1.28x10^{-4}$ mol/L by 336 h, with this linear increase repeated by the Fe^{3+} ions, the concentration of which increases from $3.34x10^{-4}$ mol/L to $2.96x10^{-2}$ mol/L over 336 h. The total S measured in solution also displays a linear increase from $3.95x10^{-2}$ mol/L to $1.09x10^{-1}$ mol/L over the same period. In each case, the initial concentration of the respective ions is greater in the *A. brierleyi* cultures than the media control solutions, which also increase in concentration in a linear fashion. The *A. brierleyi* culture leaching solution displays an increase in Fe^{2+} ions of $4.23x10^{-5}$ mol/L up to $1.37x10^{-4}$ mol/L, an increase in Fe^{3+} ions of $3.79x10^{-2}$ mol/L up to $5.45x10^{-2}$ mol/L, and an increase in total S also of $1.13x10^{-1}$ mol/L up to $1.60x10^{-1}$ mol/L over the course of 336 h. This suggests, although the concentration of all ions is higher in the *A. brierleyi* culture for this period of exposure, the leaching rate and oxidation rate is greater in the DSMny 150 medium solution.

The previous studies that investigated the iron and sulfur concentrations of *A. brierleyi* leachate on a variety of substrates are summarised in Chapter 6, section 6.3.1.3 [3, 4, 20, 22]. The ferrous iron concentrations reported in in the literature range between 0 mol/L and $6.27x10^{-3}$ mol/L, and the results presented here are fall well within this range [9, 14, 22, 28]. The ferric iron concentrations previously reported range between $8.95x10^{-8}$ mol/L and $2.81x10^{-2}$ mol/L, with values reported in this study falling within that range or greater [9-11, 14, 22]. The sulfate concentrations previously reported in the literature range between $1.97x10^{-3}$ and 0.45 mol/L, a range which agrees with the total soluble sulfur measured in this study [8, 10, 11].

The ion concentrations reported in this study suggests two things. Firstly, the concentration of all ions greater in *A. brierleyi* culture compared to DSMny 150 medium; Secondly, both total S and Fe^{2+} are leaching from pyrite into solution at a greater rate in the *A. brierleyi* culture. However, it appears that while the Fe^{3+} concentration is greater in the culture solution, Fe^{3+} is leaching at a greater rate in the DSMny 150 medium control solution. This suggests less oxidising activity in the medium compared to the culture solution. This agrees with the Eh results, which increases as the concentration of ions in solution increases due to iron leaching from the mineral into solution [29].

The Fe^{3+} concentration increasing suggests that the acid is being consumed and releasing Fe^{3+} into solution per Equation 4.40, when bacterial numbers are at their lowest. Compared to the mesophilic strains, cell numbers do not increase significantly within 168 h of exposure, and as such so there no alteration in the rate of ion production in biotic solution. However, there is an indication that microbial action is oxidising the elemental sulfur in the surface to sulfate species to create a greater concentration of oxidised sulfur species in solution, per Equation 4.43, Chapter 4, section 4.3.1.2.

Although the exponential phase of *A. brierleyi* does not begin until day 45 of exposure to pyrite, the leaching of iron and sulfur-species from the mineral appears immediate, accompanied by a decrease in pH and an increase in Eh as sulfuric acid is produced and ferrous iron is oxidised to ferric iron and the leaching of the mineral is perpetuated. This suggests that in the early stages of exposure, the *A. brierleyi* more effective at oxidising the pyrite surface than the mesophiles. To determine whether cell attachment is at all responsible for this accelerated oxidation, or whether the cells are acting via the indirect or indirect contact mechanisms, microscopic techniques are required to investigate *A. brierleyi* on the pyrite surface. This will enable the assessment of the impact of yeast extract not only on solution conditions, but on the behaviour of *A. brierleyi* on the surface of pyrite, secondary mineral formation and leaching progression.

7.3.1.6 Comparison to A. brierleyi *Enhanced with Yeast Extract*

The concentration of all ions in both media solutions are initially identical, however the leaching rate is greater for pyrite exposed to DSMny 150 medium, leading to a higher concentration of all species over 336 h. This is most noticeable for the concentration of Fe^{2+} in solution, with a final concentration that exceeds that observed in the *A. brierleyi* culture grown on yeast extract. These results suggest that the yeast extract in the medium is hindering leaching and oxidation of the mineral.

The *A. brierleyi* cultures display the highest concentration of ions in solution throughout the course of the experiment. The results also suggest that the leaching of Fe^{2+} from the mineral is greater in the *A. brierleyi* culture without yeast extract, while the oxidation to Fe^{3+} is greater in the culture grown on yeast extract. The concentration of solubilised sulfur and the rate of increase in concentration is indistinguishable between cultures. This suggests that the iron oxidation ability of *A. brierleyi* is positively impacted by the presence of yeast extract in the medium. This agrees with the Eh results that show less oxidative conditions, and therefore higher concentrations of ferrous iron present in solution in the absence of yeast extract.

7.3.2 Scanning Electron Microscopy and Energy Dispersive X-ray Spectroscopy

Energy Dispersive X-ray (EDX) analysis was performed on the surface of the pyrite exposed to *A. brierleyi* in the absence of yeast extract using Scanning Electron Microscopy (SEM). This was done to identify the elements present in the surface and surface artefacts and their atomic ratios, which can be used to determine chemical structure. The EDX analysis of the pyrite surface exposed to *A. brierleyi* are shown in Figure 7.81 as average atomic percentage. The elements Al, Si, and Na were all detected at levels below 1.5%. After 168 h, there was a significant increase on iron species that

corresponds with a lack of detectable carbon at this period of exposure. The oxygen increases slightly at 72 h, while the iron and sulfur atomic percentages are relatively stable could be due in part to the fact that EDX penetrates he surface up to 5 µm, and presents significant bulk pyrite signal [30]. The *A. brierleyi* cells present a significant carbon signal compared to the mineral. Unlike pyrite exposed to *A. brierleyi* culture containing yeast extract, no organic aggregates were detected on the surface [31].

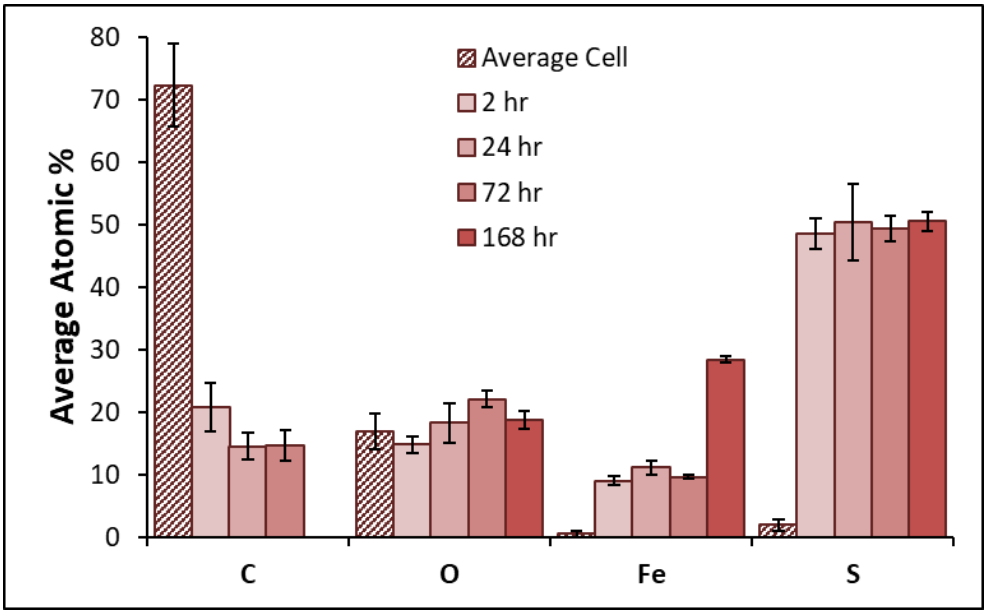

Figure 7.81: Average atomic percentage of pyrite exposed to *A. brierleyi* for 2, 24, 72 and 168 h, and the average atomic percentage of individual *A. brierleyi* cells (diagonal stripes) as detected by EDX.

The cells observed on the surface using SEM are spheroidal (see Figure 7.83(C and F)), with an average diameter of 2.77 ± 0.68 µm. This agrees with Segerer *et al*, who describes cell width of the genus *Acidianus* within a range of 0.5-2 µm, depending on growth conditions [32]. These cells can be difficult to differentiate from the debris on the surface, especially from the larger particles, with EDX being essential for initial cell and debris identification.

The EDX analysis of the pyrite surface exposed to DSMny 150 medium is shown in Figure 7.82 as average atomic percentage. The elements Mg, Si, and Al were detected at levels below 1%. The atomic percentages of pyrite exposed to DSMny 150 medium do not show the same extent of oxidation as pyrite exposed to *A. brierleyi*, with little variation over the course of exposure. In contrast to the samples exposed to *A. brierleyi*, the atomic percentage of both carbon and oxygen detected was lower. Highly visible silicate crystal inclusions in the control pyrite samples were avoided for the purposes of EDX analysis.

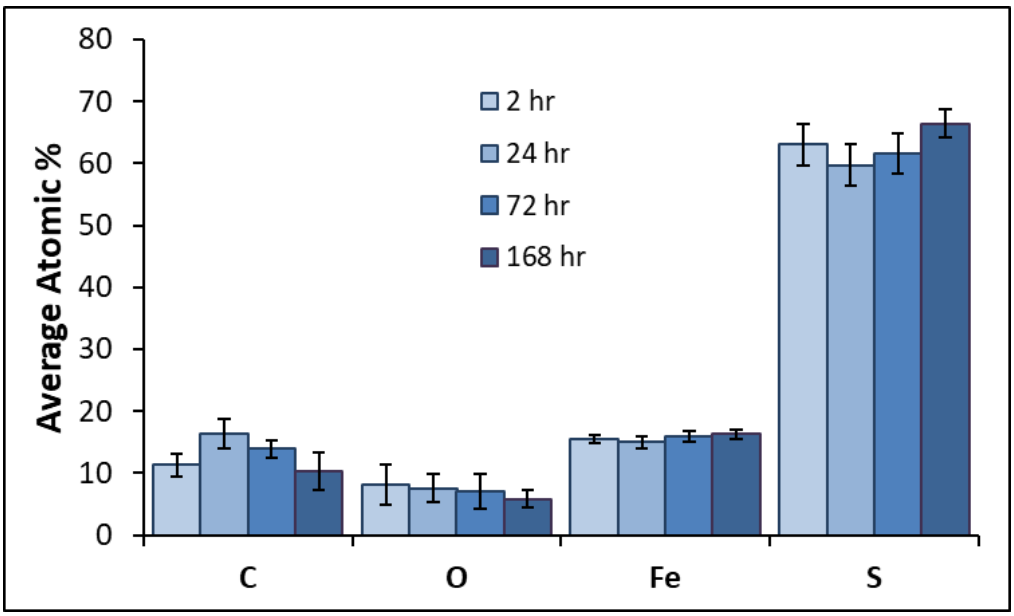

Figure 7.82: Average atomic percentage of pyrite exposed to DSMny 150 medium for 2, 24, 72 and 168 h, as determined by EDX.

Large inorganic particles such as those pictured in Figure 7.83(I) are also observed on the surface, with more found in voids in the surface than on smooth regions. This inorganic debris was also examined by EDX, with the spot spectra of 19 individual pieces of debris analysed from several samples. The average atomic percentages are shown in Table 7.11.

Table 7.11: Average atomic percentage EDX data of inorganic precipitates

Element	*Atomic %*
C	7.0 ± 3.2
O	54.5 ± 7.2
Fe	9.3 ± 1.4
S	21.3 ± 6.1
K	3.7 ± 0.5
Si, Al, Na, N	< 1.5%

This results in atomic ratios of $K_1Fe_{2.5}S_{5.8}O_{14.7}$, which agrees closely with the chemical formula for potassium jarosite observed in the previous chapter ($KFe_3(SO_4)_2.(OH)_6$) [3, 4, 14]. The elevated atomic percentage of sulfur may be due to elemental sulfur precipitates and bulk pyrite signal from the underlying mineral [30]. The results observed here agree with the studies examined in the previous chapter, section 6.3.2, with the successful identification of cells and secondary mineral precipitates [4, 14]. They also support the Eh and pH results that suggest jarosite formation may be promoted under these solution conditions.

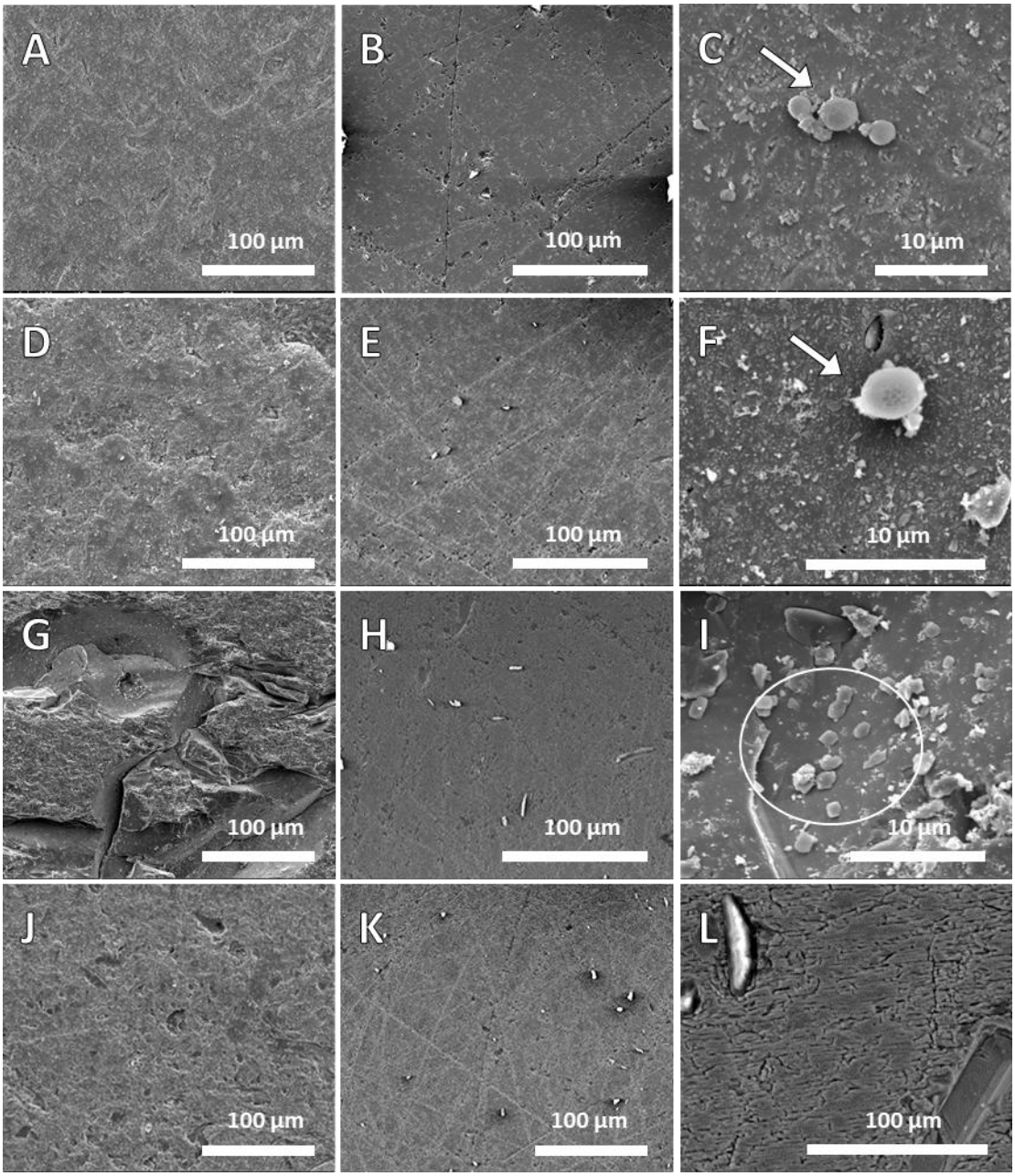

Figure 7.83: Pyrite tiles exposed to *A. brierleyi* for 2 h (A), 24 h (D), 72 h (G) and 168 h (J), pyrite tiles exposed to DSMny 150 medium for 2 h (B), 24 h (E), 72 h (H) and 168 h (K), and *A. brierleyi* cells, indicated by arrows (C, F), jarosite precipitates, indicated by circle, and sub-micron debris (I), close-up of rivers on DSMny 150 medium control 168 h (L).

Typical SEM images obtained for pyrite upon exposure to *A. brierleyi* and DSMny 150 medium are shown in Figure 7.83. Over the course of exposure to *A. brierleyi* the leaching of the pyrite appears to advance, with the surface increasingly covered in sub-micron debris, shown in Figure 7.83(A, D, G and J). The pyrite shows surface etch pits and cracks, which have been identified as leaching related to the 110 and 100 crystal faces of the pyrite in previous studies [33, 34]. As the surface leaching advances, large cracks develop all over the pyrite surface, such as those shown in Figure 7.83(G). Scratches from the polishing process are also visible on the surface at all periods of exposure. Cells are observed on the surface in clusters of no more than three such as those pictured

in Figure 7.83(C). Cells show no preference for voids or cracks and generally do not appear on the surface near each other. *A. brierleyi* cells are observed with an average coverage of less than 0.08 cells/mm^2 measured for every period of exposure examined using ImageJ, which is equivalent to a surface cover of less than 0.033%. The sub-micron debris observed on the pyrite surface is similar to that also found by Mikkelsen *et al* during pyrite leaching by *A. brierleyi* [14]. Secondary mineral precipitates, identified by EDX as jarosite, in size range of 1-2 μm^2 are observed on the surface, appearing to preferentially form in voids rather than on smoother regions, such as those pictured in Figure 7.83(I). These larger particles are similar in morphology to crystals presented by Sasaki *et al*, which were found to form both biotically and abiotically [3].

In contrast, pyrite exposed to DSMny 150 medium shows little inorganic debris on the surface. The pyrite exposed to DSMny medium for 2 h (see Figure 7.83(B)) was found to have pits and scratches, with the etch pits appearing 1-4 μm in length, and 0.3-1.5 μm in width, similar in size to those observed on the pyrite exposed to *A. brierleyi*, and more significant than those found on bare polished pyrite shown in Chapter 4, section 4.3.2, Figure 4.26. The surface is not significantly different in appearance after 24 h of exposure (see Figure 7.83(E)). After 72 h or exposure, the etch pits appear to have increased in size to 1.5-4.2 μm. The pyrite surface is much rougher than pyrite exposed to DSMny medium for 24 h, showing rivers of cracks along crystal boundaries, seen most clearly in Figure 7.83(L). These rivers have been identified by a previous study by Liu *et al*, and are due to chemical leaching of the surface [35]. The pyrite exposed to DSMny 150 medium for 168 hours (see Figure 7.83(K)) is much rougher than the previous control samples, with the rivers of cracks along crystal boundaries appearing deeper than the finer cracks observed at 72 h.

Previous applications of SEM to bioleaching by *A. brierleyi* were discussed in the previous chapter in section 6.3.2, with few able to provide images of the cells or corroborating evidence to prove cell identity. Several studies have used SEM to investigate substrates exposed to *A. brierleyi*, however the sample preparation methods involved no steps to preserve cells [1, 2, 7, 14]. The debris and leaching observed in this investigation agree with previous works that identified secondary mineral precipitates, such as jarosites [4, 14].

The results for *A. brierleyi* on pyrite are in stark contrast to the coverage measured for the mesophilic bacteria in the previous chapters for equivalent exposure times (Chapters 4 and 5), and is significantly lower coverage after 168 h than that of *A. ferrooxidans* on chalcopyrite after 1 h found by Tan *et al* (≤0.8%) [36]. There is no colonisation by *A. brierleyi* or the formation of biofilm, and no detection of cell division taking place on the surface over the course of exposure. This suggests that, even when yeast extract is removed from the medium, *A. brierleyi* does not

interact with the mineral via the direct contact mechanism. Although SEM and EDX can provide visual comparisons of the pyrite surface exposed to *A. brierleyi* in the absence of yeast extract, these techniques are not sufficient to provide information on the physical and chemical properties of the surface. The physical and chemical properties must be investigated to relate the yeast extract to the chemical species on the surface.

7.3.2.1 Comparison to A. brierleyi *Enhanced with Yeast Extract*

The EDX of pyrite exposed to *A. brierleyi* in DSMny 150 medium showed slightly less sulfur on the surface, and a higher atomic percentage of oxygen in the early stages of exposure, than pyrite exposed to *A. brierleyi* in DSM 150 medium. The iron atomic percentage did not change over the course of exposure in *A. brierleyi* in DSMny 150 medium, where the pyrite became much more iron rich when yeast extract was present in culture after 168 h. The EDX of pyrite exposed to DSMny 150 medium shows a higher atomic percentage for sulfur and oxygen, and less iron than DSM 150 medium. Although carbon was detected, it is likely due to adventitious carbon rather than debris. These results suggest pyrite leaching and oxidation of the surface is accelerated when there is no yeast extract present in the culture, leaving more oxygen on the surface in both media and culture samples. This agrees with the higher levels of solubilised iron and sulfur species measured using ICPOES (section 7.3.1.5).

Compared to the SEM images collected of pyrite exposed to DSM 150 medium (Chapter 6, section 6.3.2), the pyrite exposed to DSMny 150 medium showed more frequent and larger cracking by 24 h. Further surface analysis techniques will be applied to properly quantify the roughness of the surface in the following section. Considerably less submicron debris found on the surface of the pyrite in the absence of yeast extract, which was observed as a uniform covering on pyrite in DSM 150 medium. The SEM images of *A. brierleyi* on pyrite in DSMny 150 medium showed less cells adhered to the surface compared to culture in DSM 150 medium, and the cells observed were generally smaller in size, which may be due to the difference in available nutrients [32]. The pyrite exposed to *A. brierleyi* and DSM 150 medium displayed organic aggregates on the surface, while no organic aggregates were found on the pyrite exposed to (a)biotic DSMny 150 medium. This suggests the presence of yeast extract is contaminating the surface under both biotic and abiotic conditions.

7.3.3 Atomic Force Microscopy

The yeast extract in DSM 150 medium has the potential to influence surface roughness by three possible mechanisms. Firstly, it may form a physical barrier over the surface, altering mineral

leaching behaviour by either accelerating or hindering mineral dissolution. Secondly, it may agglomerate, forming organic debris on the surface that alters the physical properties of local areas of the surface without altering overall surface chemistry. Finally, yeast extract may not directly impact the mineral, but it may alter the behaviour of the cells in ways that prevent them from interacting with the mineral as if the extra nutrients were not present, especially in early stages of exposure. The effects *A. brierleyi* on the roughness of pyrite without the influence of yeast extract is explored here using AFM, to quantify the impact on surface leaching. Typical AFM images of pyrite exposed to *A. brierleyi* in the presence of yeast are shown in Figure 7.84.

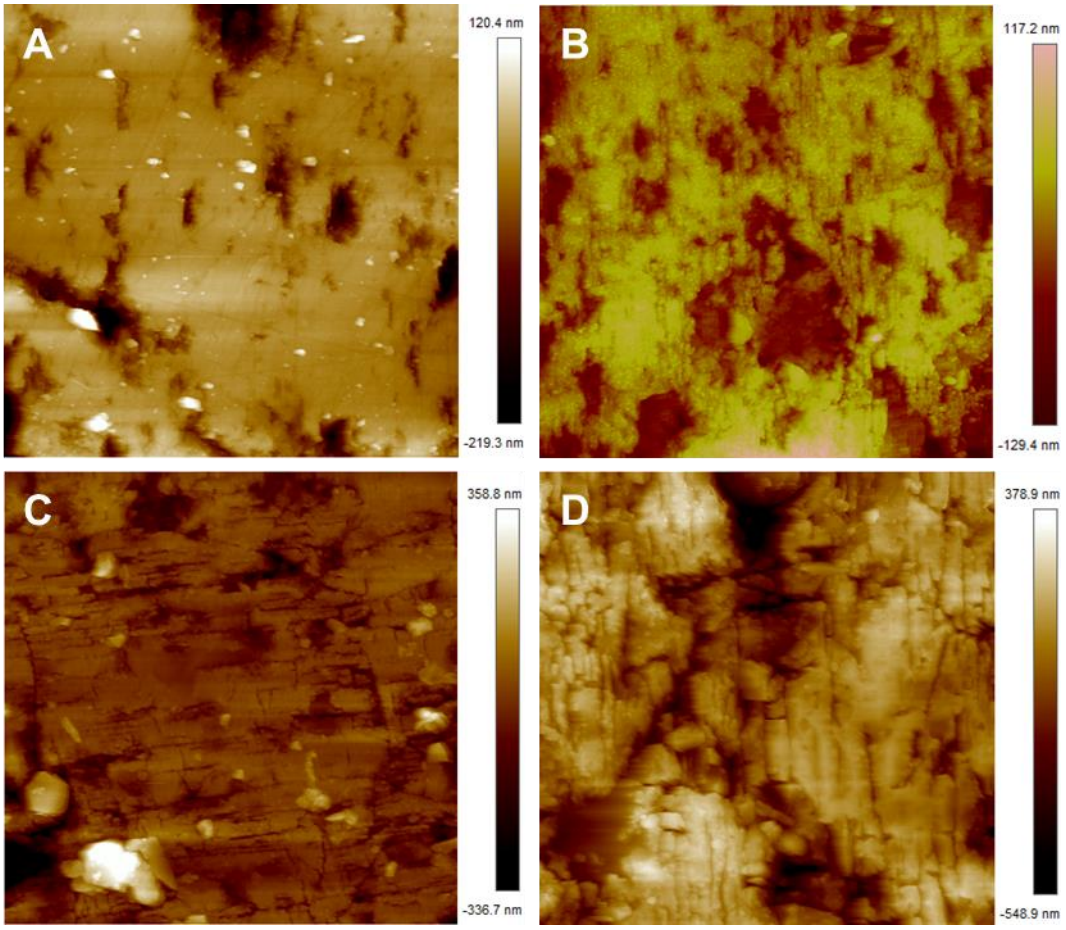

Figure 7.84: 10 x 10 µm AFM height images of pyrite exposed to *A. brierleyi* for 2 h (A); 24 h (B); 72 h (C); 168 h (D).

The roughness of the pyrite surface exposed to *A. brierleyi* and DSMny medium as calculated by Ra and Rq are shown in Figure 7.85, with the error bars representing the 95% confidence interval. The two different methods used to calculate the average roughness of the pyrite surface was described in Chapter 3, section 3.10.2.

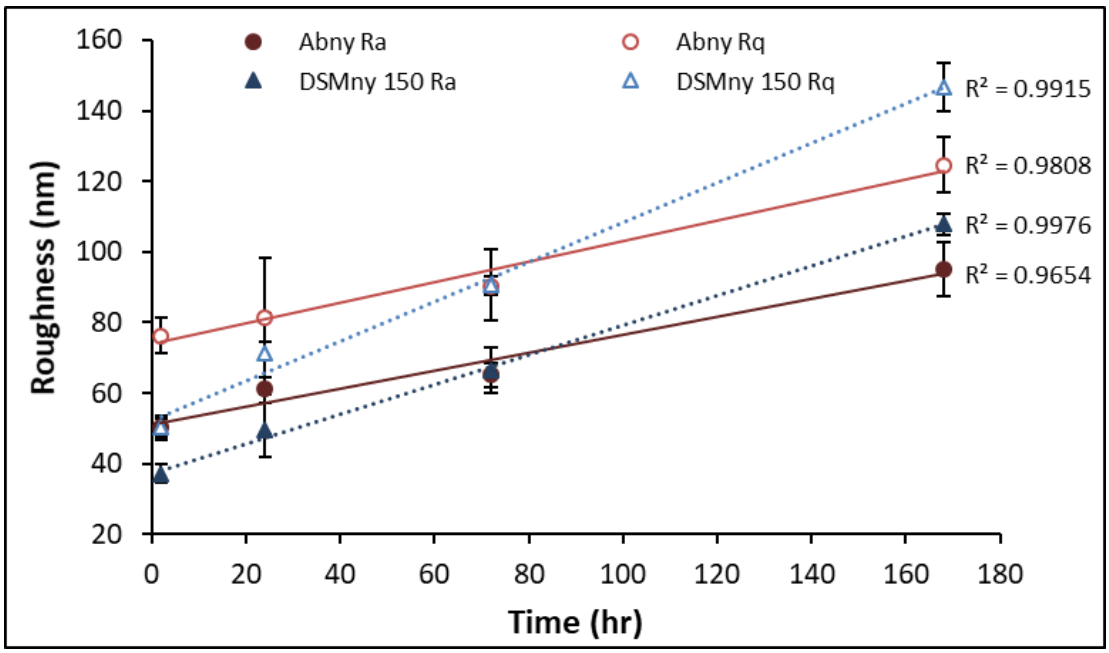

Figure 7.85: The roughness of pyrite exposed to *A. brierleyi* as calculated by Ra (●) and Rq (○), and DSMny 150 medium as calculated by Ra (▲) and Rq (Δ).

As can be seen in the results presented above, the roughness of pyrite exposed to DSMny 150 medium increases linearly over 168 h. Both the Ra and Rq values of the pyrite surfaces show the same trend, with correlation coefficients of 0.9976 and 0.9915, respectively. The roughness of pyrite samples exposed to *A. brierleyi* also display a linear increase in surface roughness over 168 h. Both the Ra and Rq values of the pyrite surfaces showing the same trend, with correlation coefficients of 0.9654 and 0.9808, respectively. Initially, the surface of pyrite exposed to *A. brierleyi* was found to be rougher than the surface of pyrite exposed to DSMny 150 medium, with the measured surface roughness converging over 72 h. As has been previously discussed (Chapter 4, section 4.3.3), it can safely be assumed that the roughness of bare polished pyrite is statistically insignificant from the roughness of pyrite exposed to the mesophiles and abiotic HH medium for 2 h, which coincides with the roughness of pyrite exposed to DSMny 150 medium at the same period. After 168 h, the surface of the pyrite exposed to DSMny 150 medium was slightly rougher than the pyrite exposed to *A. brierleyi*. The initial increase in roughness of pyrite exposed the culture may be due to the accelerated leaching observed in thermophilic cultures caused by increased temperature [11, 21, 24, 37]. This agrees with the SEM results, which show increasingly large etch pits on the pyrite surfaces exposed to *A. brierleyi* and to DSMny 150 medium solution as periods of exposure increase.

Previous studies have not yet investigated this strain of archaea using AFM, however, this technique has been applied to other bioleaching microorganisms, as have been discussed in chapters 3 and 4.

Such studies have investigated preference of cells for specific locations on pyrite surfaces [38-41], cell adhesion onto sulfide mineral surfaces [42, 43], and cell morphology [44-46].

As was the case with *A. brierleyi* grown with yeast extract, these observations of the nature of the mineral surface must be compared to the measured hydrophobicity of the sample, to fully understand how *A. brierleyi* impacts the mineral surface in terms of its ability to depress or float pyrite without the influence of yeast extract in the medium solution.

7.3.3.1 Comparison to A. brierleyi *Enhanced with Yeast Extract*

The pyrite exposed to *A. brierleyi* in DSMny 150 medium is consistently rougher than culture with yeast extract in the medium. After 72 h of exposure, the roughness of the pyrite exposed to DSMny medium is greater than that of pyrite exposed to *A. brierleyi* in DSM 150 medium. The pyrite exposed to DSM 150 and DSMny 150 media are very similar at 2 h of exposure, but longer periods of exposure result in pyrite exposed to DSMny 150 medium being rougher than that measured for the DSM 150 medium. This suggests that the yeast extract is impacting the leaching of the surface when present in the medium solution, with the roughness significantly reduced compared to both *A. brierleyi* grown in DSM 150 medium, and the DSM 150 medium control.

7.3.4 Captive Bubble Contact Angle

The results of the previous chapter suggested the presence of yeast extract in the medium may be impacting both the surface wettability of pyrite and the activity of the *A. brierleyi* when presented with the pyrite surface. Captive bubble contact angle enables the measurement of the pyrite surface hydrophobicity of samples exposed to *A. brierleyi* in the absence of this potential contaminant, isolating the impact of this archaea and its excretions on the hydrophobicity. Figure 7.86 shows the average advancing and receding contact angles of every individual angle measured, with the error bars representing the standard deviation of those measurements.

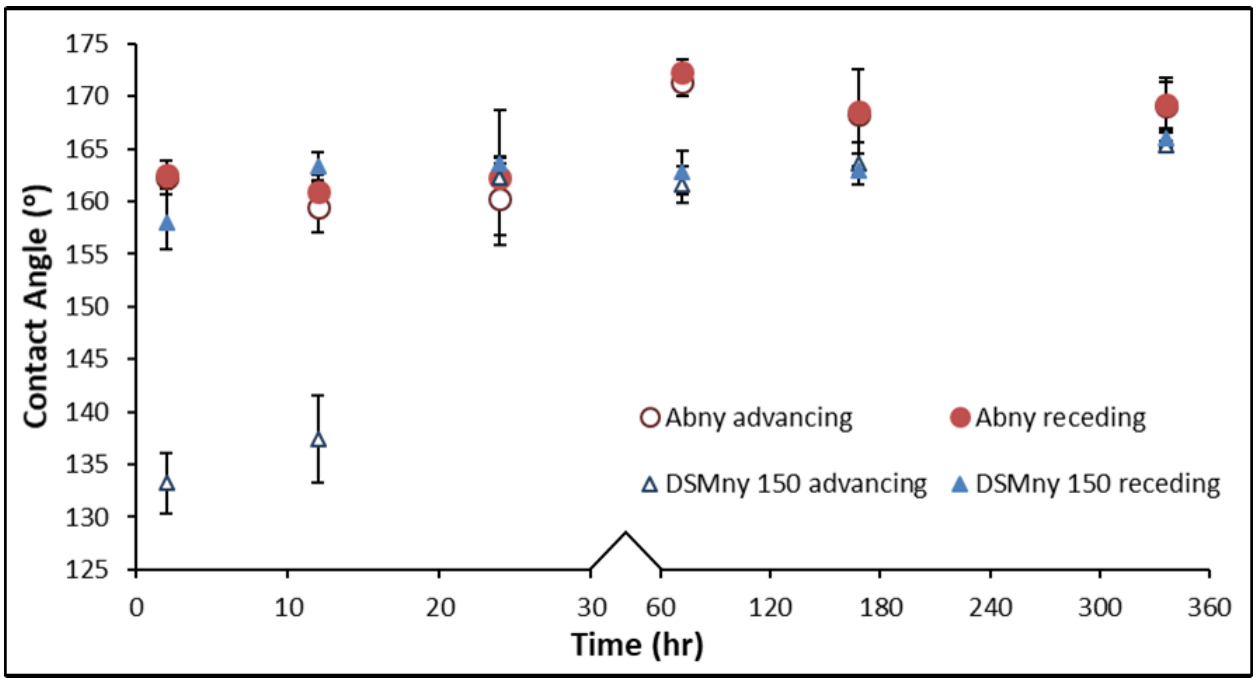

Figure 7.86: Advancing captive bubble contact angle of pyrite exposed to *A. brierleyi* (○) and DSMny 150 medium (∆). Receding captive bubble contact angle of pyrite exposed to *A. brierleyi* (●) and DSMny 150 medium (▲). Error bars represent sample standard deviation.

The surface of the pyrite exposed to *A. brierleyi* displayed greater heterogeneity compared to the surface exposed to DSMny 150 medium in the early stages of exposure (2-12 h), where there is up to 24° difference in advancing and receding angle values. By 24 h, there is no difference in the hydrophobicity of pyrite exposed to culture or DSMny 150 medium, with the hydrophobicity of the pyrite exposed to the medium remaining constant for the remainder of the exposure. After 72 h, it appears that *A. brierleyi* causes a significant decrease in hydrophobicity to the pyrite of nearly 10° compared to DSMny 150 medium. The hydrophobicity of the pyrite exposed to *A. brierleyi* increases by 168 h, remaining only slightly less hydrophobic than pyrite exposed to DSMny 150 medium for the remainder of the exposure. Depending on the particle size of minerals used in a flotation system, a difference in measured contact angle of just 3° may suggest an improvement of up to 18% in mineral recovery [47]. These results suggest that an exposure of either 2 h or 72 h could promote the depression of pyrite by *A. brierleyi* by a significant percentage, depending on particle size.

The SEM results have shown a lack of cell adhesion to the pyrite surface, and little relation with changes in surface roughness to the contact angles measured here, although both the DSMny 150 medium and the *A. brierleyi* are impacting the pyrite surface hydrophobicity. These results suggest that in the absence of yeast extract, the *A. brierleyi* may be producing EPS components that alter mineral hydrophobicity over short periods of time via the indirect contact mechanism, potentially in combination with the indirect mechanism. To separate the physical changes on the surface from

potential chemical effects, and to isolate the impact of yeast extract identified in the previous chapter (Chapter 6), surface chemical analysis must be performed on the pyrite surface. This chemical analysis will be explored using ToF-SIMS in section 7.3.5.

7.3.4.1 Comparison to A. brierleyi *Enhanced with Yeast Extract*

The pyrite exposed to DSM 150 medium appears has greater wettability than the pyrite exposed to DSMny medium for 2 h by up to 22° (advancing angle), with samples appearing similar in contact angle from 72 h. Pyrite exposed to DSMny 150 medium are also more heterogeneous in early stages of exposure (≤ 24 h) than samples exposed to DSM 150 medium. The pyrite exposed to *A. brierleyi* grown in DSMny 150 medium has greater wettability by approximately 3° compared to pyrite exposed to *A. brierleyi* in DSM 150 medium after 2 h. The difference becomes even greater between 72 to 336 h, with pyrite exposed to *A. brierleyi* in DSMny 150 medium improving pyrite wettability by 2°-5.9° compared to culture in DSM 150 medium.

These results suggest that the yeast extract is interacting with the surface of abiotic samples early in the exposure, increasing the hydrophobicity of the samples at short exposure times (≤ 24 h). The yeast extract is also altering the surface of the mineral when being utilized by *A. brierleyi* as a nutrient source, causing a loss of potential improvement to mineral wettability essential for bioflotation purposes by decreasing pyrite hydrophobicity relative to culture exposures. This is further evidence that the presence of yeast extract may be masking the presence of potential EPS produced by *A. brierleyi* acting on the surface, suggesting this archaeon may interact with the mineral surface by the indirect and/or indirect contact mechanisms.

7.3.5 Time of Flight – Secondary Ion Mass Spectrometry

Figure 7.87 shows the positive ions on the surface of pyrite exposed to *A. brierleyi* and DSMny 150 medium for 2, 24, 72 and 168 h. The ToF-SIMS analysis of bare polished pyrite was discussed in Chapter 4, section 4.3.6; briefly, the positive ion spectra were dominated by Fe^{+}, with very low proportions of carbonaceous fragments, while the negative ion fragments indicated surface oxidation through exposure to the atmosphere. Negligible amounts of large molecular weight fragments were detected.

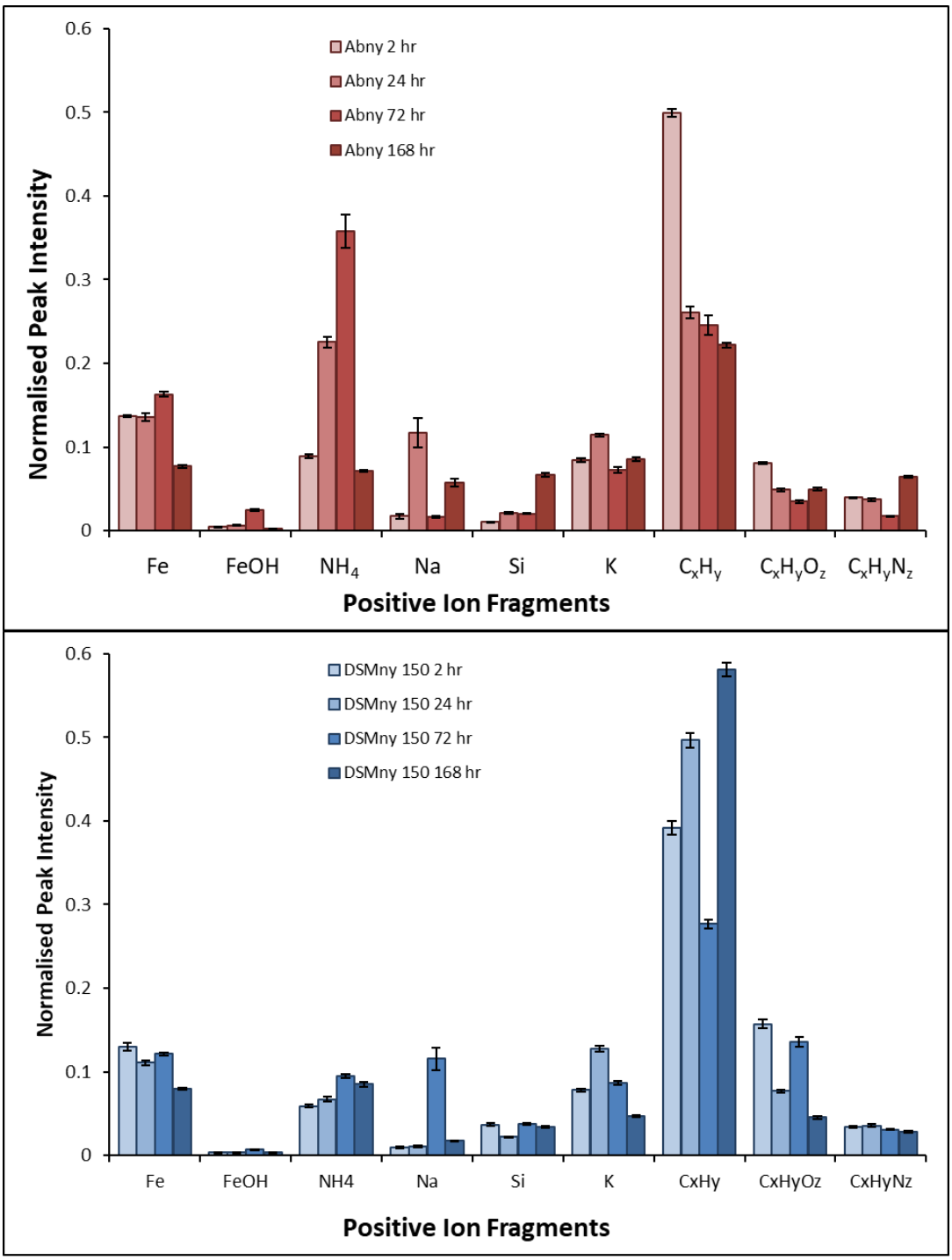

Figure 7.87: Average normalised peak intensities of positive fragments of pyrite exposed *A. brierleyi* (top) for 2, 24, 72 and 168 h, and pyrite exposed to DSMny 150 medium (bottom) for 2, 24, 72 and 168 h.

The fragment profiles of pyrite exposed to *A. brierleyi* are dominated by short chain $C_xH_y^+$ ($x \leq 6$) fragments early on in the exposure. The $C_xH_yO_z^+$ ($x \leq 4$, $z \leq 2$) and $C_xH_yN_z^+$ ($x \leq 5$, $z \leq 2$) fragments decrease in proportion over the first 72 h of exposure, before increasing after 168 h. The proportion of the $C_xH_yO_z^+$ and $C_xH_yN_z^+$ fragments were consistently lower than that of elemental ions detected. The proportion of Fe^+ detected was consistent over the first 72 h of exposure, decreasing after 168 h. This suggests that the pyrite surface is coated with secondary mineral formations and

proteinaceous material after 168 h of exposure to *A. brierleyi*. The proportion of Si^+ remains low over the course of exposure to 72 h, increasing in after 168 h. Some silicate inclusions are expected, as was suggested by the EDX data in Chapter 6, section 6.3.2. The proportions of Na^+, K^+ and NH_4^+ are variable over the course of exposure, with Na^+ and K^+ following the same trend. This could be due to jarosite formations, as was seen in the SEM and EDX, or medium salt precipitates, and coincides with the increase in inorganic debris on the surface observed in the SEM results. Because DSMny 150 medium contains ammonium sulfate, the NH_4^+ fragment can be expected on the surface, and therefore is not on its own a reliable indicator of whether proteins are present on the surface. The $FeOH^+$ fragment remains low in proportion on the surface over the course of the exposure.

The fragment profiles of pyrite exposed to DSM 150 medium is dominated by $C_xH_y^+$ fragments across all periods of exposure. The proportions of $C_xH_yO_z^+$ fragments are variable across the exposure and high in proportion compared to pyrite exposed to *A. brierleyi*, while $C_xH_yN_z^+$ remains consistent over the course of exposure. This suggests little EPS production by *A. brierleyi* is occurring, with no significant increase in organic material on the pyrite surface compared with the control. The lack of significant organic fragments indicates that the mechanism through which *A. brierleyi* interacts with pyrite is likely to be the indirect mechanism, with little to no impact through the indirect contact mechanism. The proportion of Fe^+ decreases over the course of exposure, however it remains the third most frequently occurring fragment at each period, suggesting that the pyrite surface remains rich in iron for the duration. The frequency of the NH_4^+ fragment remains consistent over the first 72 h, increasing after 168 h of exposure, while K^+ varies greatly over the course of exposure. This suggests medium salt precipitates are forming heterogeneously on the surface. The proportions of Si^+ and $FeOH^+$ remain low over the course of exposure, indicating the presence of some silicate inclusions and potential secondary mineral precipitates on the surface. The silicate inclusions and jarosites are expected, as indicated by the EDX data (section 7.3.2). The Na^+ remains in low proportion on the surface for every period of exposure except 72 h, with the larger associated error indicating uneven distribution over the surface that may cause this fragment to be over-represented on this sample.

Figure 7.88 shows the complementary negative fragments and elements of interest and significance collected by ToF-SIMS on pyrite exposed to *A. brierleyi* and DSMny 150 medium for 2, 24, 72 and 168 h. The fragment profiles of pyrite exposed to *A. brierleyi* show oxygenated sulfur fragments occur with greater frequency on the surface than the polysulfide fragments for all periods of exposure. Every sample is dominated by the O^- ion, except for the sample exposed to *A. brierleyi* for 24 h, where Cl^- ion is the most frequently occurring and O^- is the second most frequent. This

corresponds to high proportions of K^+ measured in the positive ion spectra, suggesting the precipitation of the medium salt potassium chloride (KCl) on the surface, which occurs to greater or lesser extent on all samples. The OH^- fragment is consistently the second or third most frequently occurring fragment over the course of exposure, while the proportion of S^- and SH^- increases from 2 to 24 h, decreases from 24 to 72 h, and increases again by 168 h [48]. These changes correspond with the contact angle results, which suggest the surface is hydrophilic, with little difference in the first 24 h, and least hydrophobic after 72 h exposure.

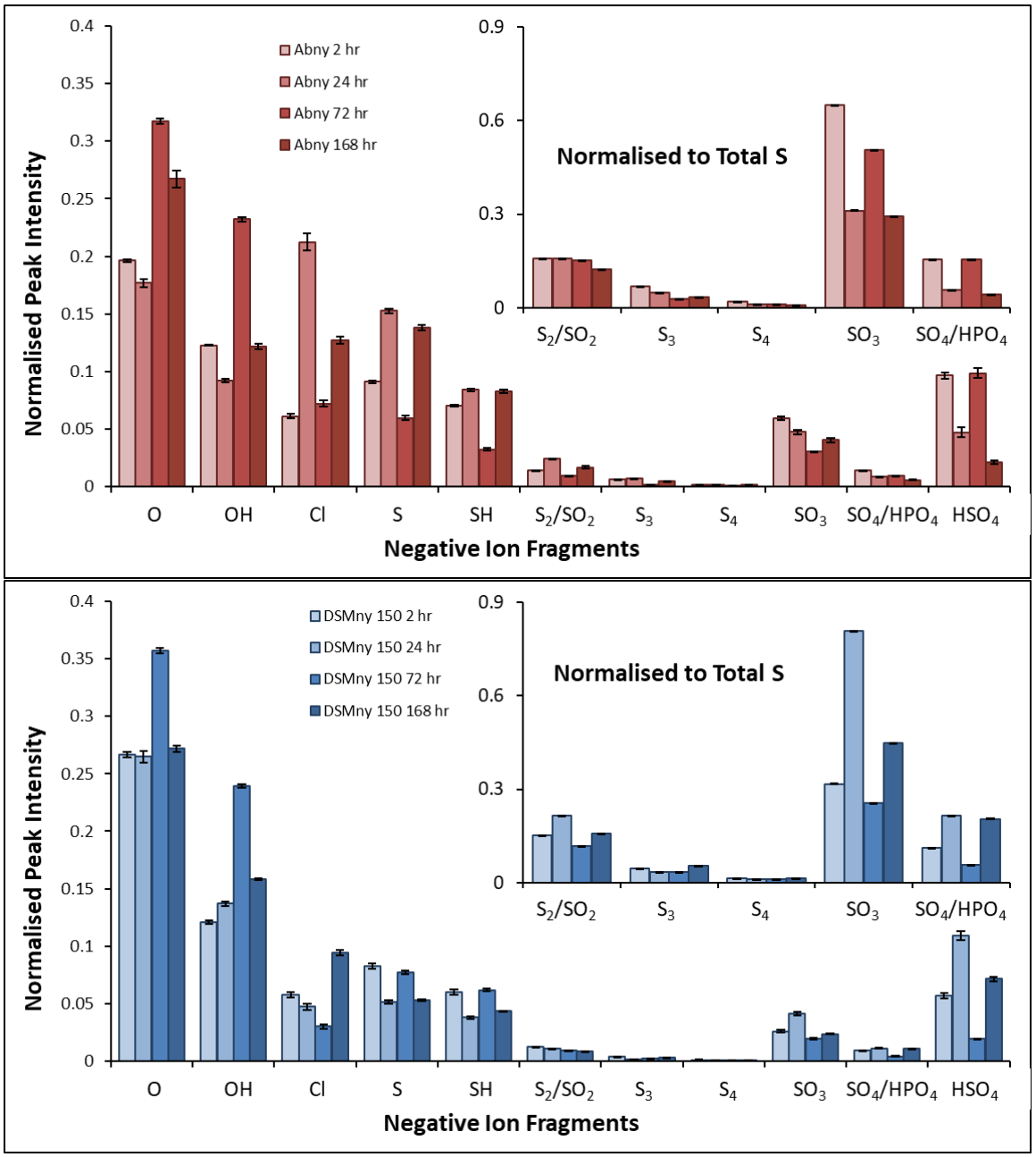

Figure 7.88: Average normalised peak intensities of negative fragments of pyrite exposed *A. brierleyi* (top) for 2, 24, 72 and 168 h, and pyrite exposed to DSMny 150 medium (bottom) for 2, 24, 72 and 168 h.

The fragments detected on pyrite after exposure to DSMny 150 medium are dominated by the O^- and OH^- fragments for every period of exposure. The proportion of S^- and SH^- appears to decrease over the course of exposure. For all periods of exposure, oxygenated sulfur species such as SO_3^- and SO_4^- are in greater proportion on the surface than polysulfide species such as S_3^- and S_4^-, shown inset in Figure 7.88(bottom). The proportion of Cl^- increases over the course of exposure, suggesting the precipitation of medium salts accumulating on the surface as exposure time increases. These results suggest that the surface is heavily oxidised even at early periods of exposure of the pyrite to DSMny 150 medium. The higher proportions of oxygen containing species on the surface are contributing to the decrease in hydrophobicity of the surface, which agrees with the captive bubble contact angle results that suggest the pyrite exposed to the DSMny medium is similar in hydrophobicity to pyrite exposed to *A. brierleyi* for the majority of the exposure.

Figure 7.89 shows the large molecular mass positive fragments collected by ToF-SIMS on pyrite exposed to *A. brierleyi* and DSMny 150 medium for 2, 24, 72 and 168 h. Compared to the large molecular weight fragment patterns obtained from pyrite exposed to the mesophilic cultures in Chapters 4 and 5, there appears to be a much lower proportion of large molecular weight fragments across all periods of exposure. The fragments examined here are identical to those shown in the previous chapter, with details of proposed peak identities discussed in Chapter 6, section 6.3.5.

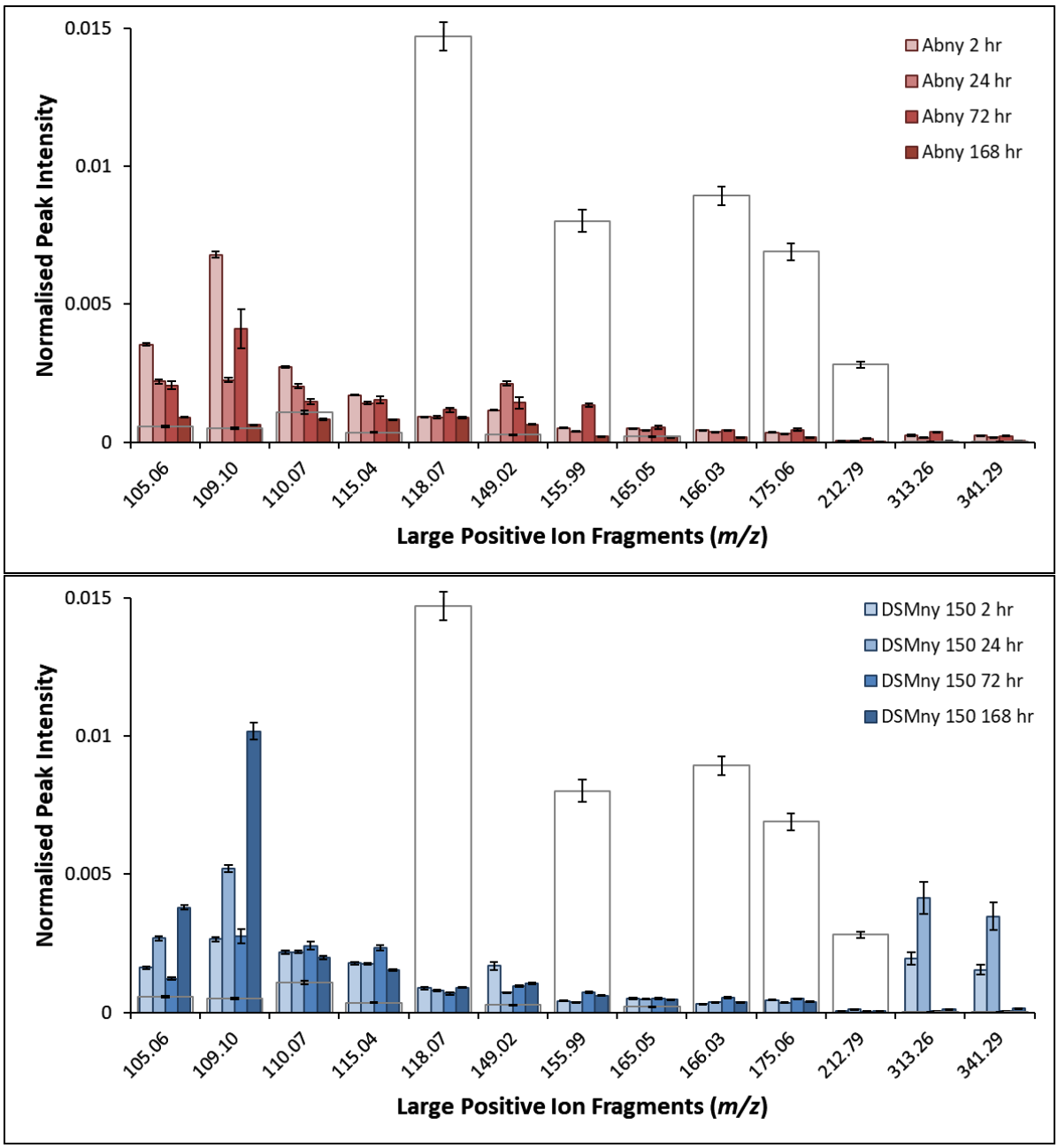

Figure 7.89: Average normalised peak intensities of large molecular weight positive fragments of pyrite exposed *A. brierleyi* (top) for 2, 24, 72 and 168 h, and pyrite exposed to DSMny 150 medium (bottom) for 2, 24, 72 and 168 h, and yeast extract (outline).

The proportion of large molecular weight fragments detected on the pyrite surface after exposure to *A. brierleyi* is very low, with the fragments that also appear in the spectra of yeast extract occurring less frequently. Most noticeable are the fragments at *m/z* 118.07, 165.05, 166.03, 175.06, and 212.79, which are very low in proportion on the surface. The fragments at *m/z* 105.06, 109.10 and 115.04 appear to be higher in proportion on the surface early in the exposure, although they decrease in frequency over the course of exposure. These fragments have been previously identified as carbohydrate or lipid fragments, with the exception of *m/z* 109.1 and 212.79, which were unable to be identified [49-57]. These results suggest *A. brierleyi* is a low EPS producer compared to the

mesophilic cultures investigated in chapters 4 and 5, which produce larger quantities of EPS in early stages of exposure to mineral.

The large molecular weight fragments detected on the pyrite surface after exposure to DSMny 150 medium are also occurring with low frequency. The most noticeable decreases in proportion occurred in fragments *m/z* 110.07, 118.07, 165.05, 166.03, 175.06, 212.79, suggesting these fragments were likely due to yeast extract proteins and carbohydrates [49-60]. The fragments *m/z* 313.26 and 341.29 occur in higher proportions early in the exposure (2 and 24 h), which have been identified as major components of several lipid and fatty acid structures [49, 52, 55, 56, 61].

Previous studies of pyrite surfaces using ToF-SIMS were focused mainly on identifying pyrite particles within a mixture of sulfide minerals, and focussed mainly on the ions associated with the pyrite surface and ions of interest to flotation. These were discussed in detail in Chapter 4, section 4.3.6. Previous studies that have utilised ToF-SIMS for the investigation of various microorganisms and their excretions were discussed in the previous chapter [44, 50, 51, 58, 62, 63]. These findings agree that the most sulfur rich sample, pyrite exposed to DSMny 150 medium for 2 h, is also the most hydrophobic sample. The presence of the yeast extract in the medium is altering the surface species present on the pyrite, and as such is impacting the wettability of the pyrite.

7.3.5.1 Comparison to A. brierleyi *Enhanced with Yeast Extract*

As was observed in the previous chapter (Chapter 6), the presence of yeast extract in the medium is causing organic carbon contamination of the pyrite surface, making it impossible to determine the impact of *A. brierleyi* and potential EPS on the pyrite surface. The chemical analysis of pyrite exposed to both the DSMny 150 medium and *A. brierleyi* is crucial for separating the action of yeast extract from the action of the cells.

The pyrite exposed to DSM 150 medium had a higher proportion of K^+ and $C_xH_yN_z^+$ fragments (Chapter 6, section 6.3.5) compared to the fragments detected on pyrite exposed to DSMny 150 medium. Sulfur species, especially polysulfides, are in higher proportion on the surface of pyrite exposed to DSMny 150 medium compared to DSM 150 medium, where polysulfides are almost non-existent. This suggests the removal of yeast extract from the medium, which was shown to impact the cell activity (section 7.3.1), may negatively impact the ability of cells to utilise pyrite as a nutrient source over this time frame.

Compared to the pyrite exposed to *A. brierleyi* grown in DSM 150 medium, pyrite exposed to DSMny 150 medium shows a much lower proportion of $C_xH_yN_z^+$ fragments and a much higher proportion of Fe^+ on the surface. This suggests that protein or amino acid-type fragments are more

prolific on the surface of pyrite exposed to medium or culture when yeast extract is present. This is likely due to the yeast extract in the medium, the composition of which is mostly peptides and amino acids (Chapter 3, section 3.1). After 72 h of exposure, the proportions of oxygenated species on the surface of pyrite (SO_3^-, SO_4^-, etc.) are significantly greater in pyrite exposed to *A. brierleyi* in DSMny 150 medium, agreeing with the lowest measured hydrophobicity at this period of exposure.

There are significantly lower proportions of many high molecular weight fragments on pyrite exposed to both culture and medium in the absence of yeast extract compared to the results presented in the previous chapter. Most noticeable among these fragments is the *m/z* 110.07 histidine fragment. This indicates there is indeed contamination of the surface in both biotic and abiotic samples by components of yeast extract on the surface, and that *A. brierleyi* does not appear to be a producer of significant amounts of EPS. This agrees with the SEM results, which showed little to no attachment of *A. brierleyi* cells on the surface, regardless of the presence of yeast extract in the medium. The results observed here confirm the conclusions of the previous chapter, that yeast extract is acting on the surface and changing the behaviour of *A. brierleyi* upon exposure to pyrite.

7.4 Conclusions

It was observed using SEM that very little attachment of *A. brierleyi* cells occurs over the period of 168 h of exposure to pyrite, and the few cells that were observed on the surface showed no preference for surface defects. Leaching of the pyrite surface appeared to be enhanced by the presence of the archaea in solution in the early stages of exposure (2 to 24 h), with little quantifiable difference in roughness for longer periods of exposure, as measured by AFM. The period at which there was the smallest difference in roughness between the control and the pyrite exposed to *A. brierleyi*, was also the period at which the contact angle results suggest pyrite exposed to cells is the least hydrophobic, around 72 h. ToF-SIMS confirmed the chemical species on the surface exposed to *A. brierleyi* had the highest proportion of hydrophilic species on the surface at this period, including oxygenated sulfur fragments.

These observations suggest that *A. brierleyi* is unlikely to alter the surface through direct attack, with little to no cell attachment observed that might contribute to the alteration of the pyrite surface. This suggests *A. brierleyi* interacts with the surface through the indirect mechanism, as there is little evidence of the EPS production that is required for the indirect contact mechanism. Although the production of EPS is significantly lower than the mesophilic bacteria explored in previous chapters, *A. brierleyi* is still suitable for bioflotation applications over shorter exposure periods due to the

accelerated oxidation of the surface and its tolerance of higher temperatures (60 °C) that are likely to be found in industrial applications. The conflation of the effects of yeast extract on the system, however, is an important consideration for studies that intend to apply this organism to the processing of minerals, as it has been established in this investigation that there is significant impact of this nutrient on the surface.

7.5 References

1. Bharadwaj, A., Ting, Y.-P., *Bioleaching of spent hydrotreating catalyst by acidophilic thermophile Acidianus brierleyi: Leaching mechanism and effect of decoking.* Bioresource Technology, 2013. **130**(0): p. 673-680.
2. Gerayeli, F., Ghojavand, F., Mousavi, S. M., Yaghmaei, S., Amiri, F., *Screening and optimization of effective parameters in biological extraction of heavy metals from refinery spent catalysts using a thermophilic bacterium.* Separation and Purification Technology, 2013. **118**: p. 151-161.
3. Sasaki, K., Takatsugi, K., Hirajima, T., *Effects of initial Fe2+ concentration and pulp density on the bioleaching of Cu from enargite by Acidianus brierleyi.* Hydrometallurgy, 2011. **109**(1–2): p. 153-160.
4. Takatsugi, K., Sasaki, K., Hirajima, T., *Mechanism of the enhancement of bioleaching of copper from enargite by thermophilic iron-oxidizing archaea with the concomitant precipitation of arsenic.* Hydrometallurgy, 2011. **109**(1–2): p. 90-96.
5. Rastegar, S.O., Mousavi, S. M., Rezaei, M., Shojaosadati, S. A., *Statistical evaluation and optimization of effective parameters in bioleaching of metals from molybdenite concentrate using Acidianus brierleyi.* Journal of Industrial and Engineering Chemistry, 2014. **20**(5): p. 3096-3101.
6. Konishi, Y., Kogasaki, K., Asai, S., *Bioleaching of pyrite by Acidianus brierleyi in a continuous-flow stirred-tank reactor.* Chemical Engineering Science, 1997. **52**(24): p. 4525-4532.
7. Konishi, Y., Asai, S., Tokushige, M., Suzuki, T., *Kinetics of the bioleaching of chalcopyrite concentrate by acidophilic thermophile acidianus brierleyi.* Biotechnol Prog, 1999. **15**(4): p. 681-8.
8. Konishi, Y., Tokushige, M., Asai, S., Suzuki, T., *Copper recovery from chalcopyrite concentrate by acidophilic thermophile Acidianus brierleyi in batch and continuous-flow stirred tank reactors.* Hydrometallurgy, 2001. **59**(2–3): p. 271-282.
9. Meng, C., Shi, X., Lin, H. , Chen, J., Guo, Y., *UV induced mutations in Acidianus brierleyi growing in a continuous stirred tank reactor generated a strain with improved bioleaching capabilities.* Enzyme and Microbial Technology, 2007. **40**(5): p. 1136-1140.
10. Zhu, W., Xia, J.-L., Yang, Y., Nie, Z.-Y., Zheng, L., Ma, C.-Y., Zhang, R.-Y., Peng, A.-A., Tang, L., Qiu, G.-Z., *Sulfur oxidation activities of pure and mixed thermophiles and sulfur speciation in bioleaching of chalcopyrite.* Bioresource Technology, 2011. **102**(4): p. 3877-3882.
11. Zhu, W., Xia, J.-L., Peng, A.-A., Nie, Z.-Y., Qiu, G,-Z., *Characterization of apparent sulfur oxidation activity of thermophilic archaea in bioleaching of chalcopyrite.* Transactions of Nonferrous Metals Society of China, 2013. **23**(8): p. 2383-2388.
12. Brierley, J.A., *A perspective on developments in biohydrometallurgy*. Hydrometallurgy, 2008. **94**(1–4): p. 2-7.
13. Watling, H.R., *The bioleaching of sulphide minerals with emphasis on copper sulphides — A review*. Hydrometallurgy, 2006. **84**(1–2): p. 81-108.

14. Mikkelsen, D., Kappler, U., Webb, R. I., Rasch, R., McEwan, A. G., Sly, L. I., *Visualisation of pyrite leaching by selected thermophilic archaea: Nature of microorganism–ore interactions during bioleaching.* Hydrometallurgy, 2007. **88**(1–4): p. 143-153.
15. Govender, Y., Gericke, M,, *Extracellular polymeric substances (EPS) from bioleaching systems and its application in bioflotation.* Minerals Engineering, 2011. **24**(11): p. 1122-1127.
16. Shiers, D.W., Ralph, D. E., Watling, H. R., *A comparative study of substrate utilisation by Sulfobacillus species in mixed ferrous ion and tetrathionate growth medium.* Hydrometallurgy, 2010. **104**(3–4): p. 363-369.
17. Franzmann, P.D., Haddad, C. M., Hawkes, R. B., Robertson, W. J., Plumb, J. J., *Effects of temperature on the rates of iron and sulfur oxidation by selected bioleaching Bacteria and Archaea: Application of the Ratkowsky equation.* Minerals Engineering, 2005. **18**(13–14): p. 1304-1314.
18. Norris, P.R., Burton, N. P., Clark, D. A., *Mineral sulfide concentrate leaching in high temperature bioreactors.* Minerals Engineering, 2013. **48**(0): p. 10-19.
19. Nemati, M., Harrison, S. T. L., *A comparative study on thermophilic and mesophilic biooxidation of ferrous iron.* Minerals Engineering, 2000. **13**(1): p. 19-24.
20. Konishi, Y., Nishimura, H., Asai, S., *Bioleaching of sphalerite by the acidophilic thermophile Acidianus brierleyi.* Hydrometallurgy, 1998. **47**(2–3): p. 339-352.
21. Deveci, H., Akcil, A., Alp, I., *Bioleaching of complex zinc sulphides using mesophilic and thermophilic bacteria: comparative importance of pH and iron.* Hydrometallurgy, 2004. **73**(3–4): p. 293-303.
22. Larsson, L., Olsson, G., Hoist, O., Karlsson, H. T., *Oxidation of pyrite by Acidianus brierleyi: Importance of close contact between the pyrite and the microorganisms.* Biotechnology Letters, 1993. **15**(1): p. 99-104.
23. Konishi, Y., Matsui, M., Fujiwara, H., Nomura, T., Nakahara, K., *Zinc Leaching from Fly Ash in Municipal Waste Incineration by Thermophilic Archaean Acidianus brierleyi Growing on Elemental Sulfur.* Separation Science and Technology, 2003. **38**(16): p. 4117-4130.
24. Deveci, H., Jordan, M. A., Powell, N., Alp, I., *Effect of salinity and acidity on bioleaching activity of mesophilic and extremely thermophilic bacteria.* Transactions of Nonferrous Metals Society of China, 2008. **18**(3): p. 714-721.
25. Dopson, M., Johnson, D. B., *Biodiversity, metabolism and applications of acidophilic sulfur-metabolizing microorganisms.* Environ Microbiol, 2012. **14**(10): p. 2620-31.
26. Sharma, P.K., Das, A., Hanumantha Rao, K., Forssberg, K. S. E., *Surface characterization of Acidithiobacillus ferrooxidans cells grown under different conditions.* Hydrometallurgy, 2003. **71**(1–2): p. 285-292.
27. Ralston, J., *Eh and its consequences in sulphide mineral flotation.* Minerals Engineering, 1991. **4**(7): p. 859-878.
28. Jordan, M.A., Barr, D. W., Phillips, C. V., *Iron and sulphur speciation and cell surface hydrophobicity during bacterial oxidation of a complex copper concentrate.* Minerals Engineering, 1993. **6**(8–10): p. 1001-1011.
29. Xia, J.-L., Yang, Y., He, H., Zhao, X.-J., Liang, C.-L., Zheng, L., Ma, C.-Y., Zhao, Y.-D., Nie, Z.-Y., Qiu, G.-Z., *Surface analysis of sulfur speciation on pyrite bioleached by extreme thermophile Acidianus manzaensis using Raman and XANES spectroscopy.* Hydrometallurgy, 2010. **100**(3–4): p. 129-135.
30. Microanalysis, C.F.f.A.M.a. *Introduction to Energy Dispersive X-ray Spectrometry (EDS).* 2015 [cited 2017; Available from: http://cfamm.ucr.edu/manuals.html.
31. Watling, H.R., Perrot, F. A., Shiers, D. W., *Comparison of selected characteristics of Sulfobacillus species and review of their occurrence in acidic and bioleaching environments.* Hydrometallurgy, 2008. **93**(1–2): p. 57-65.

32. Segerer, A., Neuner, A., Kristjansson, J. K., Stetter, K. O., *Acidianus infernus gen. nov., sp. nov., and Acidianus brierleyi comb. nov.: Facultatively Aerobic, Extremely Acidophilic Thermophilic Sulfur-Metabolizing Archaebacteria.* International Journal of Systematic Bacteriology, 1986. **36**(4): p. 559-564.
33. Liu, H., Gu, G., Xu, Y., *Surface properties of pyrite in the course of bioleaching by pure culture of Acidithiobacillus ferrooxidans and a mixed culture of Acidithiobacillus ferrooxidans and Acidithiobacillus thiooxidans.* Hydrometallurgy, 2011. **108**(1–2): p. 143-148.
34. Ndlovu, S., Monhemius, A. J., *The influence of crystal orientation on the bacterial dissolution of pyrite.* Hydrometallurgy, 2005. **78**(3): p. 187-197.
35. Karavaiko, G.I., Smolskaja, L. S., Golyshina, O. K., Jagovkina, M. A., Egorova, E. Y., *Bacterial pyrite oxidation: Influence of morphological, physical and chemical properties.* Fuel Processing Technology, 1994. **40**(2): p. 151-165.
36. Tan, S.N., Chen, M., *Early stage adsorption behaviour of Acidithiobacillus ferrooxidans on minerals I: An experimental approach.* Hydrometallurgy, 2012. **119–120**(0): p. 87-94.
37. Duarte, J.C., Estrada, P. C., Pereira, P. C., Beaumont, H. P., *Thermophilic vs. mesophilic bioleaching process performance.* FEMS Microbiology Reviews, 1993. **11**(1–3): p. 97-102.
38. Mangold, S., Laxander, M., Harneit, K., Rohwerder, T. , Claus, G., Sand, W., *Visualization of Acidithiobacillus ferrooxidans biofilms on pyrite by atomic force and epifluorescence microscopy under various experimental conditions.* Hydrometallurgy, 2008. **94**(1–4): p. 127-132.
39. Gehrke, T., Telegdi, J., Thierry, D., Sand, W., *Importance of Extracellular Polymeric Substances from Thiobacillus ferrooxidans for Bioleaching.* Appl Environ Microbiol, 1998. **64**(7): p. 2743-7.
40. Sand, W., Gehrke, T., Jozsa, P.-G., Schippers, A., *(Bio)chemistry of bacterial leaching—direct vs. indirect bioleaching.* Hydrometallurgy, 2001. **59**(2): p. 159-175.
41. Rohwerder, T., Sand, W., *Mechanisms and biochemical fundamentals of bacterial metal sulfide oxidation,* in *Microbial Processing of Metal Sulfides*, E.R.D.a.W. Sand, Editor. 2007 Springer. p. 35-58.
42. Diao, M., Nguyen, T. A. H., Taran, E., Mahler, S., Nguyen, A. V., *Differences in adhesion of A. thiooxidans and A. ferrooxidans on chalcopyrite as revealed by atomic force microscopy with bacterial probes.* Minerals Engineering, 2014. **61**(0): p. 9-15.
43. Zhu, J., Li, Q., Jiao, W., Jiang, H., Sand, W., Xia, J., Liu, X., Qin, W., Qiu, G., Hu, Y., Chai, L., *Adhesion forces between cells of Acidithiobacillus ferrooxidans, Acidithiobacillus thiooxidans or Leptospirillum ferrooxidans and chalcopyrite.* Colloids and Surfaces B: Biointerfaces, 2012. **94**: p. 95-100.
44. Dague, E., Delcorte, A., Latgé, J.-P., Dufrêne, Y. F., *Combined Use of Atomic Force Microscopy, X-ray Photoelectron Spectroscopy, and Secondary Ion Mass Spectrometry for Cell Surface Analysis.* Langmuir, 2008. **24**(7): p. 2955-2959.
45. Florian, B., Noël, N., Sand, W., *Visualization of initial attachment of bioleaching bacteria using combined atomic force and epifluorescence microscopy.* Minerals Engineering, 2010. **23**(6): p. 532-535.
46. Florian, B., Noël, N., Thyssen, C., Felschau, I., Sand, W., *Some quantitative data on bacterial attachment to pyrite.* Minerals Engineering, 2011. **24**(11): p. 1132-1138.
47. Chipfunhu, D., Zanin, M., Grano, S., *Flotation behaviour of fine particles with respect to contact angle.* Chemical Engineering Research and Design, 2012. **90**(1): p. 26-32.
48. Brito e Abreu, S., Brien, C., Skinner, W., *ToF-SIMS as a New Method to Determine the Contact Angle of Mineral Surfaces.* Langmuir, 2010. **26**(11): p. 8122-8130.
49. Biesinger, M.C., Miller, D. J., Harbottle, R. R., Possmayer, F., McIntyre, N. S., Petersen, N. O., *Imaging lipid distributions in model monolayers by ToF-SIMS with selectively deuterated components and principal components analysis.* Applied Surface Science, 2006. **252**(19): p. 6957-6965.

50. Berman, E.S.F., Kulp, K. S., Knize, M. G., Wu, L., Nelson, E. J., Nelson, D. O., Wu, K. J., *Distinguishing Monosaccharide Stereo- and Structural Isomers with TOF-SIMS and Multivariate Statistical Analysis.* Analytical Chemistry, 2006. **78**(18): p. 6497-6503.
51. Berman, E.S.F., Wu, L., Fortson, S. L., Kulp, K. S., Nelson, D. O., Wu, K. J., *Chemometric and statistical analyses of ToF-SIMS spectra of increasingly complex biological samples.* Surface and Interface Analysis, 2009. **41**(2): p. 97-104.
52. Belu, A.M., Davies, M. C., Newton, J. M., Patel, N., *TOF-SIMS Characterization and Imaging of Controlled-Release Drug Delivery Systems.* Analytical Chemistry, 2000. **72**(22): p. 5625-5638.
53. Urquhart, A.J., Taylor, M., Anderson, D. G., Langer, R., Davies, M. C., Alexander, M. R., *TOF-SIMS Analysis of a 576 Micropatterned Copolymer Array To Reveal Surface Moieties That Control Wettability.* Analytical Chemistry, 2008. **80**(1): p. 135-142.
54. Vaidyanathan, S., Fletcher, J. S., Jarvis, R. M., Henderson, A., Lockyer, N. P., Goodacre, R., Vickerman, J. C., *Explanatory multivariate analysis of ToF-SIMS spectra for the discrimination of bacterial isolates.* Analyst, 2009. **134**(11): p. 2352-2360.
55. Baldwin, P.M., Melia, C. D., Davies, M. C., *The Surface Chemistry of Starch Granules Studied by Time-of-Flight Secondary Ion Mass Spectrometry.* Journal of Cereal Science, 1997. **26**(3): p. 329-346.
56. Heim, C., Sjövall, P., Lausmaa, J., Leefmann, T., Thiel, V., *Spectral characterisation of eight glycerolipids and their detection in natural samples using time-of-flight secondary ion mass spectrometry.* Rapid Communications in Mass Spectrometry, 2009. **23**(17): p. 2741-2753.
57. Breitenstein, D., Rommel, C. E., Stolwijk, J., Wegener, J., Hagenhoff, B., *The chemical composition of animal cells reconstructed from 2D and 3D ToF-SIMS analysis.* Applied Surface Science, 2008. **255**(4): p. 1249-1256.
58. Vaidyanathan, S., Fletcher, J. S., Lockyer, N. P., Vickerman, J. C., *TOF-SIMS investigation of Streptomyces coelicolor, a mycelial bacterium.* Applied Surface Science, 2008. **255**(4): p. 922-925.
59. Schilke, K.F., McGuire, J., *Detection of nisin and fibrinogen adsorption on poly(ethylene oxide) coated polyurethane surfaces by time-of-flight secondary ion mass spectrometry (TOF-SIMS).* Journal of Colloid and Interface Science, 2011. **358**(1): p. 14-24.
60. Sanni, O.D., Wagner, M. S., Briggs, D., Castner, D. G., Vickerman, J. C., *Classification of adsorbed protein static ToF-SIMS spectra by principal component analysis and neural networks.* Surface and Interface Analysis, 2002. **33**(9): p. 715-728.
61. Robinson, M.A., Graham, D. J., Morrish, F., Hockenbery, D., Gamble, L. J., *Lipid analysis of eight human breast cancer cell lines with ToF-SIMS.* Biointerphases, 2016. **11**(2): p. 02A303.
62. Jungnickel, H., Jones, E. A., Lockyer, N. P., Oliver, S. G., Stephens, G. M., Vickerman, J. C., *Application of TOF-SIMS with Chemometrics To Discriminate between Four Different Yeast Strains from the Species Candida glabrata and Saccharomyces cerevisiae.* Analytical Chemistry, 2005. **77**(6): p. 1740-1745.
63. Pradier, C.M., Rubio, C., Poleunis, C., Bertrand, P., Marcus, P., Compère, C., *Surface Characterization of Three Marine Bacterial Strains by Fourier Transform IR, X-ray Photoelectron Spectroscopy, and Time-of-Flight Secondary-Ion Mass Spectrometry, Correlation with Adhesion on Stainless Steel Surfaces.* The Journal of Physical Chemistry B, 2005. **109**(19): p. 9540-9549.

8 Summary and Future Work

In this thesis, the physical and chemical alteration of pyrite by the bacteria *A. ferrooxidans* and *L. ferrooxidans* and the archaea *A. brierleyi* has been investigated to establish the role of EPS and cell attachment in the alteration of hydrophobicity of sulfide minerals. Several analytical techniques have been utilised to provide detailed descriptions of the pyrite surface, the culture solutions, and the cells of *A. ferrooxidans*, *L. ferrooxidans*, and *A. brierleyi* over different periods of exposure. These techniques include Scanning Electron Microscopy (SEM), Energy Dispersive X-ray Spectroscopy (EDX), titration, Inductively Coupled Plasma Optical Emission Spectroscopy (ICPOES), Atomic Force Microscopy (AFM), Photoelectron Emission Microscopy (PEEM), Scanning Transmission X-ray Microscopy (STXM), Near Edge Adsorption Fine Structure Spectroscopy (NEXAFS), Time of Flight – Secondary Ion Mass Spectroscopy (ToF-SIMS) and both sessile drop and captive bubble contact angle measurements.

What follows is a summary of the major findings from these experiments and the potential pathways for future work to build on the knowledge presented here.

8.1 Thesis Summary

The mechanisms through which *A. ferrooxidans*, *L. ferrooxidans* and *A. brierleyi* interact with pyrite was found to vary across strains. The results from the investigations of the mesophilic strains suggest that EPS mediates attachment of both bacteria to the surface, but that cells are not required to colonise the surface for EPS to decrease surface hydrophobicity in short periods of time. This supports the indirect contact mechanism as how initial interactions with the mineral surface are occurring. The surface studies of *A. brierleyi* on pyrite found that EPS was not in significant proportion on the pyrite surface, with cells appearing in isolation or in small groups of no more than three in 168 h, achieving coverage no greater than 0.1 cell/mm^2. This suggests EPS is required for cell attachment, as the cells do not appear to attach to the pyrite surface and do not produce EPS in large enough quantities to attach. The lack of attachment may be due to preferential consumption of yeast extract rather than the mineral. This suggests that this archaeon does not directly interact with the surface, acting instead as a catalyst for oxidation of ferrous ions in solution via the indirect mechanism, or that the presence of yeast extract as a food source. After the removal of yeast extract from the growth medium, the lack of attachment and evidence of significantly less EPS production compared to the mesophilic bacteria supports the conclusion that *A. brierleyi* acts as a catalyst for oxidation of ferrous iron via the indirect mechanism.

The surface studies of *A. ferrooxidans* and *L. ferrooxidans* on pyrite showed EPS is produced early (2 h) upon exposure of new culture to the mineral surface, with bacterial colonies observed increasing in population on the surface over time. Changes occur in EPS composition as the initial attachment becomes the building of biofilm, with greater amounts of polysaccharides detected on the surface over short periods of exposure (2 h), and more proteinaceous character over longer periods of exposure. The larger amounts of hydrophilic polysaccharides [1-3] produced by *A. ferrooxidans* and *L. ferrooxidans* at 2 h exposure correlates with greater wettability of the pyrite surface compared to media controls of up to 18° and 36°, respectively. The proportion of EPS on the surface of pyrite exposed to *L. ferrooxidans* is greater, suggesting this strain would be ideal for EPS extraction experiments, and that fewer cells are required for better separation. This is important for bioflotation, as short processing times, low cell concentrations and high EPS production by these cells will reduce cost and increase production.

In the presence of yeast extract, *A. brierleyi* appears to create only a small improvement made to pyrite wettability, with the greatest difference of 16° observed at 24 h compared to the control pyrite surface. The surface of the control pyrite in the presence of yeast extract also showed much greater hysteresis that the mesophilic control, suggesting a more heterogeneous surface, while the similarity between the control and biotic pyrite suggests potential yeast extract contamination of the surface. The removal of yeast extract promoted significant improvements in surface wettability of pyrite exposed to *A. brierleyi* of up to 30°. The hysteresis on the surface of the control is also improved compared by the removal of yeast extract, suggesting the yeast extract is making the surface more heterogenous, negatively impacting the effective interaction of bubbles with the pyrite. The improvement to pyrite wettability in the absence of yeast extract suggests cells are more actively oxidising the surface, and that the yeast extract inhibited pyrite oxidation. This is important for both bioleaching and bioflotation, as the archaea can survive at elevated temperatures than the mesophiles, closer to conditions in some flotation cells requiring the depression of galena or the use of oleate collectors of above 60 °C [4]. The removal of yeast extract, which causes unwanted effects on the mineral surface, has been proved to provide no significant benefit to cultures used for the purposes of mineral surface alteration, and as such its inclusion in media adds unnecessary cost to the use of *A. brierleyi* as a mineral modification agent.

In conclusion, the indirect contact mechanism has been successfully elucidated as the mechanism behind the interaction of the mesophilic bacteria with pyrite, while the indirect mechanism is behind the interactions of the thermophilic archaea with the mineral. Polysaccharides have been found to be major EPS components during the early stages of exposure for both *A. ferrooxidans* and *L. ferrooxidans*, with increased protein production occurring at longer exposure periods as cells

colonise the surface. Little EPS was found on the surface of pyrite exposed to *A. brierleyi*. All species accelerated the oxidation of the mineral surface over short periods of exposure, imparting decreased hydrophobicity to the sample. This suggests the time cells are harvested and the length of exposure to the mineral is of crucial importance to mineral surface modification by microorganisms and must be taken into consideration by future explorations into effective separation of minerals by bioflotation. The elevated temperature of the *A. brierleyi* culture was not found to decrease hydrophobicity in comparison to the mesophilic strain conditions, and the removal of yeast extract from the growth medium was found to be beneficial to future bioflotation applications. Each microorganism, and the EPS components they produce has the potential for wider application as bioflotation reagents.

8.2 Future Work

The findings of this thesis suggest significant improvements to pyrite hydrophobicity might be gained in early stages of exposure to microorganisms. To confirm these observations are true for separation by bioflotation, it will be necessary to perform corresponding microflotation experiments on single mineral. For effective separation, mixed ore should also be tested to assess selectivity for depression of pyrite by the cells.

There are still many challenges regarding the analysis and application of extracellular polymeric substances to bioflotation. The extraction of compounds in the EPS of the microorganisms investigated in this study needs to be refined, and the extracts then applied to microflotation tests to assess their suitability for larger scale bioflotation.

If a single EPS component can be identified that provides selectivity and improved recovery, it would provide an environmentally friendly alternative to chemical depressants currently used in industry.

8.3 References

1. Behera, S.K., Mulaba-Bafubiandi, A. F., *Microbes Assisted Mineral Flotation a Future Prospective for Mineral Processing Industries: A Review.* Mineral Processing and Extractive Metallurgy Review, 2017. **38**(2): p. 96-105.
2. Poorni, S., Natarajan, K. A., *Flocculation behaviour of hematite–kaolinite suspensions in presence of extracellular bacterial proteins and polysaccharides.* Colloids and Surfaces B: Biointerfaces, 2014. **114**(0): p. 186-192.
3. Vilinska, A., Hanumantha Rao, K., *Leptospirillum ferrooxidans-sulfide mineral interactions with reference to bioflotation and bioflocculation.* Transactions of Nonferrous Metals Society of China, 2008. **18**(6): p. 1403-1409.

4. Wills, B.A., *Wills' Mineral Processing Technology*. 7th ed, ed. T.J. Napier-Munn. 2006, Oxford: Elsevier. 444.